



Universidade do Porto  
Faculdade de Engenharia  
**FEUP**

# **A NEW HIGH POWER EFFICIENT ELECTRONIC CONVERTER FOR FUEL CELL APPLICATIONS**

Thesis submitted to the Degree of  
Doctor of Philosophy  
At the Faculty of Engineering of Porto University

Presented by  
Maria Teresa Duarte Barroca Delgado do Outeiro  
2012





Universidade do Porto

Faculdade de Engenharia

**FEUP**

# **A NEW HIGH POWER EFFICIENT ELECTRONIC CONVERTER FOR FUEL CELL APPLICATIONS**

Supervisor

Professor Doctor Adriano da Silva Carvalho

Faculty of Engineering of Porto University

Department of Electrical and Computer Engineering

University of Porto

PORTUGAL

Co-supervisor

Professor Doctor Rui Filipe Marques Chibante

Department of Electrical Engineering

Institute of Engineering of Porto

PORTUGAL





## ABSTRACT

Sustainable development requires a sustainable supply of clean and affordable energy resources that do not cause negative social impacts. The continuous drop in crude-oil production and the gradual increase in oil prices have emphasized the need for suitable alternatives to our oil-based economy. Clean and efficient technologies based on renewable energy sources must consider addressing this issue. In this context, the fuel cells can provide a clean energy for the future, as they produce electricity from hydrogen through an electrochemical process, which is virtually free of emissions and noise and only water and heat are the by-products. In addition, the fuel cells have several advantages such as; silent, high potential for cogeneration applications, adaptable to a wide range of power and applications.

The design and implementation of power generation systems based on fuel cells require careful selection of both the fuel cell model and the power converter. Therefore, a semi-empirical model of the PEM fuel cell is proposed in this thesis. In this context, a method to extract the parameters that characterizes the PEM fuel cell is secondary but also an important objective.

This thesis also proposes a new efficient high power converter to improve the performance and optimize the hydrogen consumption. The converter follows a resonant approach that provides low component stresses, high frequency operation, soft-switching commutation, and operation under a wide range of input and output conditions.

The control is divided into two parts, namely: i) the voltage controller, which is responsible for keeping constant the output voltage of the converter under loading variations and ii) the PEM controller, which is responsible for improving the performance by keeping the PEM fuel cell in its optimal operating point.

The experimental setup composed by a DC-DC converter and a PEM fuel cell were developed and the obtained results were analyzed. The results confirm the simulation ones that were performed using the MatLab/Simulink software.

In addition, the setup experimental allows us to extend the analysis to new loading conditions such as electrical vehicles and renewable energy sources like solar energy.

This thesis provides an accurate and useful tool for future research on these types of energy conversion systems.



## RESUMO

Para um desenvolvimento sustentável são necessários novos recursos energéticos de energia limpa e acessível e que não causem impactos sociais negativos. A diminuição contínua da produção de petróleo bruto e o aumento dos preços do petróleo têm enfatizado a necessidade de alternativas adequadas para a nossa economia baseada no petróleo. As tecnologias limpas e eficientes com base em fontes de energia renováveis têm vindo a ser exploradas para a resolução desta questão. Neste contexto, as células de combustível podem contribuir para uma energia limpa, uma vez que a energia que produzem a partir do hidrogénio resulta de um processo electroquímico que é virtualmente livre de emissões e ruído, no qual apenas água e calor são os subprodutos. Por outro lado, as células de combustível têm vantagens como, eficiência elevada em relação aos sistemas convencionais, são silenciosas, excelentes para aplicações em cogeração, e adaptáveis a uma vasta gama de potências e de aplicações.

O projeto e implementação de sistemas de geração de energia baseado em células de combustível exige uma cuidadosa seleção tanto o modelo de célula de combustível como do conversor de potência.

Assim é proposta uma abordagem semi-empírica para o modelo da célula a combustível e um método de extração dos seus parâmetros.

É proposto um novo conversor DC-DC, o qual se baseia no princípio da ressonância, cujo funcionamento em alta frequência e com comutação suave para uma ampla gama de condições de entrada e saída, bem como flexibilidade em termos de controlo lhe dão amplas vantagens sobre outros tipos de conversores. O controlo é composto por duas malhas a saber: i) pelo controlador de tensão, que é responsável por manter constante a tensão de saída do conversor, sob variações de carga e ii) pelo controlador da PEM, que é responsável pelo desempenho ótimo da PEM, ou seja, responsável por mantê-la no seu ponto ótimo de operação.

A configuração experimental, constituída pelo conversor DC-DC e pela célula de combustível permitiu a realização de ensaios, cujos resultados foram analisados. Os resultados experimentais obtidos confirmam os de simulação obtidos através do software MatLab/Simulink.

A configuração experimental desenvolvida permite analisar novas condições de carga, como veículos elétricos e outras fontes de energia renováveis como a energia solar.

Finalmente, esta tese fornece muita informação útil e constitui uma ferramenta precisa para os investigadores interessados neste tipo de sistemas de conversão de energia.



## ACKNOWLEDGEMENTS

First of all I thank the University of Porto and the Institute for Systems and Robotics (ISR-Porto) who have welcomed me to realize my PhD. Then and especially, I am grateful to Professor Dr. Adriano Carvalho, from which I received the guidance the support and supervision of my work. In fact, I have been very fortunate to have had the guidance and supervision of Professor Dr. Adriano Carvalho during my investigation because his great capabilities and competence in both academic and research areas have increased my knowledge. On numerous occasions, it was his experience, suggestions and encouragement that made the progress of the work possible. For all of that, I would like to express my gratitude to him. I am grateful also to Professor Dr. Rui Chibante for the support received in the implementation of the optimization method and parameters extraction of the PEM model and to the committee members of my PhD research, Professor Dr. Carlos Couto and Professor Dr. João Peças Lopes for their valuable suggestions, encouragement, time and concern. For the all friends, colleagues and Professors, who accompanied and helped me along this journey I say thank you. Specially, I would like to thank Professor Dr. António Pina Martins, Professor Dr. Armando Araújo and Professor Dr. Carlos Ramos of the Electrical Department of Engineering of Porto University and of course to Eng. Pedro Alves, for his enthusiasm, availability and great professionalism.

Many thanks to Professor Dr. Adélio Mendes, Dra Lúcia Brandão, José Luís Moreira and Roberto of the Chemical Department of Engineering of Porto University, for their support in the implementation and the tests made with the hydrogen.

I would like also to thank Professor Dr. Traça de Almeida of the Institute of Systems and Robotics of Coimbra University, who has encouraged me to start my investigation on fuel cells. I thank also Professor Dr. Alberto Cardoso and Professor Dr. Eduardo Saraiva of Coimbra University for the friendship and support they gave me.

I wish to express my deepest gratitude to my husband José and my sons Samuel and Isaac, for their love, support and great patience during this work.

Finally, I would like to thank the Foundation for Science and Technology (FCT) for the financial support received and the Institute of Engineering of Coimbra (ISEC) for the time and conditions provided for the realization of my PhD.



## AGRADECIMENTOS

Primeiro de tudo, eu agradeço à Universidade do Porto e ao Instituto de Sistemas e Robótica (ISR-Porto) por me terem acolhido para a realização do meu doutoramento. Depois e especialmente, eu agradeço ao Professor Dr. Adriano Carvalho, de quem eu recebi, o apoio orientação e supervisão durante a realização deste trabalho. Na verdade, eu tive a sorte de ter tido o apoio, orientação e supervisão do Professor Dr. Adriano Carvalho durante o meu doutoramento porque a sua grande capacidade de compreensão e competência em ambas as áreas, académicas e de investigação aumentaram os meus conhecimentos. Em numerosas ocasiões, foram a sua experiência, as sugestões e o seu encorajamento que tornaram o progresso dos trabalhos possível. Por tudo isso, expresso a minha gratidão ao Professor Dr. Adriano de Carvalho. Agradeço ainda ao Professor Dr. Rui Chibante o apoio recebido na implementação do método de otimização e extração de parâmetros do modelo da PEM e também aos membros da comissão de acompanhamento do meu doutoramento, Professor Dr. Carlos Couto e Professor Dr. João Peças Lopes, pelas valiosas sugestões, incentivos, tempo e preocupação.

Para todos os amigos, colegas e professores, que acompanharam e me ajudaram ao longo desta jornada eu digo, muito obrigado. Especialmente, gostaria de agradecer ao, Professor Dr. António Pina Martins, Professor Dr. Armando Araújo e Professor Dr. Carlos Ramos, do Departamento de Engenharia Electrotécnica da Universidade do Porto e, naturalmente ao Eng. Pedro Alves, pelo seu entusiasmo, disponibilidade e grande profissionalismo.

Agradeço ao Professor Dr. Adélio Mendes, à Dra Lúcia Brandão, ao José Luís Moreira e ao Roberto do Departamento de Engenharia Química da Universidade do Porto, por todo o apoio recebido na implementação e realização dos testes com o hidrogénio.

Gostaria também de agradecer ao Professor Dr. Traça de Almeida, do Instituto de Sistemas e Robótica da Universidade de Coimbra (ISR-Coimbra), o qual me incentivou a começar a minha investigação sobre as células de combustível. Agradeço ainda ao Professor Dr. Alberto Cardoso e Professor Dr. Eduardo Saraiva da Universidade de Coimbra pela amizade, apoio e disponibilidade que me deram.

Dirijo a minha mais profunda gratidão ao meu marido José e aos meus filhos Samuel e Isaac, pela enorme paciência, pelo amor e apoio constantes durante esta pesquisa.

Finalmente, agradeço à Fundação para a Ciência e Tecnologia (FCT) o apoio financeiro recebido, e ao Instituto Superior de Engenharia de Coimbra (ISEC), o tempo e condições proporcionadas para a realização do meu doutoramento.





*This thesis is dedicated  
to my guardians*



## TABLE OF CONTENTS

<i>Abstract</i> -----	i
<i>Acknowledgements</i> -----	v
<i>Table of contents</i> -----	xi
<i>List of symbols and abbreviations</i> -----	xviii
<i>List of figures</i> -----	xxi
<i>List of tables</i> -----	xxvi
<b>1. Introduction .....</b>	<b>3</b>
1.1. Motivation.....	3
1.2. Thesis objectives.....	4
1.3. Thesis organization .....	4
1.4. Thesis contributions .....	9
1.5. Publications.....	11
1.5.1. Book Chapters.....	11
1.5.2. Journals.....	11
1.5.3. Conference Proceedings .....	12
1.5.4. Presentation of speeches and seminars .....	13
<b>2. State of the art on fuel cells .....</b>	<b>17</b>
2.1. Literature review .....	17
2.2. Fuel cell types, comparison and selection .....	18
2.2.1. Classification of fuel cells based on their applications.....	18
2.2.2. Classification of the fuel cells based on the electrolyte .....	18
2.2.3. Fuel cell type selected.....	20
2.3. PEM fuel cell operation principle .....	21
2.3.1. Fuel cell losses .....	22
2.3.2. Optimal operating point .....	23
2.3.3. Summary description of the setups.....	24
<b>3. PEM fuel cell characterization.....</b>	<b>27</b>
3.1. Selection of the model.....	27
3.2. Electrochemical model of the PEM .....	27
3.2.1. Static analysis.....	28
3.2.2. Dynamic analysis.....	30
3.2.3. Efficiency and power .....	31
3.2.4. Parameters .....	32
3.3. Identification of the parameters.....	33

3.3.1.	Overview of optimization methods.....	33
3.3.2.	Selection of the optimization method.....	34
3.3.3.	Simulated Annealing (SA) .....	34
3.3.4.	Execution of the method.....	38
3.3.5.	Validation of the method .....	38
3.4.	<i>Identification of time constants.....</i>	39
3.5.	<i>Linear identification of the time constants.....</i>	39
3.5.1.	Poles system identification.....	40
3.5.2.	Transfer function in continuous-domain .....	40
3.5.3.	Validation of the method .....	41
3.6.	<i>Nonlinear identification of the time constants.....</i>	43
3.6.1.	Neural Network design .....	44
3.6.2.	Selection of the data for training and validation.....	45
3.6.3.	Training of the Network.....	45
3.6.4.	Performance and validation.....	46
3.7.	<i>Model of the PEM in MatLab/Simulink.....</i>	48
3.7.1.	Accuracy of the model implemented in MatLab/Simulink.....	49
3.8.	<i>Analysis of the static behaviour of the PEM.....</i>	49
3.8.1.	Influence of the temperature on the static behaviour of the PEM.....	51
3.9.	<i>Analysis of the dynamic behaviour of the PEM.....</i>	53
3.9.1.	Effect of the capacitor on the dynamic behaviour of the PEM .....	53
3.10.	<i>Conclusions .....</i>	54
<b>4.</b>	<b>State of the art on power converters for fuel cells and control .....</b>	<b>57</b>
4.1.	<i>Introduction.....</i>	57
4.2.	<i>Requirements for selecting the converter topology.....</i>	60
4.3.	<i>DC-DC converter topologies .....</i>	61
4.3.1.	Series resonant converter with capacitive output filter .....	63
4.3.2.	Series resonant converter with inductive output filter.....	64
4.3.3.	PWM full-bridge converter with inductive output filter.....	64
4.3.4.	Full-bridge converter with secondary side controlled .....	65
4.3.5.	Current-fed two-inductor boost converter.....	66
4.3.6.	Bidirectional current-fed converter.....	67
4.3.7.	Z-Source converter.....	67
4.4.	<i>Topology of converter selected .....</i>	69
4.5.	<i>Operation of converter selected .....</i>	70
4.6.	<i>Methods of control of DC-DC converters.....</i>	70

4.6.1.	Overview of control methods.....	71
4.6.2.	PID control.....	71
4.6.3.	Voltage control .....	73
4.6.4.	Current control.....	73
4.6.5.	Adaptive control .....	74
4.7.	<i>Methods of control of resonant converters.....</i>	75
4.7.1.	Variable frequency control.....	75
4.7.2.	Self-sustained oscillation control .....	76
4.7.3.	Optimal control .....	77
4.8.	<i>Structure of control selected.....</i>	78
4.9.	<i>Integration of energy storage devices .....</i>	79
4.9.1.	Energy storage options .....	79
4.10.	<i>Conclusions .....</i>	81
<b>5.</b>	<b>Design of the series resonant converter .....</b>	<b>85</b>
5.1.	<i>Introduction .....</i>	85
5.2.	<i>Constraints imposed by the fuel cell.....</i>	85
5.3.	<i>Requirements of ripples of current and voltage.....</i>	86
5.4.	<i>Converter design .....</i>	86
5.4.1.	HF transformer design .....	87
5.4.2.	Selection of the resonant components $L_r$ and $C_r$ .....	87
5.4.3.	PEM filter Design .....	88
5.4.4.	Output filter Design .....	89
5.5.	<i>Conclusions.....</i>	90
<b>6.</b>	<b>Modelling and Simulation results .....</b>	<b>93</b>
6.1.	<i>Model of the converter in MatLab/Simulink .....</i>	93
6.1.1.	Power circuit modelling .....	93
6.1.2.	Control circuit modelling .....	93
6.1.3.	Voltage control in MatLab/Simulink.....	95
6.1.4.	Frequency divider and gate drive signals in MatLab/Simulink .....	96
6.1.5.	PEM control in MatLab/Simulink.....	97
6.2.	<i>Simulation results.....</i>	104
6.3.	<i>Dynamics of the system.....</i>	105
6.3.1.	Output voltage and current.....	105
6.3.2.	VCO signal.....	105
6.3.3.	Effect of the VCO signal on variables of the system .....	106

6.3.4.	Resonant circuit operation .....	108
6.3.5.	Fuel cell voltage and current.....	108
6.4.	<i>PEM controller and optimization of the hydrogen consumption .....</i>	<i>109</i>
6.4.1.	PEM controller operation.....	109
6.5.	Conclusions.....	112
<b>7.</b>	<b>Experimental implementation.....</b>	<b>115</b>
7.1.	<i>Layout of the SRC.....</i>	<i>115</i>
7.2.	<i>Selection of power devices .....</i>	<i>116</i>
7.2.1.	Selection of the IGBTs .....	116
7.2.2.	Selection of the power diodes .....	117
7.3.	<i>Selection of the heat sinks.....</i>	<i>118</i>
7.3.1.	Types and materials of heat sinks .....	118
7.3.2.	Thermal equivalent Ohm's Law.....	119
7.3.3.	Selection of the heat sink for each module .....	121
7.4.	<i>Design of the magnetic parts.....</i>	<i>127</i>
7.5.	<i>Design of the inductors.....</i>	<i>127</i>
7.5.1.	Inductor of PEM filter.....	129
7.5.2.	Inductor of output filter .....	130
7.5.3.	Implementation of the inductors .....	131
7.6.	<i>Selection of the capacitors.....</i>	<i>132</i>
7.6.1.	PEM filter capacitor .....	132
7.6.2.	Resonant capacitor.....	132
7.6.3.	Output filter capacitor .....	132
7.7.	<i>Design of the high frequency transformer.....</i>	<i>134</i>
7.7.1.	Selection of the appropriate material and type of core.....	134
7.7.2.	Calculation of the primary and secondary turns number .....	137
7.7.3.	Calculation of the primary and secondary wire-diameter.....	137
7.7.4.	Software used in the design of the transformer .....	138
7.7.5.	Coil and core transformer data.....	139
7.7.6.	Analysis of the skin effect.....	140
7.7.7.	Electrical equivalent circuit.....	142
7.7.8.	Transformer parameters .....	143
7.7.9.	Selection of the transformer .....	144
7.8.	<i>Design and implementation of the control circuits .....</i>	<i>146</i>
7.8.1.	The voltage control oscillator.....	147
7.8.2.	The frequency divider.....	153

7.8.3.	Test and validation of the voltage control circuit.....	155
7.9.	<i>Design of the drive circuits</i> .....	157
7.9.1.	Requirements and protection of the gates .....	158
7.9.2.	Test and validation of the gate drive signals .....	161
7.10.	<i>Design of the PEM controller</i> .....	162
7.10.1.	Actions during $T_{ON}$ .....	163
7.10.2.	Actions during $T_{OFF}$ .....	164
7.10.3.	Test and validation of the PEM control signals.....	165
7.11.	<i>Test and validation of the signals to IGBT converter</i> .....	167
7.12.	<i>Output voltage measurement</i> .....	168
7.12.1.	Using a LEM sensor .....	168
7.12.2.	Using an optocoupler .....	169
7.13.	<i>Voltage regulator power supply</i> .....	171
7.14.	<i>Variation of the load</i> .....	173
<b>8.</b>	<b>Experimental results</b> .....	<b>177</b>
8.1.	<i>Introduction</i> .....	177
8.2.	<i>Dynamics of the system</i> .....	178
8.2.1.	Output voltage and current.....	178
8.2.2.	PI output.....	178
8.2.3.	Input voltage and current.....	179
8.2.4.	Resonant circuit operation.....	180
8.3.	<i>PEM control with optimization of the hydrogen consumption</i> .....	181
8.3.1.	PEM controller operation .....	181
8.3.2.	Effects of the PEM controller in the variables of the system .....	183
8.4.	<i>Conclusions</i> .....	186
<b>9.</b>	<b>Conclusions and future work</b> .....	<b>189</b>
9.1.	<i>Conclusions</i> .....	189
9.2.	<i>Suggestions for further work</i> .....	190
9.3.	<i>Personal retrospection</i> .....	192





## LIST OF SYMBOLS AND ABBREVIATIONS

### *Symbols:*

$A$	$\text{cm}^2$	Cell active area
$\vec{B}$	T(Tesla)	Magnetic flux density
$C$	Farad	Equivalent electrical capacitance
$C_{\text{PEM}}$	Farad	Capacitor of the PEM filter
$C_r$	Farad	Capacitor of the resonant circuit
$C_f$	Farad	Capacitor of the output filter
$C_T$	$\text{J}/^\circ\text{C}$	Thermal capacitance
$C_{\text{O}_2}$	$\text{mol}/\text{cm}^3$	Concentration of oxygen in the catalytic interface of the cathode
$E_{\text{Nernst}}$	V	Thermodynamic potential of the cell
$f_r$	Hz	Resonant frequency
$f_c$	Hz	Cut-off frequency
$f_s$	Hz	Switching frequency
$\vec{H}$	A/m	Magnetic field
$i_{\text{FC}}$	A	Cell operating current
$I_{\text{out}}$	A	Output current
$I_F$	A	Forward current
$J$	$\text{A}/\text{cm}^2$	Actual cell current density
$J_n$	$\text{A}/\text{cm}^2$	No-load current density
$J_{\text{max}}$	$\text{A}/\text{cm}^2$	Maximum current density
$L_{\text{PEM}}$	Henry	Inductor of the PEM filter
$L_r$	Henry	Inductor of the resonant circuit
$L_f$	Henry	Inductor of the output filter
$l_{\text{fe}}$	mm	Magnetic length of the core
$P_{\text{H}_2}$	atm	Partial pressure of hydrogen
$P_{\text{O}_2}$	atm	Partial pressure of oxygen
$P_{\text{FC}}$	W	Fuel cell output power
$P_{\text{out}}$	W	Output power
$P_{\text{loss}}$	W	Loss power
PF	-	Power factor
Q	-	Quality factor
$R$	$\Omega$	Real part of Z
$R_M$	$\Omega$	Equivalent membrane resistance to proton conduction

$R_C$	$\Omega$	Equivalent contact resistance to electron conduction
$R_{js}$	$^{\circ}\text{C}/\text{W}$	Thermal resistance, junctions to heat sink
$R_{sa}$	$^{\circ}\text{C}/\text{W}$	Thermal resistance, heat sink to ambient
$R_{cs}$	$^{\circ}\text{C}/\text{W}$	Thermal resistance, case-to-heat sink
$T$	$^{\circ}\text{C}$ or $\text{K}$	Absolute cell temperature
$T_j$	$^{\circ}\text{C}$ or $\text{K}$	Maximum semiconductor junction temperature in
$T_s$	$^{\circ}\text{C}$ or $\text{K}$	Heat sink temperature
$T_a$	$^{\circ}\text{C}$ or $\text{K}$	Ambient air temperature
$V_{\text{act}}$	$\text{V}$	Voltage drop due to the activation of the anode and cathode
$V_{\text{ohmic}}$	$\text{V}$	Ohmic voltage drop
$V_{\text{con}}$	$\text{V}$	Voltage drop of concentration of the reactants gases
$V_{\text{out}}$	$\text{V}$	Output voltage
$V_{\text{ref}}$	$\text{V}$	Reference voltage signal
$V_d$	$\text{V}$	Dynamical voltage
$V_{\text{FC}}$	$\text{V}$	Cell output voltage
$V_F$	$\text{V}$	Forward voltage
$V_{\text{RRM}}$	$\text{V}$	Repetitive peak reverse voltage
$X$	$\Omega$	Imaginary part of $Z$
$Z$	$\Omega$	Impedance
$Z_r$	$\Omega$	Characteristic impedance of resonant circuit
$\omega$	$\text{rad/s}$	Operating angular frequency
$\omega_r$	$\text{rad/s}$	Resonant angular frequency

***Greek symbols:***

$\varepsilon$	-	Error measurement
$\lambda$	$\text{cm}$	Thickness of the membrane
$\rho_M$	$\Omega.\text{cm}$	Membrane specific resistivity
$\eta$	%	Efficiency
$\mu_f$	-	Fuel utilization coefficient
$\xi_1$	-	Model coefficients
$\xi_2$	-	Model coefficients
$\xi_3$	-	Model coefficients
$\xi_4$	-	Model coefficients
$\psi$	-	Empirical parameter

$\tau$	s	Time constant
$\tau_{\text{error}}$	s	Error between experimental and simulated time constant
$\tau_{\text{sim}}$	s	simulated time constant
$\theta$	$^{\circ}\text{C/W}$	Thermal resistance
$\rho$	mm	skin depth
$\phi$	rad or $^{\circ}$	Phase angle

***Abbreviations:***

ARX	Autoregressive Exogenous Input method
BP	Back propagation algorithm
BJT	Bipolar Junction Transistor
GA	Genetic Algorithms
IGBT	Insulated Gate Bipolar Transistor
LF	Low frequency
MOSFET	Metal Oxide Semiconductor Field Effect Transistor
MLP	Multilayer-perceptron
MFC	Mass Flow Controller
MFM	Mass Flow Meter
n	Transformer turns ratio
NN	Neural Network
PEM	Proton exchange membrane
PWM	Pulse with modulation
RBF	Radial basis function
RMS	Root mean square
SA	Simulated Annealing
SRC	Series resonant converter
SQL	Sequential Quadratic Programming
SLM	Standard Liters per Minute
ZVS	Zero-voltage switching
ZCS	Zero-current switching
PID	Proportional, integral and derivative control
$k_P$	Proportional gain
$k_D$	Integral gain
$k_I$	Derivative gain

VCO	Voltage control signal
SSOC	Self-sustained oscillation control
VF	Variable frequency
LQR	Linear quadratic regulator control
Vref	Reference voltage
HF	High frequency

## LIST OF FIGURES

Figure 2.1 – Classification of the fuel cells based on their applications.....	19
Figure 2.2 - Scheme of a single cell.....	21
Figure 2.3– Typical polarization curve of a PEM fuel cell.....	23
Figure 3.1 – Electrical equivalent circuit of the PEM fuel cell.....	28
Figure 3.2 –Dynamic block model implemented in MatLab/Simulink. ....	31
Figure 3.3 – Typical graphs of the efficiency and the electrical power of a PEM fuel cell.....	32
Figure 3.4 – SA and its local and global minimums. ....	35
Figure 3.5 – Flowchart of the SA algorithm. ....	35
Figure 3.6 - Performance of SA. ....	38
Figure 3.7 - Temperature of the PEM for different values of the load. ....	41
Figure 3.8 – Validation of ARX function for 18A.....	42
Figure 3.9 –Validation of ARX function for 28A.....	42
Figure 3.10 – Estimated results for $\tau_1$ . ....	43
Figure 3.11 – Estimated results for $\tau_2$ . ....	43
Figure 3.12 – Architecture of the NN selected. ....	44
Figure 3.13 – Data used to train the Neural Network. ....	46
Figure 3.14– Performance of the NN method.....	47
Figure 3.15 –Accuracy of the NN method.....	47
Figure 3.16 - Validation of the NN for 18A .....	48
Figure 3.17 - Validation of the NN for 28A. ....	48
Figure 3.18– Fuel cell subsystem models implemented in MatLab/Simulink.....	48
Figure 3.19 – Circuit of test of the static behaviour of the PEM model. ....	50
Figure 3.20 – Output voltage and power of the static behaviour of Nexa <sup>TM</sup> . ....	51
Figure 3.21 – Fuel cell stack voltage for different temperatures values. ....	52
Figure 3.22 - Effect of the capacitor value on the output voltage.....	53
Figure 3.23 - Effect of the capacitor value on the electrical power. ....	53
Figure 4.1 – DC-DC power converter family tree. ....	58
Figure 4.2 – Switching loci trajectories of the diferent converter types. ....	58
Figure 4.3 - General structure of a resonant converter, where ZVS or ZCS can be obtained. ....	59
Figure 4.4 - Voltage-fed topologies for fuel cells.....	60
Figure 4.5 - Current-fed topologies for fuel cells. ....	60
Figure 4.6 - Configuration of a DC-AC converter interfaced directly to the grid. ....	62

Figure 4.7 - Configuration of a DC-DC and a DC-AC converter. ....	62
Figure 4.8 - Configuration of a DC-AC and an AC-AC converter. ....	62
Figure 4.9 – Generic scheme of a DC-DC converter for fuel cell application. ....	63
Figure 4.10 - Series Resonant converter with capacitive output filter. ....	63
Figure 4.11 - Schematic of resonant converter with inductive output filter. ....	64
Figure 4.12 – Schematic of a PWM full-bridge converter. ....	65
Figure 4.13 – Schematic of full-bridge secondary controlled converter. ....	66
Figure 4.14 – Schematic of current-fed two-inductor boost converter. ....	66
Figure 4.15 – Schematic of a soft-switched bidirectional current-fed boost converter. ....	67
Figure 4.16 – Z-Source converter scheme. ....	68
Figure 4.17 - Operation modes of the Z-Source converter. ....	68
Figure 4.18 - Typical application for a Z –Source in fuel cell system. ....	69
Figure 4.19 – Electrical circuit of the SRC. ....	70
Figure 4.20 –Common methods used in the control of the DC-DC converters. ....	71
Figure 4.21 - PID control. ....	73
Figure 4.22 - Voltage mode control. ....	73
Figure 4.23 - Current mode control. ....	74
Figure 4.24 - Adaptive control. ....	75
Figure 4.25 - Variable frequency controller of a resonant converter. ....	76
Figure 4.26 - Self-sustained oscillation control of a resonant converter. ....	77
Figure 4.27 - Optimal control of a resonant converter. ....	78
Figure 4.28 - Structure of control selected for the SRC. ....	79
Figure 4.29 – Electrical energy storage options. ....	80
Figure 4.30 – Example of a power system application combining a fuel cell and super capacitors. ....	81
Figure 5.1 – Electrical circuit of the SRC. ....	86
Figure 6.1 –Implementation of the power converter circuit in MatLab/Simulink. ....	94
Figure 6.2 – Voltage control subsystem of the converter. ....	95
Figure 6.3 – Frequency control subsystem of the converter. ....	96
Figure 6.4 – Parameterization of the two continuous-time VCO blocks. ....	97
Figure 6.5 - Characterization of the optimal operating point of the PEM. ....	98
Figure 6.6 - Flowchart of PEM controller. ....	99
Figure 6.7 – PEM controller implemented in MatLab/Simulink. ....	100
Figure 6.8 – DELTA Subsystem. ....	101
Figure 6.9 – Parameterization of relay function in DELTA. ....	102

Figure 6.10 – Subsystem Vcontrol.....	103
Figure 6.11 – Parameterization of Relay function in Vcontrol.....	103
Figure 6.12 – Output voltage (Vout) and Current (Iout).....	105
Figure 6.13 – VCO signal .....	106
Figure 6.14 - Effects of the VCO on the amplitude of the output voltage.....	107
Figure 6.15 - Effects of the VCO on the frequency and amplitude of the resonant current. ....	107
Figure 6.16 – Output voltage and current and resonant circuit operation.....	108
Figure 6.17 - Fuel cell voltage and current. ....	109
Figure 6.18 – VCO signal. ....	110
Figure 6.19 - Output voltage and current.....	110
Figure 6.20 – Resonant voltage and resonant current. ....	111
Figure 6.21 - Fuel cell voltage and current. ....	111
Figure 7.1 – Layout of the SRC implemented experimentally. ....	115
Figure 7.2 – a) Equivalent Circuit of an IGBT and b) Symbols of the IGBT.....	116
Figure 7.3 – circuit diagram of IGBTs module F4-50R12MS4.....	117
Figure 7.4 – Extruded heat sink profiles commercially available.....	119
Figure 7.5 – Thermal semiconductor example and its equivalent circuit. ....	120
Figure 7.6 – Graph of the output characteristic of IGBT module, $I_C = f(V_{CE})$ . ....	122
Figure 7.7 – Average forward power versus average forward current. ....	124
Figure 7.8 – Average current versus temperature ambient. ....	124
Figure 7.9 – Dimensions of the heat sink profile –PADA N° 8175.....	125
Figure 7.10 – The ferrite cores E/20/21/30 of Siemens and P66/56 of Ferroxcube.....	131
Figure 7.11 – Typical Magnetic core of an HF transformer. ....	134
Figure 7.12 – Typical hysteresis curve of a ferromagnetic material.....	135
Figure 7.13 – Hysteresis of UI93/104/30 for N27 material at 25°C (Blue) and 150°C (Black). ....	135
Figure 7.14 – Appearance and magnetic characteristics of ferrites UI and EE. ....	136
Figure 7.15 – Preparation of ferrite for the HF transformer of type A. ....	137
Figure 7.16 – Full-Bridge Push-Pull Converter topology.....	138
Figure 7.17 – Skin effect exemplification (a) depth (b) LF operation, (c) HF operation. ....	141
Figure 7.18 – Wire impedance versus skin depth. ....	142
Figure 7.19 - Transformer equivalent circuit referred to the primary.....	142
Figure 7.20- Schemes of test transformer. ....	144
Figure 7.21 - Modular scheme of the main blocks of control.....	146
Figure 7.22 – Modular scheme with the device names.....	147

Figure 7.23 – Orcad scheme of voltage control oscillator.....	148
Figure 7.24 - Internal schemes of INA101 and AD706.....	148
Figure 7.25 - Reference voltage signal (Vref) to INA101.....	149
Figure 7.26 - Output-offset voltage. ....	150
Figure 7.27 - Simplified "block diagram" of an NE555.....	151
Figure 7.28 - Schematic of the NE555 in astable operation. ....	152
Figure 7.29 - Schematic of the HEF4013B. ....	153
Figure 7.30 - Schematic of the NE555 in monostable operation.....	154
Figure 7.31 – Layout of the voltage control oscillator circuit. ....	155
Figure 7.32 –Response of PI to the error signal produced in INA. ....	156
Figure 7.33 – Oscillator response to the PI controller signal produced in AD706.....	156
Figure 7.34 –Period of oscillation showing the charge and discharge of the capacitors at pin6.....	156
Figure 7.35 – Frequency divider performed by the 4013B device. ....	157
Figure 7.36 - Schematic of the driver circuits for the IGBTs 2 and 4. ....	160
Figure 7.37 - Layout of the drive circuits for IGBT2 and IGBT4.....	161
Figure 7.38 – Gate driver circuits of the IGBTs.....	161
Figure 7.39 - Principle of operation and components involved controlling the PEM.....	163
Figure 7.40 – Orcad schematic of the PEM control circuit. ....	165
Figure 7.41 – Layout of the frequency divider and PEM control circuits.....	165
Figure 7.42 – Signals at pins 3 and 6 of the NE555 of the PEM and input of relay. ....	166
Figure 7.43 – Signals of input relay and perturbation of NE555 of the converter. ....	166
Figure 7.44 – Signals at capacitor C' with emphasis to its discharge time $\ll 1s$ . ....	166
Figure 7.45 - Layout of IGBT module and pins number.....	167
Figure 7.46 – Conduction of IGBTs 2&4.....	167
Figure 7.47 - Schematic of the LEM sensor.....	169
Figure 7.48 - Experimental implementation of LEM sensor board.....	169
Figure 7.49 - Schematic of the Optocoupler 6N136.....	170
Figure 7.50 - Schematic of the power supply source (+/- 15V). ....	172
Figure 7.51 - Experimental implementation of the voltage regulator power supply (+/- 15V). ....	172
Figure 7.52 – Control of the load. ....	173
Figure 8.1- Experimental setup in the laboratory I-002 of FEUP. ....	177
Figure 8.2 – Output voltage (Vout) and Current (Iout). ....	178
Figure 8.3 - Output of PI. ....	179
Figure 8.4 – Input voltage and current with improvement of the controller. ....	180



Figure 8.5 – Output voltage and current and resonant circuit operation.....	180
Figure 8.6 –Principle of operation of the PEM controller. ....	181
Figure 8.7 - PEM controller operation. ....	182
Figure 8.8 - Effects of the perturbation on VCO signal and currents. ....	184
Figure 8.9 – Effects of the perturbation on VCO signal (pin 6 of NE555).....	184
Figure 8.10 - Effects of the perturbation on ifc, vfc and Iress. ....	185
Figure 8.11 - Effects of the perturbation on the amplitude of resonant current.....	185

## LIST OF TABLES

Table 2.1 – Characteristics of the fuel cells based on their electrolyte. ....	19
Table 3.1 – List of PEM fuel cell model parameters. ....	33
Table 3.2 - Time constants of several load levels.....	43
Table 3.3 – Accuracy of the PEM fuel cell model in MatLab/Simulink. ....	49
Table 3.4 –Static behaviour of the PEM Nexa <sup>TM</sup> . ....	50
Table 3.5 - Accuracy of the PEM fuel cell model considering the influence of the temperature. ....	52
Table 5.1 - Constraints imposed by the Nexa <sup>TM</sup> fuel cell.....	85
Table 5.2 - Constraints imposed by the Mark1020 fuel cell.....	85
Table 5.3 - Requirements of the converter .....	87
Table 5.4 - PEM filter components. ....	89
Table 5.5 - PEM filter components. ....	89
Table 6.1 – Summary of the PEM control actions performed. ....	98
Table 7.1 –Characteristics of IGBTs module F4-50R12MS4. ....	117
Table 7.2 – Power diode characteristics .....	118
Table 7.3 – Thermal conductivity of materials.....	119
Table 7.4– Thermal versus electrical characteristics.....	120
Table 7.5 – Thermal manufacturer characteristics of FP-40R12KE3 module. ....	121
Table 7.6 – Datasheet Information of module BYV255.....	124
Table 7.7 –Thermal resistance vs heat sink length of the profile PADA N° 8175. ....	126
Table 7.8 – Some of the heat sink profiles available in the lab. ....	126
Table 7.9 –Ferrite core options to perform the PEM inductor. ....	130
Table 7.10 – Ferrite core options to perform the output filter inductor.....	130
Table 7.11 – Summary of the specifications of the inductors and capacitors. ....	133
Table 7.12 – Output data for the converter (Nexa).....	139
Table 7.11 – Information of core selected for the HF transformer.....	140
Table 7.14 – Skin depth versus available area of a round conductor for various frequencies .....	141
Table 7.15–Parameters of each HF transformer implemented experimentally .....	145
Table 7.16 – Specifications of the gate drive circuitry HCPL-3120. ....	157
Table 7.17 – Recommended operation conditions of the IGBT/Mosfet driver HCPL-3120. ....	158
Table 7.18 – IGBT parasitic capacitances. ....	159
Table 7.19 - Summary of the gate signal for each igbt.....	162
Table 7.20 – Specifications of the OMROM Relay. ....	164

Table 7.21 – Specifications of the voltage transducer LV25P.....	168
Table 7.22 – Specifications of the voltage regulated L200.....	171



---

# *CHAPTER 1*

## **INTRODUCTION**

---



# 1. INTRODUCTION

## 1.1. Motivation

There has been an increased interest in the use of renewable energy sources, which is due to the limitations in fossil fuel reserves and to planet pollution. The research in the new sources of energy, such as photovoltaic, wind and fuel cells can be used to enhance the safety, reliability and sustainability of the planet, because they are environmentally friendly, highly efficient and renewable cycles. Particularly the fuel cells appear in this context as an attractive power source because of their inherently clean, efficient and reliable service. They generate electricity from hydrogen through an electrochemical process. Therefore, they are essentially energy converters. Fuel cells resemble batteries in many ways, but in contrast to them they do not store the chemical energy: fuel has to be continuously provided to the cell to maintain the power output. In this context two relevant areas of research can be defined such as, firstly, in the optimization of the electrochemical process. fuel cells are still in a stage of free development, with many issues still unresolved and consequently, several models have been presented in the literature [1-9]. These models are normally established based on analytical formulations of the electrochemical process, based on the behaviour of some parameters, which reflects mainly the physical and chemical phenomena that occur within the cell. However, only a minor interest is paid to its dynamics and control. Then a goal of this thesis is to contribute to a better understanding of its dynamics and to suggest a new control strategy that maximizes its efficiency.

Secondly, in the investigation of power electronic converters and its integration with the fuel cells as energy generator clearly allows the checking of the appropriate characterization of the load present to the cell. In fact, the fuel cell systems can also be classified according to their applications, with the two major types, namely automotive and stationary applications. Due to their diversity and complexity, these applications have sometimes low-efficiency energy. In particular, the output characteristic of the power generated by the cell is highly nonlinear, which requires the system to be optimized for a given value of current when the output voltage is well defined (search of the optimal operation point).

Thus, the optimization of the energy provided by the fuel cell system is only possible with a method of control capable of following this optimum operation point, with maximum power transferred from source to load. Accordingly, it is important to select the appropriate power conversion circuits

and systems with high frequency switching and control that improves the performance and simultaneously optimizes the cost, size, and weight of the power system.

## **1.2. Thesis objectives**

The main objective of the thesis is the design and implementation of a power generation system based on fuel cells. Accordingly, the design and implementation of an efficient high power converter system is presented. Moreover the objectives include also the adoption of an accurate model for the PEM fuel cell and the analysis of its performance. A method to extract the parameters of the PEM fuel cell is in this context secondary, but also an important objective of the thesis. A particular attention is done to the controller, which ensures a constant output voltage of the converter, in order to satisfy the requirements of the power system application and simultaneously keeps the PEM operating within its optimum operating point.

## **1.3. Thesis organization**

The thesis is divided into two main parts. The first part starts with the selection of the fuel cell type presented in chapter 2. Its characterization is done in chapter 3, using a simplified electrochemical model whose parameters are determined by comparing the simulation and experimental results for different commercial fuel cell systems. The Simulated Annealing (SA) algorithm was chosen to achieve this process. The second part begins in chapter 4 with the state of the art on power converters for fuel cells and once selected the converter type, the characterization, implementation and validation is presented in chapters 5, 6 and 7 respectively.

In order to make the document of the thesis more attractive to the reader, some details related to the characterization, analysis and implementation have been treated in appendix. Consequently, in Appendix A, a more detailed analysis of the PEMs characteristics is made. The Appendix B, presents an approach of the PEM modelling using the neural networks, the Appendix C presents a numerical analysis of the resonant converter, in particular the series-resonant full-bridge topology, the Appendix D is focused on the operation of the series resonant converter and finally the Appendix E provides some useful considerations about the safe use of the hydrogen and methodologies adopted during this research.

Below it is presented a brief summary of each chapter in order to provide the reader with a quick way to query the various addressed subjects .



## **Chapter 1:** Introduction

**Summary:** This chapter introduces the thesis main goal, motivations, objectives and contributions. A summary of each chapter is presented as well as the list of publications made during this research.

## **Chapter 2:** State of the art on fuel cells

**Summary:** This chapter provides first a general approach to the various types of fuel cells, according to their type of construction, implementation and application. A comparative analysis of the different types of fuel cells, currently available in the market, their advantages, disadvantages and common applications suited to each type are presented. This comparison has led to the selection of the PEM fuel cell type to be used among the various types analyzed due to its simplicity, low operating temperature, easy maintenance, and effectiveness, among others. The principle of operation of the PEM fuel cell is presented. The optimum operating condition, which gives the maximum output power with minimum use of hydrogen for a certain power condition is also presented as well as a brief description of the various used setups.

## **Chapter 3:** PEM fuel cell characterization

**Summary:** The model of the PEM fuel cell is defined and characterized in this chapter. After the analysis and comparison of different type models for fuel cells, the electrochemical model is selected. The selected model is based on a theoretical approach, characterized by some parameters, which are difficult to determine. The solution that has been found to overcome this problem is through an optimization process. In this context the Simulated Annealing (SA) algorithm was selected. The SA is a random-search technique, which exploits the analogy between the way in which a metal cools and freezes into a minimum energy crystalline structure (the annealing process) and the search for a minimum in a more general system. The SA has a major advantage over other methods due to its ability to avoid becoming trapped in local minima.

A short explanation of the PEM model implemented in MatLab/Simulink is presented, followed by the analysis of the static and dynamic behaviour of the PEM fuel cell, as this is a very important issue in researching control strategies for electronic converters applied to fuel cells.

The chapter finishes with the analysis of the electrical and thermal time constants, which are identified and characterized based on linear and non-linear approaches, which showed to be suitable to predict each values variable. The analysis and conclusions obtained in this chapter are of extreme

importance before grouping the PEM fuel cell and the DC-DC converter because only the exact knowledge of the static and dynamic behaviour of the PEM allows at getting good results

#### **Chapter 4:** State of the art on power converters for fuel cells and control

**Summary:** a literature review on the DC-DC converters is made. Suitable topologies of power converters for fuel cells are discussed and compared. The selection of the topology for the application is made. Suitable methods of control of DC-DC converters are presented and compared; the disturbances influencing the behaviour of the converter and its stability are considered in the analysis. The control structure of the system is made. The energy storage technologies such as batteries, super capacitors, and flywheels, which can be applied to operate the fuel cell efficiently, were also discussed in this chapter. A power system combining fuel cell and super-capacitors is presented as an application example.

#### **Chapter 5:** Design of the series resonant converter

**Summary:** The design of the series resonant converter is made in accordance either with the constraints imposed by the fuel cell or with the requirements of the resonant converter. In particular the design has respected the requirements of voltage, current and power to be transferred. Thus, this chapter summary characterizes the conversion system components, namely; the HF transformer, the resonant components and filters. Since this is an extensive and delicate topic, it was decided to make a close relationship with the experimental implementation, which is presented in Chapter 7 and the analysis of the SRC, which is presented in Appendix C.

#### **Chapter 6:** Modelling and Simulation

**Summary:** An accurate model of the global system is implemented in Matlab/Simulink. Once defined the structures of power and control, the implementation in MatLab/Simulink software is presented and the simulation results are presented and discussed. the comparizon between those and the experimental ones is made. The comparison between these and the corresponding experimental is made.

#### **Chapter 7:** Experimental implementation

**Summary:** Once characterized and validated the power elements and the strategy of control of the SRC, the experimental implementation of the SRC is presented in this chapter. Similarly to simulation this chapter is divided in two main components namely: the power chain and the system controller. The power component comprehends the selection of the devices, dimension of the heat

sinks and the design and implementation of the magnetic parts such as; the inductors and the HF transformer. Accordingly the capacitors are also selected and implemented. The control component comprehends the design and implementation of several PCB boards, namely: 1) VCO control board that implements the PI controller and gives the reference of control to the VCO, module 2) FREQUENCY control board, which includes the frequency-divider circuit and actuation in the operating point of the PEM, 3) PCB boards to driver the IGBTs, 4) the LEM board, which measures the output converter voltage, processes it and gives this information to the controller and a 5) variable voltage regulated power source.

## **Chapter 8: Experimental results**

**Summary:** After a brief presentation of the complete system implemented in the laboratory, this chapter analyses the results focusing the two major points, such as:

### **1) The stability of the system**

The stability of the system is demonstrated through the analysis of the voltage control loop of the converter, with the output voltage remaining constant even for load variations imposed to the system. The dynamics of the system is evaluated by the analysis of the PI control signal to step-up and step-down of load condition. And it is also demonstrated that the controller of the resonant converter suits perfectly the variations of load imposed to the system by changing its operating frequency correspondently.

### **2) The PEM control with optimization of the hydrogen consumption**

The characterization of the optimum point of operation as function of the hydrogen consumption is presented.

The experimental results allows at concluding that the researched system provides excellent stability, robustness and good dynamic response making it a strong candidate for industrial applications in various areas of energy in accordance with the current tendencies in the sector.

## **Chapter 9: Conclusions and suggested future work**

**Summary:** In accordance with the motivations and the objectives defined in Chapter 1, this chapter summarizes the main conclusions of the thesis and gives some suggestions for further improvements on the system and implementation of new ideas to investigate.

## **Appendix A:** PEM's characterization

**Summary:** The main characteristic of the various PEM's used is presented in this Appendix. Particularly, the analysis of the output voltage, the output power, the efficiency and the hydrogen consumed were analyzed. The SA was applied to each case, and it was always verified a high correlation between the experimental results and those obtained with the model, allowing the extraction of parameters safely. Despite the similarities between the various systems analyzed it was positive to investigate all of them because each one in its own way contributes to enrich the research presented in this thesis.

## **Appendix B:** Model of the PEM in Neural Networks

**Summary:** In this Appendix a Neural Networks model as an alternative to the analytical and empirical modelling methods characterizes the PEM fuel cell. A multilayer perceptron trained by the Levenberg-Marquardt Back Propagation (BP) algorithm is used. The NN proves to be well adapted to predict the behaviour of the PEM, however, the NN model operates like a “black box” and no detailed information about the PEM system is provided.

## **Appendix C:** Numerical analysis of the series resonant converter

**Summary:** The analysis of the SRC is presented in this Appendix based on sinusoidal approximation and on second-order differential equation methods. The analysis based on sinusoidal approximation neglects the harmonics of the switching frequency, and the resonant waveforms are assumed to be purely sinusoidal. The analysis based on the second order differential equation the analysis led to the selection of the resonant components, which in turn determined the frequency of operation of the system. as well as the maximum power transferred.

## **Appendix D:** Operation of the series resonant converter

**Summary:** The simulation results of the series resonant converter model implemented in Matlab/Simuink software are analyzed and discussed in open loop and closed loop operating conditions. A special attention is given to the control component of the system, with detailed explanation to each subsystem, namely: the voltage control, the frequency control and the PEM control subsystems.

## **Appendix E:** Considerations on handling hydrogen safety

**Summary:** this appendix provides some useful information about some procedures that have been taken during this work thesis for a safe handling of the hydrogen.

## 1.4. Thesis contributions

The main contributions of the thesis can be summarized as follows:

### *On the Efficiency and Optimization of the System:*

The development and implementation of a power generation systems based on PEM fuel cells is the main contribution of the thesis. The efficiency of the system is improved on both sides; that is, by the adoption and optimization of an accurate dynamic model for the PEM fuel cell and by the selection, design and implementation of a high efficient DC-DC conversion system.

### *On the Efficiency of the DC-DC Power Converter:*

To improve the conditions of energy transfer generated by the PEM fuel cell with minimum of losses with maximum efficient conversion, a DC-DC series resonant converter is selected, designed and implemented. The thesis provides a guideline for the design of an SRC, assuming that the converter operates with a well-defined input voltage range, a well-defined output power range and a maximum frequency operation. This guideline intends to be a very useful tool for designers to select the optimum values, which ensure the maximum transfer of power for this type of system.

Through the adoption of a new control structure well adapted to the characteristics of the PEM fuel cell, the following objectives were achieved: 1) a constant output voltage of the converter for any load condition, 2) a minimum of switching losses in the converter due to the soft-switching commutation and 3) the PEM fuel cell operating in its optimal operating point i.e., with maximum efficiency.

### *By the Adoption of an Accurate PEM Fuel Cell Model with Optimum Parameters:*

The adoption of an accurate model for the PEM, which faithfully reproduces the electrochemical process involved and inserts it effectively in the electrical circuit. At this point the thesis also contributes to the implementation of the method of SA to extract the parameters of the model.

### *Development of an Accurate Model of the Complete System in Matlab/Simulink:*

An accurate model of the complete system is implemented in Matlab/Simulink. The model developed is an excellent tool to help designers in the analysis and development on this and similar systems.

*Prototype Implementation:*

Implementation of a converter prototype to validate the results obtained. In particular:

- 1) Validating the controller of output voltage.
- 2) Validation of the controller's point of optimal PEM.

In addition, the prototype allows for the extension to new load types such as electrical vehicles and new sources like solar energy.

## **1.5. Publications**

### **1.5.1. Book Chapters**

R. Chibante, M. T. Outeiro, A. S. Carvalho, “Simulated Annealing as a method to support parameters identification for power electronics systems, in *Advances in Mathematics Research*, Chapter 1, Volume 11, Nova Science Publishers Inc., 2010. ISBN: 1608769704.

A. S. Carvalho, M. T. Outeiro, "MatLab/Simulink as accurate design tool of electrical power systems and power electronics", in "MatLab / Book 3", Edited by InTech an Open Access publisher of Journals and Books, 2011.ISBN 978-953-307-315-6.

### **1.5.2. Journals**

M. T. Outeiro, R. Chibante, A. S. Carvalho, A. T. de Almeida, “A Parameter Optimized Model of a PEM Fuel Cell Including Temperature Effects”, *ELSEVIER, Journal of Power Sources*. Doi:10.1016/j.jpowsour.2008.08.019. Available Online.

M. T. Outeiro, R. Chibante, A. S. Carvalho, A. T. de Almeida, “A new parameter extraction method for accurate modelling of PEM fuel cells”, *WILEY INTERSCIENCE, International Journal of Energy Research*. DOI: 10.1002/er.1525. Available Online.

M. T. Outeiro, A. S. Carvalho, “Control Strategy for Minimum Hydrogen Consumption in PEM Fuel Cell”, *ELSEVIER, International Journal of Hydrogen Energy*. Submitted in February 2012.

M. T. Outeiro, A. S. Carvalho, “Analysis Design and Implementation of an Isolated DC-DC Series-Resonant Converter for Improving the Performance of PEM Fuel Cell Systems”, *ELSEVIER, International Journal of Energy Conversion and Management*. Submitted in March 2012.

A. S. Carvalho, M. T. Outeiro, “Application of a DC-DC Series-Resonant Converter to improve the Efficiency of a PEM Fuel Cell”, *IEEE Transactions on Industrial Electronics*. Submitted in February 2012.

### **1.5.3. Conference Proceedings**

M.T. Outeiro, A. T. de Almeida, A. S. Carvalho, “Performance analysis of a proton exchange membrane fuel cell system (pemfc) applied to the distributed energy systems”, oral presentation at “ENESPE – Encontro Nacional de Equipamentos e Sistemas para a Poupança de Energia, Porto, Portugal, 13-14 December 2006.

M. T. Outeiro, R. Chibante, A. S. Carvalho, A. T. de Almeida, “Dynamic Modelling and Simulation of an Optimized Proton Exchange Membrane Fuel Cell System”, XCLEEE - 10th Portuguese Spanish Congress in Electrical Engineering. Funchal, Madeira, 5-7 July 2007.

M. T. Outeiro, R. Chibante, A. S. Carvalho, A. T. de Almeida, “Dynamic Modelling and Simulation of an Optimized Proton Exchange Membrane Fuel Cell System”, “Proceedings of IMECE07 2007 ASME International Mechanical Engineering Congress and Exposition”, Seattle, Washington USA, 11- 15 November 2007.

M. T. Outeiro, R. Chibante, A. S. Carvalho, A. T. de Almeida, “Parameters Optimization of a PEM Fuel Cell through a Random-Search Technique”, 2nd Conference on Electrical Engineering - CEE’07, Institute of Engineering of Coimbra (ISEC), 26-28 November 2007.

M. T. Outeiro, A.J.L. Cardoso, R. Chibante, A. S. Carvalho, “Electrical and thermal time constants fuel cell system identification – a linear versus neural network approach”, “Proceedings of FuelCell2008 - Sixth International Fuel Cell Science, Engineering and Technology Conference, Denver, Colorado, USA, June 16-18, 2008.

M. T. Outeiro, R. Chibante, A. S. Carvalho, “A novel soft-switching dc/dc converter applied to improve the efficiency of a PEM fuel cell system, 35th Annual Conference of the IEEE Industrial Electronics Society (IECON’09) 3-5 November, Porto, Portugal, 2009.

M. T. Outeiro, A. S. Carvalho, “MatLab/Simulink as design tool of PEM fuel cells as electrical generation systems”, European Fuel Cell Forum 2011, Lucerne, Switzerland June 28 - July 1, 2011.



A. S. Carvalho, M. T. Outeiro, “Design and Validation of a new DC-DC Converter to optimize the efficiency of PEM Fuel Cell, III Iberian Symposium on Hydrogen, Fuel Cells and Advanced Batteries. Zaragoza, June 27<sup>th</sup> -30<sup>th</sup> 2011.

A. S. Carvalho, M. T. Outeiro “Accurate Matlab/Simulink model of a Power Generation System Based on Fuel Cells, 38th Annual Conference of the IEEE Industrial Electronics Society (IECON’12) 25-28 October, Québec, Canada, 2012. Submitted in March 2012.

#### **1.5.4. Presentation of speeches and seminars**

M. T. Outeiro, "Fuel Cells: Strategies of Control and Optimization ", Faculty of Engineering, Catholic University of Portugal (FEUCP), presentation made in the “Program of Colloquium of the Faculty of Engineering; Theme: "Engineering in the XXI Century" on February 18, 2010.

M. T. Outeiro, “MatLab/Simulink: Part1) Fuel Cell Modelling and Parameter Identification. Part2) Power Electronics Converter for Fuel Cell “, presentation made in Faculty of Engineering the University of Porto (FEUP), in the “Program of Colloquium of the "Industrial Electronics & Automation Group" of the Institute of Systems and Robotics (ISR-Porto) on July 28, 2010.



---

## *CHAPTER 2*

### **STATE OF THE ART ON FUEL CELLS**

---



## **2. STATE OF THE ART ON FUEL CELLS**

### **2.1. Literature review**

Fuel cells technology family shares the principle of electrochemical oxidation of the fuel and spatial separation of oxidation of fuel and reduction of oxidant. The history of the fuel cells began in 1839 when Sir William Grove, a British Scientist, discovered this technology. However, it did not have a great reputation, until the mid-90s, when fuel cells began to impose itself onto the space industry [10] . Shortly after that, several private companies became interested in fuel cell technology, but the economic and technological barriers were difficult to overcome. Despite their success in space programs, fuel cell systems were limited to space missions and other special applications, where high cost could be tolerated.

But, several innovations drove the cost of fuel cells down, especially those contributing to the development and viability of the PEM fuel cell systems. The most notable improvement was the invention of thin-film electrodes, which lead to reduction of platinum loading. Recently, the fuel cell has been revived and shows tremendous promise in the transportation and utility sectors.

They emerge as a highly promising alternative to the conventional power generation systems due to their high conversion efficiency, very low emissions, reliability, compactness, modularity, quiet operation and fuel flexibility [11]. In the last two decades, the automotive industry and distributed energy generation sector have been the main driving forces behind fuel cell research and development, and more recently the interest is extended to the power portable electronics, e.g. laptop computers, which is increased with the increasing requirements for higher energy density, specific energy and longer operational time.

The introduction of fuel cell systems into the power generation market as an alternative renewable energy source will not only supply clean renewable energy but it help reduce the dependence on oil, which is of crucial importance. Although fossil fuel reserves are still large, they are finite and the world's crude oil production is projected to peak sometime in the early 21<sup>th</sup> century. Moreover, fuel cells are ideal for distributed power generation applications, since they are clean, silent and efficient systems that make them suitable for remote locations. They are similar to batteries but with the advantage to continuously output production of electricity from an external fuel supply as opposed to the limited stored energy of batteries.

However, some of the limitations that need to be overcome before they can be utilized in a large-scale integration are the following: i) the high cost of the overall equipment, specially the catalyst material; ii) the short lifetime; and iii) the hydrogen storage and reforming will require additional

support systems. Therefore, current research aims to lowering the cost to a competitive level by replacing expensive materials and improving the performance. Moreover, fuel cell needs an additional power conditioning systems, which is necessary to integrate the low and fluctuation dc-output-voltage into the existing power systems. The power conditioning system must also take into account the problems associated with the relative long start-up process and the slow dynamic responses under transient load conditions, thus these devices should have fast dynamic response.

## **2.2. Fuel cell types, comparison and selection**

### **2.2.1. Classification of fuel cells based on their applications**

As shown in Figure 2.1, the fuel cell systems can be classified according to their application. The two major groups of fuel cell applications are the electric mobility and the stationary electrical energy generation. Stationary applications of fuel cell systems branch can be divided in two new groups namely: those functions as storage units and those functions as generators. When the FC system is used as a generator, it can be further divided into two groups: stand-alone and grid-connected systems. The stand-alone systems provide power without the grid, while the type of grid-connected systems can branch into applications that are grid-parallel and those that are grid-interconnected. In grid-parallel applications the power is used locally and it cannot be sanded to the grid. They do not need energy storage devices. In grid-interconnected applications the power can flow in both directions, from the FC system to the grid and vice-versa. In this case an energy storage device is required.

### **2.2.2. Classification of the fuel cells based on the electrolyte**

Fuel cells are usually classified in function of their electrolyte, temperature of operation, transported ion and fuel. Despite the difficulty to provide a comprehensive list of cell types under development today, some of the more common cells types available now are the following: the phosphoric acid fuel cell (PAFC), the proton exchange membrane fuel cell (PEMFC), the molten carbonate fuel cell (MCFC), the solid oxide fuel cell (SOFC) and most relatively new members of the fuel cell family is the direct methanol fuel cells (DMFC). A summary of these fuel cells types is presented in Table 2.1.

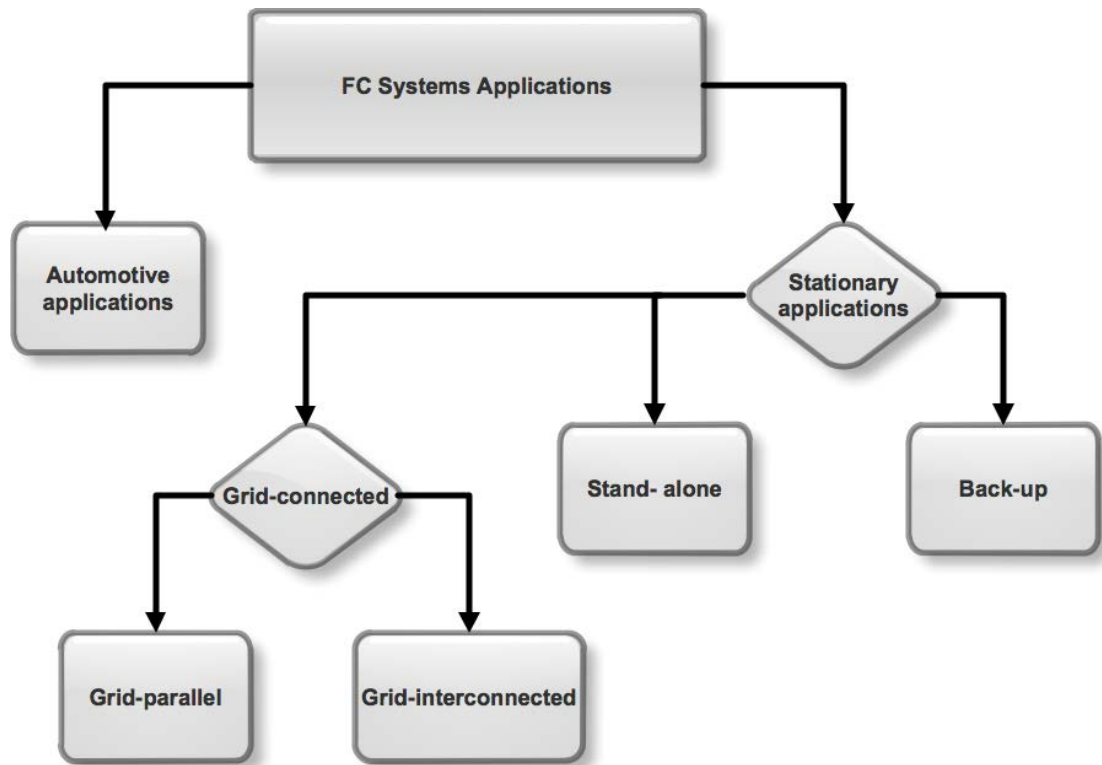


Figure 2.1 – Classification of the fuel cells based on their applications.

Table 2.1 – Characteristics of the fuel cells based on their electrolyte.

	PAFC	PEMFC*	MCFC	SOFC
<b>Electrolyte</b>	Phosphoric Acid	Membrane Polymer	Molten Carbonate	Ceramic
<b>Catalyst</b>	Platinum	Platinum	Nickel	Perovskites
<b>Temperature Operating</b>	400°C	50- 80°C	≈650°C	800-1000°C
<b>Output Power Range</b>	< 200 KW	50-250KW	10KW-2MW	< 100KW
<b>Electrical Efficiency</b>	40-80%	40-50%	60-80%	~60%
<b>Applications</b>	Distributed generation	Small distributed generation Backup power Portable power Transportation	Large distributed generation	Auxiliary power Large distributed generation

From Table 2.1 the molten carbonate fuel cells and solid oxide fuel cells are classified as high temperature fuel cells, while the others are low temperature fuel cells, even if the operating temperature of phosphoric acid and alkaline fuel cells exceeds 200 °C.

Phosphoric acid (PAFC) was the first commercial fuel cell type and also the most commercially developed today. They are used in hospitals, nursing homes, hotels, office buildings, schools, utility power plants and airport terminals. Phosphoric acid can also be used in large vehicles such as buses and locomotives fuel cells. They produce electricity with efficiency of 40% and cells operate at temperature closer to 400F [205°C].

Proton exchange membrane cells (PEMFC) operate at temperature about 200F [93°C] and have high power density. They can vary their output in function of the power demand, and they are suitable for small applications. Proton exchange membrane cells are promising fuel cell for vehicles applications where quick start-up is required.

The focus of molten carbonate fuel cells (MCFC) has been on larger stationary or marine power plants, where slow start-up time and large footprint are not an issue. These cells operate at very high temperatures (around 1200F [650°C]) and, therefore they cannot be used in small-scale applications.

The solid oxide fuel cell (SOFC) could be used in high-power applications including industrial and large-scale electricity generation stations. Some developers also see a potential use of the solid oxide use in motor vehicles. They are suitable for stationary and distributed power generation, either in heat and power cogeneration or hybrid systems with gas turbines. A solid oxide system usually uses a hard ceramic electrolyte instead of a liquid electrolyte, allowing operating temperatures to reach 1800F [980°C]. The efficiency of power generation could reach 60%.

Direct methanol fuel cells (DMFC), are similar to the proton exchange membrane cells in that they both use a polymer membrane as the electrolyte. However, in the DMFC, the anode catalyst itself draws the hydrogen from the liquid methanol, eliminating the need for a fuel reformer. Efficiencies of about 40% are expected with this type of fuel cell, which would typically operate at a temperature between 120–190°F (50–90°C). Higher efficiencies are achieved at higher temperatures.

### **2.2.3. Fuel cell type selected**

Considering the characteristics for each type of fuel cells described in previous sections, the PEM was selected, based on its low operation temperature, start-up characteristics, and high energy density. The PEM fuel cell power modules have many unique features when compared with other fuel cell types, such as relatively low operating temperature, high power density, and high



modularity. They can be used to different applications, in particular for mobile applications and small-scale power generation. They are special promising for vehicles applications where quick start-up is required. Two negative aspects are the easy contamination of the membranes with impurities; which requires ultra-pure hydrogen and the relative low-efficiency. Nevertheless, when compared to other fuel cell types these negative aspects are well acceptable, considering the objective of this thesis as above described.

### 2.3. PEM fuel cell operation principle

A fuel cell is a simple static device that converts the chemical energy of a fuel directly, isothermally, and continuously into electrical energy. In this process, only the reaction between hydrogen and oxygen occur. The only by-products are water and heat. Similarly to a battery, a fuel cell consists of two electrodes (anode and cathode) and an electrolyte. Whereas a storage battery contains all the substances in the electrochemical oxidation-reduction reactions involved and has therefore a limited capacity, the fuel cell is supplied with its reactants externally and operates continuously as long as it is supplied with fuel. The basic scheme for a single cell is represented in Figure 2.2.

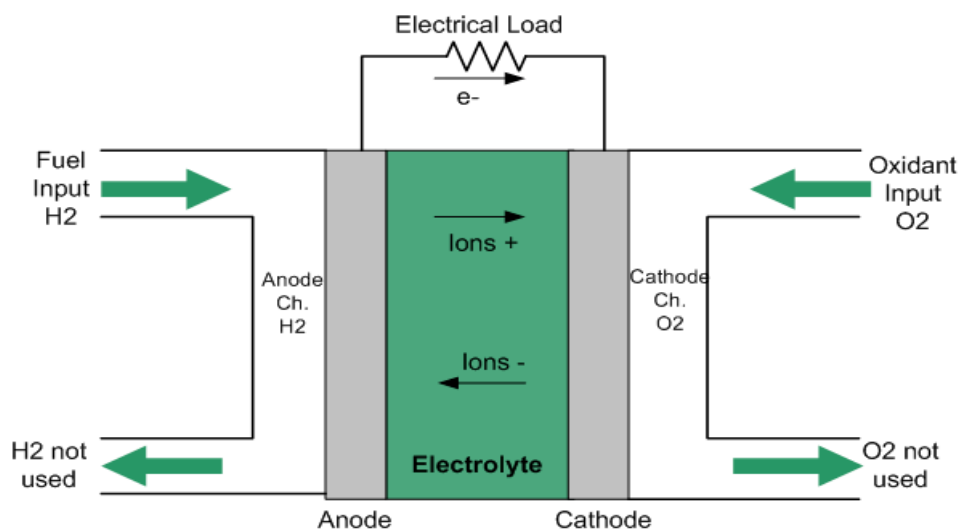
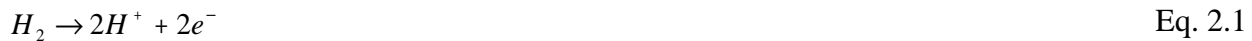


Figure 2.2 - Scheme of a single cell.

The electrochemical reactions involved in the process can be described as:

In the anode side, the diatomic hydrogen is injected through the anode channel in the separation plates and thereafter, distributed across the PEM and catalyst by the micro-porous Gas Diffusion

Layer. When the hydrogen gets near activation sites in the catalyst and transfer sites on the PEM, the molecules break up to single atoms and the hydrogen nuclei attach to the PEM. The electrons (e-) left behind attach to the conductive plate and are directed to an external circuit generating to produce electrical power. As the fuel cell produces power, some of the water from the cathode side permeates to the anode side increasing the efficiency of the proton transfer to the PEM. The equation that describes this reaction is shown below:



In the cathode side, the humidified air containing diatomic oxygen is distributed across the PEM and catalysts through the channels in the separation plates and micro-porous Gas Diffusion Layer. When the oxygen gets near activation sites in the catalyst, the molecules break up to single atoms. Electrons return from the external circuit and the cathode separation plate and the hydrogen protons (H+) are pulled from the PEM. Two electrons, two protons and an oxygen atom form a water molecule with the release of excess heat. The equation that describes this reaction is shown below:



Hence, the equation that describes the overall reaction is as follows.



### 2.3.1. Fuel cell losses

Figure 2.3 show the polarization curve of a typical single cell operating at normal air pressure. As is seen in the figure, there is a rapid initial fall in voltage (zone 1), after then the voltage falls slowly (zone 2) and at higher current the voltage falls rapidly again (zone 3). This voltage drop results from three major causes namely.

Activation losses (1): this voltage drop is caused by the slowness of the reaction on the surface of the electrodes. A proportion of the voltage generated is lost in driving the chemical reaction that transfers the electrons to or from the electrode.

Ohmic losses (2): This voltage drop results from the resistance to the flow of electrons through the material of the electrodes and the various interconnections, as well as the resistance to the flow of ions through the electrolyte. Hence, this voltage drop is proportional to the current.

Concentration losses (3): These result from the change in concentration of the reactants at the surface of the electrodes as the fuel is used. This is also called mass transport because the reduction in concentration is the results of the failure to transport sufficient reactant to the electrode.

Even though the theoretical maximum open circuit voltage is 1.23 V, the output voltage is normally 0.7 V. However the cells are normally associated in series forming a stack, to produce a useful voltage.

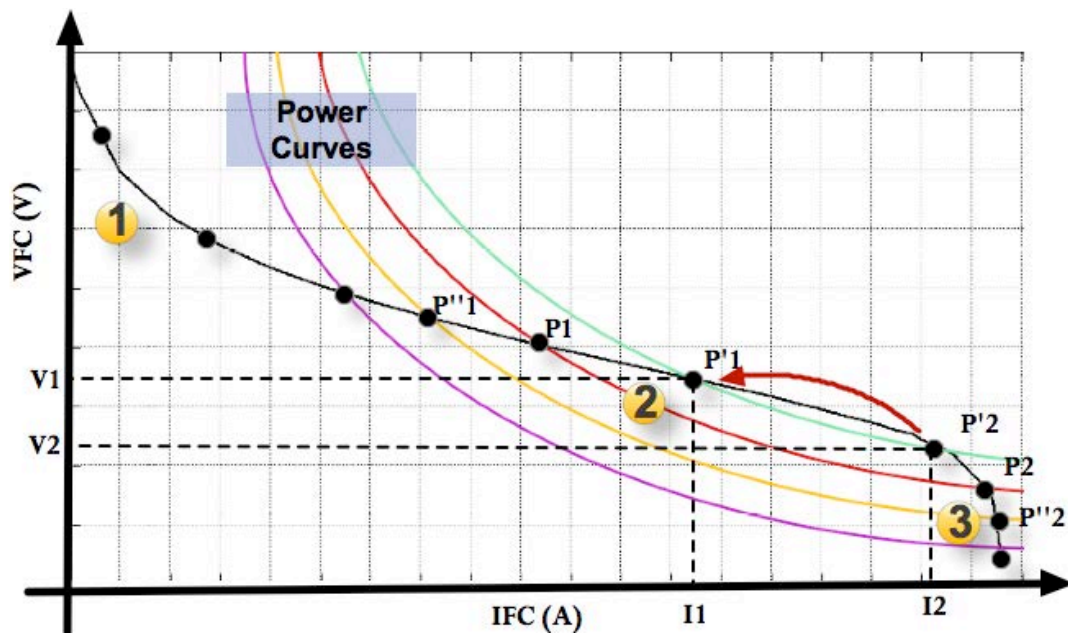


Figure 2.3– Typical polarization curve of a PEM fuel cell.

### 2.3.2. Optimal operating point

The operating condition of the PEM should be optimized to get maximum output power and minimum hydrogen consumption. To achieve the maximum output power with minimum use of hydrogen for a particular power condition, the operation of the PEM should be accomplished and maintained in an optimal operating point. As can be observed in Figure 2.3

Figure 2.3 each curve of power intersects the PEM polarization curve at two points P1 and P2. On the other hand, the hydrogen consume is proportional to the current requested to the fuel cell. Thus, the minimum hydrogen consumption for this power condition is given by the point of the polarization curve which satisfies the fuel cell current ( $I_{FC}$ ) as minimum and the fuel cell voltage ( $V_{FC}$ ) as maximum. The condition of optimal operating point of the PEM has led some researchers

[12-15] to find solutions to achieve it, in particular the investigation presented in this thesis, based on the following principle:

Considering a particular power condition  $P_i$  that intercepts the polarization curve at the points  $P'1$  and  $P'2$ , the optimal operation of the PEM consists basically of transfer the PEM operation from point  $P'2$  to point  $P'1$  during a time interval greater or equal than to five PEM time constants of the ( $\Delta t \geq 5 \times \tau_{PEM}$ ). Consequently the current requested to the PEM fuel cell moves from  $I_2$  to  $I_1$  with  $I_1 < I_2$  and  $V_1 > V_2$ .

### **2.3.3. Summary description of the setups**

Throughout the work done in this thesis, various setups of the PEM were used. In particular:

1. GENCORE 5B48 system of Plug Power [16] with a positive output nominal voltage of +48VDC, and an operating current range of 0-109 Amps and 5kW of power,
2. Nexa<sup>TM</sup> PEM system of Ballard [17], capable of providing 1.2kW with unregulated DC output voltage.
3. Mark1020 ACS fuel cell system, also a product of Ballard [17] scaled to meet power requirements from 300W to 5000W.
4. BAHIA didactic fuel cell system [18], exhibited at HELION Hydrogen Power. With 1kW of electrical power and 1kW of thermal power, enabling micro cogeneration investigation.

A detailed description of each of these systems is presented in the Appendix A.

---

# *CHAPTER 3*

## **PEM FUEL CELL CHARACTERIZATION**

---



### **3. PEM FUEL CELL CHARACTERIZATION**

#### **3.1. Selection of the model**

Many proton exchange membrane (PEM) fuel cell models have been reported in publications and some are available commercially. The process of selecting the fuel cell model needs to clarify what are the necessary features to take into account in the model [19] .

The model selection differs for each application and user and the initial decisions are important to avoid changes later in the model evaluation process. The theoretical models are normally detailed, and complex [20-23] and usually require large computation time. The semi-empirical models give a general voltage-current relationship without examining in depth the physical and electrochemical phenomena involved in the operation [2;7;24-27]. These models are usually characterized by simple implementation and faster simulation. Black-box models are typically described by neural networks, giving a relationship between the inputs and the outputs as well as the internal structure of the fuel cell system [28-30]. Neural Network models are relatively simple and are treated as non-parametric approaches, which can capture the non-linear characteristics of the system. They have the capability to recognise and associate patterns and because of their inherent design features, they can be applied to linear and non-linear problem domains. Their basic unit is the artificial neuron [31].

Faced to the objectives of the present work and the various types of models described above, two type models were investigated as the most appropriate, a semi-empirical model, which includes the static and dynamic analysis and a black-box model, which uses the Levenberg-Marquardt Back propagation (BP) algorithm to train the network. The first one is presented in this chapter as it presents characteristics satisfying the research needs of this work, while the second is presented in the Appendix B.

#### **3.2. Electrochemical model of the PEM**

The electrical equivalent circuit represented in Figure 3.1 corresponds to the semi-empirical model adopted. It includes the effects of the thermodynamic potential of the cell, and the activation, ohmic and concentration losses. The dynamics of the PEM system is represented by the capacitor C, which corresponds to the fuel cell phenomenon known as "charge double layer" on which the interface electrode/electrolyte acts as storage of energy element.

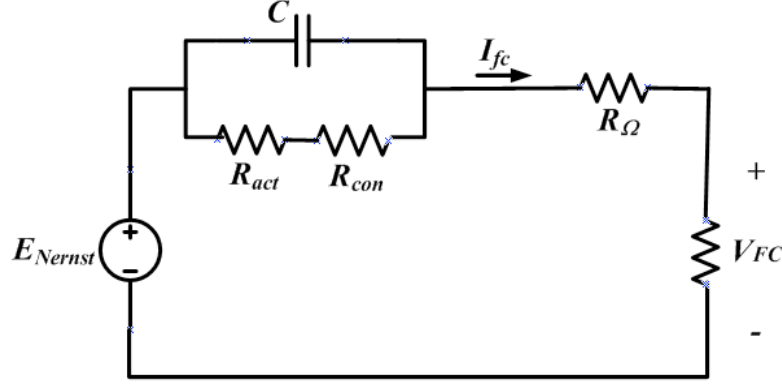


Figure 3.1 – Electrical equivalent circuit of the PEM fuel cell.

### 3.2.1. Static analysis

The static analysis of the PEM fuel cell is described in the model by a set of equations and corresponding parameters, which are essential for the analysis of its performance. Hence, for a single cell, the output voltage is defined through the following expression:

$$V_{FC} = E_{Nernst} - V_{act} - V_{Ohmic} - V_{con} \quad \text{Eq. 3.1}$$

For  $n$  cells connected in series, forming a stack, the voltage  $V_s$  is calculated by;

$$V_s = n \times V_{FC} \quad \text{Eq. 3.2}$$

In Eq. 3.1 the  $E_{Nernst}$  component is the thermodynamic potential of the cell, which corresponds to the fuel cell open circuit voltage or its reversible voltage; the  $V_{act}$ ,  $V_{Ohmic}$  and  $V_{con}$  components correspond to the previously defined losses. Additionally there is another voltage drop associated to the internal currents and the fuel crossover (not represented in Eq. 3.1). This voltage drop is included in the model by means of a fixed current density even at no-load operation (represented by  $J_n$ ). Each component is modelled separately with each of them defined by the equations below. The dynamic behaviour of the fuel cell as well as the electrical power and efficiency are also defined and modelled.

$$E_{Nernst} = 1.229 - 0.85 \times 10^{-3} \times (T - 298.15) + 4.31 \times 10^{-5} \times T \times \left[ \ln(P_{H_2}) + \frac{1}{2} \ln(P_{O_2}) \right] \quad \text{Eq. 3.3}$$



$$V_{act} = -[\xi_1 + \xi_2 \times T + \xi_3 \times T \times \ln(C_{O_2}) + \xi_4 \times T \times \ln(i_{FC})] \quad \text{Eq. 3.4}$$

Where  $\xi_1$ ,  $\xi_3$ , and  $\xi_4$  are constant parameters and  $\xi_2$  is given by;

$$\xi_2 = 0.00286 + 0.0002 \times \ln A + (4.3 \cdot 10^{-5}) \times \ln C_{H_2} \quad \text{Eq. 3.5}$$

$$V_{ohmic} = i_{FC} \times (R_M + R_C) \quad \text{Eq. 3.6}$$

$$V_{con} = -B \times \ln\left(1 - \frac{J}{J_{max}}\right) \quad \text{Eq. 3.7}$$

$$C_{O_2} = \frac{P_{O_2}}{5.08 \times 10^6 \times e^{-\left(\frac{498}{T}\right)}} \quad \text{Eq. 3.8}$$

Where,  $P_{H_2}$  and  $P_{O_2}$  are partial pressures (in atm) of the hydrogen and the oxygen, respectively and  $T$  is the cell absolute temperature (in Kelvin).

The cell operating current is  $i_{FC}$  (in A) and  $C_{O_2}$  is the concentration of oxygen in the catalytic interface of the cathode (in  $\text{mol.cm}^{-3}$ ). The parametric coefficients for each cell model are represented by  $\xi_i$  ( $i = 1, 4$ ) and  $\psi$  [9-12].  $R_M$  is the equivalent membrane resistance to proton conduction.  $R_C$  is the equivalent contact resistance to electron conduction.  $J_{max}$  is the maximum current density.  $B$  (in V) is a constant dependent on the cell type and its operation state.  $J$  is the actual cell current density (in  $\text{A.cm}^{-2}$ ) including the permanent current density  $J_n$ . The equivalent membrane resistance can be calculated by [9-12]:

$$R_M = \frac{\rho_M \times l}{A} \quad \text{Eq. 3.9}$$

Where,  $\rho_M$  is the membrane specific resistivity (in  $\Omega.\text{cm}$ ),  $A$  is the cell active area (in  $\text{cm}^2$ ) and  $l$  is the thickness of the membrane (in cm), which serves as the electrolyte of the cell.  $\rho_M$  is obtained by:

$$\rho_M = \frac{181.6 \left[ 1 + 0.03 \times \left( \frac{i_{FC}}{A} \right) + 0.062 \times \left( \frac{T}{303} \right)^2 \times \left( \frac{i_{FC}}{A} \right)^{2.5} \right]}{\left[ \psi - 0.634 - 3 \times \left( \frac{i_{FC}}{A} \right) \right] \times \exp \left[ 4.18 \times \left( \frac{T - 303}{T} \right) \right]} \quad \text{Eq. 3.10}$$

### 3.2.2. Dynamic analysis

The electrical equivalent circuit of the PEM has a first order delay applied to the activation and to the concentration losses. This phenomenon is extremely important in the analysis of the dynamics of the fuel cell, since the interface between the electrode and the electrolyte acts as storing electrical charge, that is, it behaves as a capacitor. This effect causes a delay in the dissipation of electrical charges at the interface electrode/electrolyte, which affects the  $V_{act}$  and  $V_{con}$  terms. The Vohmic term is not affected by this delay. Hence, the dynamics of the fuel cell can be represented by Eq. 3.11 and corresponds to the phenomenon known as "charge double layer".

$$\frac{dV_d}{dt} = \left( \frac{1}{C} \times i_{FC} \right) - \left( \frac{1}{\tau} \times V_d \right) \quad \text{Eq. 3.11}$$

Where  $V_d$  represents the dynamical voltage across the capacitor,  $C$  and  $\tau$  is the fuel cell electrical time constant defined as:

$$\tau = C \times Ra = C \times (R_{act} + R_{con}) = C \times \left( \frac{V_{act} + V_{con}}{i_{FC}} \right) \quad \text{Eq. 3.12}$$

The output voltage to the fuel cell considering the dynamic behaviour is given by:

$$V_{FC} = E_{Nernst} - V_{Ohmic} - V_d \quad \text{Eq. 3.13}$$

Figure 3.2 corresponds to the implementation in MatLab/Simulink of the dynamic block model.

Where, the integrator block "1/s" handles the voltage drop  $V_d$ .

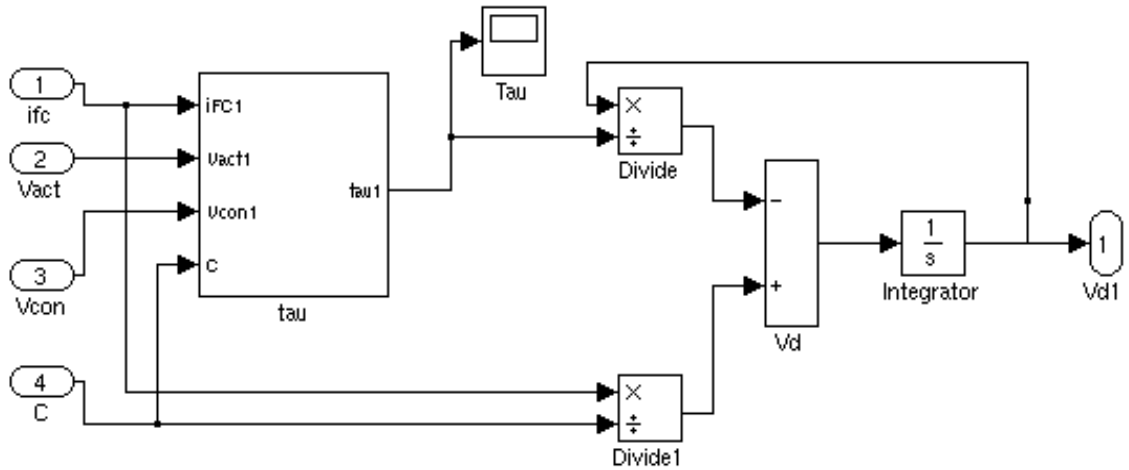


Figure 3.2 –Dynamic block model implemented in MatLab/Simulink.

### 3.2.3. Efficiency and power

The calculation of the electrical efficiency of a fuel cell power system is done as for any power generating system. The percentage of electrical efficiency of the fuel cell power system is calculated by the equation below [32].

$$\eta_{electrical} = \left( \frac{\text{Net electrical energy output}}{\text{Total energy input}} \right) \times 100\% \quad \text{Eq. 3.14}$$

A practical definition of the cell efficiency as a function of the cell voltage is defined in Eq. 3.15:

$$\eta_{cell} = \frac{V_{cell}}{1.25V} \quad \text{Eq. 3.15}$$

From the point of view of fluid dynamics, the cells in a fuel cell stack are connected in parallel whereas the electrical connection is in series; therefore, the individual voltages corresponding to different cells are summed and the total voltage is being represented by  $V_{FC}$ . If the fuel supplied by the cells is not all converted in energy, efficiency loss occurs. Then the fuel utilization  $\mu_f$  can be defined as:

$$\mu_f = \frac{\dot{m}H_{2,u}}{\dot{m}H_{2,ref}} \quad \text{Eq. 3.16}$$

Where  $\dot{m}H_{2,u}$  is the hydrogen converter in energy and  $\dot{m}H_{2,ref}$  is the hydrogen input.

The instantaneous electrical power ( $P_{FC}$ ) supplied by the cell is determined by Eq. 3.17:

$$P_{FC} = i_{FC} \times V_{FC} \quad \text{Eq. 3.17}$$

The typical graphs of the efficiency and the electrical power for the PEM fuel cell are represented in Figure 3.3.

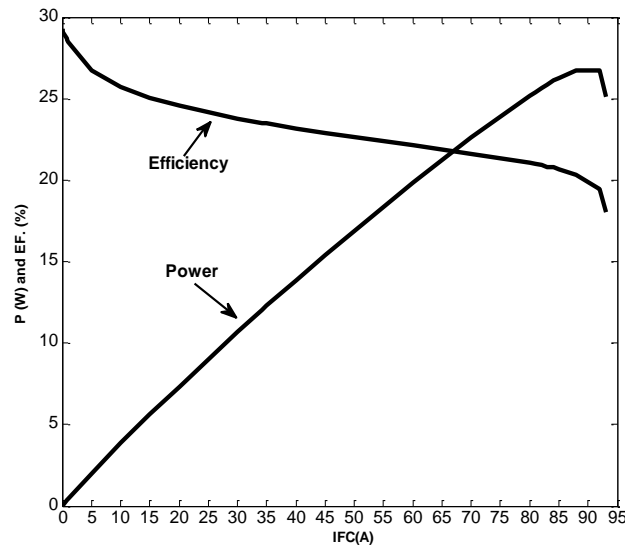


Figure 3.3 – Typical graphs of the efficiency and the electrical power of a PEM fuel cell.

### 3.2.4. Parameters

The performance of fuel cell can be significantly improved by using optimum operating conditions. In this aspect, the PEM fuel cell model must be precisely defined in order to reproduce faithfully a particular fuel cell system. The set of equations introduced above, which represents mathematically the PEM fuel cell behaviour is characterized by the set of parameters listed in Table I, which must be carefully identified in order to get accurate simulation results.

Table 3.1 – List of PEM fuel cell model parameters.

Symbol	Unit	Description
$A$	cm <sup>2</sup>	Cell active area
$\lambda$	μm	Membrane thickness
$R_C$	Ω	Contact resistance
$\xi_1$	No dimensional	Model coefficient 1
$\xi_2$	No dimensional	Model coefficient 2
$\xi_3$	No dimensional	Model coefficient 3
$\xi_4$	No dimensional	Model coefficient 4
$\psi$	No dimensional	Empirical parameter
$B$	V	Empirical parameter
$J_{max}$	A/cm <sup>2</sup>	Maximum current
$C$	F	Charge double layer

### 3.3. Identification of the parameters

The performance of the PEM fuel cell is influenced by many operating parameters such as; temperature, pressure and current. In order to improve its performance, it is essential to know these parameters and their effect on the fuel cell operation [1;4;6;27;33].

#### 3.3.1. Overview of optimization methods

Various studies and methods have been published in the literature to support the extraction of PEM fuel cell parameters [34-39]. Thus, in order to improve the accuracy of the models and make them reflect the actual PEM fuel cell performance, it is necessary to extract parameters values through optimization techniques. The most popular methods of optimization are; Simulated Annealing (SA) [40-45], Genetic Algorithms (GA) [38;46], Sequential Quadratic Programming (SQP) [47], Tabu Search (TS) [38], and Particle Swarm Optimization (PSO) [48-50].

The SA and GA are global optimization algorithms, while the SQP is a local optimization algorithm. The SQP algorithm does not produce results similar to the global optimization methods. Then it will be clear that the objective function is not unimodal and smooth, but contains local minima, which “trapped” the local optimization algorithm. Similarly to the SQP method, TS is a local search method, which uses memory structures. The PSO method is an alternative to GA method.

### **3.3.2. Selection of the optimization method**

The simple concept, easy implementation, robustness, and computational efficiency, when compared to other optimization methods, have led to the selection of Simulated Annealing (SA) [40-45] algorithm as a method of extraction and optimizing the parameters of the PEM. In fact it presents good characteristics for the application besides to be having much attention in various and similar fields and applications. Thus, SA is adopted in the present study.

### **3.3.3. Simulated Annealing (SA)**

Annealing is the term used in metallurgical processes for heating up a solid, which is then cooling slowly until it crystallizes. The atoms of this material have high energies at very high temperatures [41]. This gives the atoms a great deal of freedom in their ability to restructure themselves. As the temperature is reduced, the energy of these atoms decreases. SA algorithm seeks to emulate this process. The SA algorithm begins at a very high temperature where the input values are allowed to assume a large range variation. As the algorithm progresses the temperature will decrease. This restricts the degree to which inputs are allowed to vary, which often leads the algorithm to a better solution, just as a metal achieves a better crystal structure through the actual annealing process. The SA is used to find the minimum of an objective function, i. e.; it allows finding the set of inputs that will produce a minimum value for this function. The method does not aim at obtaining an absolute minimum, but can guarantee that local minimum is achieved. Global methods handle to obtain the absolute minimum of a function. Figure 3.4 illustrates the evolution of the objective function when finding local and global minimums. The correspondent flowchart of the method is represented in Figure 3.5.

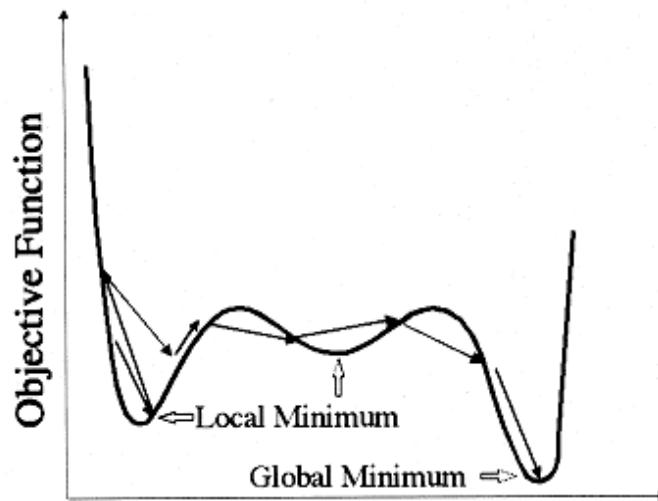


Figure 3.4 – SA and its local and global minimums.

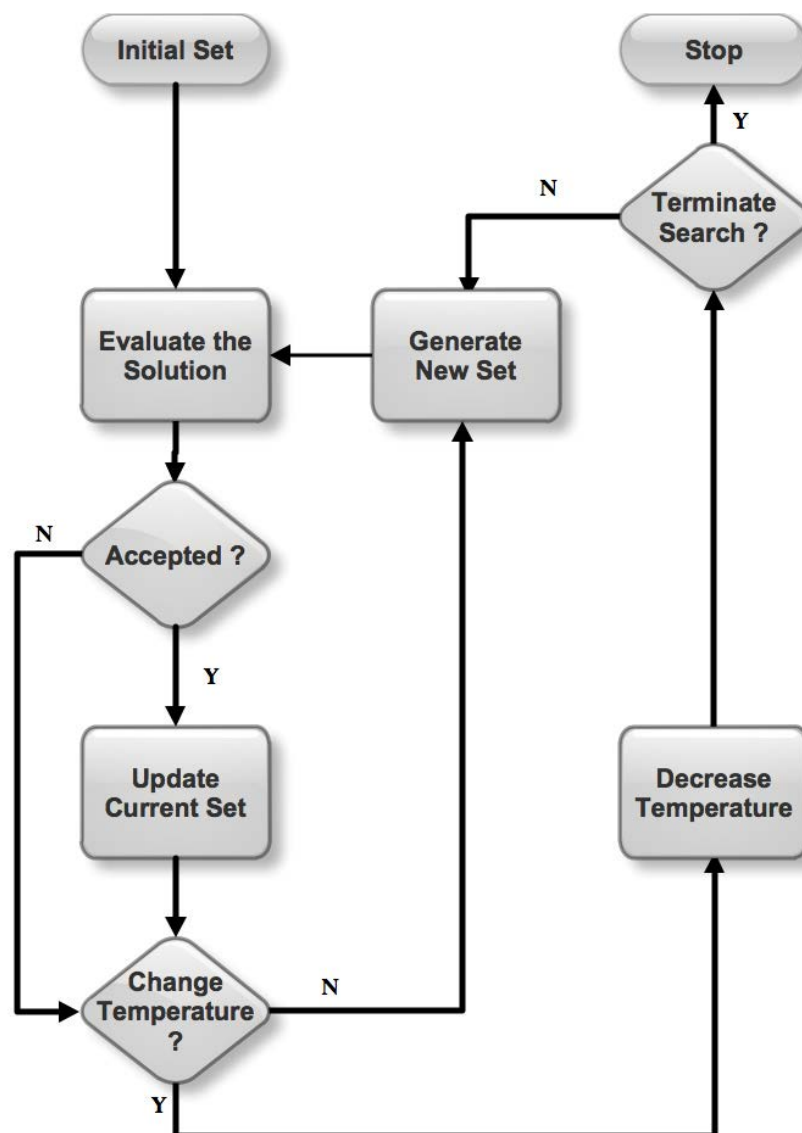


Figure 3.5 – Flowchart of the SA algorithm.

In the design of the SA algorithm, some parameters should be specified, namely: 1) Initial set of parameters, 2) the initial temperature, 3) the rate of temperature reduction or perturbation mechanism, 4) define the objective function and 5) the number of iterations performed for each temperature and 6) the cooling schedule, 7) Moreover it is necessary to define a condition or criterion termination of the algorithm.

### **1. Initial set of parameters**

The initialization of the parameter values can be made using two main approaches, namely; to randomly select a value within a given range of admissible values or just consider the values published in literature [40-44]. In the present case it is adopted the second approach.

### **2. Initial temperature**

Temperature managing controls the SA performance. This implies to choose the adequate initial temperature value as well as defining adequate rules of decreasing its value during the optimization process. The temperature value must be large enough to enable the algorithm to move off a local minimum but small enough not to move off a global minimum. This is related to the acceptance probability of a worst solution that depends on temperature and magnitude of objective function. In the present case the initial temperature value,  $T_0=1$  was used with good convergence result.

### **3. Perturbation mechanism**

The perturbation mechanism is the method used to create a new set of values that is a new solution of the parameters. For each new solution, a random step normally distributed with mean zero and a parameter dependent standard deviation is generated. Since for each parameter the range variation is very different a *sigma* vector that contains the standard deviation values associated with each parameter is created.

The definition of *sigma* values is dependent on the confidence, on the initial guess. Although optimum solution should be obtained running the algorithm at once, the optimization process should be carried out several times in some situations. In the present case a starting sigma vector has been defined, reducing its values iteratively until the global optimum has been achieved. For each parameter  $j$ , the new value is obtained by equation below:



$$x_{new}(j) = x(j) + \text{sigma}(j), j = 1:10 \quad \text{Eq. 3.18}$$

#### 4. Objective function

The cost or objective function is defined by comparing the relative error between simulated and experimental data using the normalized sum of the squared errors. The function objective measures the goodness of each trial vector; that is, how good simulated data fits experimental data. The general expression of the objective function is obtained by the following equation:

$$f_{obj} = \sqrt{\sum_i \left( \frac{(g^e(x_i) - g^s(x_i))^2}{g^e(x_i)} \right)} \quad \text{Eq. 3.19}$$

Where  $g^s(x_i)$  refers to the simulated data and  $g^e(x_i)$  refers to the experimental data to be optimized.

#### 5. Cooling schedule

One of the factors that strongly affect the algorithm's performance is the way that the temperature decreases. In fact, temperature is the main control parameter, which determines the algorithm's evolution and performance. Once defined the initial temperature value ( $T_0$ ) this should decrease monotonously, usually by a geometric series, in which the value of the temperature of the next iteration is obtained by multiplying the value of the temperature in the current iteration that is, by the cooling schedule  $s$ . This parameter can be fixed or variable according to the nature of the problem of optimization. However it always has a positive value lower the unit ( $s \leq 1$ ). In the present case it is adopted a constant rate value of 0,97 with good convergence results.

$$T_{i+1} = sT_i, \quad i = 0,1,2,3,... \quad \text{Eq. 3.20}$$

#### 6. Terminating criterion

The criterion for terminating the algorithm can be a maximum number of iterations, a minimum temperature value, a minimum of objective function, or a combination of these three factors. Considering the algorithm's termination by setting a maximum number of iterations, the

performance of the SA method can be analysed by the evolution of the objective function during the optimization process, as can be observed in Figure 3.6 below.

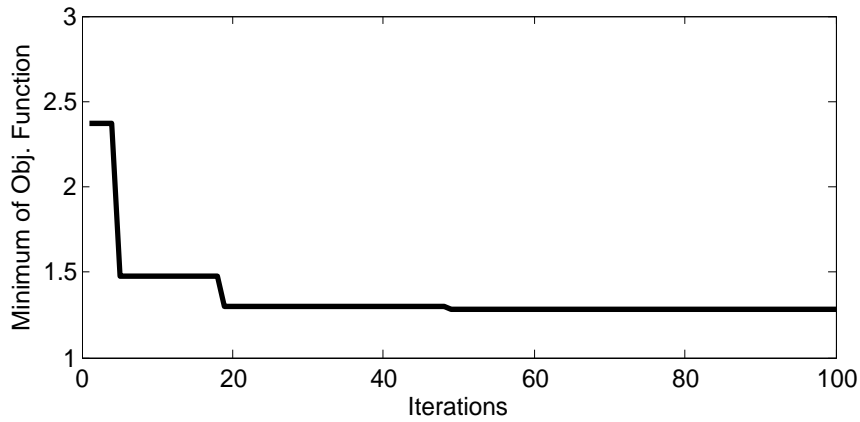


Figure 3.6 - Performance of SA.

### 3.3.4. Execution of the method

Normally, several runs of the optimization process need to be carried out. Sometimes local minimums are detected producing optimum sets lightly different from the optimum. This can be explained by two main reasons: i) the SA algorithm could be better tuned in order to overcome those local minimum and ii) the empirical nature of some model parameters can give rise to the existence of some similar sets of parameters associated to very close values of the objective function. In fact, it must be pointed out that all those sets of parameters produce simulation results that are not distinguishable. The main objective of the optimization process is carried out once it finds a set of parameters that ensures accurate and repeatable results covering the full range of fuel cell current as a significant variable in analyzing the electrical behaviour of the fuel cell.

### 3.3.5. Validation of the method

The optimum set of parameters achieved by SA that characterizes the performance of each PEM used in this thesis is presented in the Appendix A. The accuracy of the method is evaluated through the measurement of the error between experimental and simulation results (just for the Nexa case). Through this study it is concluded that the model developed reproduces the fuel cell behaviour with an error less than 1%.

### 3.4. Identification of time constants

The electrical and thermal time constants are important variables in the design of the PEM model, especially if the PEM is used as energy generating source of an electric vehicle, in which the time response of the source system is crucial. In the identification of the time constants two methodologies are used, the linear is appropriated around the most significant operation points of the PEM system and the nonlinear allows at obtaining a nonlinear global model.

### 3.5. Linear identification of the time constants

The typical identification of the linear process consists iteratively in selecting a model structure, in computing the best model of this structure, and evaluates the model properties. In the present case the parameters are estimated through the Autoregressive exogenous (ARX) function, which can be applied in continuous and discrete time domains. The data to be analysed are in discrete time domain and the ARX function returns a model containing the correspondent coefficients of numerator and denominator of a discrete time transfer function that characterizes the system. The syntax of the function ARX is:

```
m=arx(data,orders)
```

```
m=arx(data,'na',na,'nb',nb,'nk',nk)
```

Where, *data* is an *iddata* object that contains the input-output data. Both time and frequency-domain signals are supported, and data can also be a frequency-response data object. However, multi output continuous-time models are not supported by ARX; *orders* is given as *orders* = [*na nb nk*] defining the orders and delay of the ARX model.

The parameters of ARX model structure can be estimated using the least squares method represented by Eq. 3.21

$$A(q)y(t) = B(q)u(t) + e(t) \quad \text{Eq. 3.21}$$

Specifically, in discrete time the application of ARX function can be represented by:

$$na:A(q)=1+a_1q^{-1}+....+a_{na}q^{-na} \quad \text{Eq. 3.22}$$

$$nb:A(q)=1+b_1q^{-1}+....+b_{nb}q^{-nb+1} \quad \text{Eq. 3.23}$$

For models with one output, continuous-time models can be estimated from continuous-time data. The orders are then interpreted as  $na$  being the number of estimated denominator coefficients and  $nb$  being the number of estimated numerator coefficients.

This means that if  $na = 4$  and  $nb = 2$  the model can be represented by Eq. 3.24 below:

$$G(s) = \frac{b_1s + b_2}{s_4 + a_1s^3 + a_2s^2 + a_3s + a_4} \quad \text{Eq. 3.24}$$

For continuous-time models the delay parameters  $nk$  have no meaning and should be omitted.

### 3.5.1. Poles system identification

Residue function is applied in the identification of the poles system. The number of poles is  $n = \text{length}(A) - 1 = \text{length}(R) = \text{length}(P)$ . Function *residue* converts a quotient of polynomials to pole-residue representation, and back again.

The syntax of *residue* function is:  $[r, p, k] = \text{residue}(B, A)$ , where;  $r$  corresponds to the column vector of the residues,  $p$  is the column vector of pole locations and  $k$  is the row vector of direct terms. Vectors  $A$  and  $B$  specify the coefficients of the numerator and denominator polynomials in descending powers of  $s$  as follows.

$$\frac{B(s)}{A(s)} = \frac{R(1)}{s - P(1)} + \frac{R(2)}{s - P(2)} + \dots + \frac{R(n)}{s - P(n)} + K(s) \quad \text{Eq. 3.25}$$

### 3.5.2. Transfer function in continuous-domain

The expression of the transfer function of the system in continuous-time domain corresponds to the estimated data and is represented by Eq. 3.26 below:

$$f(t) = A \times \left[ 1 - \left( k_1 \times e^{-(t/\tau_1)} + k_2 \times e^{-(t/\tau_2)} \right) \right] \quad \text{Eq. 3.26}$$

Where  $A$  is the step value or input  $u(t)$ ,  $k_1$  is the constant value,  $\tau_1$  is the electrical time-constant of fuel cell system,  $k_2$  is the constant value and  $\tau_2$  is the thermal time constant of the fuel cell system.

### 3.5.3. Validation of the method

The linear identification of the time constants is validated for the Nexa<sup>TM</sup> PEM, considering a sampling time of one second ( $T_{\text{Sample}}=1\text{s}$ ). Figure 3.7 shows the experimental data of the stack temperature to different operating conditions.

As is observed in Figure 3.7 the stack temperature evolves proportionally to the load level. It is also observed a time delay, which is associated with the internal control of the system. Since the methodology adopted does not include this time delay this effect is not considered for analysis. The error between the experimental and estimated results is therefore validated by Eq. 3.27 below.

$$\tau_{\text{error}} = \left[ \frac{\tau_{\text{sim}} - \tau}{\tau} \right] \times 100\% \quad \text{Eq. 3.27}$$

Where,  $\tau_{\text{sim}} = \tau_1 + \tau_2$  corresponds to the estimated time constant and  $\tau$  corresponds to the experimental one.

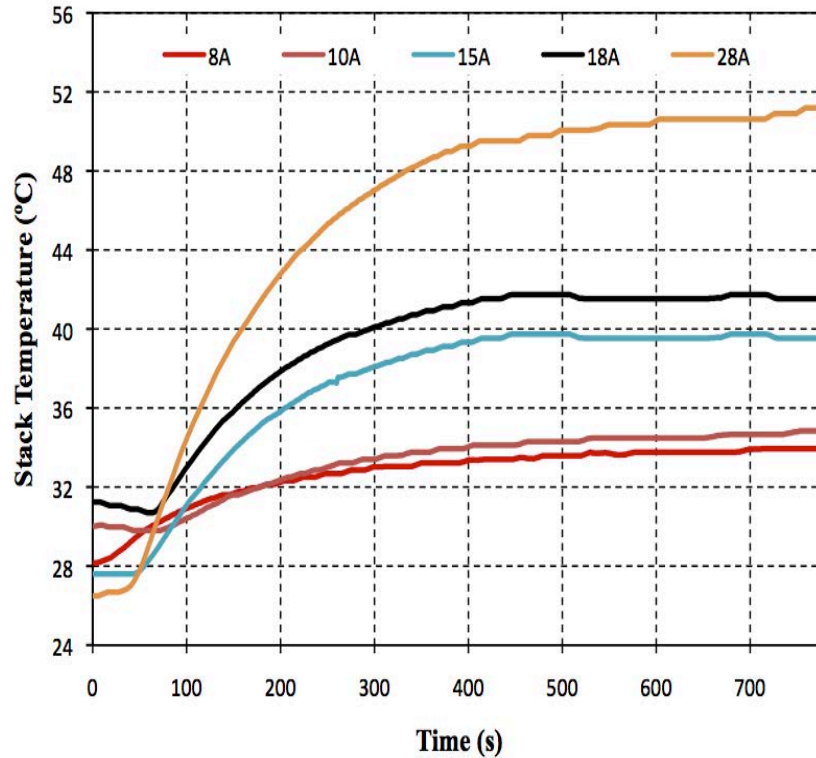


Figure 3.7 - Temperature of the PEM for different values of the load.

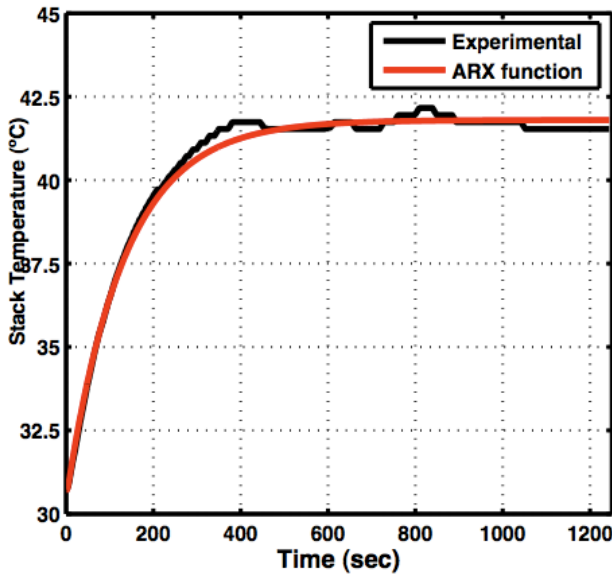


Figure 3.8 – Validation of ARX for 18A

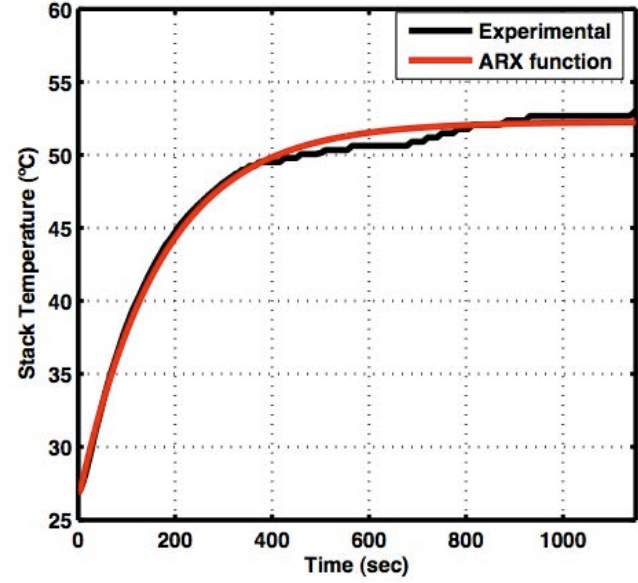


Figure 3.9 –Validation of ARX for 28A

The evolution of the stack temperature is presented Figure 3.8 and Figure 3.9 for the load levels of 18 A and 28 A respectively, which demonstrates the effectiveness of the ARX method. Thus it appears that the identification with ARX methodology is appropriate around the most significant points of operation and perfectly suits the goal. The Table 3.2 below summarizes the information achieved with this methodology.

From Table 3.2, Figure 3.10 and Figure 3.11 it can be concluded that:

1. Results obtained through the tests made with the PEM fuel cell system clearly presents two time constants  $\tau_1$  and  $\tau_2$ , which corresponds to a second-order system.
2. The value of the thermal time-constant  $\tau_2$  is higher than the value of the electrical time-constant  $\tau_1$ .
3. The time-constant value achieved with the Nexa system is the sum of electrical time-constant  $\tau_1$  and thermal time-constant  $\tau_2$ .
4. The electrical time-constant value  $\tau_1$  depends of the operation condition of fuel cell system. It increases with the increase of the load current.
5. The thermal time-constant value  $\tau_2$  is much higher than the electrical time-constant and is independent on the load current.
6. The error obtained from Eq. 3.28 is less than 1 %. The mean value is 0.64 % and the standard deviation is 0.19 %.

Table 3.2 - Time constants of several load levels.

Step	$\tau(s)$	Simulation				Error (%)
		K1	K2	$\tau1(s)$	$\tau2(s)$	
8A	140	-0.012	0.69	1.11	138.47	0.30
10A	190	-0.007	0.51	1.47	187.03	0.78
15A	140	-0.013	0.81	1.01	140.08	0.77
18A	130	-0.015	0.63	2.10	131.65	0.53
28A	170	-0.020	0.92	2.63	168.77	0.82
Mean value (%):						0.64
Standard deviation (%):						0.19

**NOTE:**  $\tau1$ : Electrical time-constant,  $\tau2$ : Thermal time- constant,  $\tau \approx \tau1 + \tau2$ .

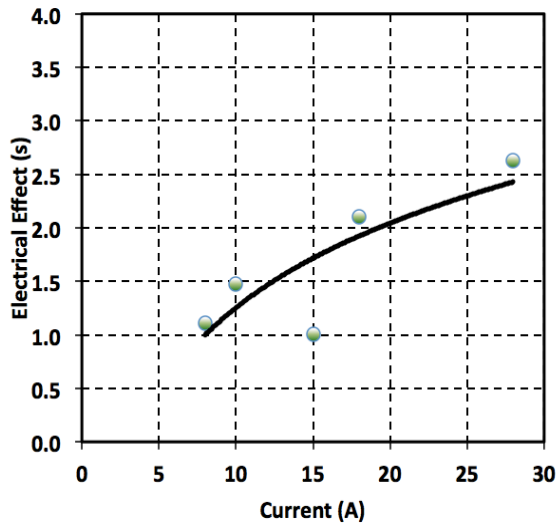


Figure 3.10 – Estimated results for  $\tau1$ .

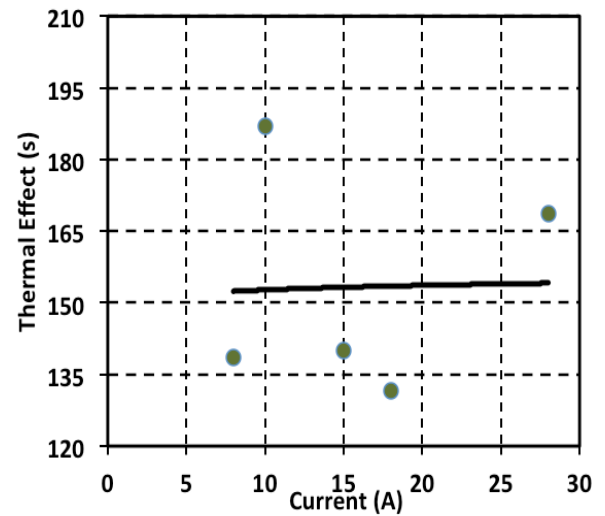


Figure 3.11 – Estimated results for  $\tau2$ .

### 3.6. Nonlinear identification of the time constants

The identification of the time constants according to the ARX methodology gives good results for specific operation point of the PEM system, as is demonstrated above. However, the adoption of a method that allows at establishing a nonlinear global model should be made and the NN approach shows to be very appropriate to overcome this issue.

The term “Neural Network” (NN) usually refers to a Multilayer Perceptron Network. However, there are many other types of neural network models including Probabilistic Neural Networks, General Regression Neural Networks, Radial Basis Function Networks, among others. The Multilayer Perceptron NN model was selected and is shown in Figure 3.12 below.

In this case the neurons are organized by layers and trained generally with the, back-propagation (BP) algorithm.

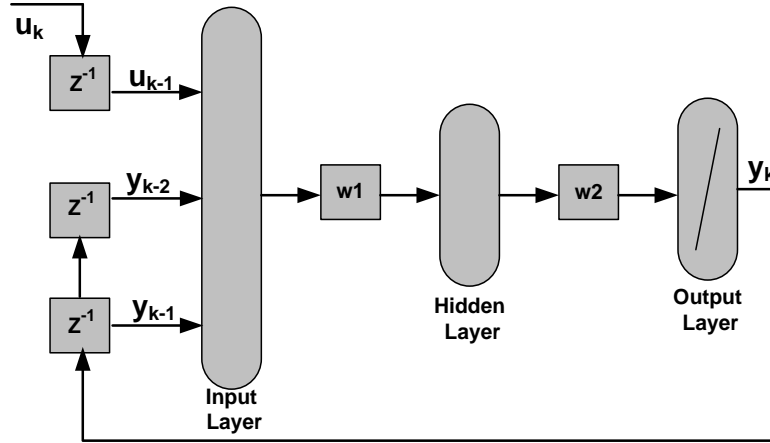


Figure 3.12 – Architecture of the NN selected.

The configuration of the model requires defining the network design, selecting the data, selecting the training algorithm and also taking in account practical considerations [28;51-53].

### 3.6.1. Neural Network design

The design of a NN includes determining the number of input and output nodes to be used, the number of hidden layer of the network and the number of hidden nodes used in each hidden layer [28-30]. The number of input nodes is typically the same as the number of the state variables. In the case of feed-forward architecture, the outputs of a layer are the inputs of the following one. The hidden layer is composed by an adequate number of neurons, specified by the user, while the output layer possesses the neurons as the outflow of the system, which is only one in this case. Accordingly, the input layer should present a number of inputs ( $y_{k-1}, y_{k-2}, \dots, u_{k-1}, \dots$ ) as described by Eq. 3.28 below.

$$y_k = f(y_{k-1}, y_{k-2}, \dots, y_{k-na}, u_{k-1}, u_{k-2}, \dots, u_{k-n}) \quad \text{Eq. 3.28}$$



### 3.6.2. Selection of the data for training and validation

A commercial PEM fuel cell system is used to provide the necessary data to the NN. The data collected is the stack current (A) as the input and the stack temperature (°C) as the output. The stack current varies from 1 A to 42.8 A while the stack temperature varies from 28 °C to 56 °C both with a total of 1008 points

Usually is selected a set of training data and a set of validation data that satisfies substantially the system under evaluation being that, the training data set should be large enough to contain as much information as possible of the system. Hence in the present case, from a total of 1008 experimental data points, 770 points are considered to train the network while all of the data points are used for validation. This data is shown in Figure 3.13.

### 3.6.3. Training of the Network

When training data set is presented to the network, the weights and biases are up until the entire training data set is completed. This process is called one “epoch”. The number of “epoch” indicates the speed of the training method that is, its convergence. The training phase is repeated until the network performs well according to an error goal defined by the user. As a consequence when the data validation is presented to the network, it is used to ensure that the network has learned the general patterns, and not just simply has memorized the data set. If the network still performs well, in validation phase, the training is completed and the neural network can be used whatever the input data.

Among the various possible algorithms available, the Levenberg-Marquardt-BP has proved to be the best solution to suit the problem, due to its own characteristics of efficiency, convergence and easily implementation. Using the *newff* function of the NN library of Matlab a feed-forward back propagation network was created and validated.

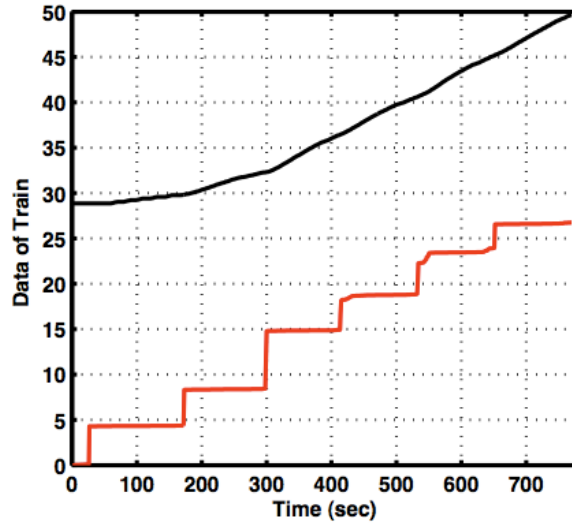


Figure 3.13 – Data used to train the Neural Network.

#### 3.6.4. Performance and validation

The method was performed for the case of the Nexa<sup>TM</sup> system accordingly to the following criteria:

- (a) Considering the number of epochs, which indicate the efficiency of the method;
- (b) Measuring the error function (E) given by the Eq. 3.29 below.

$$E = \frac{1}{n} \sum_{i=1}^n e_i^2 \quad \text{Eq. 3.29}$$

During the training process the error function (E) is minimized as the number of epochs increases. In this process, the network adjusts its weights and biases until the output error reaches the designated error goal. The performance of the method is represented in Figure 3.14 and the validation of the method is in Figure 3.15.

The performance of the method is 3.978e-5 for a goal of 4e-5, achieved after 190 “epoch”. Observing Figure 3.15 it appears that the results obtained through the NN model, accurately follows the corresponding experimental data, i. e., the model developed in NN represents the electrical and thermal time constants in its entire operating range.

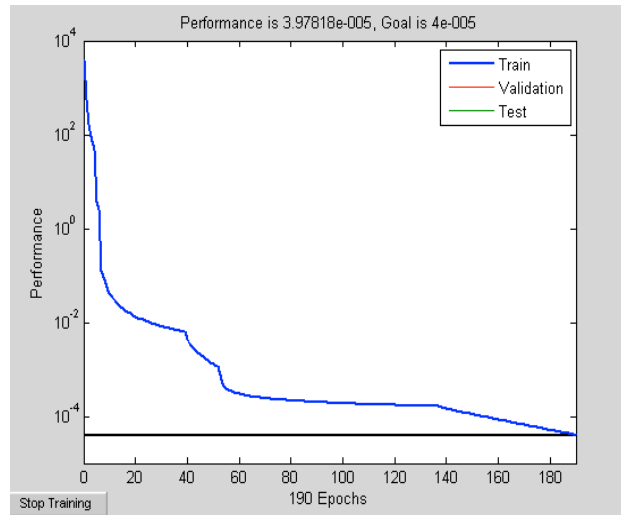


Figure 3.14– Performance of the NN method.

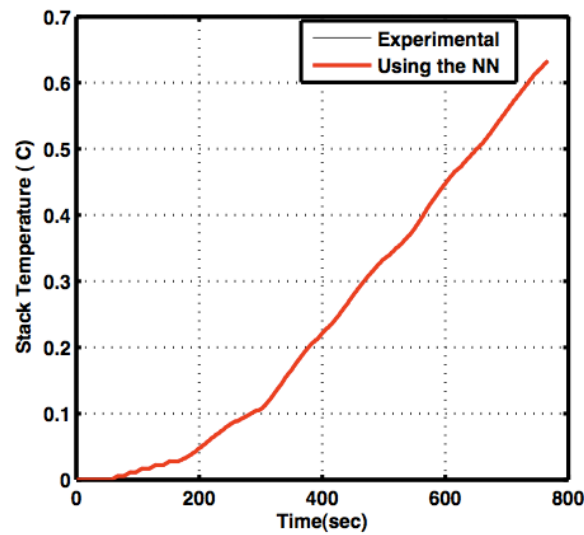


Figure 3.15 –Accuracy of the NN method.

This method is validated for the Nexa<sup>TM</sup> PEM using the experimental data of Figure 4.7

Thus, comparing the results shown in Figure 3.8 with its corresponding Figure 3.16 for the load condition of 18A, it is concluded that the both methods give accurate results, however, the linear identification by the ARX function is appropriated around the most significant operation points of the PEM system while nonlinear identification using the NN allows at obtaining a nonlinear global model. The same conclusion is obtained concerning the load condition of 28A.

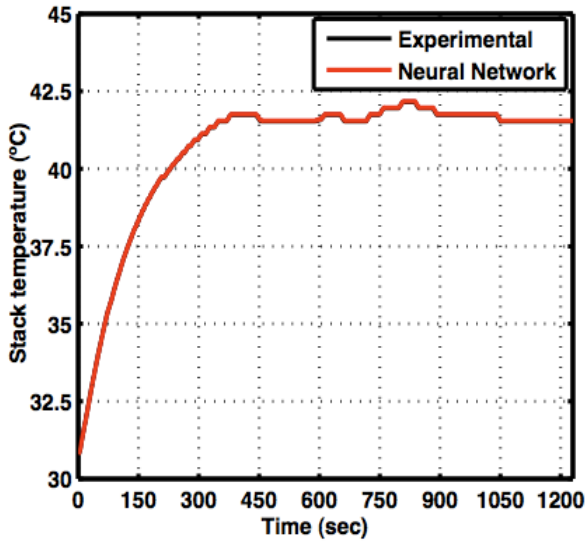


Figure 3.16 - Validation of the NN for 18A

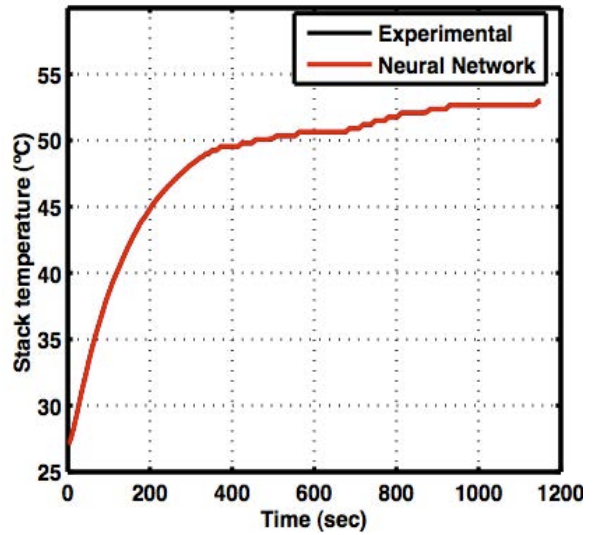


Figure 3.17 - Validation of the NN for 28A.

### 3.7. Model of the PEM in MatLab/Simulink

The model of the PEM in MatLab/Simulink is implemented a voltage-source controlled in current. It is composed by two subsystems, as shown in Figure 3.18. The static model and the dynamic model are implemented by the equations of the electrochemical equivalent circuit defined in section 3.2. As can be observed the output signals of the static model are used as the input signals of the dynamic model, accordingly to the analytical formulation. The optimal parameters found by the SA algorithm are used in this model and the temperature is considered by an input variable, defined by a vector associated with PEM to analyze.

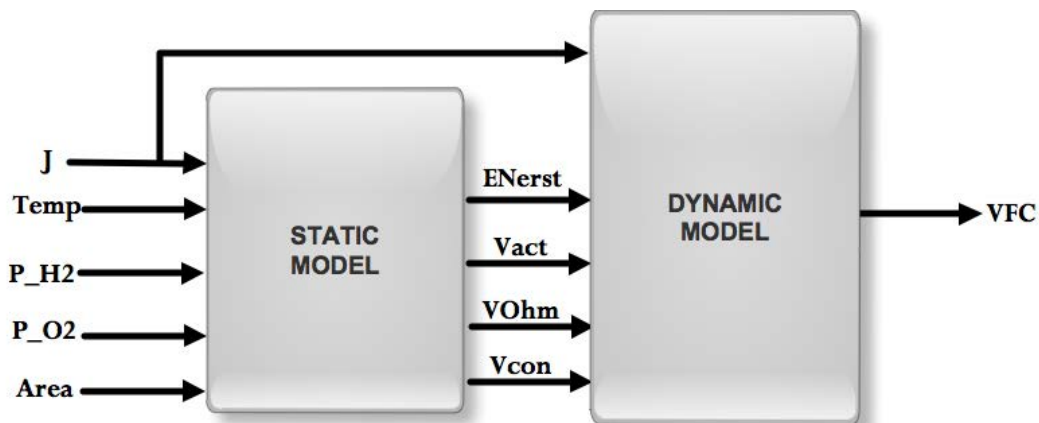


Figure 3.18– Fuel cell subsystem models implemented in MatLab/Simulink.

### 3.7.1. Accuracy of the model implemented in MatLab/Simulink

The accuracy of the model is determined from the error value between the experimental and the simulation data of the fuel cell voltage ( $V_{FC}$ ), whose values are presented in Table 3.3. As can be seen, the mean value of the error is 0.65% and the standard deviation is 0.35%. These results clearly demonstrate the robustness of the model implemented, which accurately represents the operation of the PEM.

Table 3.3 – Accuracy of the PEM fuel cell model in MatLab/Simulink.

Experimental Results		Simulation Results	Error
$I_{FC}$ (A)	$V_{FC}$ (V)	$V_{FC}$ (V)	(%)
$\approx 5$ (5.61)	40.78	40.27	1.25
$\approx 10$ (9.66)	38.76	38.66	0.26
$\approx 15$ (16.07)	36.74	36.95	0.57
$\approx 20$ (19.99)	35.85	35.92	0.20
$\approx 25$ (25.07)	34.52	34.72	0.58
$\approx 30$ (28.03)	34.27	34.03	0.70
$\approx 35$ (35.11)	32.70	32.83	0.40
$\approx 40$ (42.01)	31.66	31.91	0.79
42.87 (max.)	31.66	31.32	1.07
Mean value (%):			0.65
Standard Deviation of the mean value (%):			0.35

### 3.8. Analysis of the static behaviour of the PEM

The analysis of static behaviour of the PEM is based on the circuit of Figure 3.19. Particularly, the polarization curve, the efficiency, hydrogen consumption and power of the PEM are the variables analyzed. Thus, considering the data provided by the manufacturer of the Nexa system, the current varies from 0 to 45 A the output voltage varies from 43 V<sub>DC</sub> to 34 V<sub>DC</sub> and for the power from zero (at start-up system) to 1400 W at rated power.

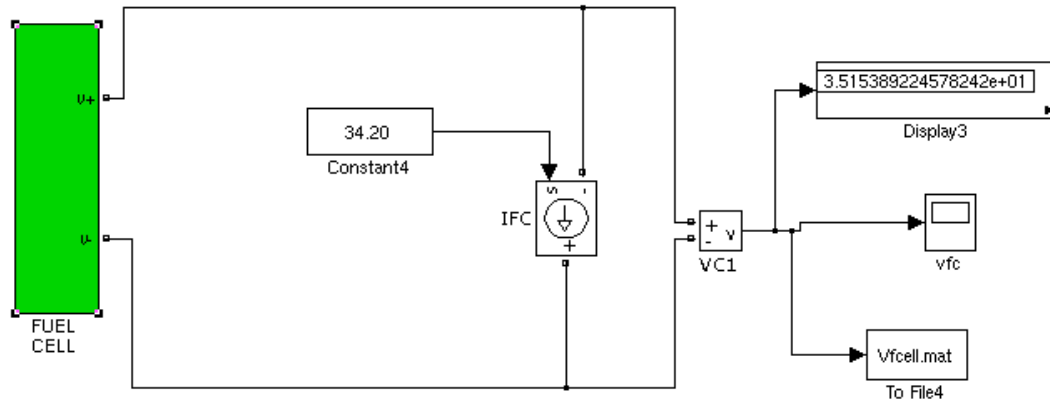


Figure 3.19 – Circuit of test of the static behaviour of the PEM model.

Table 3.4 –Static behaviour of the PEM Nexa™.

Current (A)	Voltage (V)	Power (W)
0	42.67	0
5	39.95	199.8
10	38.43	385.3
15	37.44	562.7
20	36.70	734.0
25	36.08	902.2
30	35.55	1066.7
34.2	35.15	1202.3
35	35.08	1227.8
40	34.64	1385.8
45	34.23	1540.7

The results of Table 3.4, obtained from the model shows they are in accordance with the data provided by the manufacturer. Figure 3.20 shows graphically the evolution of the output voltage and power.

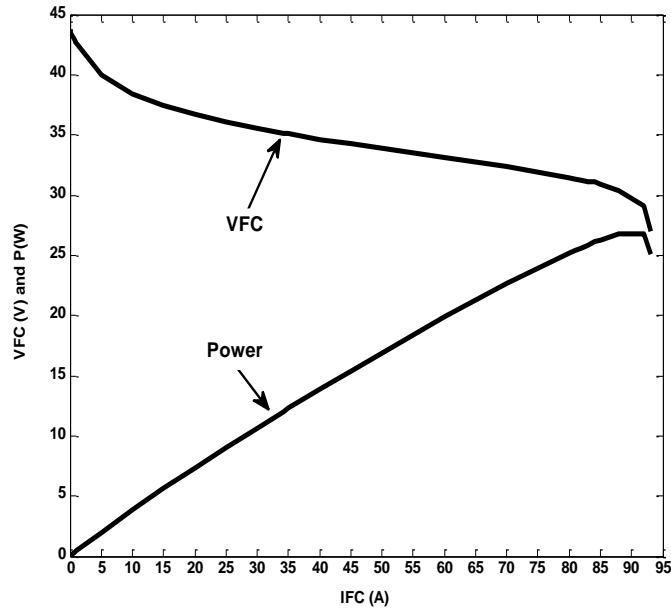


Figure 3.20 – Output voltage and power of the static behaviour of Nexa™.

### 3.8.1. Influence of the temperature on the static behaviour of the PEM

As already referred, the temperature is considered a variable input of the model. In order to analyze the influence of the temperature on the static behaviour of the PEM and also to demonstrate that the temperature dependencies is correctly described in the model formulation proposed, this is simulated at different temperature values, namely: 310 K, 320 K and 330 K and considering the experimental data of the temperature of the PEM under study, shown in Table 3.5 and Figure 3.21. As it is observed, the error between simulation and experimental results for constant temperature values is significantly higher than the error obtained when using the experimental data of the temperature variable in the model.

Thus, it can be concluded that the modelling approach proposed is a valuable tool for handling the behaviour of the fuel cell effective both in the analysis of performance of fuel cells systems or in the design of power generation systems.

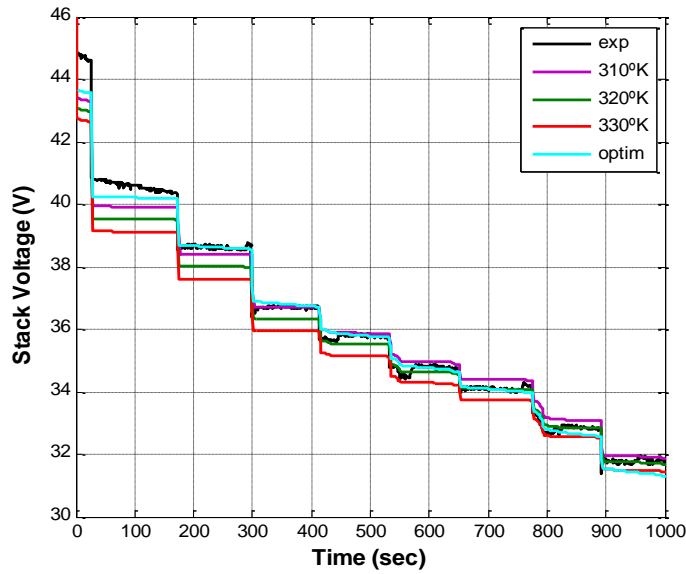


Figure 3.21 – Fuel cell stack voltage for different temperatures values.

Table 3.5 - Accuracy of the PEM fuel cell model considering the influence of the temperature.

Experimental			Simulation				Error			
Time	Ifc	Vfc	Vfc (310K)	Vfc (320K)	Vfc (330K)	Vfc (*)	Vfc (310K)	Vfc (320K)	Vfc (330K)	Vfc (*)
(s)	(A)	(V)	(V)	(V)	(V)	(V)	(%)	(%)	(%)	(%)
200	9.62	38.67	38.41	38.02	37.61	38.67	0.67	1.68	2.74	0.00
400	16.15	36.69	36.71	36.34	35.94	36.75	0.05	0.95	2.04	0.16
600	24.74	34.77	34.97	34.65	34.28	34.77	0.58	0.35	1.41	0.00
800	35.11	32.70	33.18	32.92	32.62	32.82	1.47	0.67	0.24	0.37
1000	42.75	31.76	31.86	31.68	31.42	31.76	0.31	0.25	1.07	0.00
Mean value (%):							0.62	0.78	1.50	0.11
Standard deviation (%):							0.53	0.57	0.95	0.16

(\*) These results consider experimental data of temperature variable in the model.



### 3.9. Analysis of the dynamic behaviour of the PEM

The dynamic behaviour of the PEM fuel cell described in section 3.2.2 is analysed considering the influence on the fuel cell voltage of several variables namely: the temperature, the hydrogen pressure and the capacitor value which corresponds to the fuel cell phenomenon known as "charge double layer".

#### 3.9.1. Effect of the capacitor on the dynamic behaviour of the PEM

The capacitor element that appears in the electrical equivalent circuit of the PEM affects the dynamic behaviour of the fuel cell, which takes some time to react. The time delay it takes is due to the charge (and discharge) of this capacitor and affects the output variables of the fuel cell such as; the fuel cell voltage in Figure 3.22 and the fuel cell power, in Figure 3.23. This analysis is performed for a step-up current at the instant of 27s and for three-capacitor values.

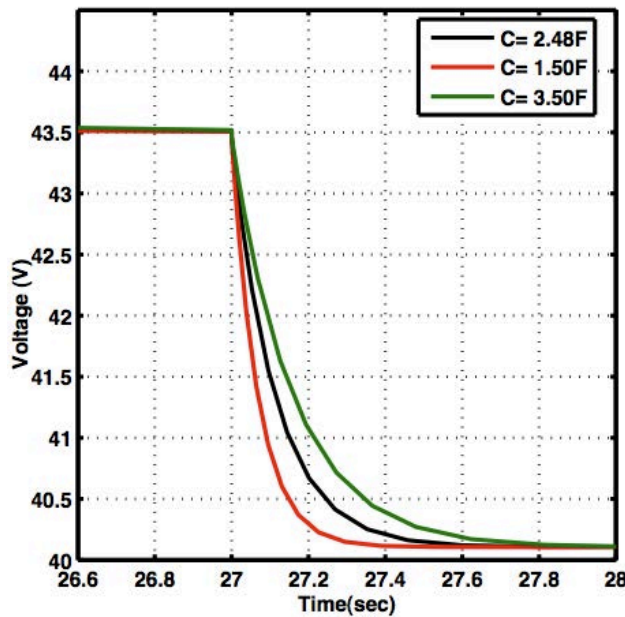


Figure 3.22 - Capacitor effect on the output voltage.

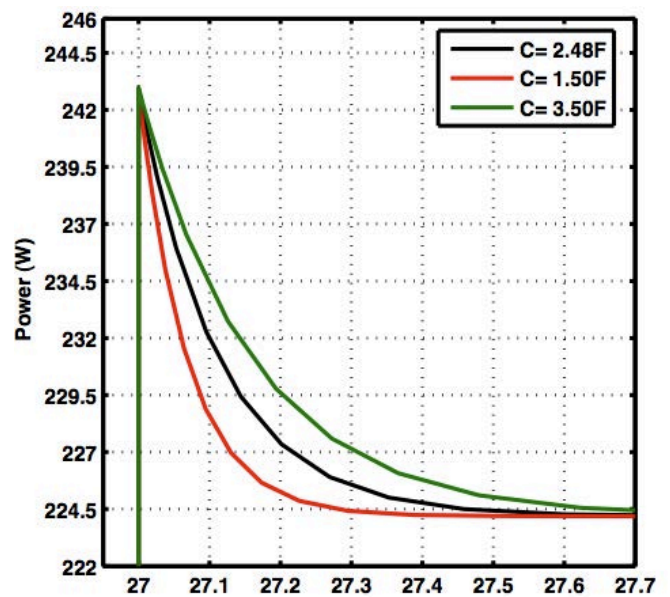


Figure 3.23 - Capacitor effect on the electrical power.

### 3.10. Conclusions

This chapter begins with an overview of the fuel cell types and selection of PEM type using some criteria. Once selected the fuel cell type and described some experimental setups, some possible modelling approaches are presented and discussed. The selection is focused at two models, an electrochemical model and a Neural Networks model,

The semi-empirical model is based on a theoretical and analytical approach characterized mathematically by a set of equations representing the PEM fuel cell behaviour, which parameters are normally difficult to determine. A solution to overcome this difficulty is based on the SA algorithm, which extracts the best set of parameters, which optimizes the error between experimental and simulated data.

The Neural Networks proves to be well adapted to predict the behaviour of the PEM. However, the NN model operates like a “black box” and no detailed information about the PEM system is provided. The author adopts the first approach in order to persecute the goal of direct improvement of fuel cell efficiency.

The identification of the electrical and thermal time constants was also performed, by linear and nonlinear methodologies.

A short explanation of the model implemented in MatLab/Simulink is presented, followed by the analysis of the static and dynamic behaviour of the PEM fuel cell, as this is a very important issue in researching control strategies for electronic converters applied to fuel cells.

---

*CHAPTER 4*

**STATE OF THE ART ON  
POWER CONVERTERS FOR FUEL CELLS  
AND CONTROL**

---



## 4. STATE OF THE ART ON POWER CONVERTERS FOR FUEL CELLS AND CONTROL

### 4.1. Introduction

Power converters are used in fuel cell (FC) systems to convert the DC electrical power generated by the fuel cell into usable AC or DC power through power electronic circuits [54-63]. In this context the DC-DC power electronic converters are used whenever it is wanted to change the DC electrical power efficiently from a level to another. In many ways, the DC-DC converter is equivalent to a transformer, and like a transformer, a DC-DC converter essentially changes the input energy into a different impedance level i.e.,  $P_{in}=P_{out}+P_{loss}$ .

As it can be seen in Figure 4.1 the DC-DC power converters can be divided according to operation mode into three types; 1) the linear, 2) the switching-mode and 3) the soft-switching or resonant converters [55;64].

The main difference between them is caused by efficiency. The soft-switching or resonant one has some advantages compared to the linear mode like; the high switching frequency, which enables the use of a small ferrite transformer core, it may operate in a much larger DC input voltage range than the linear regulators, and it often has a higher efficiency. However, there are some drawbacks associated too. The noise of the supply may be increased due to the power switching techniques, and the control circuitry is more complicated compared to the linear one. The switching-mode topologies are divided into two types, the isolated and the non-isolated one. The Buck, Boost and Buck-Boost converters; and further, the Cuk converter constitute the non-isolated DC-DC converters family. However, for many applications, isolation is a necessary requirement within the converter between the input and the output [59-61]. By inserting isolation transformers into the four basic non-isolated switching topologies presented above, four single-ended isolated switching DC-DC converters can be obtained as is represented in Figure 4.1, Forward converter, Isolated Boost converter, Flyback converter and Isolated Cuk converter. Nonetheless, the single switch topology is not an ideal solution for higher power converters, since these converters need a higher power transformer. Therefore, another group of DC-DC isolated converters utilizing more than one switch are identified; Push-pull, Half-bridge and Full-bridge converters.

In the switched-mode power converters to control the power to transfer there are two problems, the first is the energy dissipated in the switches and the second is the generated noise caused by virtually unlimited rates of voltage and current changes.

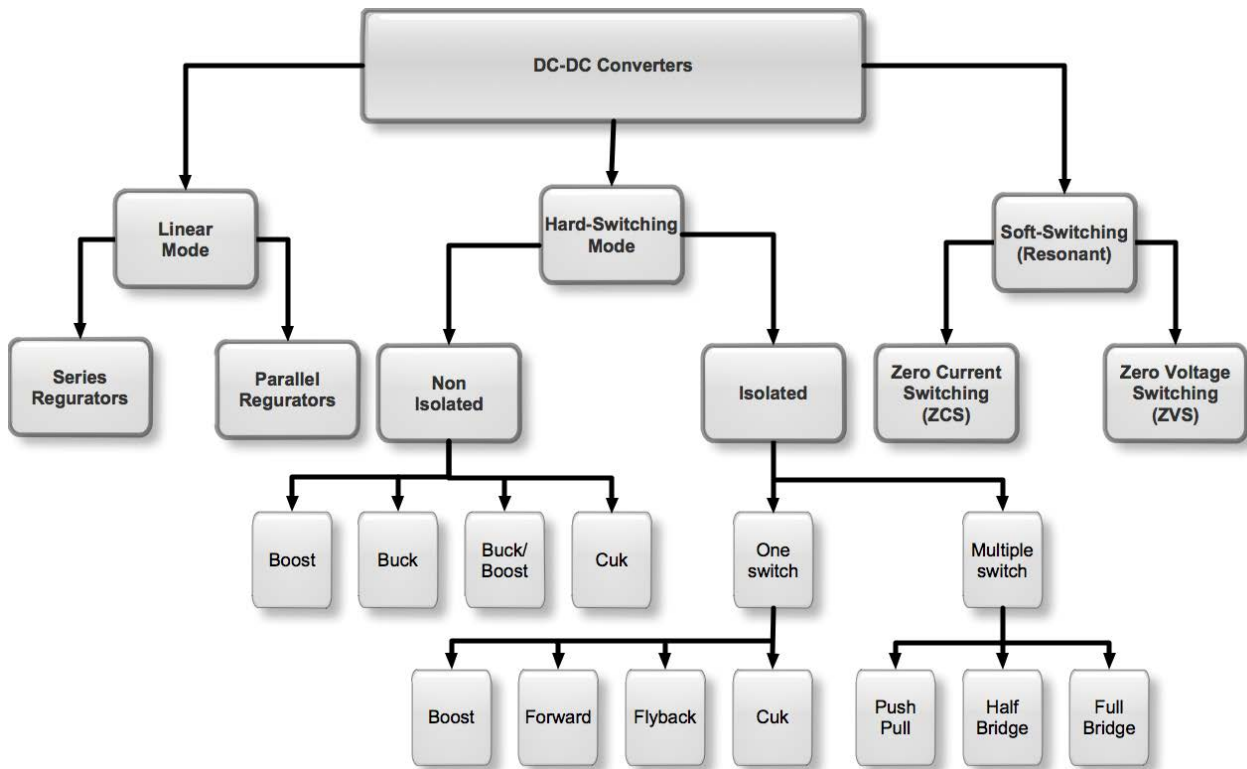


Figure 4.1 – DC-DC power converter family tree.

In switched-mode topologies, finite duration of the switching transitions will cause high peak pulse power dissipation in the devices, degradation of the converter efficiency and, also can lead to transistor damage during the turn-off transition. Employing load-line snubbers can reduce this problem. When using snubbers the stress of the switches are minimised, as shown in Figure 4.2. However, with the appearance of new power electronic converters based on soft-switching technologies, [59;61;65-73], the reduction of switching losses and the continual improvement of power switches allow at being able to increase the switching frequency. In this type of converter the turning on and turning off of the converter switches appears when the switch voltage or the switch current is zero, as shown in Figure 4.2 [74].

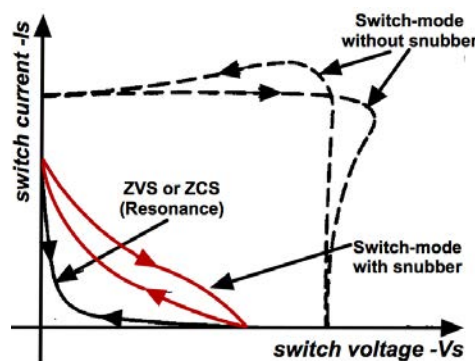


Figure 4.2 – Switching loci trajectories of the different converter types.

An increased switching frequency means that the passive filter requirements and/or the output current ripple are decreased [75]. There is a variety of possible topologies, which can be implemented as ZVS [61;63;69;76;77] or ZCS [59;61;65;69;78].

Figure 4.3 provides an arrangement for a soft-switching resonant converter. An inductor  $L_s$  and a capacitor  $C_s$  have been added to help the switch action. A similar  $LdCd$  pair is added to the diode. In any of these soft switching cases, switch action at a zero crossing cuts off the ringing resonant waveform. This technique is often called quasi-resonance [79].

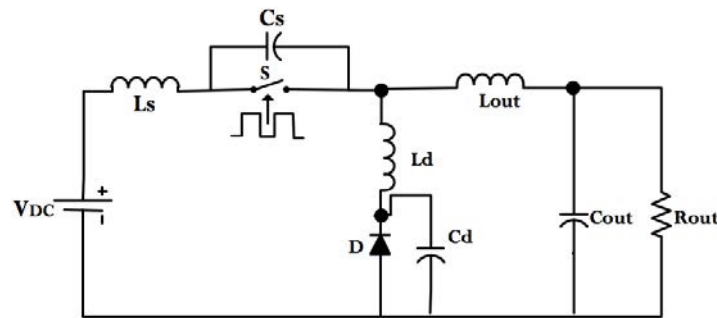


Figure 4.3 - General structure of a resonant converter, where ZVS or ZCS can be obtained.

To create conditions for the ZCS or ZVS in DC-DC converters, the resonance or soft switching approach can be used. The ZVS or ZCS can be obtained by re-arranging the resonant component in Figure 4.3 which combinations offer several possibilities for resonant action as follows:

- 1) If the parts are chosen so that  $C_s$  and  $L_d$  are very small and have minimal effect on the circuit action. With  $L_s$  and  $C_d$  forming an LC series combination, the transistor operation can take advantages of current zero crossing for ZCS.
- 2) If the values of  $C_s$  and  $L_d$  are small, then the transistor supports ZVS.
- 3) It is also possible to use all four parts to support ZVS and ZCS action together, called multi-resonance, but this is not a common technique.

ZCS can eliminate the switching losses at turn-off and reduce the switching losses at turn-on. If a relatively large capacitor is connected across the output diode during resonance, the converter operation becomes insensitive to the diode's junction capacitance. The major limitations associated with ZCS when power Mosfets are used are the capacitive turn-on losses. Thus, the switching loss is proportional to the switching frequency, during turn-on, considerable rate of change of voltage can be coupled to the gate drive circuit through the Miller capacitor, thus increasing switching loss and noise. Another limitation is that the switches are under high current stress, resulting in high conduction loss. ZVS eliminates the capacitive turn-on loss. It is suitable for high-frequency operation. For single-ended configuration, the switches could suffer from excessive voltage stress,

which is proportional to the load. The output regulation of the ZCS and ZVS resonant converters can be achieved using variable frequency control. The ZCS operates with constant on-time control, while ZVS operates with constant off-time control.

## 4.2. Requirements for selecting the converter topology

On the selection of the converter topology the following requirements are considered in order to ensure the maximum efficiency and minimum cost of the system:

- ✓ Control of output voltage according to a given reference
- ✓ Deliver current with little ripple
- ✓ High efficiency in the whole operating range
- ✓ Properly operation in all conditions

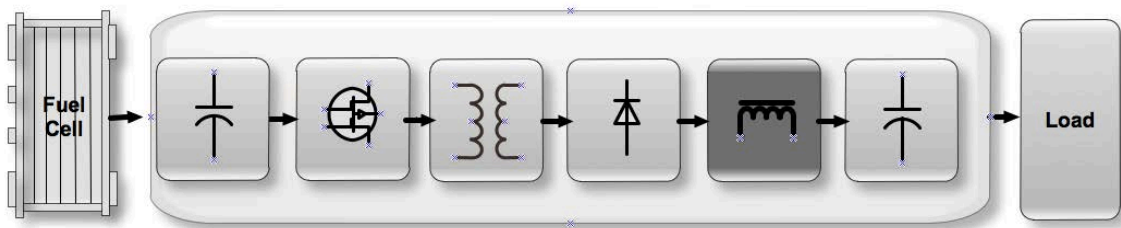


Figure 4.4 - Voltage-fed topologies for fuel cells.

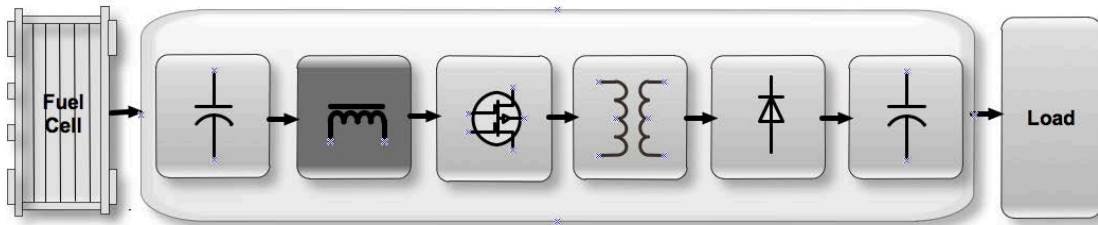


Figure 4.5 - Current-fed topologies for fuel cells.

Basically, the DC-DC converter can operate as a current-fed or a voltage-fed type. According to the literature [57;58;80], the voltage-fed converters are popular for high voltage; low current input and low voltage output applications and the current-fed converters are a good selection for applications with low voltage, high current input and high voltage output. The fuel cell stack has normally a low voltage. Therefore; it needs to step-up to the utility line voltage. This process must be doing by the application of DC-DC converter. But, the boost ratio is very high and cannot be achieved simply by a non-isolated boost converter; therefore, an isolated DC-DC converter topology with isolated transformer is necessary. Then, the first requirement excludes all topologies without a transformer



and also excludes all topologies for which a controller cannot be designed for a stable output voltage, during variations of output current and input voltage.

The high power to transfer by the converter is another requirement not to despise when selecting the topology of the converter, because it results in a large size of the transformer and/or its saturation. High-frequency operation reduces the size of transformer, filters and other reactive components conducting to a compact, low cost and low weight converter, [61].

Using high-frequency operation, the hard-switched converters suffer from high switching losses, electromagnetic interferences and component stresses. The switching losses increases with increase in switching frequency, reducing the efficiency of the converter. Therefore, soft-switching is required for the operation of the converter at higher frequency in order to achieve higher efficiency [61]. The soft-switched DC-DC converters for fuel cells have been analysed by many researchers [59;60;66;73;76;78;81;82] and they present some comparative advantages. The three most important are:

- 1- DC-DC converters operating with high switching frequency enables the use of a small ferrite transformer core.
- 2- DC-DC converters operating with high switching frequency may operate in a much larger DC input voltage range than the linear regulators
- 3- DC-DC converters operating with high switching frequency present higher efficiency

Nevertheless, two drawbacks are also associated to the switched-mode regulators, namely:

- 1- The use of high frequency techniques increases the noise
- 2- The methods of control are more complicated than compared to the linear ones.

However, due to their advantages over other converters, soft switching converters are good selection for fuel cell applications when adequate control strategies are used. A comparative analysis of the major topologies is made in the section below.

#### **4.3. DC-DC converter topologies**

Power electronic converters in general and DC-DC converters in particular[63;83-85] [86]have a great importance on the performance and efficiency of energy production process based on fuel cells. The control of the operation point of the fuel cell requires appropriate use of static power converters, capable of providing accurate support to the control methods [57;62;65;83;87-92]. The main objective to be achieved when applying the converters to fuel cells is obtaining the maximum efficiency using the most appropriate control strategies, taking into account requirements such as;

cost, efficiency, ripple current and efficient operation under transient load conditions. In this context, there are several possible converter topologies in cascade that can be used: DC-DC together with DC-AC, DC-AC interfacing directly the FC to the grid or DC-DC together with AC-AC isolated by a transformer. Usually the DC-DC converter is put between the fuel cell and the inverter which performs two functions namely; 1) acts as a DC isolation for the inverter; and 2) produces sufficient voltage for the inverter input so that the required magnitude of the AC voltage can be produced [91]. The inverter can be single-phase or three-phase depending on the utility connection. Some typical configurations used in the conversion of fuel cell energy to the grid are shown below.

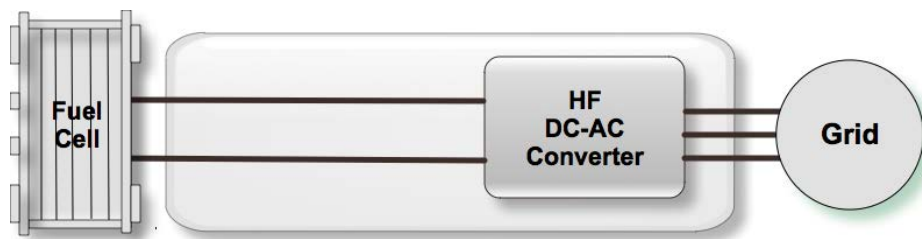


Figure 4.6 - Configuration of a DC-AC converter interfaced directly to the grid.

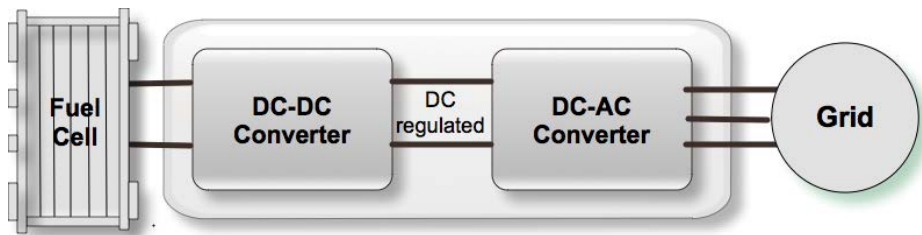


Figure 4.7 - Configuration of a DC-DC and a DC-AC converter.

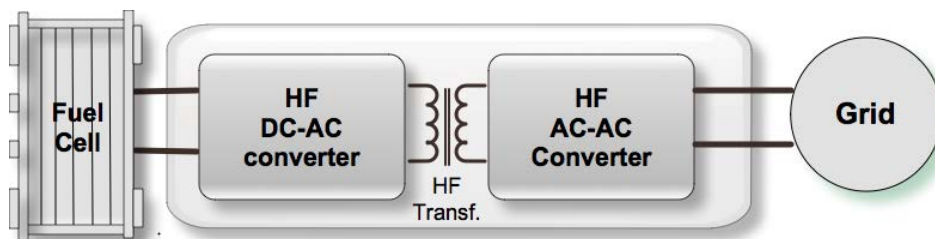


Figure 4.8 - Configuration of a DC-AC and an AC-AC converter.

As mentioned above, the soft-switching or resonant converters are getting more and more interest because of their advantages over other converters such as: higher frequency operation, which implies in small size, lighter weight, reduced EMI and low component stresses. The analysis and comparison of these converters have been performed by many researchers [59;61;69;76;93]. Considering the analysis made in [61], the generic scheme for the DC-DC converter is presented in

Figure 4.9. The primary side of the HF transformer is an HF inverter using Mosfets or IGBTs that are soft switched in the zero of voltage. For the soft switching, L and C components must be used. The secondary of the HF transformer has an AC-DC converter, which may consists of diodes or active switches (Mosfets or IGBTs). Another important aspect to consider is the insertion of low pass filters in both the input and output.

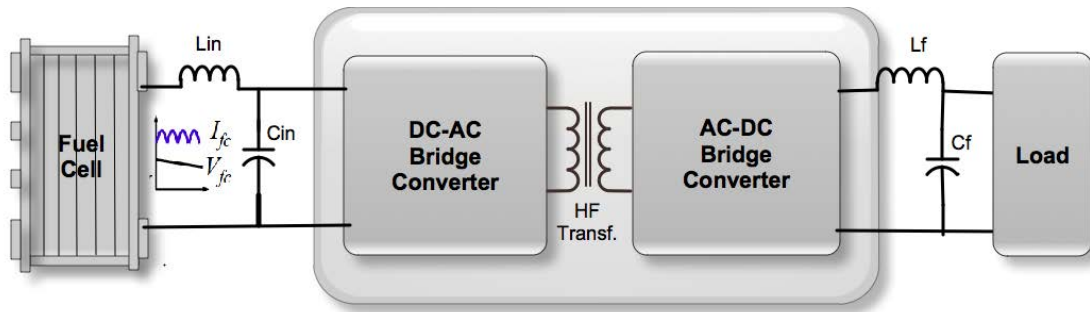


Figure 4.9 – Generic scheme of a DC-DC converter for fuel cell application.

#### 4.3.1. Series resonant converter with capacitive output filter

The converter topology shown in Figure 4.10 is in conformity with the considerations presented above. This is a modified series resonant converter (SRC), which uses an (L-C)||L resonant tank for soft switching of HF switches. The main characteristics of such type of converter can be summarized as follows:

- 1- This configuration gives high efficiency at all varying load and line conditions but it decreases with increase in input voltage.
- 2- The full range ZVS (full load to light load) is achieved.
- 3- Switch peak current reduces with load but increases significantly with change in input voltage.

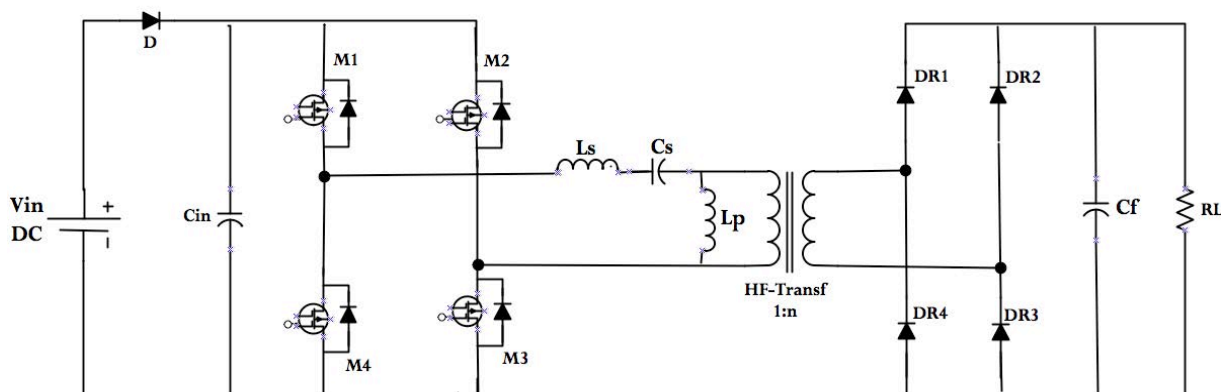


Figure 4.10 - Series Resonant converter with capacitive output filter.

### 4.3.2. Series resonant converter with inductive output filter

The converter topology shown in Figure 4.11 is an LCL type SRC with inductive output filter. This uses an LCL resonant tank for soft switching of high frequency switches and an inductive output filter. Its main characteristics can be summarized as follows:

- 1- The full range ZVS (full load to light load) is achieved.
- 2- Rectifier diode voltage rating is higher, but with application of ultra fast recovery diodes of high voltage rating with low forward voltage drop does not affect the efficiency much.

Note: This configuration can also be modified to a series resonant converter (SRC), which uses an (L-C)||C resonant tank for soft switching of high frequency switches, which, in this case is also called series-parallel resonant converter (SPRC).

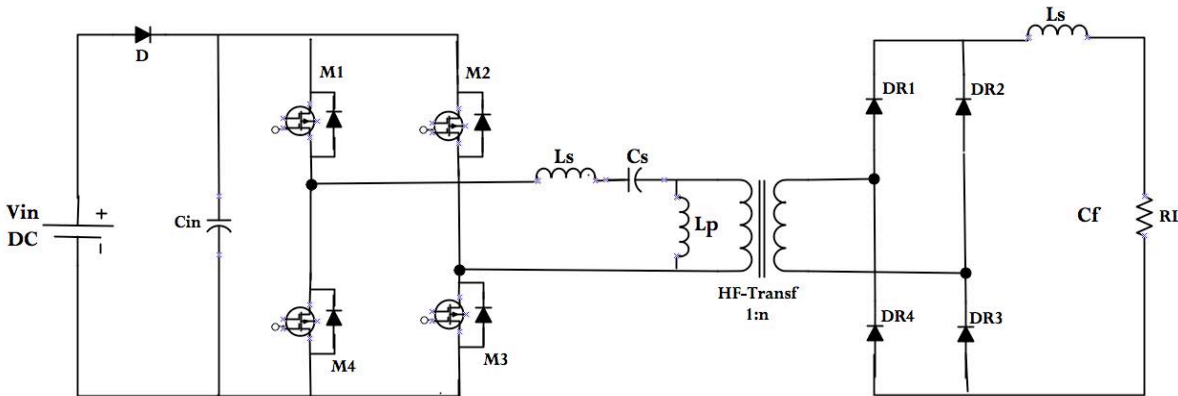


Figure 4.11 - Schematic of resonant converter with inductive output filter.

### 4.3.3. PWM full-bridge converter with inductive output filter

The configuration shown in Figure 4.12 is Phase-shifted full bridge converter with inductive output filter. This is most widely used soft-switched configuration for high power applications. This constant frequency converter features ZVS of the primary switches with relatively small circulating current. The ZVS is achieved by filter inductance, transformer leakage inductance, snubber capacitance and parasitic junction capacitances of switches. The control of the output voltage at constant frequency is achieved by phase shift technique. Its main characteristics can be summarized as follows:

- 1- The major limitation of this configuration is loss of duty cycle on the secondary side.
- 2- High voltage stress on rectifier diodes on secondary side.
- 3- Parasitic ringing at the secondary side of transformer.

- 4- Large inductor may increase ZVS range but needs a transformer turns-ratio ( $N_p/N_s$ ) to be decreased at the same time, which increases primary side current, causing large conduction losses which decreases converter efficiency.
- 5- A good compromise between the transformer turns-ratio and leakage inductance is required to keep conduction losses lower.

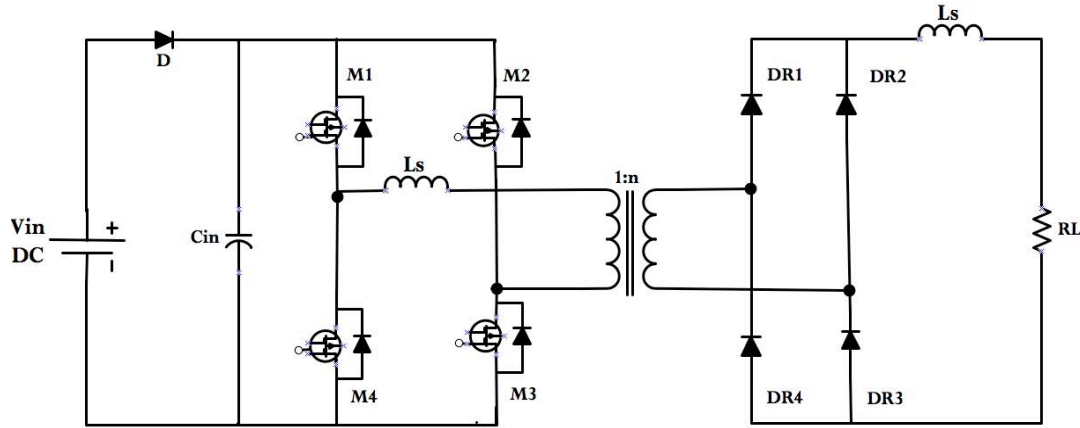


Figure 4.12 – Schematic of a PWM full-bridge converter.

#### 4.3.4. Full-bridge converter with secondary side controlled

The configuration shown in Figure 4.13 corresponds to a secondary side controlled converter with a full-bridge inverter on primary side and phase-controlled rectifier on secondary side. The switches on primary side are operated by complementary gating scheme with fixed duty ratio. The switches on secondary side are controlled to produce phase difference between primary and secondary side voltages of HF transformer to control the output voltage with load and input line voltage variations.

The main characteristics of this configuration can be summarized as follows:

- 1- Control is easy and simple.
- 2- The switches on secondary side show ZVS or ZCS depending upon the line and load. Which represents a drawback of the converter.
- 3- The switches on secondary side show ZVS for lower input voltage and ZCS for higher input voltage conditions.
- 4- The efficiency of this converter is near to 92%, obtained at full load and varying line voltage.

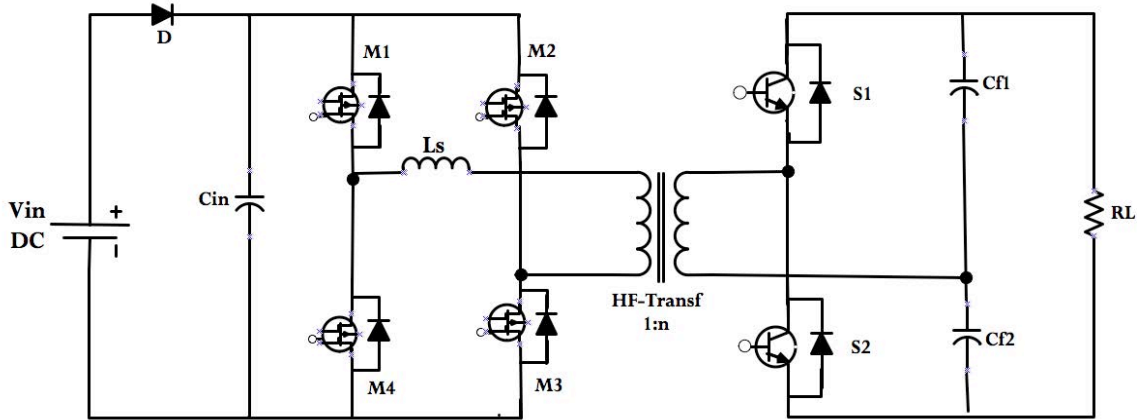


Figure 4.13 – Schematic of full-bridge secondary controlled converter.

#### 4.3.5. Current-fed two-inductor boost converter

Figure 4.14 shows the current-fed two-inductor boost converter, which is a dual of voltage-fed half-bridge converter configuration. This topology requires a very small turns ratio transformer with only two switches used on the primary side. The turn off of the primary switches is smooth since voltage across the switches is sinusoidal. Also the same for turn on and turn off of rectifier diodes. However, the peak and average current through rectifier diodes is high and this is very difficult to achieve ZVS at variable line input and load condition. This topology is a good selection for constant-input and constant-output voltage applications.

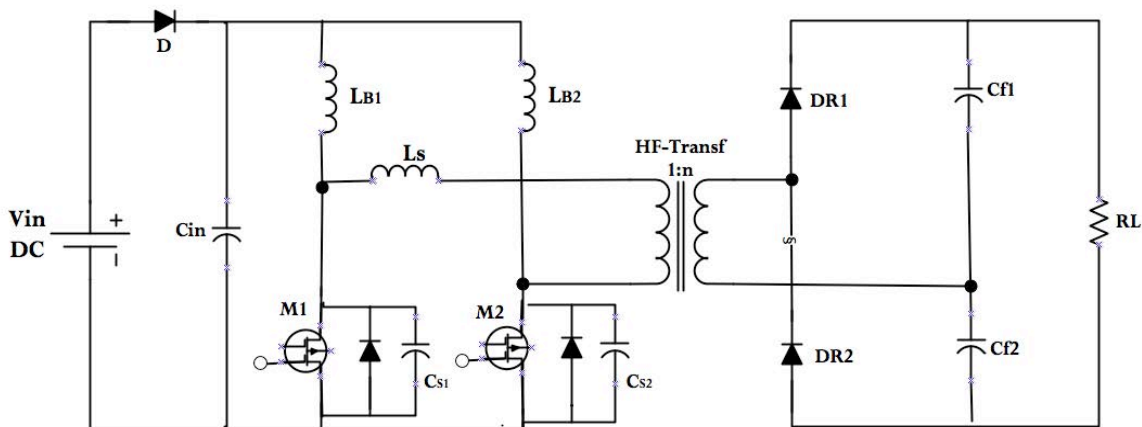


Figure 4.14 – Schematic of current-fed two-inductor boost converter.

### 4.3.6. Bidirectional current-fed converter

The configuration of Figure 4.15 corresponds to a soft-switched bidirectional current-fed boost converter. The active switches in the both sides of the transformer make this converter bidirectional. Normally, the Mosfets are used in the low voltage side and the IGBTs are used in the high voltage side. This configuration can be in push-pull, half-bridge or full-bridge, with the full-bridge considered one of the best topology choices for fuel cell applications.

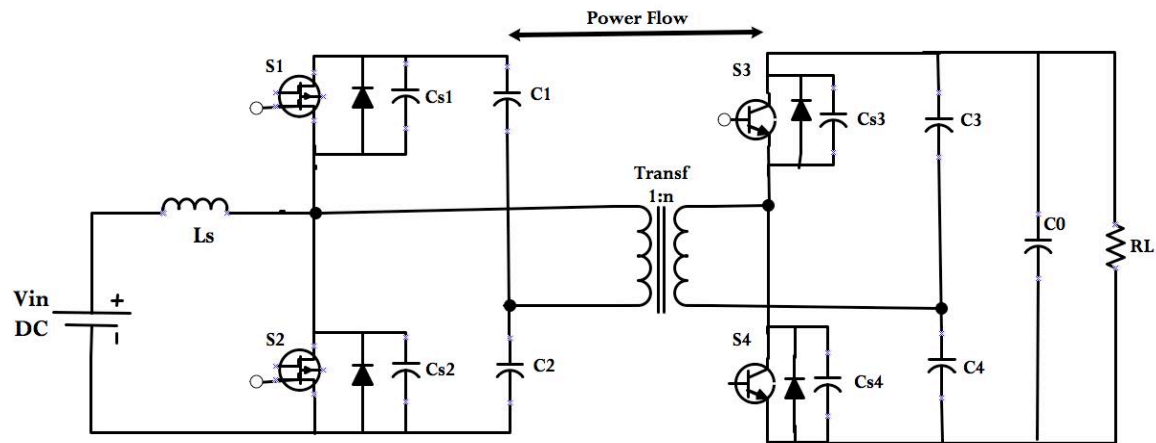


Figure 4.15 – Schematic of a soft-switched bidirectional current-fed boost converter.

### 4.3.7. Z-Source converter

The impedance-source converter or Z-Source converter is a relative new electronic circuit recently recognized because of its applications in power conversion [94-98]. The Z-source converter overcomes the conceptual and theoretical barriers and limitations of the traditional voltage-source converter and current-source converter and provides a novel power conversion concept. It can be applied to all power conversion types [96]. It has been applied in power conditioning systems and utility interface of renewable energy sources based power generation [95] such as; PV, Fuel Cell, and Wind power generation, in adjustable speed drives [99], to name a few. The configuration of the Z-Source topology is simple, two-port networks consisting of a split-inductor L1 and L2 and capacitors C1 and C2 connected in X shape, which are utilized to realize inversion and boost function in one single stage, as is shown in Figure 4.16.

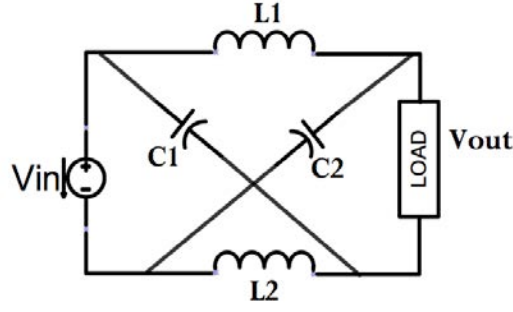
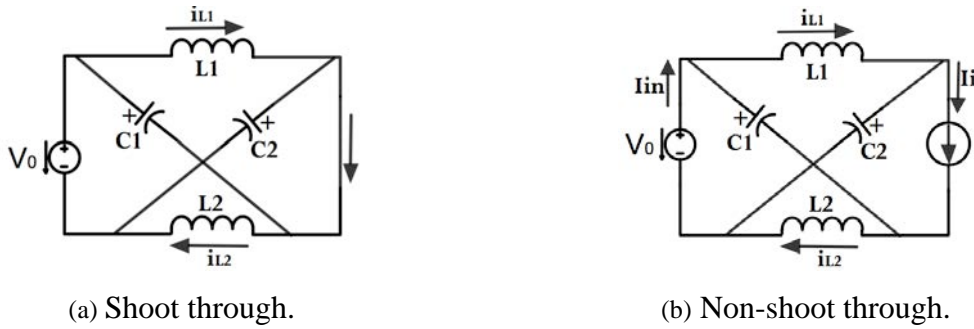


Figure 4.16 – Z-Source converter scheme.

Compared to the traditional systems, the Z-Source converter does not need big transformers or DC-DC converter to boost the voltage in the circuit. As is known, the switch in the DC-DC converter will make the efficiency lower and the cost higher. Thus, in the Z-Source inverter system, the size and cost are minimized.

Observing the Z-Source converter scheme above, there are two basic operation modes namely, shoot-through mode and non-shoot-through mode as shown in Figure 4.17.



(a) Shoot through.

(b) Non-shoot through.

Figure 4.17 - Operation modes of the Z-Source converter.

The relationship between the boost factor (B), shoot through duty cycle ( $T_0/T$ ), capacitor voltage ( $V_{C1}$ ,  $V_{C2}$ ), and output peak voltage  $v_{ac}$  are defined by the following equations;

$$B = \frac{1}{1 - \left( \frac{2T_0}{T} \right)} \quad \text{Eq. 4.1}$$

$$V_{C1} = V_{C2} = V_c \times \frac{1 - \left( \frac{T_0}{T} \right)}{1 - \left( \frac{2T_0}{T} \right)} \times V_0 \quad \text{Eq. 4.2}$$



$$v_{ac} = M \times B \times \frac{V_0}{2} \quad \text{Eq. 4.3}$$

Where  $M$  is the modulation index,  $T$  is the switching period, and  $T_0$  is the shoot-through interval. Figure 4.18 shows a typical application of the converter to a fuel cell. In this case, the DC power produced by fuel cell is converted into three-phase AC power which can be used to feed a motor, for example.

The analysis of the Z-Source converter operation under resonance conditions is analysed and described in [94].

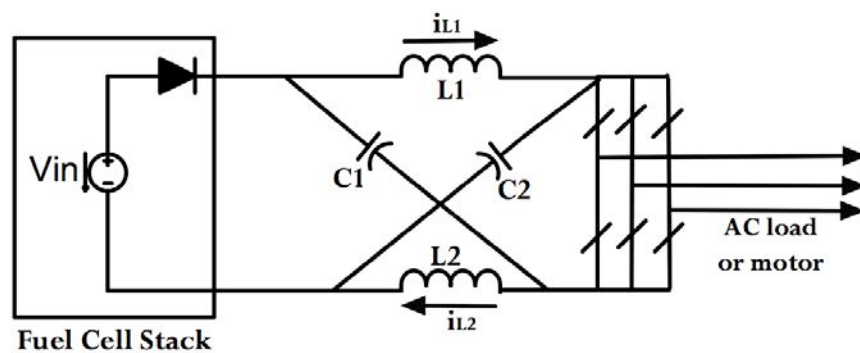


Figure 4.18 - Typical application for a Z –Source in fuel cell system.

#### 4.4. Topology of converter selected

Once analysed the various topologies discussed earlier, the main conclusions are:

- 1- For a constant input voltage or with a very small ripple variation, the LCL resonant converter is a good selection.
- 2- For an input voltage with large variations, the LCL resonant converter is not able to maintain ZVS at high input line voltage.
- 3- Other converter configurations cannot maintain ZVS at very light load condition even for a constant input voltage.
- 4- There is a compromise between overall efficiency and soft switching range.
- 5- For a large input voltage variation and higher input current (as is the case of a fuel cell system), the current-fed DC/DC converter shows ZVS at high input voltage.

Considering these conclusions, a full-bridge series-resonant inverter, followed by a high frequency transformer and a rectifier, composes the topology selected for this application. Additionally, two low-pass filters are included, one in the primary side which is used to protect the PEM of high ripple-current and another in the secondary side, to improve the quality of the energy supplied by

the power system to the load or the grid. The operation of the converter is described in the section follow and the design of each component will be discussed later.

#### 4.5. Operation of converter selected

The operation of the converter represented in Figure 4.19 can be described as follows: the voltage supplied by the fuel cell stack, which is typically low must be converted to a high and constant level, for example; 48 V or 400 V<sub>DC</sub> in order to be able to feed an electric vehicle or to be sent to the grid through an inverter. The HF transformer is a step-up voltage transformer, which also serves as galvanic isolation between the high and low voltage levels of the circuits. The waveforms of the voltage and current in the LC series resonant circuit in the primary side of the transformer are sinusoidal. Selecting appropriate values for the  $L_r$  and  $C_r$  components, the resonant frequency of the circuit is established. Then, the DC voltage of the fuel cell is firstly inverted in the primary side of the HF transformer, being rectified on the secondary side. The low pass filter in the primary side ( $L_{PEM}$ ,  $C_{PEM}$ ) allows at protecting the PEM fuel cell from the ripple current and voltage produced by the converter, and also allows the storage of energy in the DC bus. The low pass filter in the secondary ( $L_f$ ,  $C_f$ ) allows at reducing the ripples of current and voltage to the load, respectively.

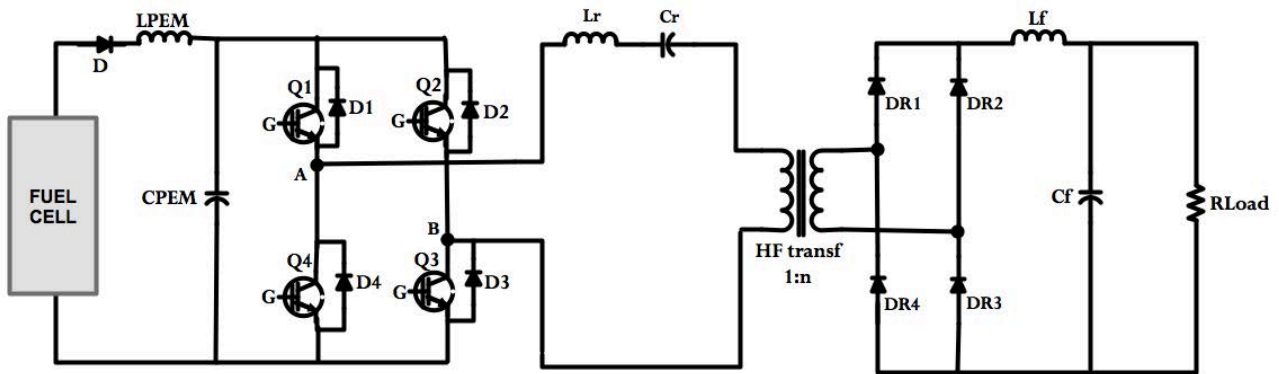


Figure 4.19 – Electrical circuit of the SRC.

#### 4.6. Methods of control of DC-DC converters

In recent years, control theory and its application in electrical and mechanical systems have developed in a notable way. Research in the field of soft switching control is done with the objective of improving the stability, reducing the losses of commutation, improving the efficiency and as well as with the objective of developing control methods to improve the system performance. The methods to control DC-DC converters are quite abundant in the literature; this section deals with the different control techniques that are frequently used in dc-dc converters. Once

characterized each technique, defined their merits and demerits, it is selected the control structure that best suits the goal of the thesis.

#### 4.6.1. Overview of control methods

The block diagram of Figure 4.20 gives an overview of common methods used to control DC-DC converters and perturbations that affect the behaviour of the converter and its stability. The feedback control is the mechanism through which the system maintains the equilibrium that is, in feedback control the variable is measured and compared with a reference; the controller handles the error, which is responsible for keeping the control variable in the required value. The feedback signal may be the output voltage, the inductor current, or both.

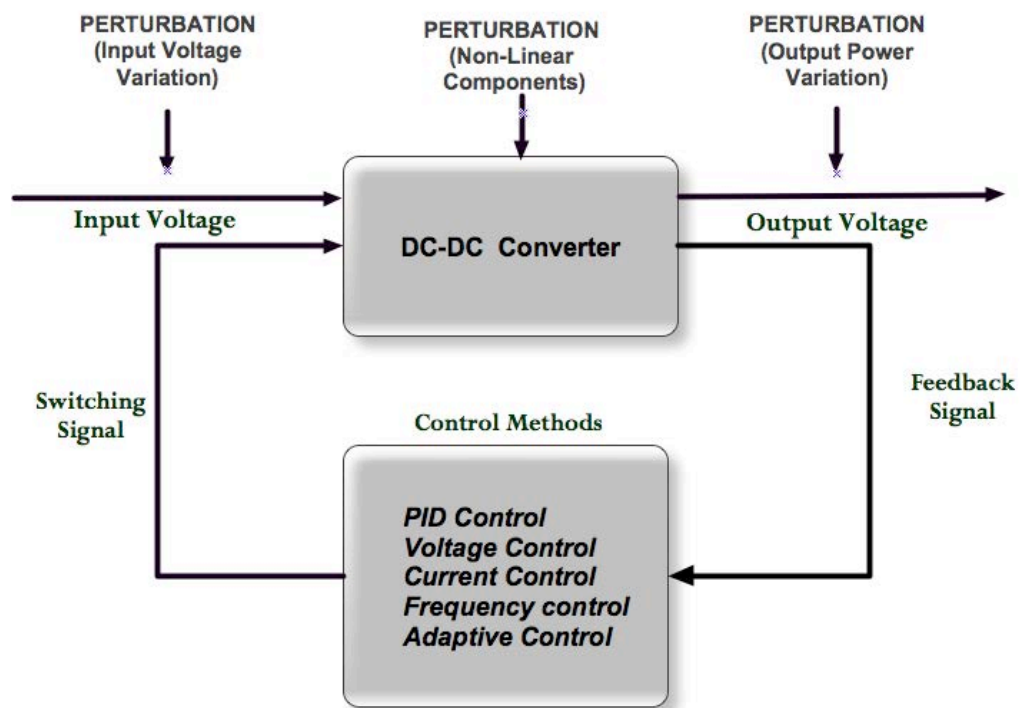


Figure 4.20 –Common methods used in the control of the DC-DC converters.

#### 4.6.2. PID control

Among the control methods normally used to in DC-DC converters the PID controller is the most widely used [79] . Over 85% of all dynamic controllers are of the PID type. There are actually a great variety of types and design methods for the PID controller. The acronym PID stands for Proportional – Integral - Differential control.

The proportional term depends only on the difference between the set point and the process variable. This difference is referred to as the Error term. The *proportional gain* ( $K_p$ ) determines the ratio of output response to the error signal.

$$P_{term} = K_p \times e(t) \quad \text{Eq. 4.4}$$

The integral term is proportional to both the magnitude of the error and the duration of the error. It accelerates the movement of the process towards set point and eliminates the residual steady-state error, which occurs with a pure proportional controller.

$$I_{term} = K_I \times \int_0^t e(t) dt \quad \text{Eq. 4.5}$$

The derivative term causes the output to decrease if the process variable is increasing rapidly. The derivative response is proportional to the rate of change of the process variable. Increasing the *derivative time* ( $T_d$ ) parameter will cause the control system to react more strongly to changes in the error term and will increase the speed of the overall control system response. It is always used in conjunction with one or more of the other control modes. It is used to reduce the magnitude of the overshoot produced by the integral component and improve the combined controller-process stability.

$$D_{term} = K_D \times \frac{d}{dt} e(t) \quad \text{Eq. 4.6}$$

In Figure 4.21 the control signal  $u(t)$  is the sum of the three terms. Each of the terms works “independently” of the other. However, the PI controller is the most common, since derivative action is sensitive to measurement noise, whereas the absence of an integral term may prevent the system from reaching its target value due to the control action. Sometimes certain of the terms are left out because they are not needed in the control design.

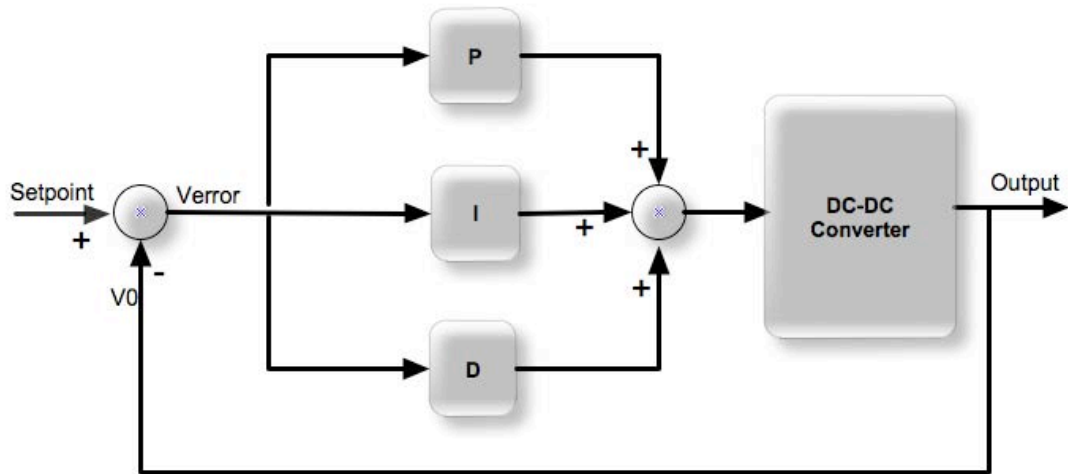


Figure 4.21 - PID control.

#### 4.6.3. Voltage control

The voltage is measured at the output and is compared to a reference voltage or a set point, to generate an error signal [100]. This error signal is applied to the input of a compensation network, and the output of the compensator drives the control signal  $d(t)$  as shown in Figure 4.22. In voltage mode control any change in the source or the load is only detected after it has propagated to the output.

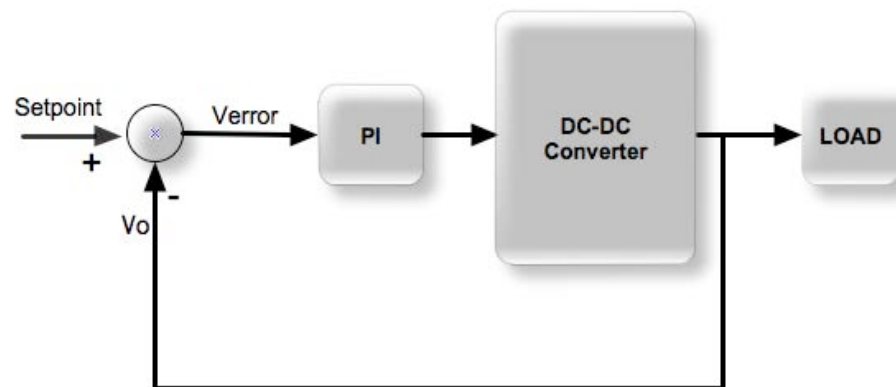


Figure 4.22 - Voltage mode control.

#### 4.6.4. Current control

In current mode control the inductor current is used as a feedback state [100]. However the current and voltage reference values are not independent and this specifically requires knowledge of the load. To overcome this obstacle the voltage error signal is used to generate a current error signal as shown in Figure 4.23. Current mode control requires knowledge of the inductor current, which is

controlled via the inner loop. The outer loop manages the output voltage error by commanding the necessary current. The inner loop makes the converter to act as a current source. There are many methods that use the current mode control, such as peak current mode control [101], average current mode control [102], sensorless current mode control [103].

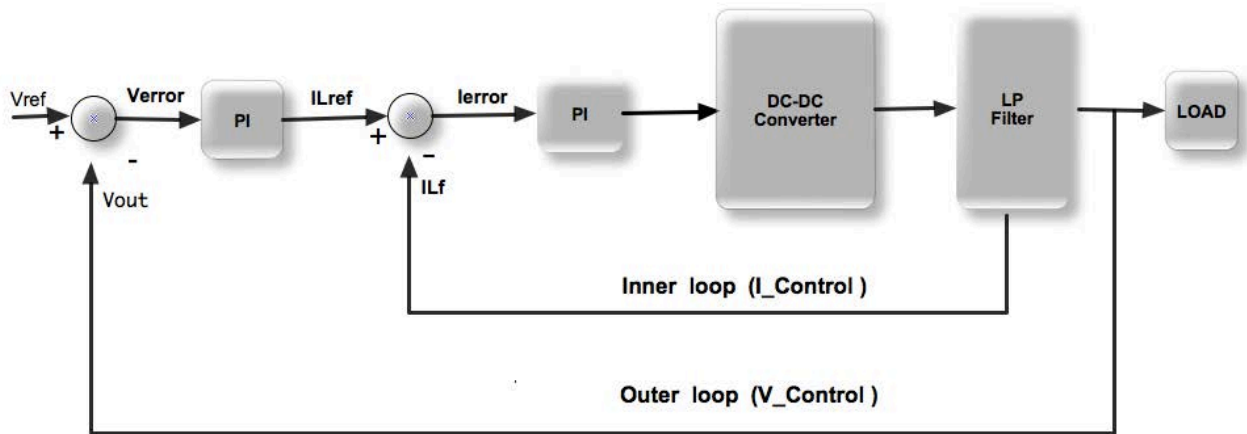


Figure 4.23 - Current mode control.

#### 4.6.5. Adaptive control

Adaptive control is the control method used by a controller, which must adapt to a controlled system with parameters that vary, or are initially uncertain[104]. Adaptive control is different from robust control in that it does not need a priori information about the bounds on these uncertain or time-varying parameters; robust control guarantees that if the changes are within given bounds the control law does not need to be changed, while adaptive control is concerned with control law changes themselves. In the adaptive control the input source varies with time and its response is highly dependent on external factors as is shown in the general block diagram of

Figure 4.24.

In order to design a good controller the following information is required:

1. Specification of the desired control loop performances.
2. Knowledge of the dynamics model of the system to be controlled.

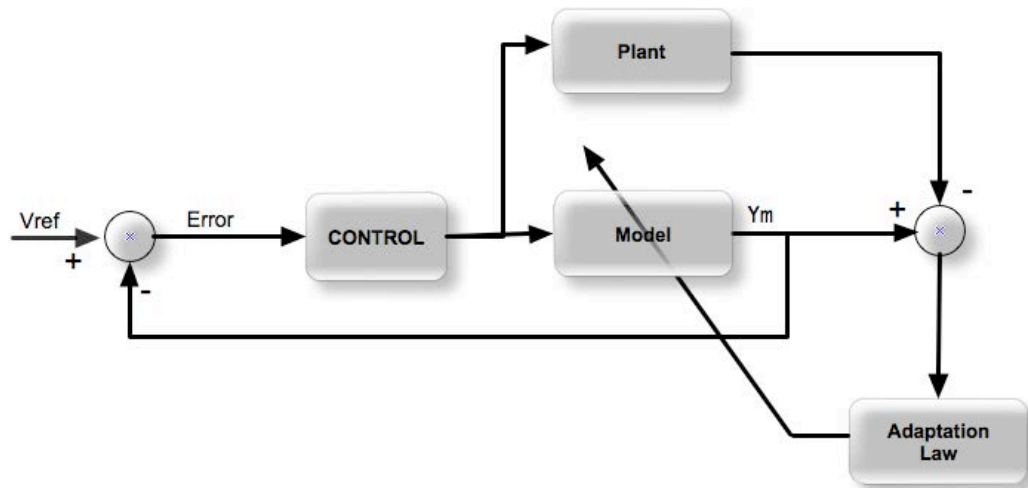


Figure 4.24 - Adaptive control.

## 4.7. Methods of control of resonant converters

The main goal of the control of resonant converters is to optimize its power conditioning by maintaining zero, or near-zero, switching losses. Some of the control techniques that are applied in resonant converters include variable frequency control, phase shift modulation control, optimal control, among others[105]. An overview of these techniques is made follow.

### 4.7.1. Variable frequency control

The switch-control is achieved by varying the switching frequency  $f_s$ , above the resonant frequency  $f_r$  while switches in one leg of the full-bridge maintain a 50% duty cycle ratio with 180° phase shift between the control signals of the other leg of the bridge. In other words, both the on time is fixed and the off time is variable or vice-versa. The controller is composed by an amplifier and a voltage-controlled oscillator (VCO). The output voltage is normally compared with a reference, which error voltage is amplified and used to drive the VCO. The VCO output triggers the one-shot whose pulse duration is fixed as required by the converter. The block diagram representing this controller is shown in Figure 4.25.

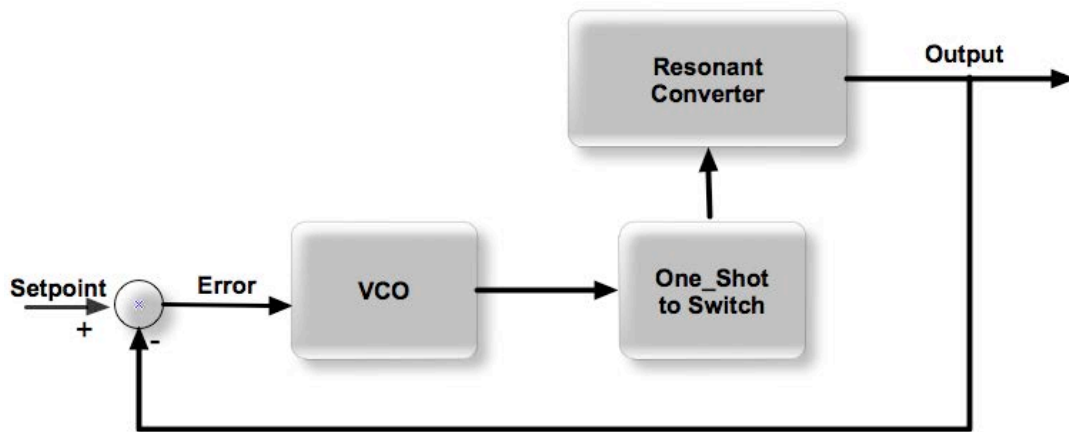


Figure 4.25 - Variable frequency controller of a resonant converter.

#### 4.7.2. Self-sustained oscillation control

The self-sustained oscillation controller technique is used to control the switching frequency that can guarantee both the output voltage regulation and the zero voltage switching (ZVS) of the converter at the same time. In order to achieve that, this technique is composed by two control loops, an inner loop and an outer loop as shown in Figure 4.26.

The inner loop adjusts the phase shift between the resonant current ( $i_r$ ) and the inverter output voltage ( $v, b$ ) to assure that ( $i_r$ ) lags behind ( $v_{ab}$ ) under any operating condition to guarantee ZVS, whilst the outer control loop adjusts the output voltage ( $v_o$ ) according to the reference value. In

other words, the self-sustained oscillation in resonant converters can be defined as a mode of operation for the resonant converter where the switching frequency is not externally imposed like the conventional variable frequency (VF) control; rather, it is let free to oscillate with a frequency dependent on both the converter parameters and the phase shift necessary for ZVS. It is important to

mention that the SSOC can work as a variable frequency controller or as a fixed frequency controller depending on the power circuit of the converter. This technique is advantageous over the variable frequency as shown in

Figure 4.25, with reduced component ratings and better working efficiency. This is due to the fact that the range of the switching frequency from no load up to full toad is smaller compared to that of variable frequency.



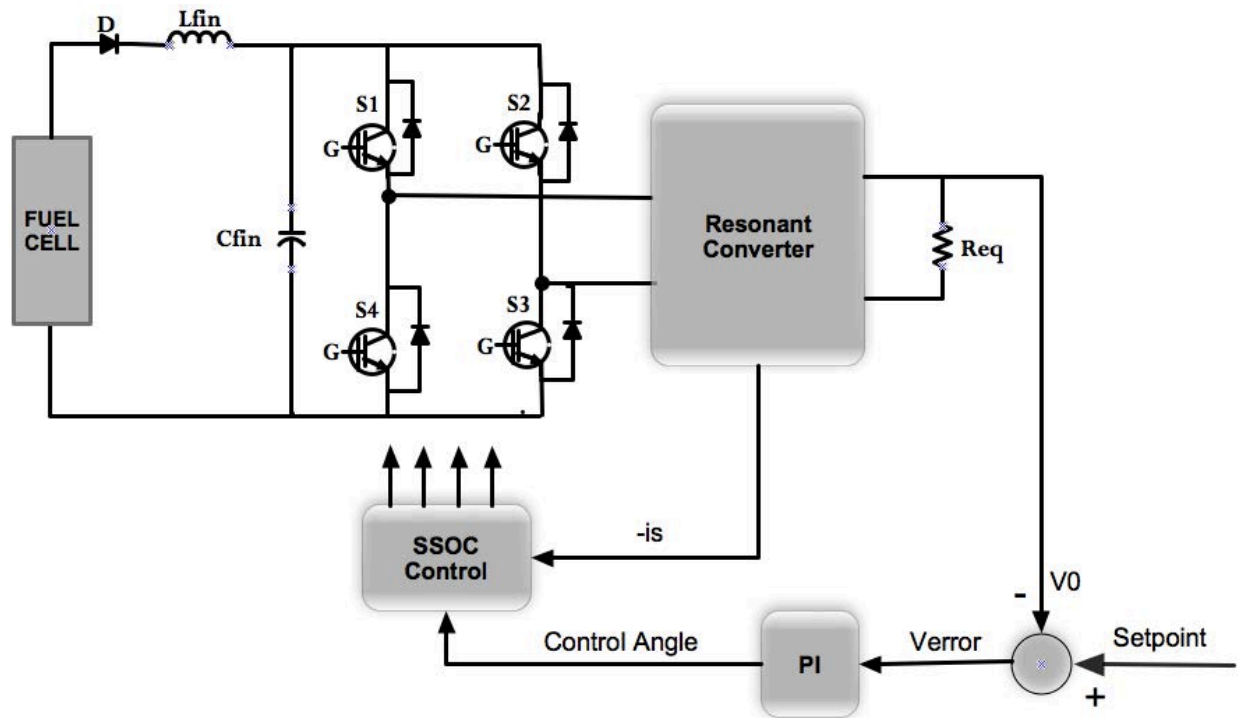


Figure 4.26 - Self-sustained oscillation control of a resonant converter.

### 4.7.3. Optimal control

The optimal control, also known as linear quadratic regulator (LQR) has advantages than the classic control methods because the designer of this method needs only to guess the values of several parameters. Usually, the energy function of the resonant tank is minimized and hence the transient response is optimized. The significant advantage of the optimal control is that when the state variables are accessible, a robust controller with quite good accuracy margins is guaranteed. The design procedure starts with the calculation of the linear state space model of the circuit at one operating point. Then, a linear quadratic regulator (LQR) is calculated for the converter at this point. Knowing that the controller has a good marginal robustness, this guarantees a good response within the operating range. However, there are some disadvantages of using this controller namely; it needs the knowledge of all the states of the system, the controller topology is more complicated and it has high sensitivity to any possibility of an uncertain model. This corresponds to a variable frequency controller for resonant converters and its controller complexity is justified for the use of more powerful and systematic method. Figure 4.27 shows the block diagram of the resonant converter with optimal control.

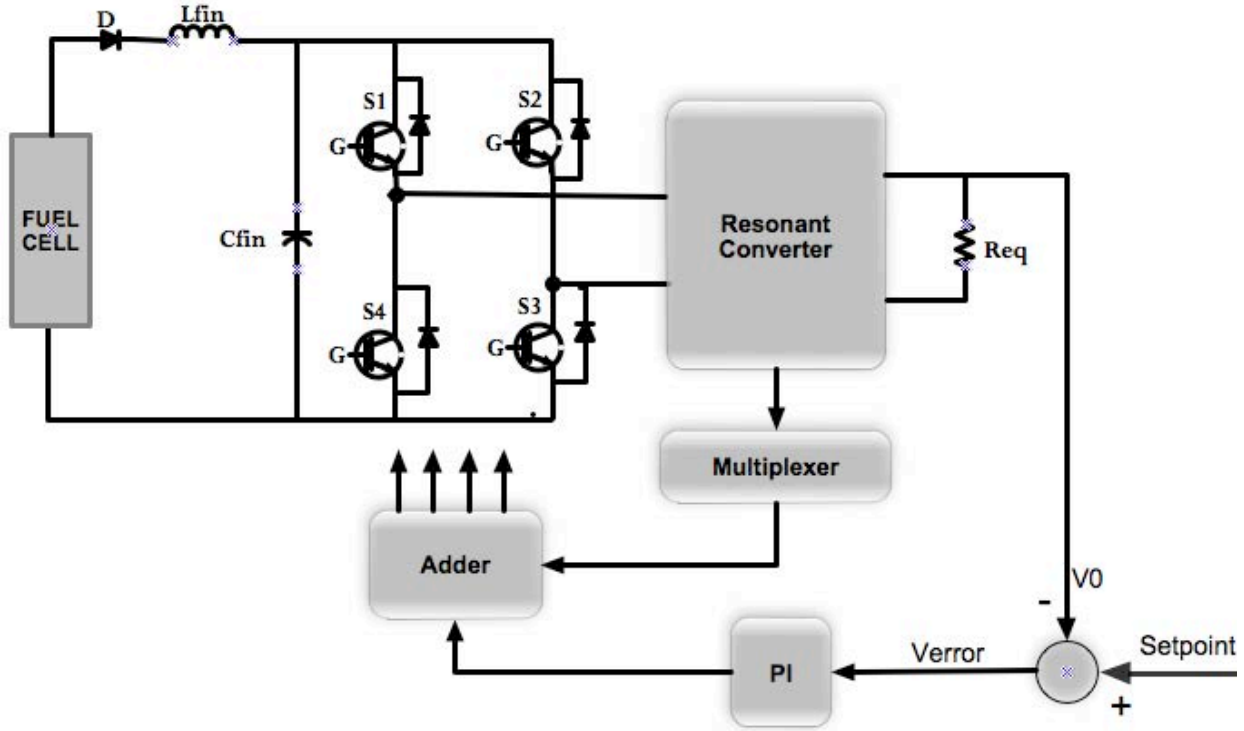


Figure 4.27 - Optimal control of a resonant converter.

#### 4.8. Structure of control selected

The performance of the DC-DC converter depends on some process parameters that cannot be controlled. Such parameters associated with nonlinear behaviour of the converter itself such as; the transformer turns-ratio and leakage inductances, and the series resistance of the filter inductors, which cannot be controlled closely and vary with the load conditions, input source, and operating frequency. Consequently it is required that they will not affect the controller. On the other hand, fuel cells have a limited ripple current capability and a slower response time, which need to be taken into consideration when designing the controller. In this context, the control structure of the DC-DC converter must be dynamically fast, noise immune and to ensure a minimum of losses as well as optimum operating points for the fuel cell.

Then, the control structure selected for the application, which is represented by the scheme of Figure 4.28 below, combines two control loops; the faster one, which is used to control the output voltage and the slow one, which is used to move the operating point of the fuel cell to its optimum point in the polarization curve.

In this context, it is selected the PI controller followed by VCO for the loop of control voltage  $V_{out}$ , as exemplified in the Figure 4.28. The output voltage  $V_{out}$ , is measured and compared to a

reference voltage  $V_{ref}$ , to generate an error signal  $V_{error}$ . The PI controller is characterized by a fast dynamic response to the errors of output voltage.

The optimum operating point of the fuel cell is performed by the slow control loop, which is adapted to the specificities of the fuel cell. The details of implementation of this control will be discussed later in the chapters on modelling and control and also in its experimental implementation.

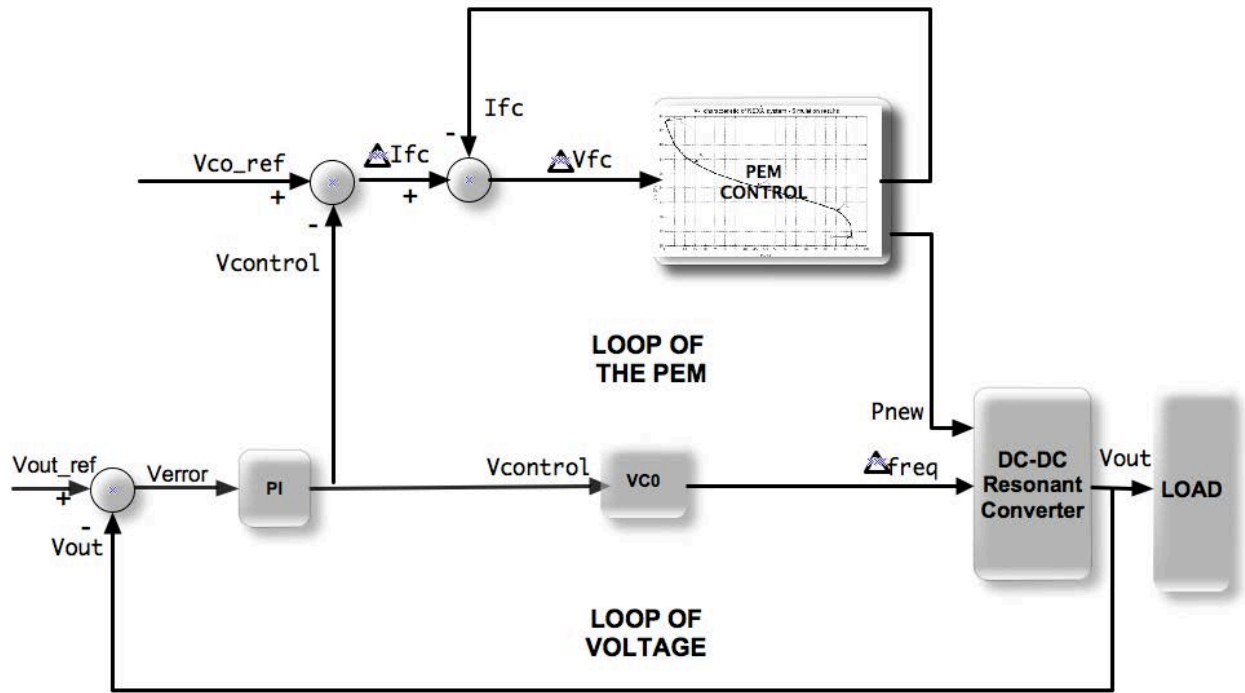


Figure 4.28 - Structure of control selected for the SRC.

## 4.9. Integration of energy storage devices

In order to operate the fuel cell efficiently, the flow rate of hydrogen must be adjusted with changes in the load. Depending on the type of fuel cell system, this flow change can be a very slow process and can have time constants in the 30-second range. Therefore, some type of supplementary energy storage devices must be used.

### 4.9.1. Energy storage options

In a lot of power electronic systems the energy is stored in the DC form. Therefore the devices are normally connected to the dc link of the converters. The different energy storage options available

are shown in Figure 4.29, where they are grouped by direct and indirect storage, and by their specific storage device type.

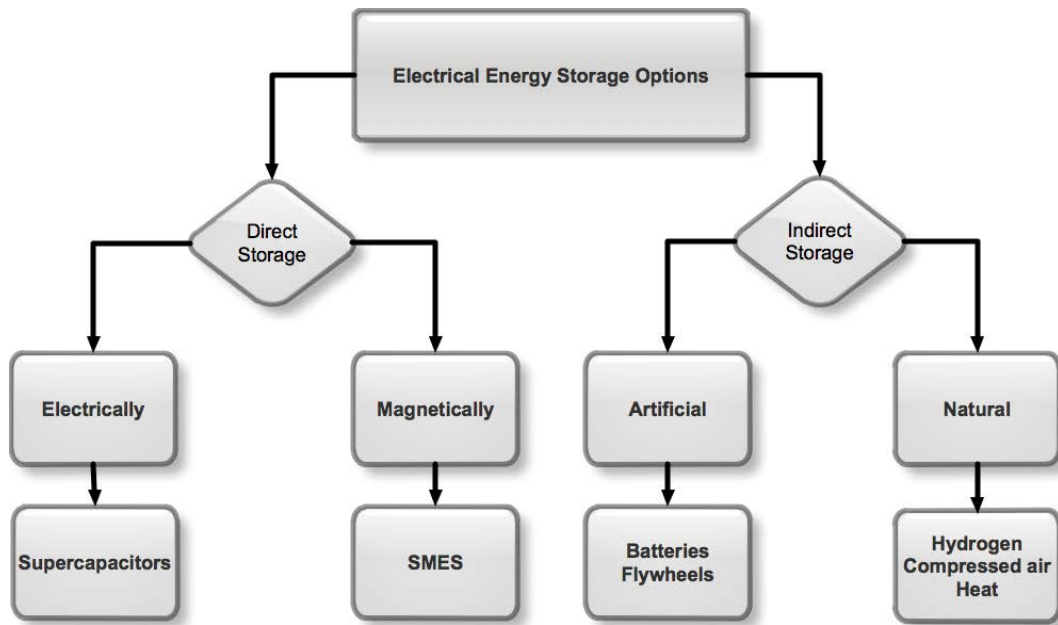


Figure 4.29 – Electrical energy storage options.

Direct energy storage devices are those where the energy is stored without transforming the energy to a different type. This process can be done both electrically and magnetically, using supercapacitors and Magnetic Energy Storage (SMES), respectively. Indirect energy storage methods have been developed over the years various, such as; batteries, flywheels, and compressed air. Most of these storage methods are not very efficient and much of the energy is lost in the process of converting the energy from its electrical form to a different one. Among the indirect energy storage devices the flywheel appears as the most convenient and efficient [106]. The batteries in general have a short lifetime and if stacked in series, often require some type of complex voltage monitoring scheme.. Flywheels only recently have evolved into a more efficient and compact technology that can be used in power electronics systems. Hence, an interesting alternative storage system is the use of supercapacitors, which have high pulse power capacity, long lifetime, high power density, low ESR (Equivalent Series Resistance), and are very compact in size, despite the two drawbacks associated with this technology namely; its low voltage and high cost.

Generally the application of an energy storage technology is characterized by two factors such as; 1) the amount of energy that can be stored in the device, which is a characteristic of the storage device itself and 2) the rate at which energy can be transferred into or out of the storage device, which depends mainly on the peak power rating of the power conversion unit, but it is also impacted by the response rate of the storage device itself.

An example of an integrated power system application combining the fuel cell as the power source and the batteries and supercapacitors as energy storage devices connected to the converters is represented in Figure 4.30.

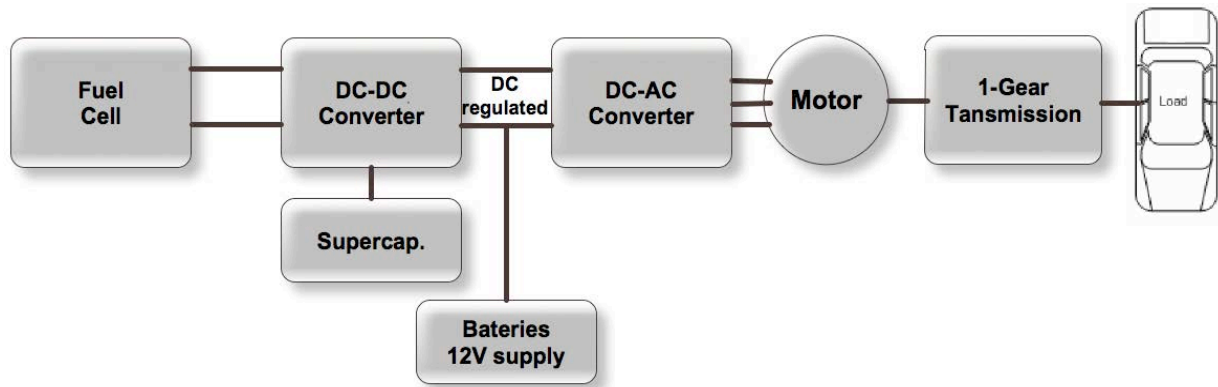


Figure 4.30 – Example of a power system application combining a fuel cell and super capacitors.

#### 4.10. Conclusions

This chapter begins with a literature review on DC-DC converters. The selection of the topology for the application is made once analysed and compared various topologies, Furthermore it is made a description of its operation. The most common methods used to control DC-DC converters, the disturbances that have influence on the behaviour of the converter and its stability are also analysed. Thus, once described and analysed the different methods of control, particularly for resonant converters, a structure of control is selected for the series resonant converter. An overview related to the integration of energy storage devices, which can be applied to operate the fuel cell efficiently, is also presented. Finally an example of a power system application combining a fuel cell and super capacitors is presented.



---

## *CHAPTER 5*

### **DESIGN OF THE SERIES RESONANT CONVERTER**

---





## 5. DESIGN OF THE SERIES RESONANT CONVERTER

### 5.1. Introduction

The design and performance analysis for components of a resonant converter are normally complex[63]. In this chapter the design of the components  $L_r$  and  $C_r$ , HF transformer and low pass filters are presented. The analysis is performed for two PEMs (Nexa and Mark1020). The Nexa PEM was used in the first studies. The simulation results that are presented in Appendix C to validate the operation of resonant converter, use data from Nexa. However, due to the discontinuity of manufacture. Nexa's been replaced by Mark1020. All experimental work was accomplished with data from PEM Mark1020. Accordingly, this chapter presents the project for both cases.

### 5.2. Constraints imposed by the fuel cell

The limitation in voltage, current and power of the Nexa<sup>TM</sup> and the Mark1020 system are presented in Table 5.1 and Table 5.2 respectively. These values correspond to the experimental tests performed of both PEMs, which are detailed presented in Appendix A. In the design of the series resonant converter only the extreme conditions of minimum power  $P_{min}$  and maximum power  $P_{max}$  are considered.

Table 5.1 - Constraints imposed by the Nexa<sup>TM</sup> fuel cell

<b>Ifc (A)</b>	<b>Vfc (V)</b>	<b>Power (W)</b>	<b>Freq. Response</b>
0.8	44	343	f<1Hz
30	35.15	1227	

Table 5.2 - Constraints imposed by the Mark1020 fuel cell

<b>Ifc (A)</b>	<b>Vfc (V)</b>	<b>Power (W)</b>	<b>Freq. Response</b>
2.8	23.71	66	f<1Hz
24	19.11	492	

### 5.3. Requirements of ripples of current and voltage

In [97; 98] it is referred that the ripple current not only affects the PEM fuel cell capacity, but also the consumption and its lifetime. The mechanical stresses resulting from continuous high current ripples reduce the system lifetime and the PEM consumes 10% more fuel. Then, considering the variation of load on the fuel cell system output and the dependency of the current to the fuel cell output voltage, the design and selection of an appropriate filter and a converter controller should be done carefully.

### 5.4. Converter design

The electrical circuit of a series resonant power converter is presented Figure 5.1, which shows the major components that need to be designed.

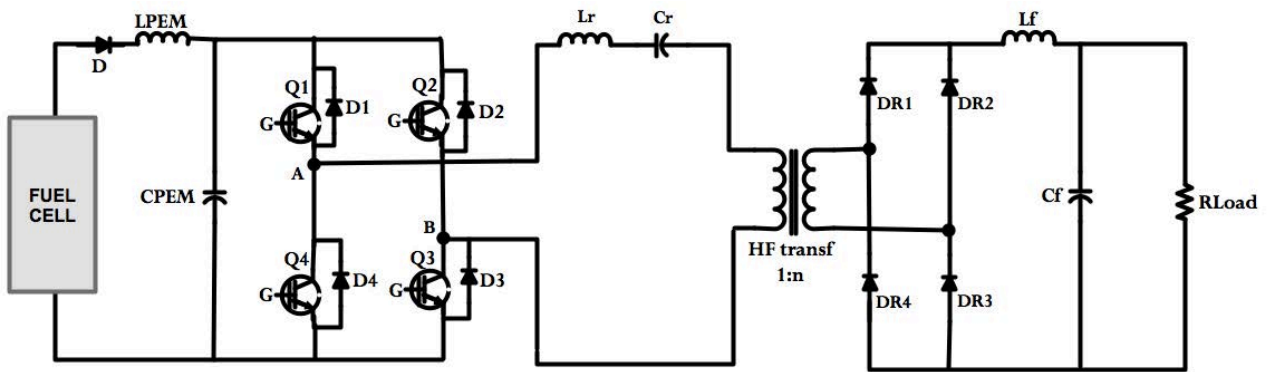


Figure 5.1 – Electrical circuit of the SRC.

The voltage source provided by the fuel cell system is typically low and not regulated and must be converted into a high and regulated voltage. Therefore the transformer is used as a step-up voltage with galvanic isolation between the low and the high voltages. The requirements of the converter are summarized in Table 5.3.

According to the constraints imposed by the PEM on one hand and the specifications of the load on the other, the design of the elements presented in the electrical circuit of Figure 5.1 such as, the inductors ( $L_{PEM}$ ,  $L_r$  and  $L_f$ ), capacitors ( $C_{PEM}$ ,  $C_r$  and  $C_f$ ), and the HF transformer are the main objective of this chapter.

Table 5.3 - Requirements of the converter

Description	Parameter	Unit	Nexa™	Mark1020
Range of Power to transfer	$P_{out}$	W	100 – 1200	66.39 – 492
Output voltage	$V_{out}$	V	400	200
Output current	$I_{out}$	V	0.33 – 3	0.26 – 2.2
Voltage output ripple	$\Delta V_{out}$	V	$\leq 2\%$	$\leq 2\%$
Ripple current to PEM	$\Delta I_{PEM}$	A	No Ripple	No Ripple

#### 5.4.1. HF transformer design

The HF transformer is used to provide isolation and to raise the output voltage.

The leakage inductance of the transformer appears in series with the resonant tank and must be considered in the design. Thus the effective impedance of the resonant tank depends on the tank elements ( $L_r$  and  $C_r$ ), the leakage inductance of the transformer ( $L_t$ ), switching frequency,  $f_s$  and the load ( $R$ ). If the converter operates with a switching frequency closed to the resonant frequency  $f_r$ , it enables the maximum transfer of power to the load. The design of the transformer depends also on the value of the input voltage, which determines the turn's number of 1<sup>st</sup> and 2<sup>nd</sup> windings. Consequently, the transformer parameters (leakage inductance, winding resistance, and parasitic capacitor) should be as low as possible. The mutual inductance should be, and it usually is high. In terms of frequency response, the poles of the transformer must be sufficiently far from the converter operation zone. During the present work, in order to improve the process four transformers were implemented and tested experimentally. The analysis and main conclusions of this study is presented in Section 7.7. the transformer which is selected to the application is the , a ratio of 1:10 and is very small (see Table 7.15).

#### 5.4.2. Selection of the resonant components $L_r$ and $C_r$

The selection of the transformer and resonant components ( $L_r$  and  $C_r$ ) can be considered the most delicate parts of the project. These components define the quality and the performance of the converter, highlighting its advantage over other types of DC-DC converters. Thus, in order to take up the maximum benefit of the resonance, the choice of  $L_r$  and  $C_r$  should be made very carefully. The main constraints are imposed by resonance frequency and amplitude of the current, as the

maximum power is dependent on. For the input voltage range, it is adopted as  $L_r$  the leakage primary inductance in order to establish the capacitor able of satisfying the compromise high resonant frequency/high primary current as the transformer operates as current transformer in the converter topology.

The analysis, comparison and conclusions related to the selection of the  $L_r$  and  $C_r$  components, is made in the Appendix C. For the case the component selected are:  $L_r=2.1 \mu\text{H}$  and  $C_r=4 \mu\text{F}$ .

### 5.4.3. PEM filter Design

The design of the PEM filter must be considered for the worst situation, that is the one for which the amplitude of the current is maximum in the resonant circuit, that is for  $I_{max}$ . The second consideration is related to the operating frequency of the converter, in which the worst situation is for its minimum; the filter cutoff frequency must be at least a decade below this one in order to smooth enough fuel cell current. The maximum current and frequency characteristics of the resonant circuit appear in the DC side as follows:

$$i_{DC} = \frac{1}{\pi} \left[ \int_0^{\pi} I_{max} \sin(\omega t) d\omega t \right] = \frac{2}{\pi} \times I_{max} \quad \text{Eq. 5.1}$$

Considering a ripple of voltage of 2% of their nominal value ( $\Delta V_C$ ) and the minimum frequency of the converter the inductor value and the capacitor value of filter can be calculated through Eq. 5.2 and Eq. 5.3 below;

$$i_C = C \frac{\Delta V_C}{\Delta t} \Leftrightarrow \Delta V_C = \frac{1}{C} \times \frac{2}{\pi} \times I_{max} \times \frac{1}{2 \times f_{conv}} \quad \text{Eq. 5.2}$$

$$2\pi f_{filter} L = \frac{1}{2\pi f_{filter} C} \quad \text{Eq. 5.3}$$

The components of the filter can be calculated through Eq. 5.4 and Eq. 5.5 below.

$$C = \frac{2}{\pi} \times I_{max} \times \frac{1}{2 \times f_{conv}} \times \frac{1}{\Delta V_C} \quad \text{Eq. 5.4}$$

$$L = \frac{1}{(2\pi f_{filter})^2 \times C} \quad \text{Eq. 5.5}$$

Then considering the particular characteristic of the PEMs used, the components are calculated accordingly to the equations presented above and are presented in the Table 5.4 below.

Table 5.4 - PEM filter components.

PEM filter for the Nexa <sup>TM</sup>	PEM filter for the Mark1020
$C_{PEM} = 57.4mF$ $L_{PEM} = 12.2\mu H$ $fc = 190Hz$	$C_{PEM} = 940\mu F$ $L_{PEM} = 933\mu H$ $fc = 170Hz$

#### 5.4.4. Output filter Design

The component values of the output filter (LC filter) must be much larger than these of the resonant circuit in order to be considered constant values in voltage and current, during a switching cycle. This filter must be characterised by a constant output voltage with minimum ripple -  $\Delta V_{out}$ . And in terms of frequency analysis, this low-pass filter reduces the ripple voltage and current associated with the switching frequency as lower the cut-off frequency is. Ideally this filter rejects all the fluctuations, due to the switching frequency and only the average DC component is presented to the load. Accordingly, the cut-off frequency must be at least a decade below the operating frequency of the converter. The elements that characterize the output filter are as follows:

Table 5.5 - PEM filter components.

Output filter for the Nexa <sup>TM</sup>	Output filter for the Mark1020
$C_f = 10mF$ $L_f = 0.1\mu H$ $fc = 503Hz$	$C_f = 110\mu F$ $L_f = 536\mu H$ $fc = 557Hz$

## 5.5. Conclusions

The constraints imposed by the PEM fuel cell on one hand and the requirements of the resonant converter by another led to the design of the components of the SRC such as, the inductors ( $L_{\text{PEM}}$ ,  $L_r$  and  $L_f$ ), the capacitors ( $C_{\text{PEM}}$ ,  $C_r$  and  $C_f$ ), and the HF transformer. The design was made considering a) the Nexa<sup>TM</sup> and b) the Mark10220 PEMs, since both were used throughout the research work done in the thesis.

---

# *CHAPTER 6*

## **MODELLING AND SIMULATION RESULTS**

---





## **6. MODELLING AND SIMULATION RESULTS**

This chapter is divided into two parts. In the first part the details of implementation of the SRC in MatLab/Simulink software are presented while in the second part the simulation results are obtained and analysed. Particularly:

- 1) Regarding to the dynamics of the system: to demonstrate that the system is fast in its dynamics and simultaneously guarantees the output voltage constant, even for load variations.
- 2) Regarding to the operation of the PEM: to demonstrate that the PEM controller imposes an operating point, which guarantees a minimum consumption of hydrogen and a maximum power transfer.

### **6.1. Model of the converter in MatLab/Simulink**

The model of the converter is performed in two parts, namely: the power circuit and the control circuit according to the circuit presented in Figure 6.1. The operation of the converter is already described in section 4.4.

#### **6.1.1. Power circuit modelling**

The elements of power converter are modelled in MatLab/Simulink according to the topology of converter selected and the tools provided by the software environment. The power elements are parameterized for its specific target, such as, DC sources, resistances, inductances, capacitors and power semiconductors such as diodes, Mosfets and IGBTs.

#### **6.1.2. Control circuit modelling**

The implementation of the control circuit in MatLab/Simulink is divided into two main subsystems: a subsystem to control the output voltage, which is composed by the modules of 1) Voltage control, 2) Frequency divider and 3) gate drive signals and a subsystem to control the operation point of the PEM composed by the PEM controller module. The detailed explanation of these modules is presented below.

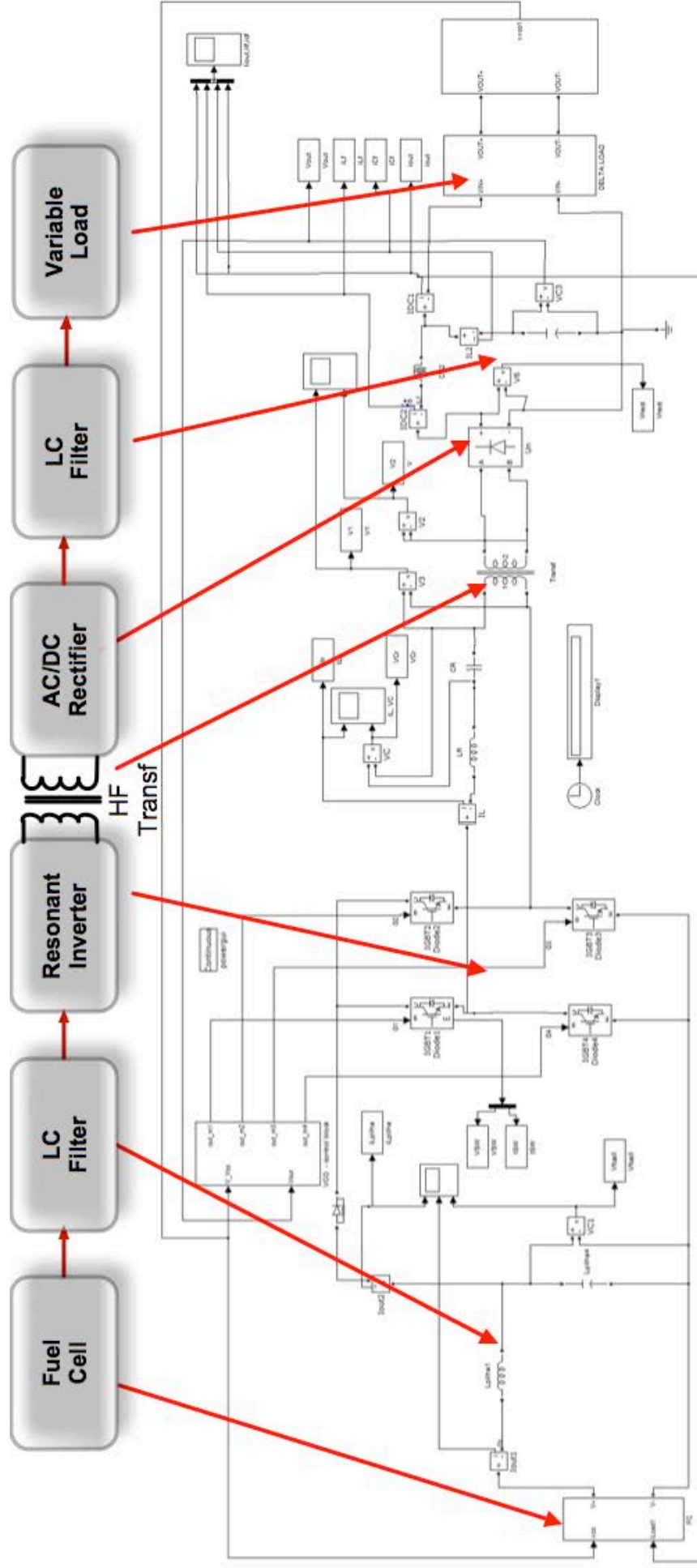


Figure 6.1 –Implementation of the power converter circuit in MatLab/Simulink.

### 6.1.3. Voltage control in MatLab/Simulink

The voltage control subsystem is implemented in MatLab/Simulink as represented in Figure 6.2.

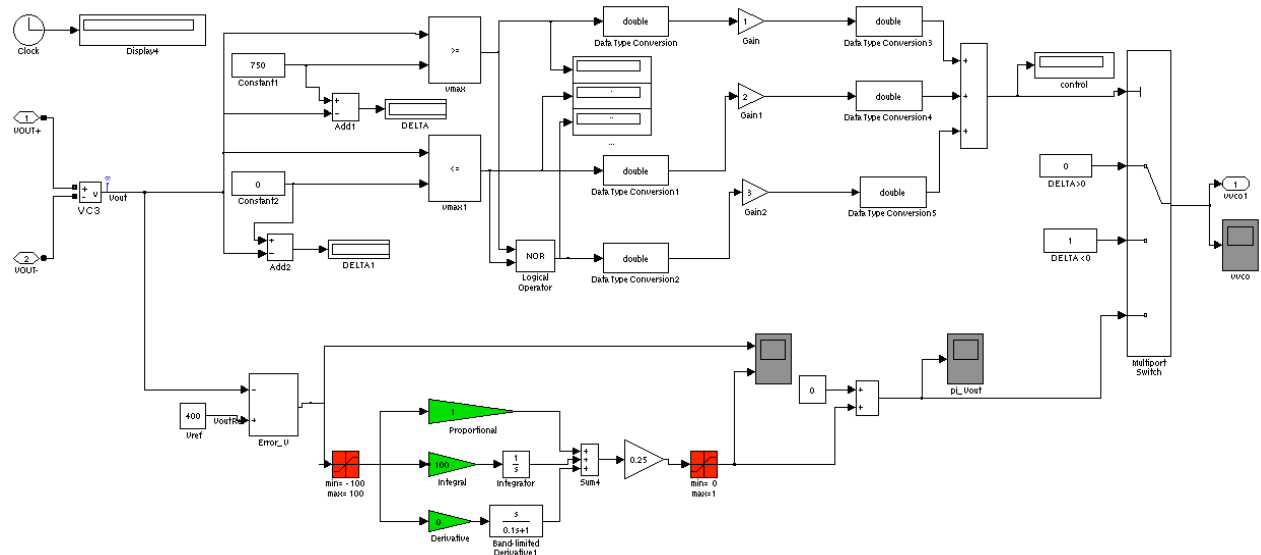


Figure 6.2 – Voltage control subsystem of the converter.

Explanation of this subsystem:

The voltage control subsystem allows at limiting the maximum and minimum values for the output voltage i.e., the control output signal,  $V_{\text{control}}$ , is always equal to zero (0), if  $V_{\text{out}} \geq 750\text{V}$  (Selector #1), on the other side is always equal to one (1), if  $V_{\text{out}} = 0\text{V}$  (Selector #2). Otherwise, the control module works according to the main goal for which it is designed, that is, through a PI controller and regardless the type and amount of load applied to the power system, it keeps the converter output voltage at 400V (Selector #3). This works as follows: the value of the output voltage ( $V_{\text{out}}$ ) of the converter is measured and compared with the reference value; an error signal is produced and processed by the P - proportional I -integral controller producing the signal of voltage control ( $V_{\text{control}}$ ). The proportional term responds immediately to the error voltage yet typically cannot achieve the required set-point accuracy without an unacceptable large gain. On the other hand, the integral term yields an error zero in steady state for a constant set point and enables the rejection of disturbances.

### 6.1.4. Frequency divider and gate drive signals in MatLab/Simulink

The frequency control subsystem implemented in MatLab/Simulink is represented in Figure 6.3.

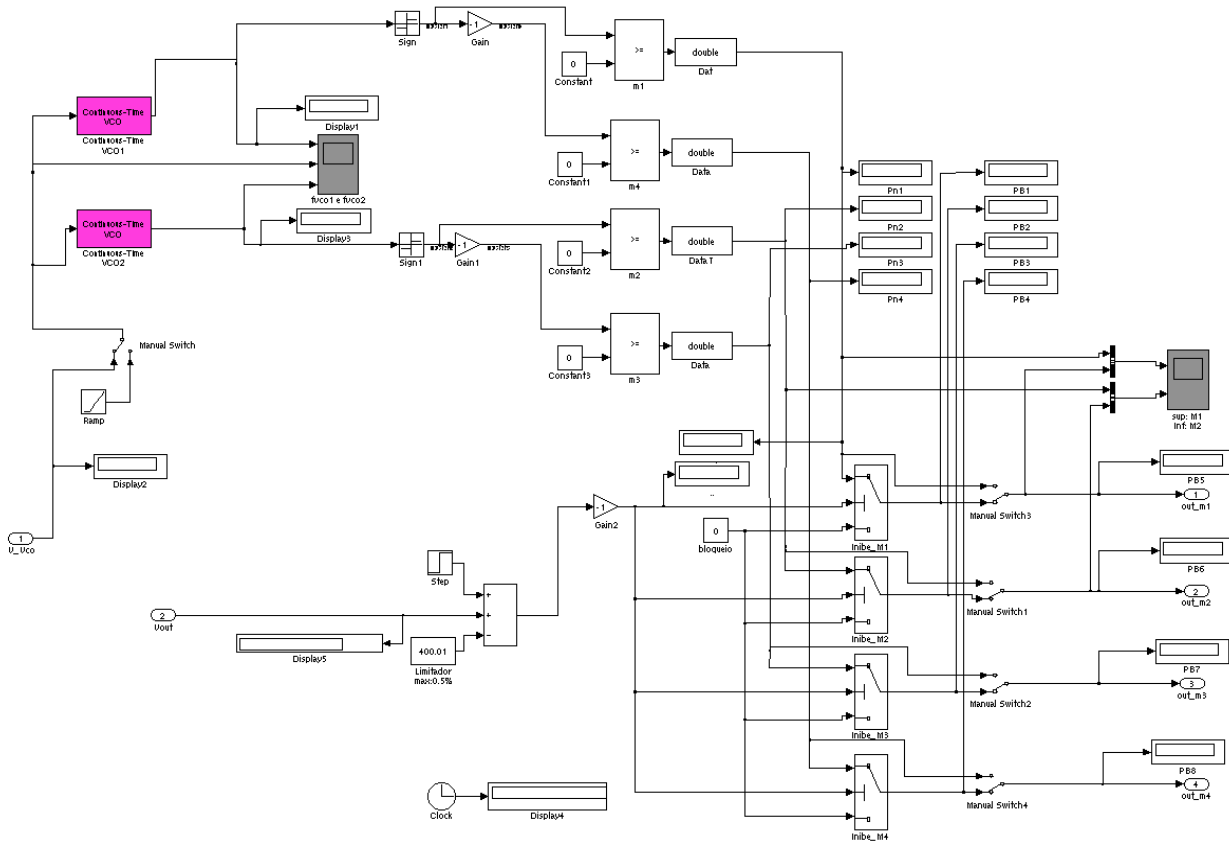


Figure 6.3 – Frequency control subsystem of the converter.

Explanation of this subsystem:

This subsystem allows generating the four gate signals to the resonant inverter bridge, which changes accordingly to the signal reference. Once it is known the reference signal, interpreted as a voltage (VCOref), established by the PI controller, the module continues-time VCO generates a sinusoidal signal whose frequency shifts from the quiescent frequency parameter ( $f_c$ ) with a sensitivity to the input parameter ( $k_c$ ) and amplitude  $A_c$ . The inverter topology is a full-bridge; then four output signals need to be generated by this subsystem, one for each transistor respectively ( $M_i$ ,  $i = 1, 2, 3, 4$ ). They are synchronized by  $\varphi$ , which is the initial phase parameter and assumes zero or  $\pi$  value in the case. Parameterization of the voltage control oscillator blocks is shown in Figure 6.4 according to the equation Eq. 6.1 below.

$$y(t) = A_c \cos\left(2\pi f_c + 2\pi k_c \int_0^t u(\tau) d\tau + \varphi\right) \quad \text{Eq. 6.1}$$

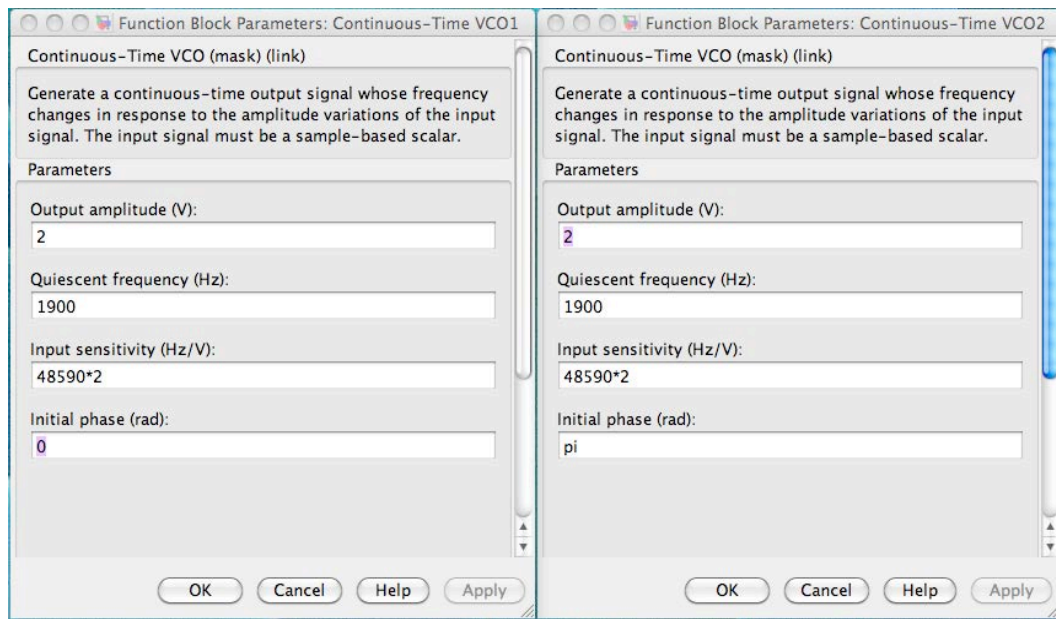


Figure 6.4 – Parameterization of the two continuous-time VCO blocks.

### 6.1.5. PEM control in MatLab/Simulink

As already mentioned, the voltage-controller is responsible to control the output voltage of the converter, while the PEM-controller is responsible to control the operation of the PEM, keeping it in its optimal operation point. Thus the control of the PEM works as follows: once characterized an operation point of the PEM and defined a constant output voltage, assuming for example that is point P of Figure 6.5 the PEM-controller has the task of improving the performance of the system, defining a new point P' or P'' that maximizes the energy produced by the PEM with a minimum consumption of hydrogen. The control algorithm that satisfies the action and conditions to be performed are represented in the flowchart of Figure 6.6. A descriptive explanation is also given in Table 6.1.

#### ➤ Flowchart explanation

The outer loop control of the PEM is as an "observer of the system," i.e., once characterized a point P of output characteristic of the PEM, this induces small perturbations in the system thus leading the cell to operate under conditions of maximum efficiency of the PEM, in other words, providing maximum power with minimal consumption of hydrogen.

However, a minimum consumption of hydrogen means the operation of the PEM with minimum current, i.e.: IFC minimum and VFC maximum, just in the sense of P' of the output characteristic of the PEM, as exemplified in the graph above.

A lowering of the current cell implies a lowering of the operating frequency of the resonant converter, so the search condition from the point of optimum operation of PEM requires the lowering of the operating frequency of the converter. Once it finds the optimum for the present conditions of load, the resonant converter is operating at a frequency that is also the minimum frequency that ensures the load conditions imposed by the system. The process is repeated whenever there is a variation of the conditions imposed by the load. The actions to be performed by the PEM controller considering a particular condition of operation of the converter are summarized in the table below.

Table 6.1 – Summary of the PEM control actions performed.

Condition	Actuation And Consequence				
$VCO \geq VCO\_OPT$	$\Rightarrow \Delta IFC < 0$	$\Rightarrow IFC = IFC + \Delta IFC$	$\Rightarrow IFC \uparrow$	$\Rightarrow VFC \downarrow$	Moves to the right in the polarization curve $V-I \rightarrow P''$
$VCO = VCO\_OPT$	$\Rightarrow \Delta IFC = 0$	$\Rightarrow IFC = IFC$	$\Rightarrow IFC =$	$\Rightarrow VFC =$	Optimum point $\rightarrow P$ Do not move.
$VCO \leq VCO\_OPT$	$\Rightarrow \Delta IFC > 0$	$\Rightarrow IFC = IFC - \Delta IFC$	$\Rightarrow IFC \downarrow$	$\Rightarrow VFC \uparrow$	Moves to the left in the polarization curve $V-I \rightarrow P'$

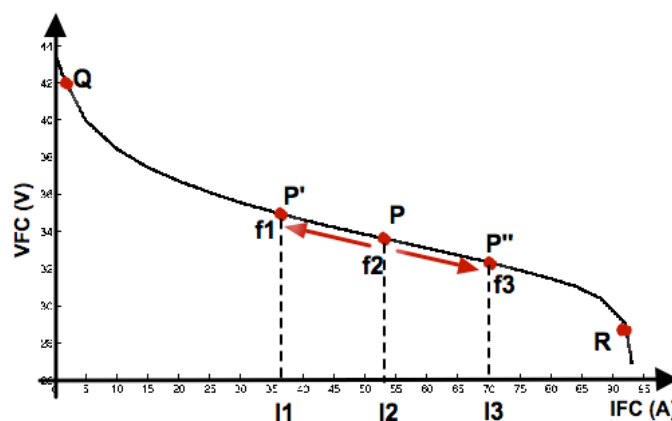


Figure 6.5 - Characterization of the optimal operating point of the PEM.

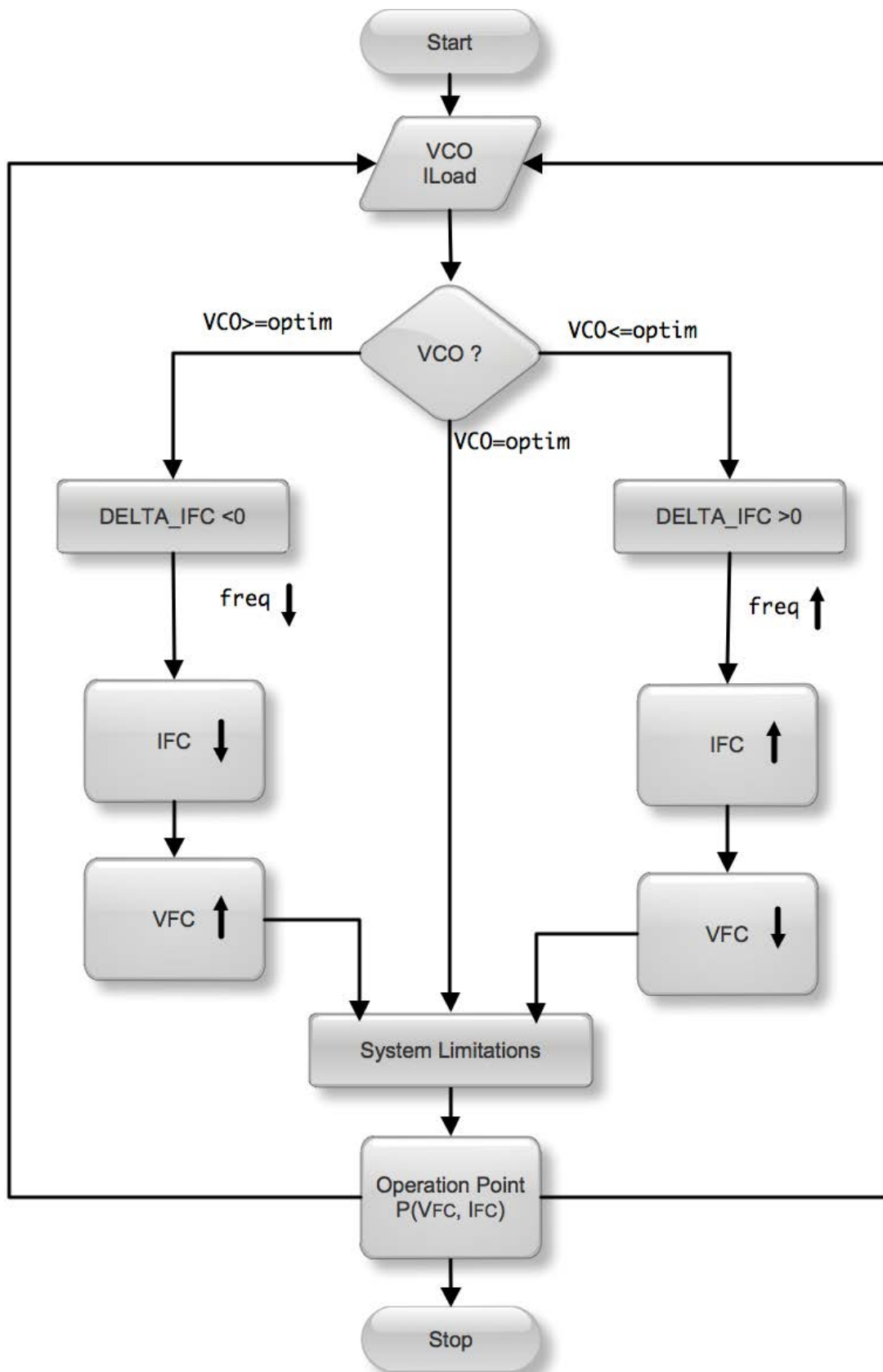


Figure 6.6 - Flowchart of PEM controller.

➤ **PEM controller subsystem**

The subsystem of the PEM controller is implemented in MatLab/Simulink as shown in Figure 6.7.

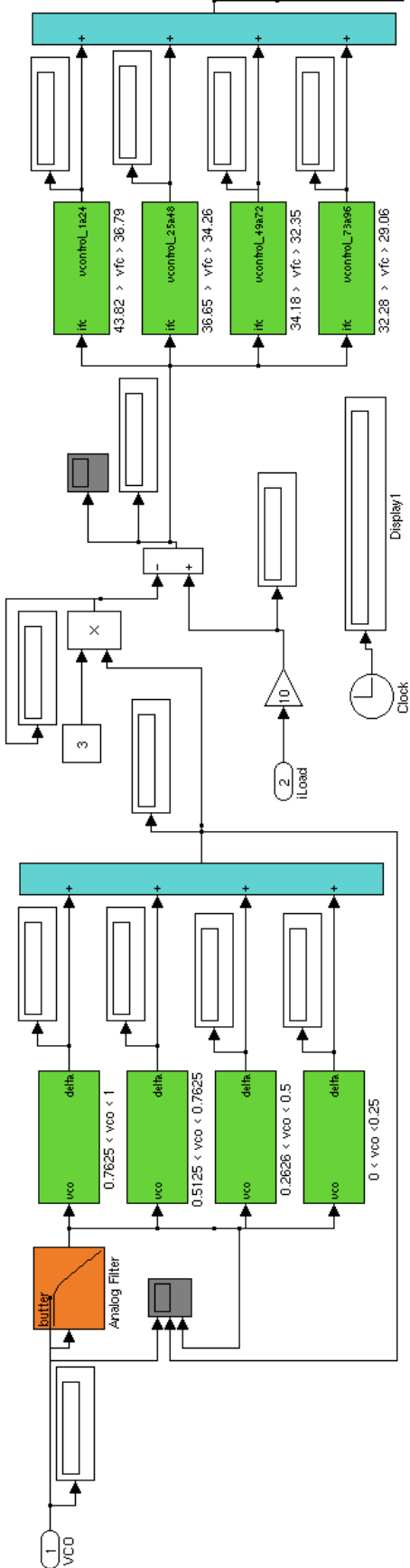


Figure 6.7 – PEM controller implemented in MatLab/Simulink.



Explanation of the PEM controller subsystem:

As shown previously the implementation in MatLab/Simulink of the slow loop control of the PEM corresponding to the scheme of Figure 4.28 as various sub-systems, such as the first step as a sub-system that generates a DELTA value. Once known, the value of DELTA, a new sub-system, generates a voltage reference value (Vcontrol), according to the variation in the value of fuel cell current  $\Delta I_{FC}$ . The term of IFC takes into account load conditions; the fact is that the power transferred from the PEM to the load has no losses and the output voltage must be kept always constant and equal to 400 V<sub>DC</sub>. The DELTA value is reduced by a factor of 0.25. Finally, there is a sub-system to control the output voltage VFC acting under the control algorithm previously explained.

$$P_{FC} = P_{out} + P_{loss} \text{ with } P_{loss} = 0 \quad \text{Eq. 6.2}$$

$$V_{FC} \times I_{FC} = I_{out} \times V_{ref} \quad \text{Eq. 6.3}$$

$$I_{FC} = \frac{I_{out} \times V_{ref}}{V_{FC}} \quad \text{Eq. 6.4}$$

### ➤ DELTA Subsystem in PEM controller

The subsystem DELTA and the correspondent parameterization of function Relay are implemented in MatLab/Simulink as shown in Figure 6.8 and Figure 6.9.

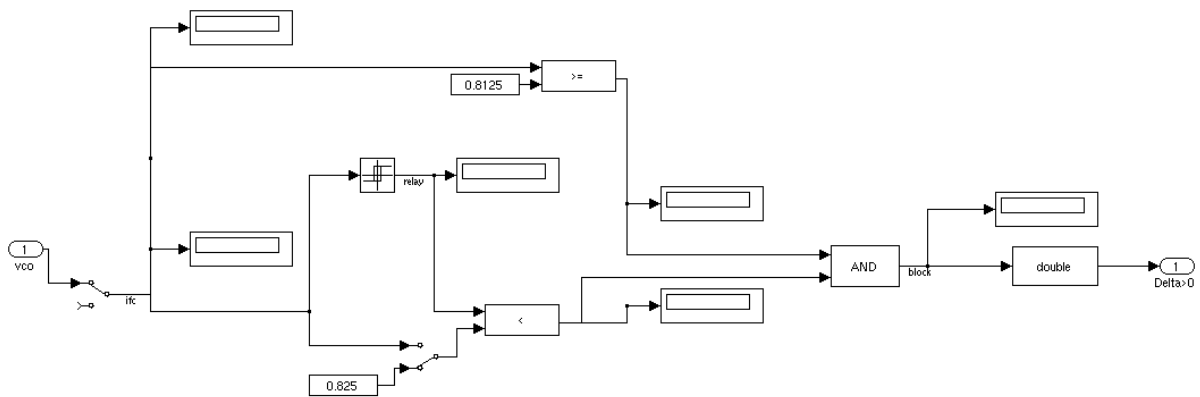


Figure 6.8 – DELTA Subsystem.

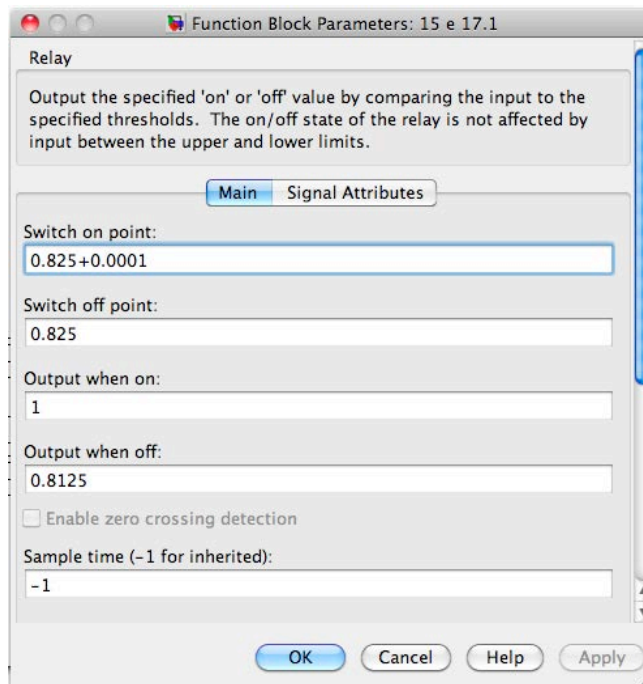


Figure 6.9 – Parameterization of relay function in DELTA.

Explanation of this subsystem:

For each module that produces a specific DELTA, it is used the following methodology:

- a) Vcontrol is compared with the lower value of the Relay;
- b) Vcontrol is compared with the upper limit value of the Relay (the top line that enters in the comparator limit value).

The higher value of the module is determined by the function 'relay'. This function determines in its output value is higher:

- i) The lower value Vcontrol to reach the ceiling value of the relay;
- ii) The higher value since the relay changes state (with Vcontrol greater than the upper value of the relay);
- iii) The output relay again put on the lower value of output relay when Vcontrol back down and reaches the lower limit value. From this moment, the relay output (value upper/lower) is defined by this cycle - then turns to step i) and the cycle repeats.

This methodology is applied for the overall DELTA steps, as an example, if the natural limit is 0.825, the Relay has the limits  $> 0.825$  and  $\leq 1$ . When Vcontrol goes up to 0.825, the output of Relay is 0.825, and in this case there is a condition of equality. Above 0.825, Vcontrol is higher and the Relay function and it goes to the 2nd block.

In the next intervals of time, the current continues to rise and when it reaches the 1 value or other value may be higher it happens a singular situation, i.e. in either case in which Vcontrol is 'exactly' equal to 1 is on the 1st block, leaving in the next block, because the voltage in the 1st block is the highest one.

### ➤ Vcontrol subsystem of the PEM controller

The subsystem Vcontrol and the correspondent parameterization of function Relay are implemented in MatLab/Simulink as shown in Figure 6.10 and Figure 6.11.

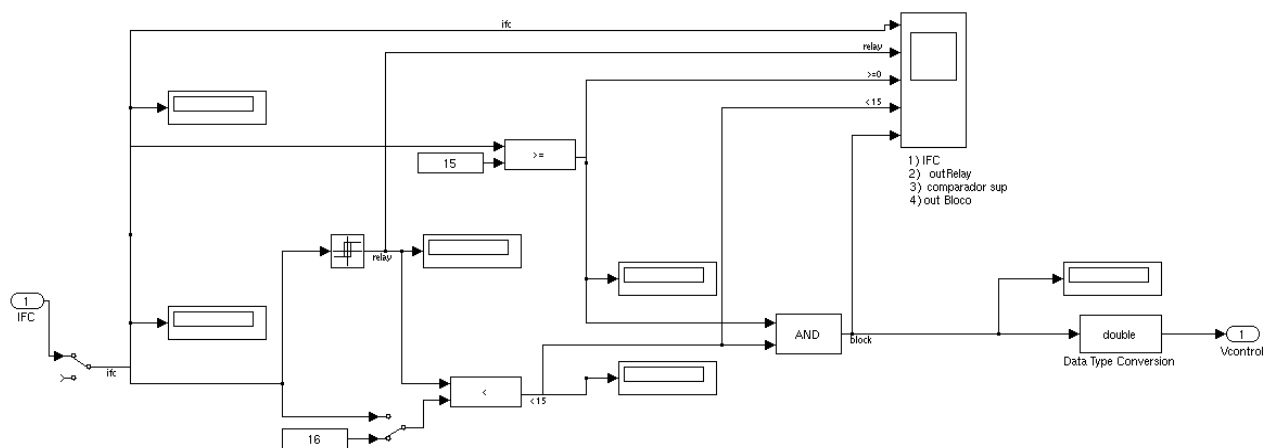


Figure 6.10 – Subsystem Vcontrol.

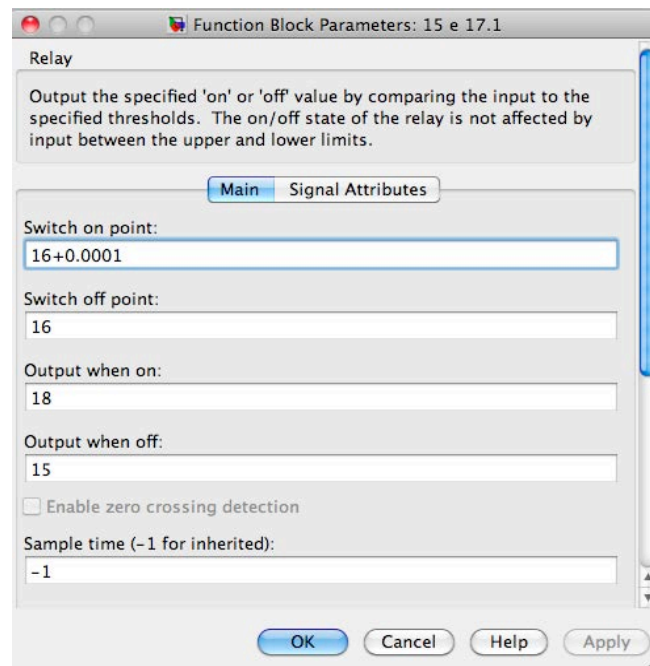


Figure 6.11 – Parameterization of Relay function in Vcontrol.

Explanation of this subsystem:

For each module that produces a specific Vcontrol, it is used the following methodology:

- a) IFC is compared with the lower value of the Relay;
- b) IFC is compared with the upper limit value of the Relay (the top line that enters in the comparator limit value).

The output value of the module is determined by the function 'relay', according to the following procedures:

- i) The lower value IFC to reach the ceiling value of the relay;
- ii) The higher value since the relay changes state (with IFC higher than the upper value of the relay);
- iii) The output relay again put on the lower value of output relay when IFC back down and reaches the lower limit value. From this moment, the relay output (value upper/lower) is defined by this cycle - then turns to step i) and the cycle repeats.

This methodology is applied for the overall Vcontrol (92 steps), as an example, if the natural limit is 15 A. The Relay has the limits  $>15$  A and  $\leq 16$  A. When IFC goes up to 15 A, the output of Relay is 15, and in this case there is a condition of equality. Above 15 A, IFC is greater and the Relay function and it goes to the 2nd block.

## 6.2. Simulation results

As already mentioned in previous chapters, various setup systems have been used, which are well characterized in Appendix A. Appendix D presents the studies carried out in Matlab/Simulink with the PEM Nexa incorporated into the global system, whose results are used to validate the operation of the resonant converter either in open loop and or in closed loop operation. Thus, the results presented in this chapter validate the global system adopting the PEM Mark1020, which are compared with the experimental ones. The following parameters are used in the process:

Simulation method: ode23t (Stiff/ Trapezoidal),

Relative tolerance:  $1e-3$

Absolut tolerance:  $1e-6$

Max step size:  $1e-7$

Output voltage reference: 48 V

### 6.3. Dynamics of the system

Regarding to the dynamics of the system, the main objectives to achieve are:

- 1) Validation of the stability of the output voltage controller, which should always guarantee a constant voltage even for loading variation in step-up, and step-down.
- 2) Validation of the system dynamics particularly, verifying if it is fast in its dynamics.

Accordingly, the variables such as; output voltage and current, control signal VCO, fuel cell voltage and current, and resonant circuit waveforms are analyzed.

#### 6.3.1. Output voltage and current

The stability of the voltage controller is observed in Figure 6.12. It appears that for a variation of the load the output voltage of the converter remains constant. This condition is valid to both situations, to a step-up of load which occurs at 0.2 seconds at Figure 6.12 a) and to a step-down of load which occurs at 1.0 seconds at Figure 6.12 b).

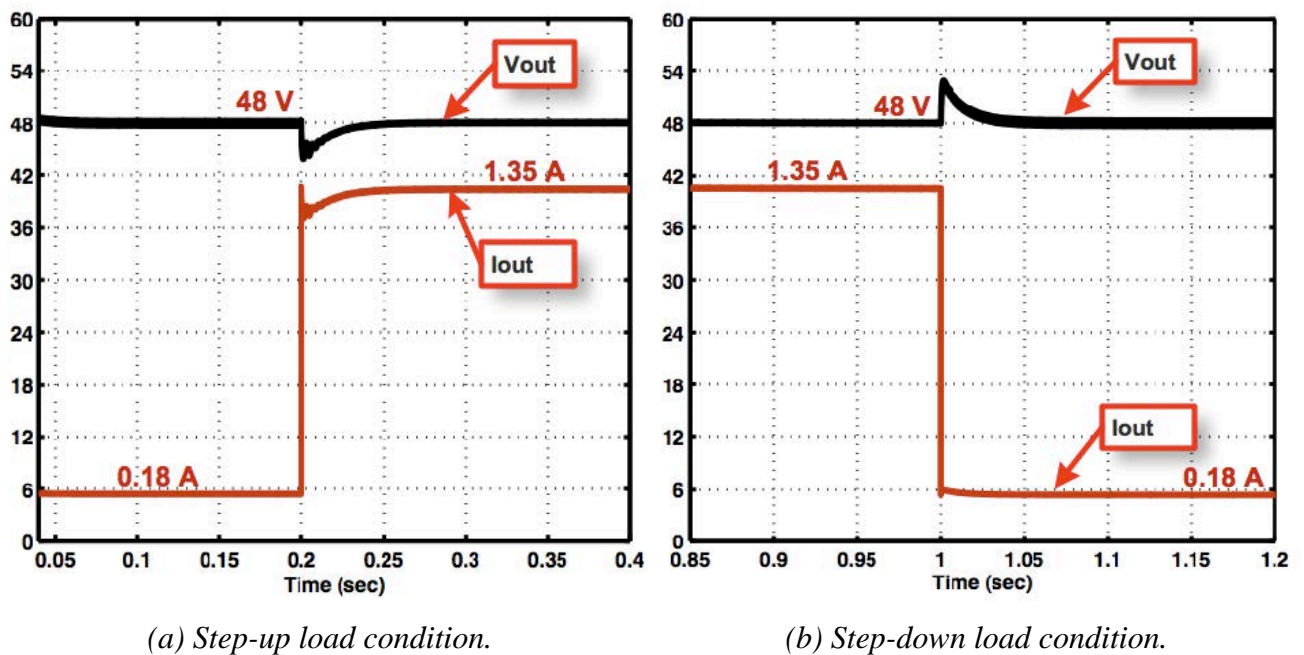


Figure 6.12 – Output voltage ( $V_{out}$ ) and Current ( $I_{out}$ ).

#### 6.3.2. VCO signal

The dynamics of the system is evaluated by the response time of the system to load variations, which for the case is performed by the control signal  $-V_{CO}$  established in the PI controller and sent

as a reference to the frequency oscillator module in the simulation model, as explained above. Whence, observing the two situations of load variation present in Figure 6.13 a) and Figure 6.13 b), respectively it appears that the delay in time response of the VCO signal is approximately 10ms for the step-up while for the step-down the time response of the VCO signal does not present any delay. A small oscillation in the VCO signal appears just in step-up load condition, which proves that the parameters of the PI controller are well adapted to the system.

Knowing that the error is generated in Simulink by the expression,  $\varepsilon = V_{\text{reference}} - V_{\text{measured}}$ , the main goal of the voltage controller is to minimize this error for any load variation, as is shown in the two figures below.

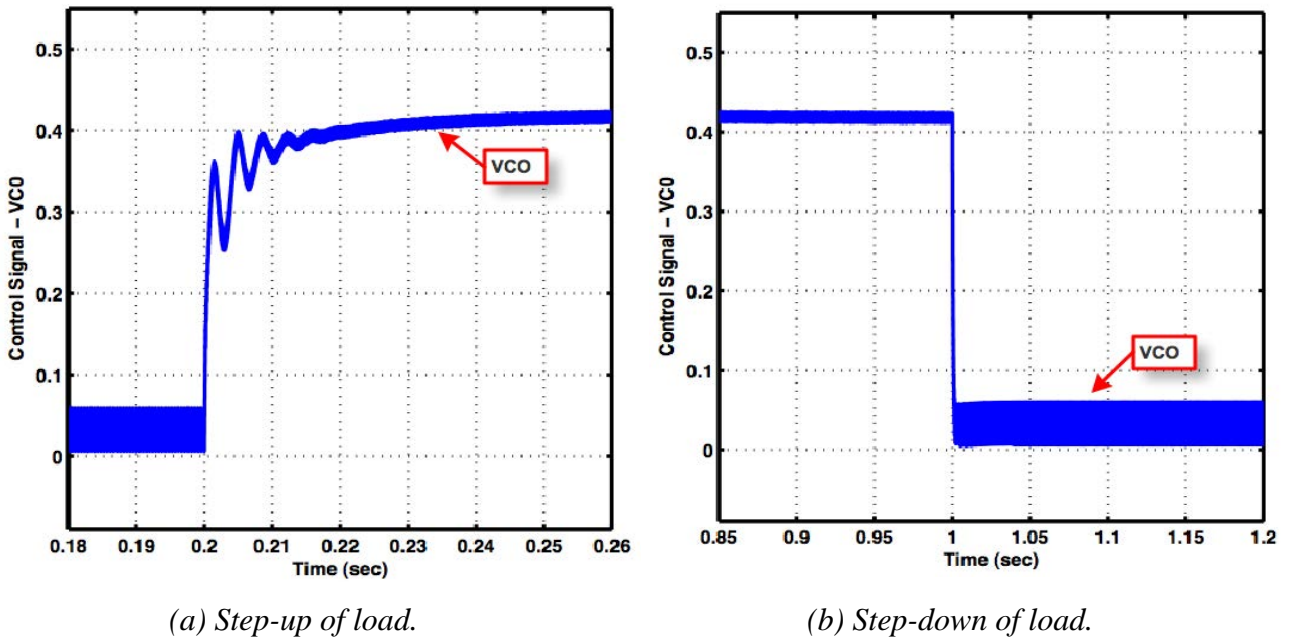


Figure 6.13 – VCO signal.

### 6.3.3. Effect of the VCO signal on variables of the system

The value of the VCO is a consequence of the error between the reference and the measured value of output voltage, which takes effects on other quantities such as, the voltage and current of the resonant circuit and the frequency operation of the converter.

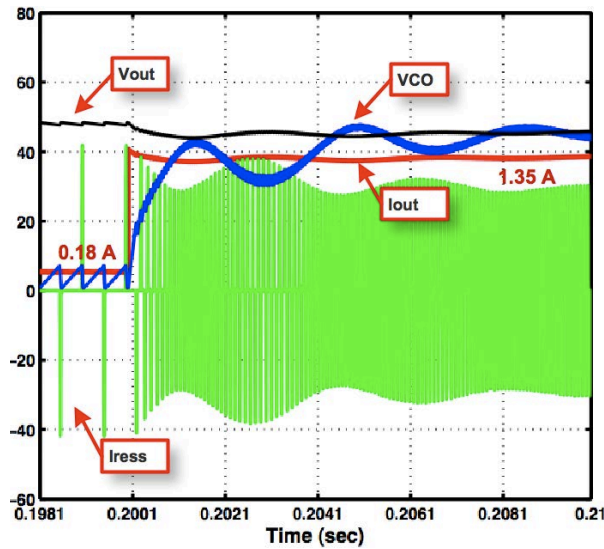
Observing the Figure 6.14 and Figure 6.15 it is verified that the controller reacts to any variation of load (up or down) by acting directly on the value of the frequency operation.

Thus, for a high load (e.g.: 5.22 A in the fuel cell) the frequency is high (e.g.: 12.5 kHz), if the load is low (e.g.: 0.57 A in the fuel cell) the frequency is too low too (e.g.: 1 kHz).

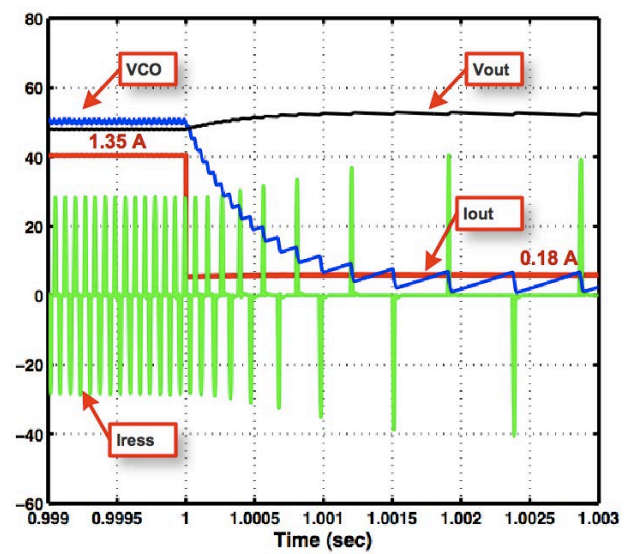
The dynamics control system sets the speed with which it reacts to a change in load, either too high, either too low.

As can be seen in the Figure 6.14 a) and Figure 6.14 b) the reaction of the controller is not the same in both cases, however the system is fast enough, with time response lower than  $<1$  sec.

In summary, it can be said that the value of the VCO is established at each instant the condition of operating of the system and consequently the transfer of power to the load.

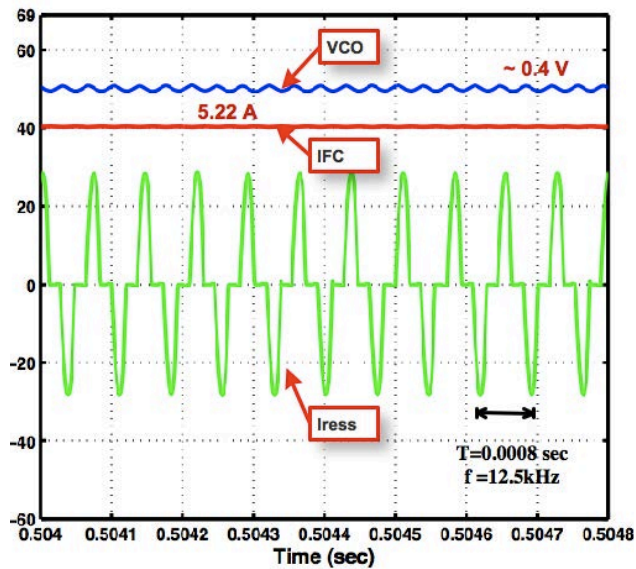


(a) Step-up load condition.

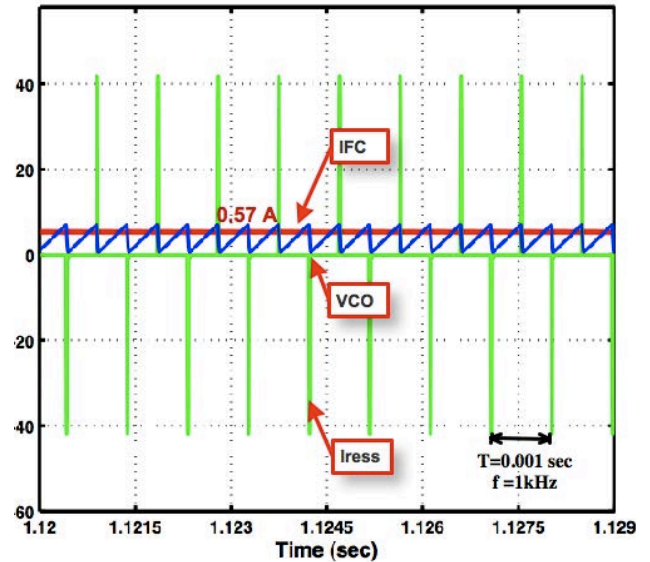


(b) Step-down load condition.

Figure 6.14 - Effects of the VCO on the amplitude of the output voltage.



(a) Zoom in the high load condition.



(b) Zoom in the low load condition.

Figure 6.15 - Effects of the VCO on the frequency and amplitude of the resonant current.



### 6.3.4. Resonant circuit operation

Through the analysis of Figure 6.16 it appears that the operating frequency of the converter varies in accordance with the load requested to the system. The frequency increases in a step-up load condition (Figure 6.16 a)) and decreases in a step-down condition (Figure 6.16 b)). In dynamic terms it can be seen that the transition of the operating frequency is instantaneous, from whence it follows that the system has good dynamic in terms of frequency as expected from a resonant converter.

From Figure 6.16 it appears also that output voltage remains constant in both cases of load variation. This is extremely important since it satisfies one of the requirements imposed to the power system under study.

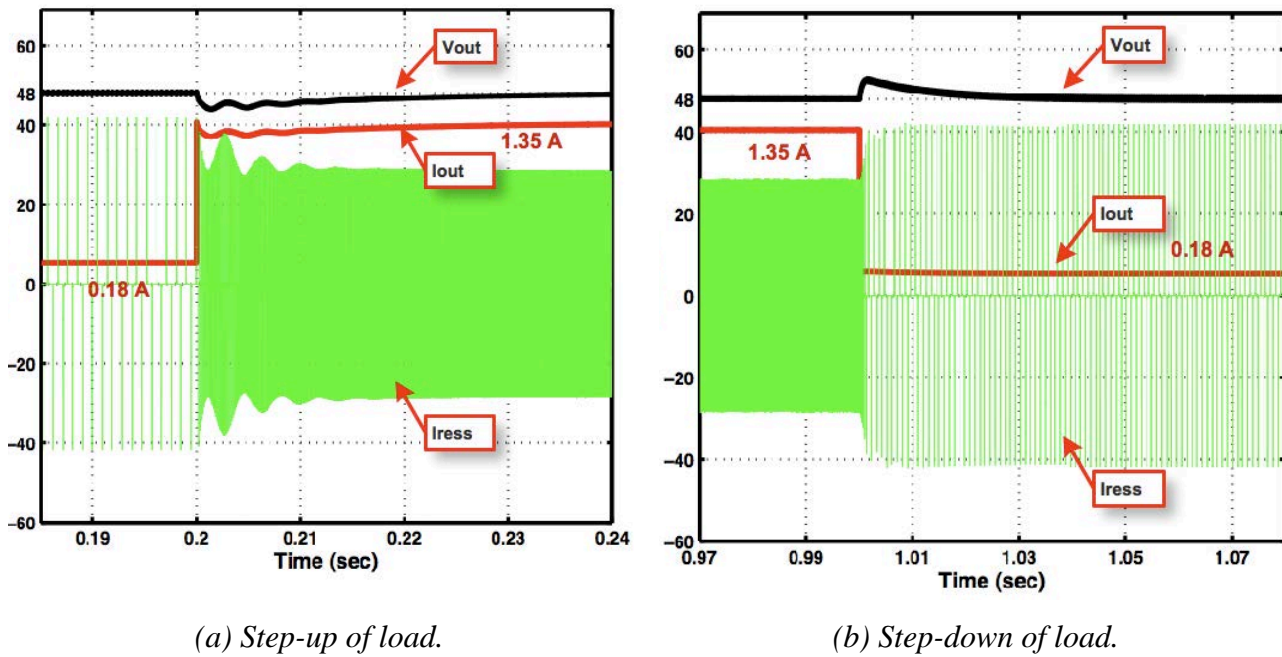


Figure 6.16 – Output voltage and current and resonant circuit operation.

### 6.3.5. Fuel cell voltage and current

In Figure 6.17 it is observed that the fuel cell current varies according to the variation imposed by the load that is this rises for a step-up of current as observed in Figure 6.17 a) and drops to a step-down as observed in Figure 6.17 b). The fuel cell voltage drops when the current rises at the same instants in which the load variation occurs. The effect of the control is present in the both situations however its effect is more accentuated in the step-up condition. A small ripple appears in the fuel



cell voltage function of the frequency operation of the converter. The ripple is smaller for the high load condition because of the increase of the frequency operation.

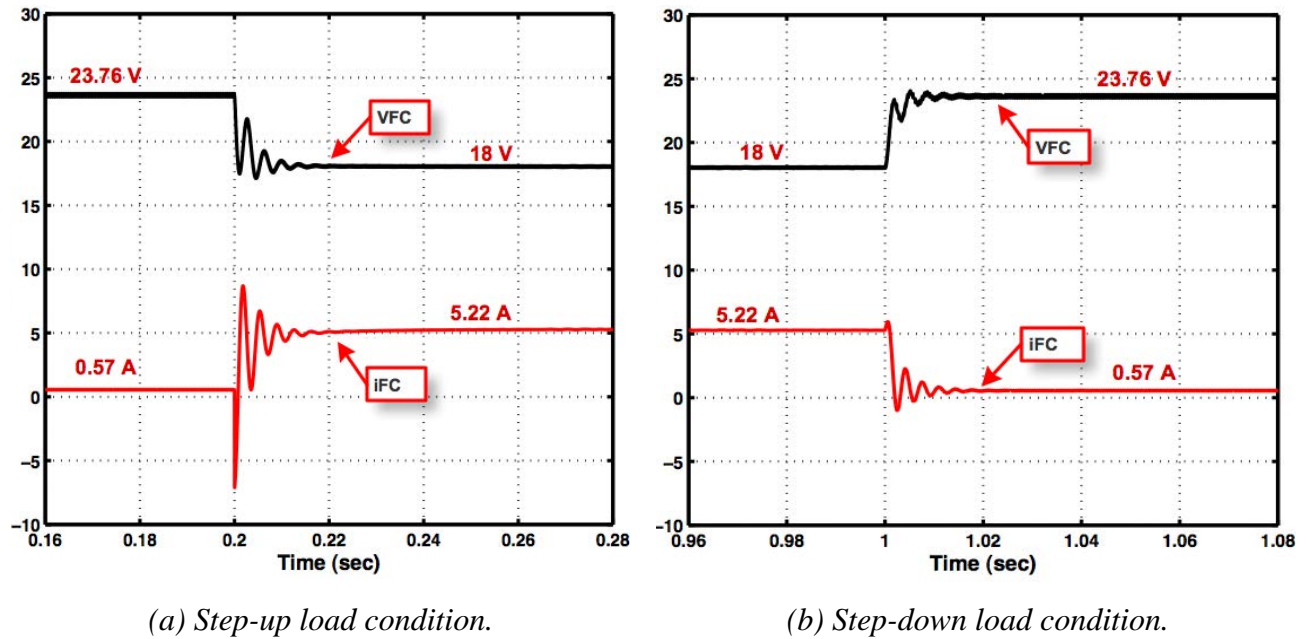


Figure 6.17 - Fuel cell voltage and current.

## 6.4. PEM controller and optimization of the hydrogen consumption

Regarding the optimum operation of the PEM, the main objectives to achieve are:

- 1) Analysis of the operation of the PEM controller.
- 2) Demonstrate that the PEM controller imposes an operating point, which guarantees a minimum consumption of hydrogen and a maximum power transfer. Once demonstrated the stability of the system in the previous section.

### 6.4.1. PEM controller operation

in order to analyse the performance of PEM controller a variation of its operating point has been imposed "forcing" the PEM lowering the voltage and consequently increasing the current. This action is opposite to the principle established by the PEM controller then, this reacts to that situation in order to find a minimum value of current ( $I_{FC}$ ) and a maximum value of voltage ( $V_{FC}$ ) which conditions ensures the requirements of the load. Simultaneously, and accordingly, the output current,  $I_{out}$ , reduces its value, while the PEM stabilizes in an optimal point, however, once the optimum point of the PEM established, the value of  $I_{out}$  returns to its steady state value. This

action, affects the system controller, which, in turn takes a time, (establishing time) necessary for searching a new operating condition.

It is also verified from the figures that, the time of establishment to the optimal operating point is  $\approx 30$  ms, which corresponds to a reduction of 0.13 A in the amplitude of the output current.

As can be also observed in Figure 6.19 in steady-state the converter output voltage and current ( $V_{out}$  and  $I_{out}$ ) do not vary when the PEM controller acts on the system.

Due to the decrease of current in the circuit, and by the fact that it has an effect immediate in the VCO value, the frequency of the converter also varies, as can be seen in Figure 6.20.

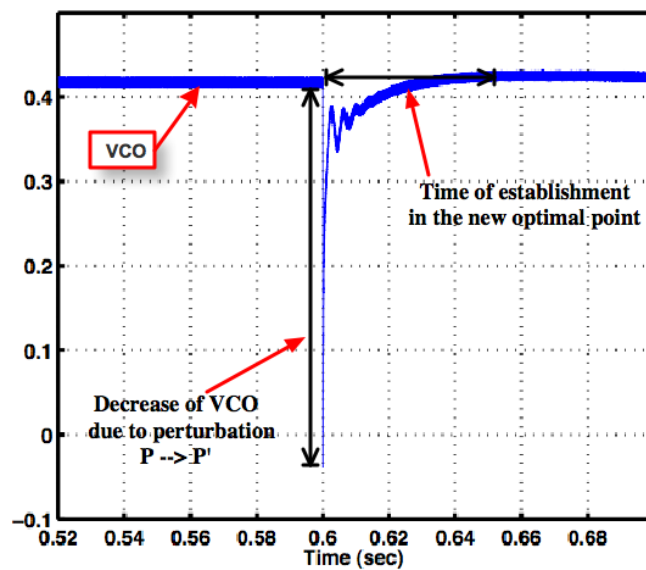


Figure 6.18 – VCO signal.

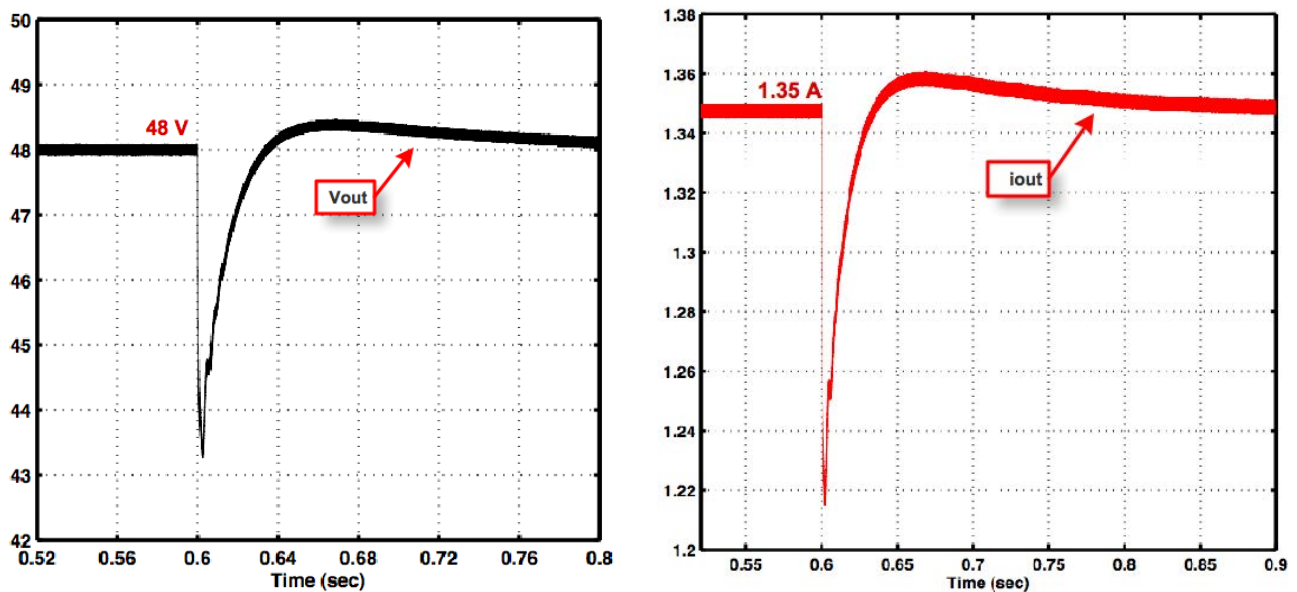


Figure 6.19 - Output voltage and current

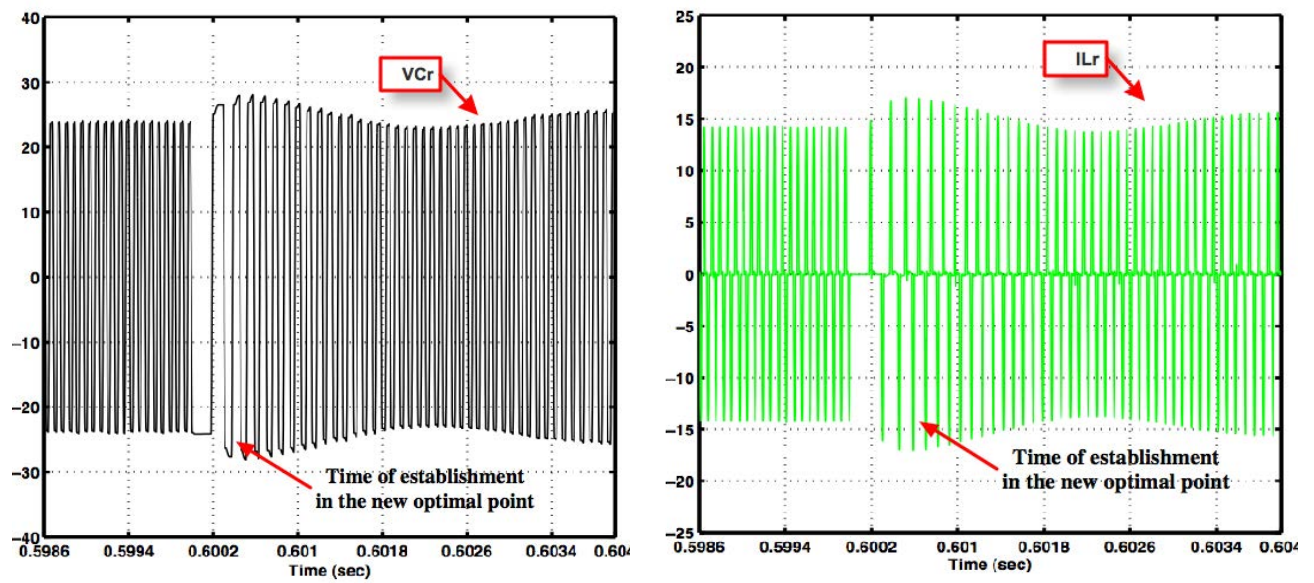


Figure 6.20 – Resonant voltage and current.

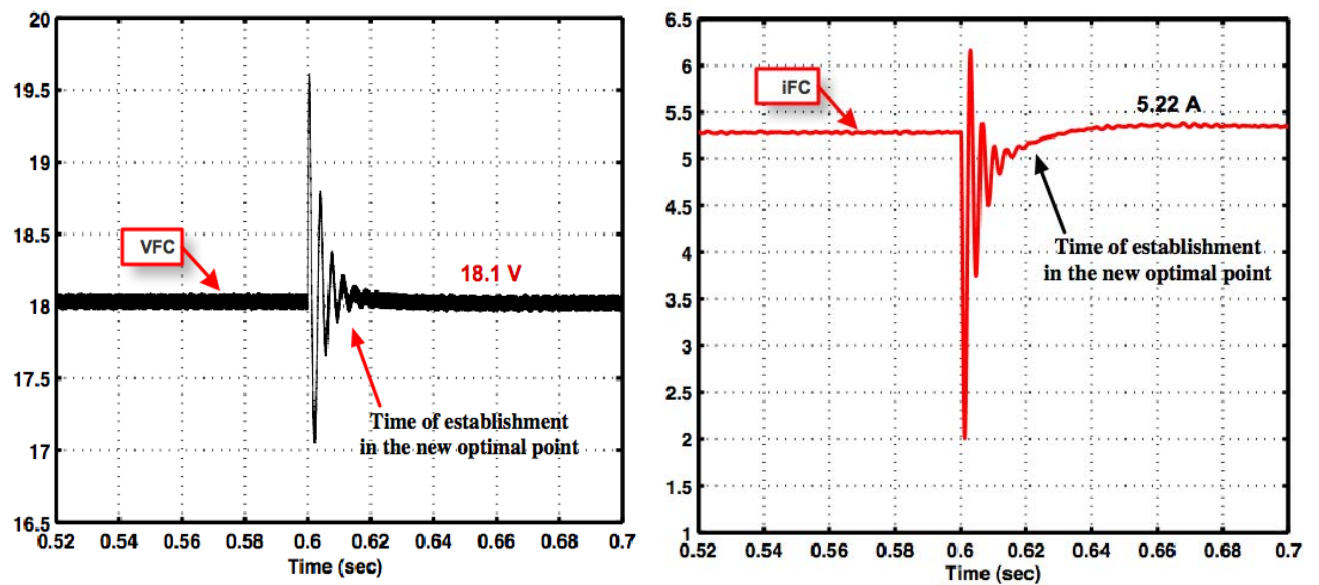


Figure 6.21 - Fuel cell voltage and current.

## 6.5. Conclusions

The SRC is modelled in this chapter, once defined its topology and control strategy. The implementation performed in MatLab/Simulink software is presented in a first part while in the second part the simulation results were discussed. A special attention is given to the control strategy, providing detailed explanation to each control subsystem, namely: the voltage control, the frequency control and PEM control. In a second part it is evaluated the performance of the power generation system implemented in MatLab/Simulink. The analysis of the results is focused in two major points namely:

### 1) The stability of the system

The stability of the system was proved by the output voltage  $V_{out}$ , which remains constant even for the load variations imposed to the system. It was also proved that the resonant converter suits perfectly the changes imposed on the system by changing its operating frequency correspondently.

### 2) The PEM control with optimization of the hydrogen consumption

The characterization of the optimum point of operation as a function of the hydrogen consumption is presented. It was demonstrated that the PEM controller imposes an operating point, which guarantees the minimum consumption of hydrogen and maximum transfer of power. Considering that the operating point is for the minimum fuel cell current and maximum fuel cell voltage, and knowing that the hydrogen consumption is proportional to the current then the minimum consumption of hydrogen is assured in this way. In addition to the good conditions established by the control system, the maximum power transfer was further ensured by suitable selection of the elements of power, namely, the components of the resonant circuit and the high frequency transformer.

Finally, the analysis of the experimental results allows concluding that the system implemented provides excellent stability, robustness and good dynamic response making it a strong candidate for industrial applications in various areas of energy in accordance with the current tendencies in the sector.

---

# *CHAPTER 7*

## **EXPERIMENTAL IMPLEMENTATION**

---



## 7. EXPERIMENTAL IMPLEMENTATION

### 7.1. Layout of the SRC

Once known and characterized the power elements of the series resonant converter (SRC) and defined the control strategy in previous chapters, the experimental implementation is discussed in this chapter. A similar procedure to those adopted in the simulation chapter is presented that is, dividing the converter in two parts such as the power and the control circuits. An overview of the SRC implemented experimentally is shown in Figure 7.1 below. As can be seen in the figure the power circuit is composed by the core components and the auxiliary components namely; semiconductor devices, heat sink devices, high frequency transformer, inductors and capacitors of the resonant circuit and filters. The figure shows also the various control circuits, from which will be discuss later. The relation established between the experimental implementation and the block diagram of the converter makes easy to recognize each component and their interaction with the others system components.

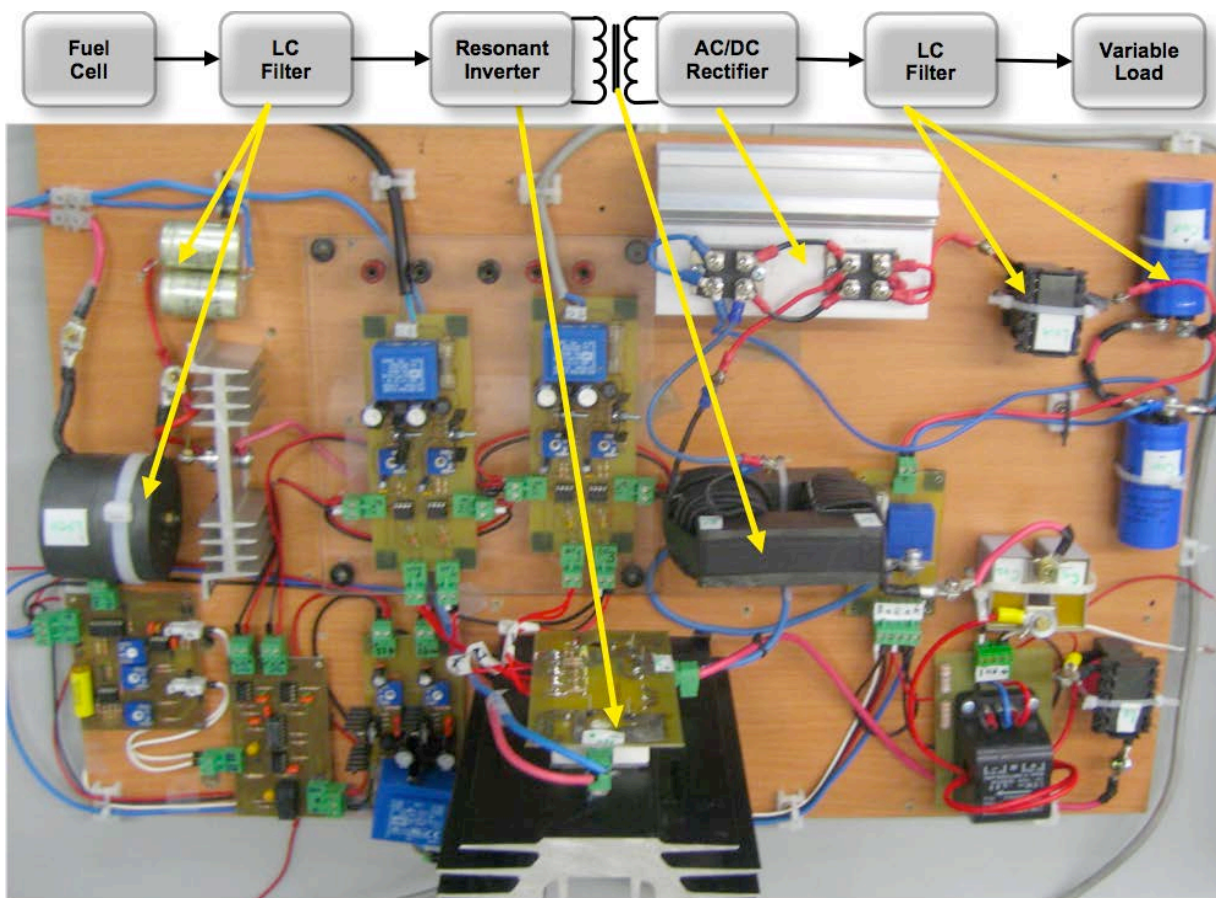


Figure 7.1 – Layout of the SRC implemented experimentally.



## 7.2. Selection of power devices

The power semiconductor devices are needed for implementing the full bridge inverter and for the full bridge rectifier. The full bridge inverter needs controlled devices such as, Insulated Gate Bipolar Transistor (IGBT), Metal Oxide Semiconductor Field Effect Transistor (MOSFET) or Bipolar Junction Transistor (BJT). It was decided to use IGBTs to implement the inverter bridge because they combine the positive aspects of the both; Mosfets and BJTs that is, the IGBT combines the fast switching capabilities of a MOSFET with the high current values of a typical BJT. In addition the IGBT has a lower on-state voltage drop and is capable of blocking higher voltages. Thus, through the combination of the low losses of the BJT, and ease control of the MOSFET, the IGBT is easy to control in voltage, and easily adapted for low power. The full bridge rectifier is uncontrolled and the semiconductors devices needed are fast diodes.

### 7.2.1. Selection of the IGBTs

Adopting a simplified analysis, the IGBT consists of a bipolar transistor controlled in current through a MOSFET, as shown in Figure 7.2. The equivalent circuit of the IGBT is purely capacitive as the same as the MOSFET.




Figure 7.2 – a) Equivalent Circuit of an IGBT and b) Symbols of the IGBT.

In the selection of power switches there are advantages in adopting modules with multiple elements, because the transistors being connected internally facilitates the interconnection with other components. Then, according to the requirements of the project, the modular solution is preferred and the module F4-50R12MS4 with the characteristics listed in the Table 7.1 were selected and used.



Table 7.1 –Characteristics of IGBTs module F4-50R12MS4.

IGBT Module	Specifications
<p><b>F4-50R12MS4</b></p> 	<p><math>V_{CE}=1200\text{ V}</math></p> <p><math>I_{Cnom}=50\text{ A (T=25 °C)}</math></p> <p><math>I_C=55\text{ A}/I_{CRM}=80\text{ A}</math></p> <p><math>Pot_{TotDiss}=355\text{ W (T=25 °C)}</math></p> <p><math>V_{CEsat}=3.2\text{ V (375 V max)}</math></p> <p><math>t_{d, on}=120\text{ ns (25 °C, R}_G=13\text{ }\Omega)</math></p> <p><math>t_{d, off}=310\text{ ns (25 °C, R}_G=13\text{ }\Omega)</math></p> <p>NTC-thermistor included</p>

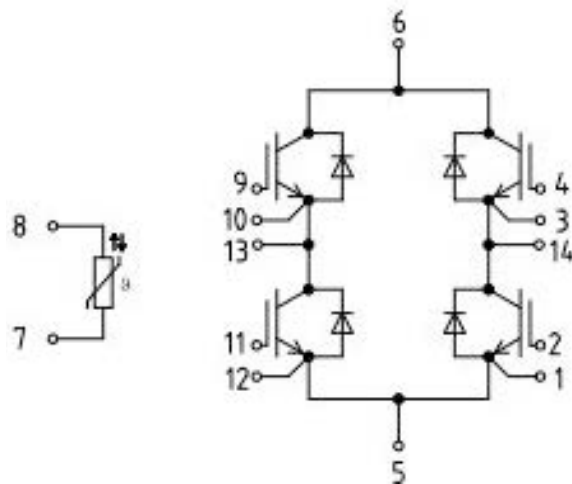



Figure 7.3 – Circuit diagram of IGBTs module F4-50R12MS4.

### 7.2.2. Selection of the power diodes

The full bridge rectifier is implemented with ultra-fast diodes. Then, soft recovery devices were selected, considering the conditions of output rectified voltage, and average output rectified current required. These devices **are well adapted to** low voltage, high frequency inverters, and freewheeling polarity protection applications. The packaged appearance and characteristics of this device are summarized in Table 7.2 below.

Table 7.2 – Power diode characteristics

Fast-Diode Module	Specifications
<p>ST MICROELECTRONICS</p> <p><b>BYV225V-200</b></p> 	<p>High surge current capability.</p> <p>Negligible switching losses.</p> <p>Insulating voltage = 2500 Vrms</p> <p>RMS Forward current <math>I_F(\text{rms}) = 150 \text{ A}</math></p> <p><math>I_F(\text{av}) = 200 \text{ A}</math>, <math>V_F = 1 \text{ V}</math> (125 °C)</p> <p>Repetitive peak reverse voltage</p> <p><math>V_{RRM} = 200 \text{ V}</math></p> <p>Capacitance = 55 pF</p> <p><math>t_{rr} = 55 \text{ ns}</math></p>

### 7.3. Selection of the heat sinks

When power semiconductor devices are switching or controlling reasonable currents they dissipate power as heat energy, because of their electrical resistance. The most common way **to facilitate this process is using a heat sink**. The primary purpose of the heat sink is to maintain the device temperature below the maximum allowable temperature specified by the manufacturer. Therefore, a reduction in the temperature corresponds to an exponential increase in the reliability and life expectancy of the device. The **selection of the proper heat sink depends** on the allowable junction temperature ( $T_{j, \text{max}}$ ), the maximum ambient temperature ( $T_{a, \text{max}}$ ), the maximum operating voltage and maximum on-state resistance. Luckily, all these data can be obtained from the manufacturer's datasheets.

#### 7.3.1. Types and materials of heat sinks

There are numerous solutions available for the thermal management problem. A large variety of heat sinks profiles are commercially available. The most well known are the stamped and the extruded. Figure 7.4 shows some of the commercially available extruder heat sinks.



Figure 7.4 – Extruded heat sink profiles commercially available.

As the more heat energy flowing thorough a material, the higher the temperature rise across it. Some metals like aluminium and copper, which have very high thermal conductivity, are especially well adapted for heat sinks. Table 7.3 summarizes some types of materials used.

Table 7.3 – Thermal conductivity of materials.

Material	Thermal Conductivity (W/Mk)
Iron	79.5
Aluminium	205
Copper	385
Air (at 0 °C)	0.024

### 7.3.2. Thermal equivalent Ohm's Law

Using the Ohm's Law, it appears that the thermal equivalent circuit is very similar to the electrical. The analogy between these two circuits is done according to the rules presented in Table 7.4, which clearly shows the equivalence between them. As an example, the thermal semiconductor equivalent circuit of Figure 7.5 (a) can be represented by the electrical equivalent circuit of Figure 7.5 (b) considering two separate thermal resistors in series. The one, inside the device package between the junction and the sink is  $R_{js}$  and other is the resistance between sink and the ambient or  $R_{ca}$ .

Table 7.4– Thermal versus electrical characteristics.

Electrical Circuit		Thermal Circuit	
Current source	Ampere (A)	Heat source P	(W)
Current	Ampere (A)	Power P	(W)
Voltage	Volt (V)	Temperature T	(°C)
Resistance	Ohm ( $\Omega$ )	Resistance $\theta$	(°C/W)
Capacitance	Farad (F)	Capacitance $C_T$	(J/°C)
Impedance	Ohm ( $\Omega$ )	Transient impedance	(°C/W)

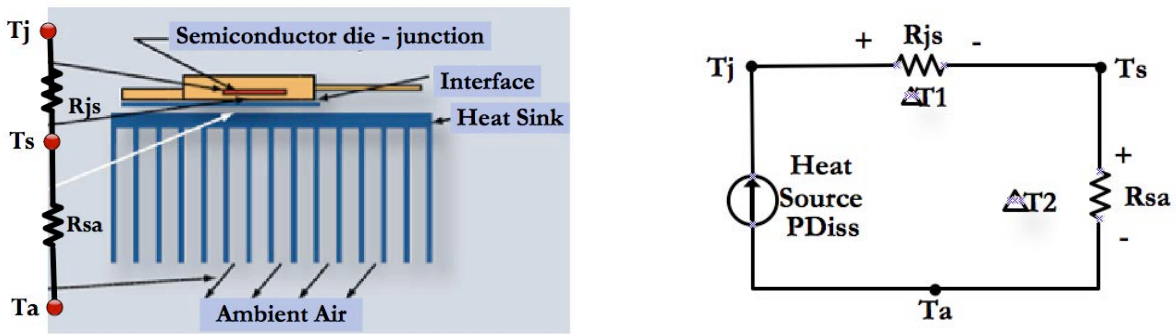


Figure 7.5 – Thermal semiconductor example and its equivalent circuit.

The thermal resistance is a quantity that represents the amount of opposition to the flow of heat. By analogy to an electrical circuit, the thermal resistance can be calculated by:

$$R_{eq} = \frac{\Delta V}{I} \quad \text{Eq. 7.1}$$

Or,

$$R_{eq} = \frac{T_j - T_a}{P} = \frac{\Delta T}{P} \quad \text{Eq. 7.2}$$

With;

$$R_{eq} = \Delta T_1 + \Delta T_2 \quad \text{Eq. 7.3}$$

$$\Delta T_1 = T_j - T_s \text{ and } \Delta T_2 = T_s - T_a \quad \text{Eq. 7.4}$$

$$R_{ja} = R_{js} + R_{sa} \quad \text{Eq. 7.5}$$

Under operating conditions, the heat power dissipated ( $P_{diss}$ ) is;

$$P_{Diss} = \frac{T_j - T_a}{R_{ja}} \quad \text{Eq. 7.6}$$

Where:

$P$  = Total power or rate of heat dissipation in W in °C.

$T_j$  = Maximum semiconductor junction temperature in °C.

$T_s$  = Heat sink temperature in °C.

$T_a$  = Ambient air temperature in °C.

$R_{js}$  = Thermal resistance, junctions to heat sink in °C/W or K/W.

$R_{sa}$  = Thermal resistance, heat sink to ambient in °C/W or K/W.

### 7.3.3. Selection of the heat sink for each module

The heat sinks for the module devices were designed and selected using the following steps:

First step: calculation of the heat sink thermal resistance  $R_{sa}$  required satisfying the thermal criteria of the component (DIODE, IGBT, MOSFET,). Second step: calculation of the length of the heat sink. Third step: look for a suitable heat sink profile available in the market (or in the lab).

#### **First step: calculation of the heat sink thermal resistance $R_{sa}$**

##### **➤ IGBT module**

The thermal information of the IGBT module F4-50R12MS4 is summarized in Table 7.5 below.

Table 7.5 – Thermal manufacturer characteristics of F4-50R12MS4 module.

Description	Parameter	Unit	Value
Thermal resistance, junction to case/IGBT	$R_{jc}$	°C/W	0.6
Thermal resistance, case-to-heat sink/IGBT	$R_{cs}$	°C/W	0.29
Thermal resistance, case-to-heat sink/module	$R_{cs}$	°C/W	0.02
Maximum temperature operation	$T_{maxop}$	°C	150
Maximum junction temperature	$T_j$	°C	150

Knowing that the maximum current thorough each IGBT of the module is 45A, and also the fact that the working period is  $[0-\pi]$ , the average current that crosses it can be calculated by:

$$I_{AV} = \frac{1}{2\pi} \int_0^{\pi} I_{max} \times \sin(\theta) d\theta = \frac{I_{max}}{2\pi} [-\cos(\pi) + \cos(0)] = \frac{I_{max}}{\pi} = 14.32A \quad \text{Eq. 7.7}$$

Considering the output characteristic of the IGBT module above, and the graph of Figure 7.6 for  $V_{GE}=15V$  and  $T_j=125^\circ C$ , the collector-emitter voltage ( $V_{CE}$ ) correspondent to the average collector current of 14.42A is approximately 1.4V.

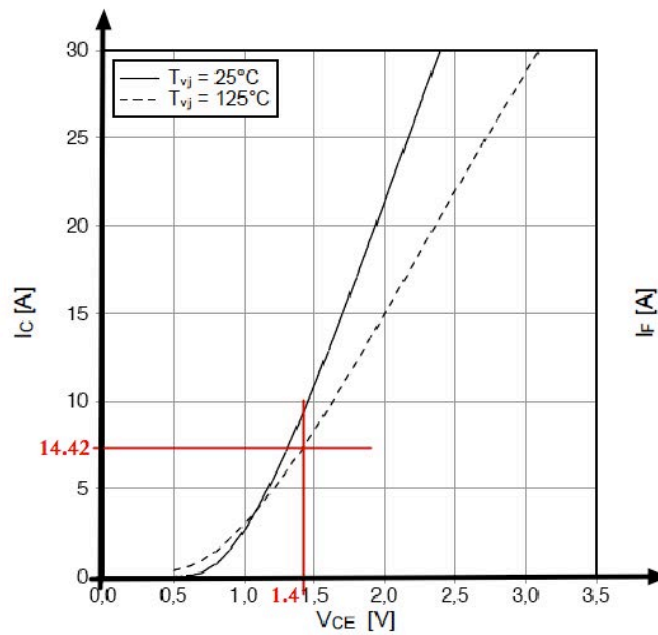


Figure 7.6 – Graph of the output characteristic of IGBT module,  $I_C = f(V_{CE})$ .

The power dissipated by each IGBT of the module is:

$$P_{DissIGBT} = I_C \times V_{CE} = 14.32 \times 1.4 = 20W \quad \text{Eq. 7.8}$$

For a full bridge, with two IGBTs conducting simultaneously, the sink must be sized to dissipate the power provided by the four IGBTs, or,

$$P_{DissTotal} = 4 \times P_{DissIGBT} = 4 \times 20 = 80W \quad \text{Eq. 7.9}$$

Then, thorough the thermal equivalent circuit it has:

$$\Delta T_1 = T_j - T_s \quad \text{Eq. 7.10}$$

Or,

$$\Delta T_1 = P_{DissTotal} \times R_{js} \text{ with, } R_{js} = R_{jc} + R_{cs} \quad \text{Eq. 7.11}$$

$$150 - T_s = 20 \times (0.6 + 0.29) \Rightarrow T_s = 132.2^\circ C \quad \text{Eq. 7.12}$$

$$\Delta T_2 = T_s - T_a \quad \text{Eq. 7.13}$$

$$\Delta T_2 = 132.4 - 25 = 107^\circ C \quad \text{Eq. 7.14}$$

$$P_{DissTotal} = \frac{\Delta T_2}{R_{sa}} \quad \text{Eq. 7.15}$$

Finally, the value of the thermal resistance (Rsa) of IGBT module is:

$$R_{sa} = \frac{107}{80} = 1.33^\circ C / W \quad \text{Eq. 7.16}$$

### ➤ Rectifier module

The information provided in the manufacturer datasheet of module BYV255 is summarized in Table 7.6. This information is for one diode, for two diodes used simultaneously, the temperature of the module must be calculated by:

$$T_j - T_c(D1) = P(D1) \times R_{jc}(\text{per diode}) + P(D2) \times R_c \quad \text{Eq. 7.17}$$

Table 7.6 – Datasheet Information of module BYV255.

Description	Parameter	Unit	Value
Thermal resistance, junction to case, per diode	$R_{jc}$	$^{\circ}\text{C}/\text{W}$	0.4
Thermal resistance, junction to case / module	$R_{jc}$	$^{\circ}\text{C}/\text{W}$	0.25
Thermal resistance, case-to-heat sink/module	$R_{cs}$	$^{\circ}\text{C}/\text{W}$	0.1
Maximum temperature operation	$T_{opmax}$	$^{\circ}\text{C}$	125
Maximum junction temperature	$T_j$	$^{\circ}\text{C}$	150

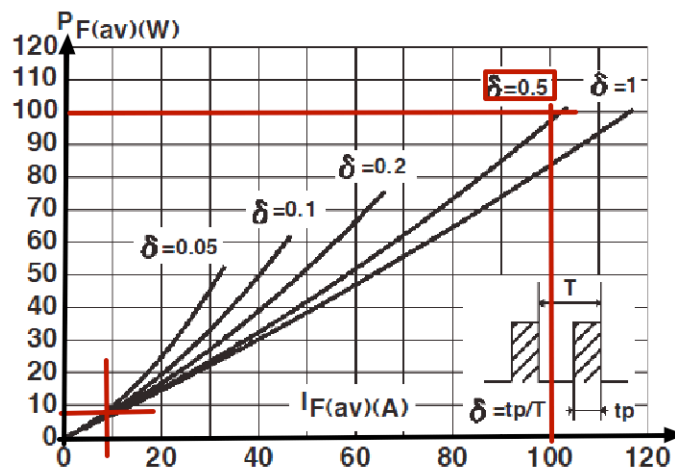


Figure 7.7 – Average forward power versus average forward current.

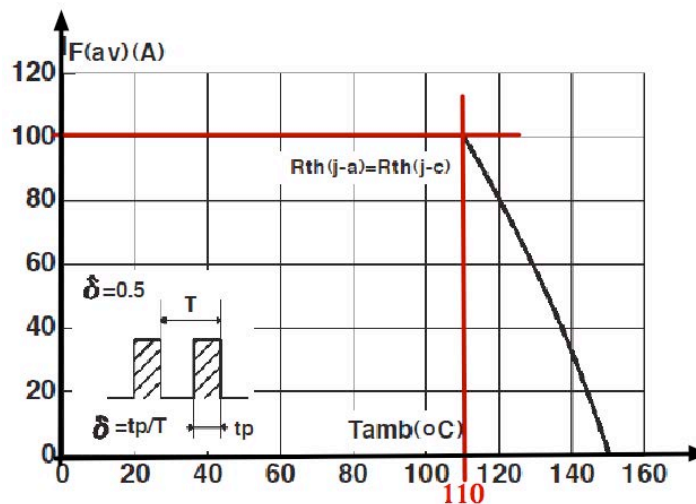


Figure 7.8 – Average current versus ambient temperature.



By the manufacturer datasheet information summarized in the Table 7.6, for the average current  $I_F=100$  A, ambient temperature above  $110^\circ\text{C}$  and  $\delta=0.5$ , as represented in Figure 7.7 the maximum power dissipated by the diode is approximately 100W.

$$P_{Diss}(\delta=0.5, I=100A) = P_{F_{AV}} = 100W \quad \text{Eq. 7.18}$$

The manufacturer information of Figure 7.8 shows that the average forward current is a function of the ambient temperature and is constant and equal to 100A. In this case the thermal resistance junction to case ( $R_{jc}$ ) and the thermal resistance junction to ambient ( $R_{ja}$ ) are equals. If the ambient temperature is higher than  $110^\circ\text{C}$  the average forward current drops abruptly. The heat-sink thermal resistance  $R_{sa}$  required is in this case, considering a medium value of ambient temperature equal to  $40^\circ\text{C}$  is:

$$R_{sa} = \frac{150 - 40}{100} = 1.1^\circ\text{C} / W \quad \text{Eq. 7.19}$$

### **Second step: calculation of the length of the heat sink**

As larger the heat sink, the lower its thermal resistance, i.e., whether to increase the size of the sink, the heat dissipation is much better. Thus, it is important to maintain a safety margin, which effectively ensures the required heat dissipation. Another important aspect is the relative position of the fins that should be as free as possible to facilitate the airflow between them. For example, the heat sink profile, PADA N° 8175 shown in Figure 7.9 is appropriate for the rectifier diodes module with a length of 64mm.

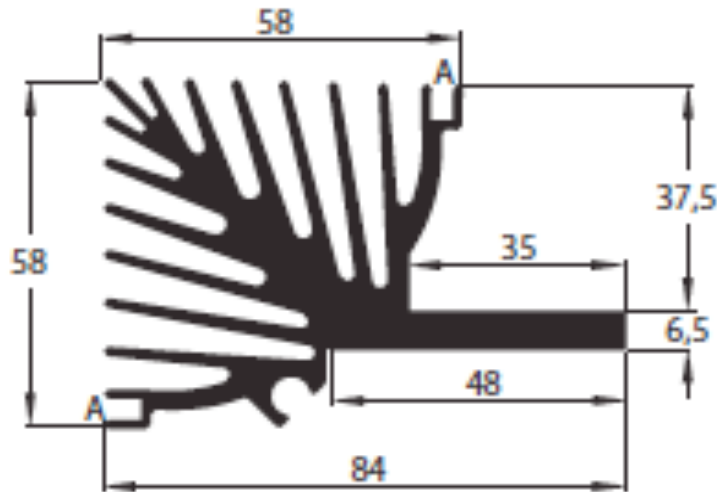
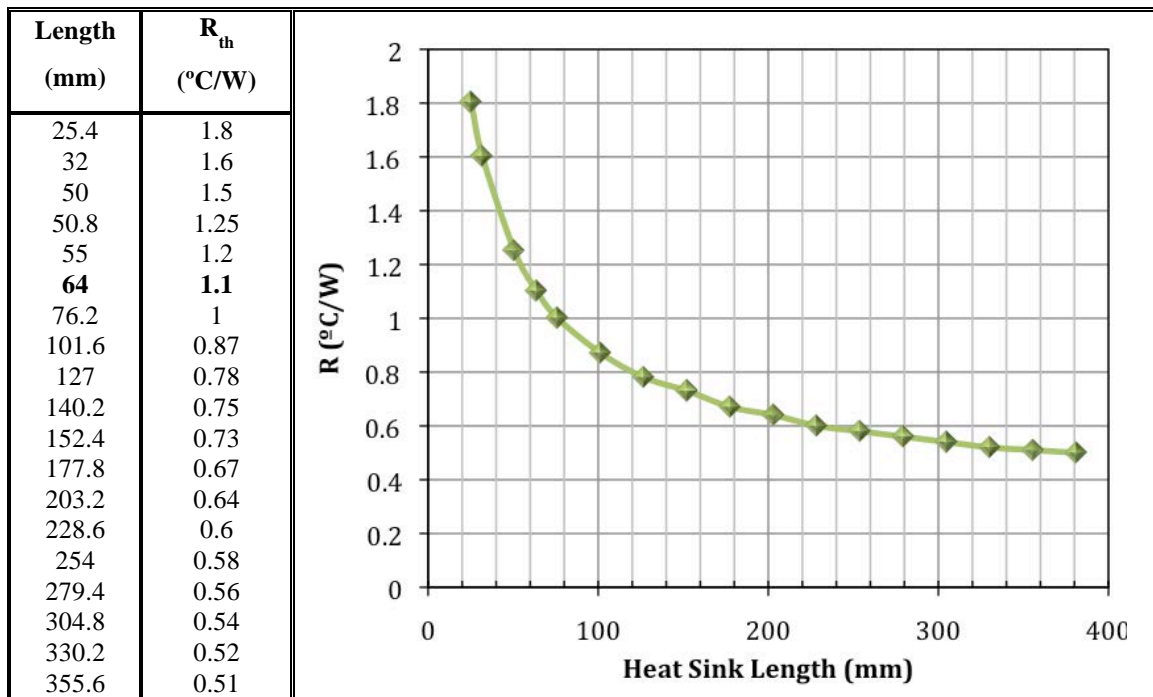


Figure 7.9 – Dimensions of the heat sink profile –PADA N° 8175.

Table 7.7 –Thermal resistance vs. heat sink length of the profile PADA N° 8175.



### Third step: Cheek for Heat sink profiles available

Using the **resources available** in the lab a comparative analysis of some **profiles** founded **was made**. In below there are represented its main features. **As can be seen in the table**, the power dissipated increases as the amount of thermal resistance decreases..

Table 7.8 – Some of the heat sink profiles available in the lab.

	(1)	(2)	(3)	(4)
Manufacturer	WIKFIELD	WIKFIELD	PADA	PADA
Width (Mm)	130	120	120	125
Height (Mm)	25	63	120	135
Length (Mm)	100	75	120	180
$R_{th}$ ( $^{\circ}C/W$ )	2.2	2	0.5	0.42
Max $P_{Diss}$ (W)	10	30	50	100

## 7.4. Design of the magnetic parts

The magnetic parts comprehend the design of the PEM filter inductor, the output filter inductor and the high frequency transformer. The implementation of these elements needs some precautions because they must be prepared for working in high frequency.

## 7.5. Design of the inductors

The design of the inductors is made following the steps below:

First step: Decide what type of core is the best.

Second step: Calculate the number of turns and wire dimension.

Third step: Check that there is enough space to hold the wire and construct and test the inductor.

The size of an inductor is approximately proportional to the stored energy. The energy stored in an inductor with inductance  $L$  and peak current  $I$ , is given by Eq. 7.20. This energy is stored as magnetic field-energy in the ferrite core; i.e. in the air-gap, the values of  $L$  and  $I_{max}$  have been previously determined in simulation project.

$$\text{Energy Storage} = \int_0^t P dt = \frac{1}{2} \times L \times I_{max}^2 \quad \text{Eq. 7.20}$$

### **First step: Selection of the core type**

The magnetic cores are significantly different for inductors and high frequency transformers because, inductors stored energy and transformers transfer energy. Hence, inductors need an air gap for storing the energy and transformers do not. For core selection, usually the inductance value ( $L$ ), maximum frequency operation ( $f_{max}$ ), and maximum current ( $I_{max}$ ) are considered. The core material is normally ferrite. The ferrite core types EE, EC and ETD are intended for high power applications such as switch mode power supplies and DC-DC converters. The energy is stored as magnetic field energy, within the ferrite core and within the air gap..

### **Second step: Calculate the number of turns and wire diameter**

Before calculating the number of turns and the wire diameter, it is important to refer how the energy is stored in a magnetic field of an inductor, which is given by the equation follow.

$$W = \frac{1}{2} \int HB dV \approx \frac{1}{2} \vec{H}_{Fe} \vec{B}_{Fe} \vec{V}_{Fe} + \frac{1}{2} \vec{H}_{\delta} \vec{B}_{\delta} \vec{V}_{\delta} \quad \text{Eq. 7.21}$$

Where:

l<sub>fe</sub>: Magnetic length of the core

H<sub>fe</sub> : Magnetic field strength within the ferrite

H<sub>δ</sub> : Magnetic field strength within the air gap

B: Magnetic flux density

In this equation, the magnetic field density  $\vec{B}$  is continuous and approximately equal for the sum of the ferrite energy and the air gap energy. The magnetic field strength  $\vec{H}$  is not continuous, within the air gap it is increased by a factor  $\mu_r$  compared to that than within the ferrite.

$$\vec{B} = \mu_0 \times \mu_r \times \vec{H} \quad \text{Eq. 7.22}$$

$$V_{Fe} = I_{Fe} \times A \quad \text{Eq. 7.23}$$

$$W = \frac{1}{2} \times \frac{B^2 \times A \times \delta}{\mu_0} \quad \text{Eq. 7.24}$$

It is known that the limit of the magnetic flux density is about 0.3T for the usual ferrite materials, hence, inductors require a certain volume for air gap to store energy, which leads to a minimum of volume of the air gap required. The minimum volume required is  $V\delta$  given by equation below. Once known the required volume of the air gap, the core can be selected from a data book of ferrite cores.

$$V\delta = \delta \times A \geq \frac{L \times I^2 \times \mu_0}{B_{\max}^2} \quad \text{Eq. 7.25}$$

With B<sub>max</sub>=0.3 T.

### Number of turns:

The number of turns  $N$  is calculated with help of the magnetic conductance  $AL$ , often simply called the  $A_L$  –value, which can be verified from the data book of the ferrite cores.

$$N = \sqrt{\frac{L}{A_L}} \quad \text{Eq. 7.26}$$

### Wire diameter:

In the calculation of the wire diameter the current density-  $S$  of the wire must be between 2 and 5 A/mm<sup>2</sup> (depending on its size and isolation). Then, the diameter of the wire  $d$  is calculated by the equation follows.

$$d = \sqrt{\frac{4 \times I_{rms}}{\pi \times S}} \quad \text{Eq. 7.27}$$

With  $S = 2 \text{ to } 5 \text{ A/mm}^2$ .

### Third step: Check of the space to hold the wire

Once known by simulation the values for the magnetic parts namely, the current, voltage and frequency values, the project of various inductors of the circuit are made using a particular software tool, the “Design of Switch Mode Power Supplies” [107], which adopts the methodology presented above and gives the necessary information required to the inductor design. Particularly, according to a database containing the different ferrite core types , and accordingly to the values of  $L$  and  $I_{max}$ , the information about the type of core, the number of turns to put on and wire-diameter are given to the user. Following sections present the inductors design through this software tool. The check of the space to hold the wire, the construction and test of each inductor are both calculated for each particular case and in each respective section.

#### 7.5.1. Inductor of PEM filter

Considering the value of the inductor of the PEM filter,  $L=122 \mu\text{H}$  and the maximum current through this one, 45 A the software used displays the information in Table 7.9 below.

As can be observed in Table 7.9 there are two options, which may perform the PEM inductor, namely; core types PM114/93 or P66/56. The other cores types presented have not enough space for the construction of the inductor (it appears in the software as “*too small*”). Thus, considering the cores available in the laboratory, the type P66/56 (of Siemens) was selected to build the PEM filter, the program gives a number of turns equal to 9 and a wire diameter not less than 4.37 mm.

Table 7.9 –Ferrite core options to perform the PEM inductor.

L/H:  Input example:  
100E-6 for an  
inductor L=100μH

$I_{max}/A$ :

Calculate

Wire dimensions: The core is...

$d \geq 4.37 \text{ mm}$  very good

$A \geq 15 \text{ mm}^2$  good  
suitable  
too small

No.	Core	Ident.	Manufacturer	$A_L/\text{nH}$	$A_{in}/\text{mm}^2$	$I_{in}/\text{mm}$	$A_{min}/\text{mm}^2$	$W_{max}/\mu\text{Ws}$	$B_{max}/\text{mT}$	N1
52	PM114/93	3.8	Siemens	630	1720	200	1380	136029	286	14
66	UU93/152/30		Siemens	840	840	354	840	37800	542	13
67	UU93/152/30	N27	Siemens	5400	840	354	840	5880	1375	5
68	E42/21/20		Siemens	4750	234	97	229	497	4730	6
78	P66/56		Ferroxcube	1700	3580	160	2800	207529	231	9

**Observation:** the core material P66/56 (of Ferroxcube) is quite different of the Siemens core used. As a result, the inductance value measured in the test phase is quite different than the required. However, since there is space available to hold the wire, it was decided to accept this value.

### 7.5.2. Inductor of output filter

The output filter inductor as the inductance and maximum current of 800μH and 3 A respectively. The core type selected to this inductor is given in the Table 7.10 follow.

Table 7.10 – Ferrite core options to perform the output filter inductor.

L/H:  Input example:  
100E-6 for an  
inductor L=100μH

$I_{max}/A$ :

Calculate

Wire dimensions: The core is...

$d \geq 1.13 \text{ mm}$  very good

$A \geq 1 \text{ mm}^2$  good  
suitable  
too small

No.	Core	Ident.	Manufacturer	$A_L/\text{nH}$	$A_{in}/\text{mm}^2$	$I_{in}/\text{mm}$	$A_{min}/\text{mm}^2$	$W_{max}/\mu\text{Ws}$	$B_{max}/\text{mT}$	N1
66	UU93/152/30		Siemens	840	840	354	840	37800	93	31
67	UU93/152/30	N27	Siemens	5400	840	354	840	5880	235	13
68	E42/21/20		Siemens	4750	234	97	229	497	808	13
69	E42/21/20			1029	234	97	229	2293	376	26
70	E42/21/20			603	234	97	229	3914	288	37
71	E/42/21/20			354	234	97	229	6666	220	48
72	E42/21/20			259	234	97	229	9111	189	56

The output filter inductor can be made by the core type E42/21/20 with an air-gap, as can be seen in the table (it appears just “*suitable*”). In the case the number of turns is 37, 48 or 56, depending of the air-gap. The diameter of the conductor must not be less than 1.13 mm.

### 7.5.3. Implementation of the inductors

Once known the wire diameter of the conductor, the number of turns to put and the type of ferrite core and also checking that there is enough space to hold the wire in accordance with the availability of the ferrites in the lab, the core E/42/21/20 of Siemens, with the material N27 was selected to implement the resonant and output filter inductors. For the same reason, it is used the core P66/56 of Ferroxcube to implement the PEM filter. Their characteristics are shown in Figure 7.10.

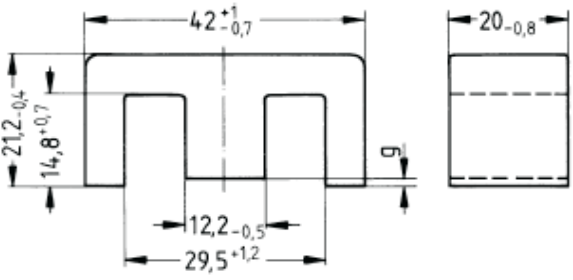
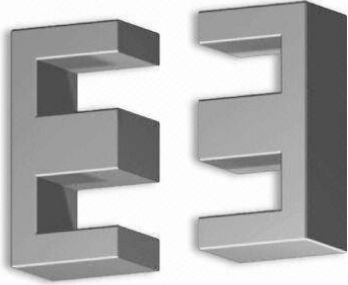
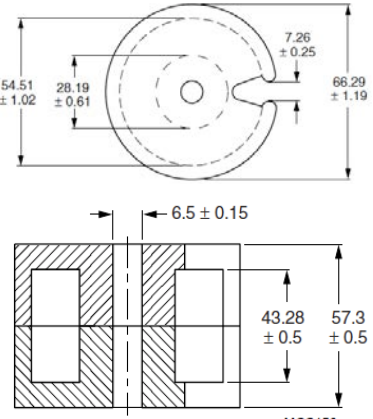

	
$\sum I / A = 0.41 \text{mm}^{-1} \quad A_e = 234 \text{mm}^2 \quad V_e = 22700 \text{mm}^3$ $l_e = 97 \text{mm} \quad A_{\min} = 229 \text{mm}^2 \quad AL = 1029 \text{nH} (g = 25 \text{mm})$	
	
$\sum I / A = 0.172 \text{mm}^{-1} \quad A_e = 717 \text{mm}^2 \quad V_e = 88200 \text{mm}^3$ $l_e = 123 \text{mm} \quad A_{\min} = 591 \text{mm}^2 \quad AL = 18200 \text{nH} (g \approx 0)$	

Figure 7.10 – The ferrite cores E/20/21/30 of Siemens and P66/56 of Ferroxcube.

## 7.6. Selection of the capacitors

Once defined and implemented the inductors its necessary to select corresponding capacitors. For the case, the capacitors were selected among those available on the lab, without neglecting the necessary conditions imposed by each situation.

### 7.6.1. PEM filter capacitor

The capacitor of the PEM is composed by two axial electrolytic capacitors connected in parallel with  $470\mu F$ ,  $100V$  each one. As aluminium construction, they present good thermal characteristics and high ripple current capabilities; they are also very attractive for high power applications. Considering the value of  $933\mu H$  of the inductor implemented experimentally and the capacitor value  $940\mu F$ , the cut-off frequency of this filter is calculated by,

$$f_{CPEM} = \frac{1}{\sqrt{L_{PEM} \times C_{PEM}}} \quad \text{Eq. 7.28}$$

That is;  $L_{PEM} = 933\mu H$  ,  $C_{PEM} = 940\mu F$  and  $f_{PEM} = 170Hz$

### 7.6.2. Resonant capacitor

Considering the transformer D that is implemented experimentally which characteristics are presented above, the leakage inductance of  $2\mu H$  is considered as the resonant inductance  $L_r$ . The correspondent resonant capacitor is implemented experimentally by two snubber capacitors of  $2\mu F$  connected in parallel that is  $C_r = 4\mu F$ . Their characteristics includes high pulse load, high current capability, and voltage up to  $2500 V_{DC}$ , which make them very well suited to applied in switching-mode power supply technologies. The resonant frequency using Eq. 7.29 is therefore  $f_r = 56kHz$ .

$$f_r = \frac{1}{2\pi\sqrt{L_r \times C_r}} \quad \text{Eq. 7.29}$$

That is;  $L_r = 2.1\mu H$ ,  $C_r = 4\mu F$  and  $f = 56kHz$

### 7.6.3. Output filter capacitor

The output capacitor is composed by two polarized electrolytic of  $220\mu F$  connected in series. Particularly, this capacitor type has a polarity, i.e. positive on one terminal and negative on the other. In use, it has its positive voltage always higher than that on the negative terminal, it matters




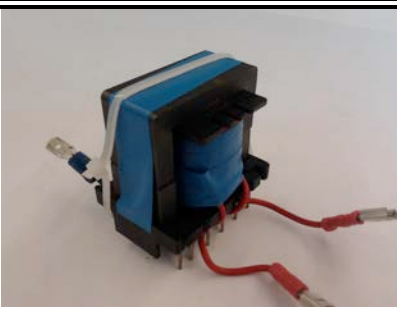




that this is the case and this gives rise to the term polarized. This sort of capacitor is commonly found in power supply filters. Then, considering the inductor previously implemented with 740  $\mu\text{H}$ , and 110  $\mu\text{F}$  values for the capacitor, the cut-off frequency of this filter is therefore.

$$f_f = \frac{1}{2\pi\sqrt{L_f \times C_f}} \quad \text{Eq. 7.30}$$

That is;  $L_f = 740\mu\text{H}$ ,  $C_f = 110\mu\text{F}$ , and  $f_r = 557\text{Hz}$

Table 7.11 represents the inductors and capacitors for the experimental implementation of the DC-DC converter in order to satisfy the requirements of the project.

Table 7.11 – Summary of the specifications of the inductors and capacitors.

PEM FILTER ( $L_{\text{PEM}}$ , $C_{\text{PEM}}$ )	RESONANT CIRCUIT ( $L_r$ , $C_r$ )	OUTPUT FILTER ( $L_f$ , $C_f$ )
		
PEM Inductor implemented experimentally  $L_{\text{PEM}} \approx 933 \mu\text{H}$	Resonant Inductor is the leakage inductance value of the transformer D implemented experimentally.  $L_r = 2.1 \mu\text{H}$	Output Inductor implemented experimentally  $L_f \approx 740 \mu\text{H}$
		
Two Capacitors in parallel, $C=470 \mu\text{F}$ (x 2) $C_{\text{PEM}} = 940 \mu\text{F}$	Two HVDC Capacitors in parallel, $C=2.0 \mu\text{F}$ (x 2) $C_r = 4 \mu\text{F}$	Two Capacitors in series, $C=220 \mu\text{F}$ (% 2) $C_{\text{feq}}=110 \mu\text{F}$
$f_c = 170\text{Hz}$	$f_{op} = 56\text{KHz}$	$f_c = 557\text{Hz}$

In the optimization of the conditions of the converter, DC-DC series resonant it was necessary to make several changes through time, particularly the values of  $L_r$  and  $C_r$  were changed, during the project.

## 7.7. Design of the high frequency transformer

The design of a high frequency transformer depends on the power to be transferred and the frequency of operation. The higher the frequency is the smaller the size of the transformer. The much greater value of saturation flux density  $B_{SAT}$  of the metal core compared to ferrite core would permit a much smaller size for these last for the same application (i.e. 0.8 T vs. 0.3 T). Then, for the high frequency applications ( $f > 20$  KHz) and large wire diameters ( $A > 1 \text{ mm}^2$ ) the skin effect must be taken into account. I.e., the major part of the magnetic component of power electronics is subjected to eddy-current losses, neglecting these eddy-currents may result in a significant error of the design. A typical magnetic core of an HF transformer is represented in Figure 7.11.

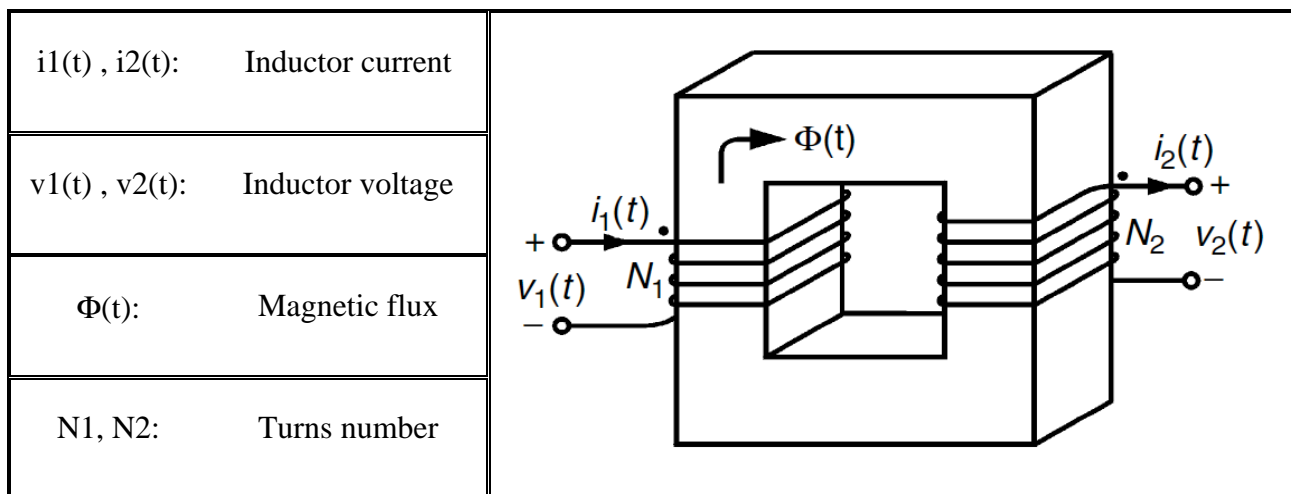


Figure 7.11 – Typical Magnetic core of an HF transformer.

### 7.7.1. Selection of the appropriate material and type of core

The first step in the design of a high frequency transformer is to choose the appropriate core to use. The size of the core is dependent on the power to be transferred and the operating frequency. A core without an air-gap is used in order to keep the magnetizing current as small as possible.

The hysteresis loop gives the relation between the induction  $B$  and the flux intensity  $H$  for a closed reversal cycle of magnetization of a ferromagnetic material. The shape of the hysteresis loop is material dependent. Other factors that influence the shape are the excitation frequency and the conditions of the treatment of the material. A typical hysteresis loop and Magnetic Properties is represented in the Figure 7.12 and the hysteresis of UI93/104/30 for N27 material at different temperature values is represented in Figure 7.13.

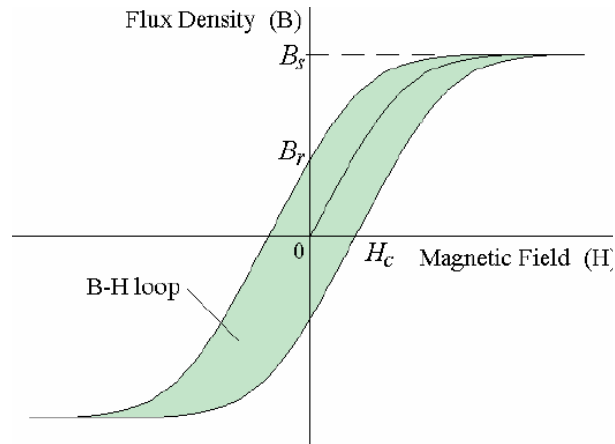


Figure 7.12 – Typical hysteresis curve of a ferromagnetic material.

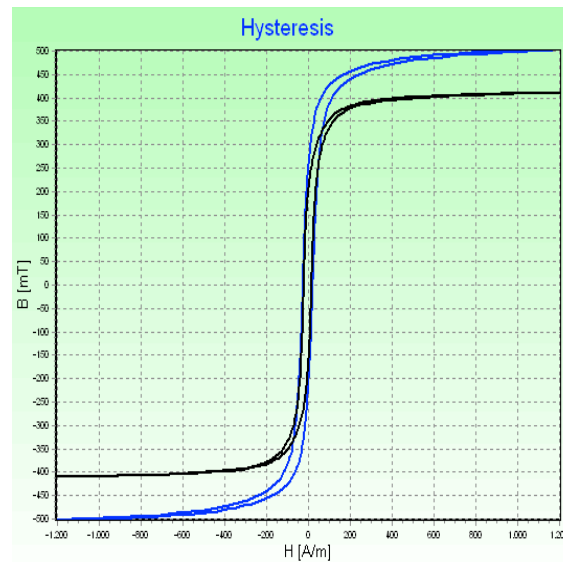


Figure 7.13 – Hysteresis of UI93/104/30 for N27 material at 25°C (Blue) and 150°C (Black).

The surface of the loop in the  $B$ – $H$  plane is the energy loss per volume in one cycle. According to their coercive force  $H_c$  the ferromagnetic materials are subdivided in two classes: 1) Hard magnetic materials and 2) Soft magnetic materials. The hard magnetic materials are characterized by a high value of the remaining induction  $B_r$  while Soft magnetic materials are characterized by an ease of

change of magnetic alignment in their structure as shown in Figure 7.13. Usually, the values of  $H_c$  of most of the used in practice materials are  $H_c < 400$  A/m for soft materials and  $H_c > 100,000$  A/m for hard magnetic materials. Ferrites are included in the group of soft magnetic materials witch can be used for applications up to 1 or 2 MHz, including the switching power supplies. NiZn ferrites have lower permeability and much higher resistivity, hence lower losses.

Referring to some of the most common ferrite types available, in the market, namely; UU, UI, EE, EC, EI and PM cores, the implementation of the HF transformer was performed according to the availability of the lab, namely: ferrite UI93/104/30 with N27 material and ferrite EE. Their appearance and magnetic characteristics are presented in Figure 7.14 below.

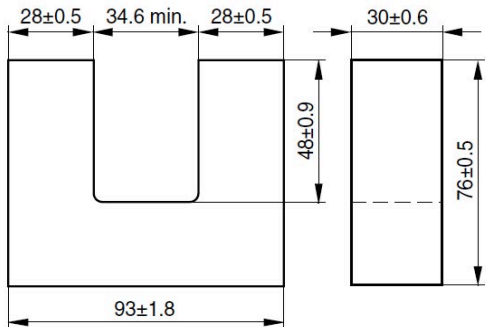

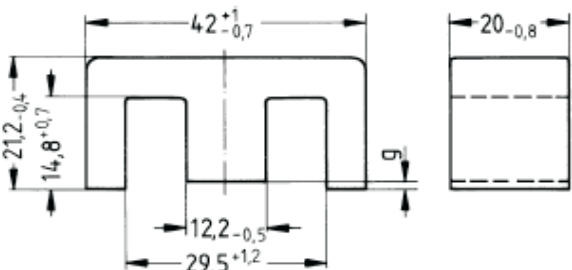
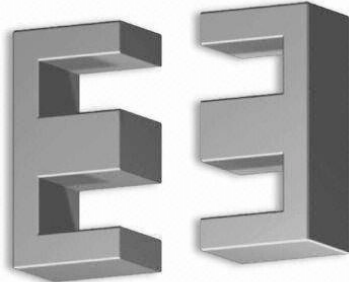
	
$\sum I / A = 0.42 \text{ mm}^{-1}$ $I_e = 354 \text{ mm}$	$A_e = 840 \text{ mm}^2$ $A_{\min} = 840 \text{ mm}^2$ $V_e = 297000 \text{ mm}^3$ $m = 1500 (\text{g} / \text{set})$
	
$\sum I / A = 0.41 \text{ mm}^{-1}$ $I_e = 97 \text{ mm}$	$A_e = 234 \text{ mm}^2$ $A_{\min} = 229 \text{ mm}^2$ $V_e = 22700 \text{ mm}^3$ $AL = 1029 \text{ nH} (g = 25 \text{ mm})$

Figure 7.14 – Appearance and magnetic characteristics of ferrites UI and EE.

HF transformers A and C were made with the chokes UI, as shown in Figure 7.15, HF transformer B was made with the chokes UU and transformer D with the chokes EE.



Step 1: Cutting machine



Step 2: polishing machine



Step 3: Transformer A with UI

Figure 7.15 – Preparation of ferrite for the HF transformer of type A.

### 7.7.2. Calculation of the primary and secondary turns number

The second step is to calculate the number of primary turns. This number determines the magnetic flux density within the core.

$$N1 = \frac{\left( V1 \times \frac{T}{2} \right)}{(\Delta B \times A_{\min})} \quad \text{Eq. 7.31}$$

Where,  $A_{\min}$  is the minimum core cross-section and  $\Delta B$  is the change of flux density, which depends on the frequency  $f=1/T$  and the number of turns  $N1$ . The minimum number of turns gives the maximum flux density. The number of secondary turns is the ratio of primary to secondary voltage. The diameters of the primary and secondary conductors can be calculated depending on the RMS-values of the currents.

### 7.7.3. Calculation of the primary and secondary wire-diameter

The wire-diameter depends on the respective rms current value of the coil. This can be calculated from the coil power. If the losses are neglected and it is assumed that with  $V_{in\_min}$  the maximum duty cycle is achieved, it follows that for the Full Bridge Push-Pull Converter, which is the case:

$$I_{1rms} = \frac{P_{out}}{V_{in\_min}} \quad \text{and} \quad I_{2rms} = \frac{P_{out}}{V_{out}} \quad \text{Eq. 7.32}$$

The current density  $S$  is chosen between 2 and 5 A/mm<sup>2</sup>, depending on the thermal resistance. Then the wire cross-section  $A_{\text{wire}}$  and the wire diameter  $d_{\text{wire}}$  can be calculated as follows:

$$A_{\text{wire}} = \frac{1}{S} \quad \text{and} \quad d_{\text{min}} = \sqrt{I \times \frac{4}{S \times \pi}} \quad \text{Eq. 7.33}$$

#### 7.7.4. Design of the transformer

Adopting the software of the “*Design of Switch Mode Power Supplies*” [108], in the design of the HF transformer a Full-Bridge Push-Pull Converter topology is selected.

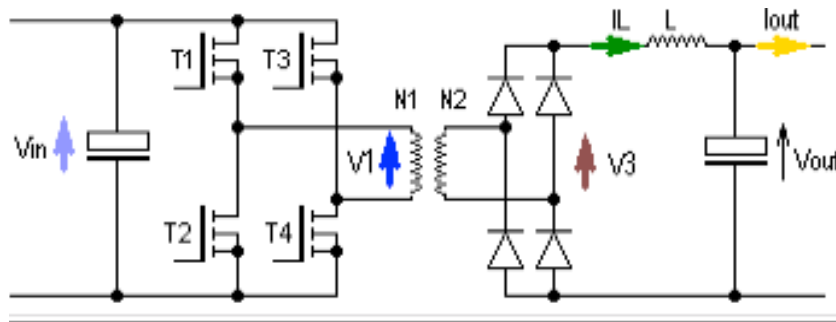


Figure 7.16 – Full-Bridge Push-Pull Converter topology.

The Push-Pull converter drives the high-frequency transformer with an AC voltage. The primary transformer voltage  $V1$  can be  $+V_{\text{in}}$ ,  $-V_{\text{in}}$  depending on which pair of transistors (T1, T4 or T2, T3) is turned on or off. On the secondary side, the AC voltage is rectified, so that  $V3$  is a pulse-width-modulated control voltage, which switches between  $V_{\text{in}} \cdot (N2/N1)$ . Due to the rectification, the pulse-frequency of  $V3$  is equal to  $2f$ . The Low-Pass filter, formed by the inductor  $L$  and the output capacitor  $C_{\text{out}}$ , produces the average value of  $V3$ . Then, considering the inductor of output filter  $L = 800\mu\text{H}$  and selecting the Full-Bridge Push-Pull topology of the spreadsheet, the following parameters are entered as input data:  $V_{\text{in\_min}}$  (V),  $V_{\text{in\_max}}$  (V),  $V_{\text{out}}$  (V),  $I_{\text{out}}$  (A), and  $f$  (kHz).

$V_{in\_min} / V$ 37	$V_{in\_max} / V$ 42.5	$V_{in} / V$ for the calculations 42	
$V_{out} / V$ 400	$I_{out} / A$ 3	$f / kHz$ 100	Calculate
<input type="checkbox"/> Proposal	$L / H$ 800E-6	$\Delta I_L / A$ for $V_{in\_max}$ 0.43	Coil Data
<input checked="" type="checkbox"/> Proposal	$N_1 / N_2 :$	87.56E-3	Transformer Data

The number of turns of primary and secondary conductors, its wire-diameter –d and wire-cross-section –A can be seen in table below for this case. The output inductor value  $L=800 \mu H$  was used in simulation results. For this particular value, the ripple current is  $\Delta I_L=0.43$  A. The voltage ratio of  $N_2/N_1=11.42 \rightarrow 12$  is the proposed value.

Table 7.12 – Output data for the converter (Nexa)

FULL-BRIDGE PUSH-PULL CONVERTER		
$V_{MIN} = 37V$	$V_{MAX} = 42.5V$	$V_{Calculated} = 42V$
$V_{out} = 400V$	$I_{out} = 3A$	$f = 100kHz$
$L = 800\mu H$	$\Delta I_{out} = 0.43A$	$N_2 / N_1 = 12$

### 7.7.5. Coil and core transformer data

As been referred previously, the wire-diameter depends on the respective rms current of the coil, then the wire-diameter –d and wire-cross-section –A of primary and secondary are as follows:

- $d_1 \geq 3.71$  mm,  $A_1 \geq 10.81$  mm<sup>2</sup> – for primary wire (with  $N_1=4$ )
- $d_2 \geq 1.13$  mm,  $A_2 \geq 1$  mm<sup>2</sup> – for secondary wire (with  $N_2=46$ )

Finally, with the previously selected core, UI93/104/30 the design of the transformer is “good “ for the application, with 4 turns in the primary and 46 turns in the secondary, as can be seen in Table 7.13 below.



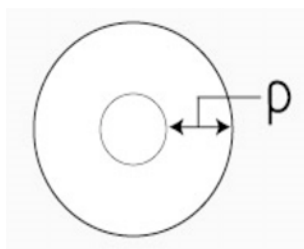
Table 7.13 – Information of core selected for the HF transformer.

No.	Core	Manufacturers	$A_{min}/mm^2$	$V_{in}/mm^3$	$\Delta B/T$	N1	N2
33	2xU93/76/16	Siemens	448	159000	0.13	4	46
34	UI 93/104/16	Siemens	448	116000	0.13	4	46
35	2xU93/76/20	Siemens	560	198000	0.13	4	46
36	UI 93/104/20	Siemens	560	144000	0.13	4	46
37	2xU93/76/30	Siemens	840	297000	0.13	3	34
38	UI93/104/30	Siemens	840	217000	0.13	3	34

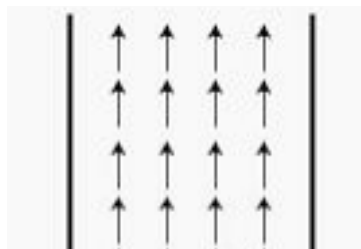
NOTE: core color means, **very good** , **good** , **suitable** and **too small**

### 7.7.6. Analysis of the skin effect

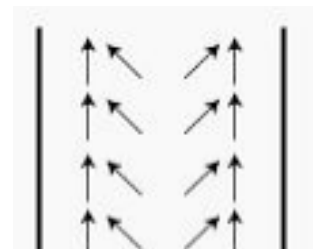
When a wire is used to carry DC current, the entire cross sectional area of copper carries the current equally. When a wire is used for AC current, the current is carried differently, that is; at low frequencies, the current flow is not significantly affected by the skin effect but in higher frequencies the outer area of the copper wire carries the current flow disproportionately. This is called the skin effect and corresponds to the tendency for high-frequency currents to flow on the surface of the conductor. Skin effect is exemplified in Figure 7.17 a) for a round conductor. In Figure 7.17 b) the DC current is equally distributed while in Figure 7.17 c) the area of the copper wire carries the current flow disproportionately. In this case the outer surface of the wire due to an increase in the inductive reactance of the system appears. By the Eq. 7.34 it is clear that an increase in frequency, results in a decrease in the skin depth. Table 7.16 shows the area of the cross sectional diameter of a round conductor for; a) DC current, b) Low Frequency AC Current, and c) High Frequency AC Current.



(a)



(b)




I



Figure 7.17 – Skin effect exemplification (a) depth (b) LF operation, (c) HF operation.

Table 7.14 – Skin depth versus available area of a round conductor for various frequencies

FREQUENCY	SKIN DEPTH (μM)	 <p>(a) DC Current   (b) LF AC-Current   (c) HF AC-Current</p>
60Hz	8470	
10KHz	660	
100KHz	210	
1 MHz	66	
10MHz	21	

The DC impedance of a round conductor is uniform and consists of a resistance per unit length given by Eq. 7.40.

$$R_0 = \frac{1}{\pi r_0^2 \sigma} \quad \text{Eq. 7.34}$$

The skin depth ( $\rho$ ) measures the distance for which an AC current can penetrate at the surface of the conductor. It depends of the permeability of the material  $\mu$ , the frequency of the signal  $f$ , and the conductivity of the material  $\sigma$ .

$\rho = \frac{1}{\sqrt{\pi f \mu \sigma}}$	Eq. 7.35
--	----------

Using Eq. 7.41 we can show that,

$\frac{R_s}{\sqrt{2}\pi r_0} = \frac{R_0 q}{2} \quad \text{where,} \quad R_s = \frac{1}{\sigma \rho} \quad \text{and,} \quad q = \frac{\sqrt{2} r_0}{\rho}$	Eq. 7.36
---	----------

Normally the factors in terms of  $R_0$  and  $q$  are more convenient to perform calculations. Also it is useful to plot normalised values in terms of  $R_0$  as is as shown in Figure 7.18 where the solid lines plotted show the values calculated from the equations above.

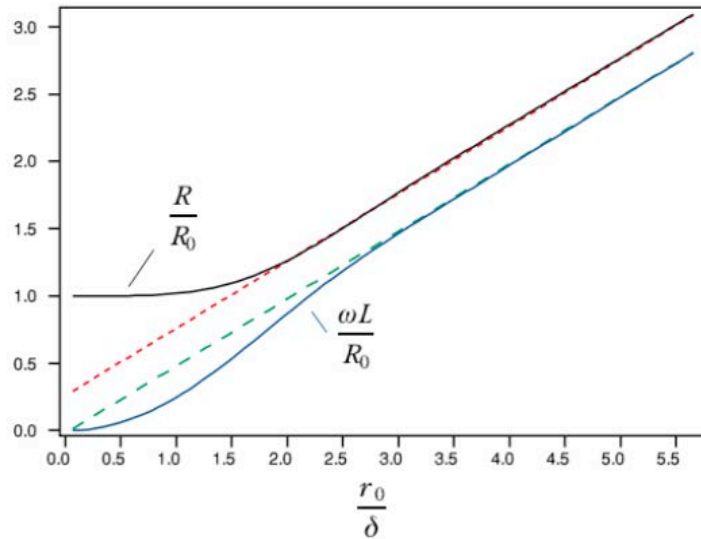


Figure 7.18 – Wire impedance versus skin depth.

### ➤ Minimization of the skin effect

In practice, a very common method to minimize the actions performed by the skin effect is using stranded wire i.e., a bundle of thin strands of conductors. Indeed this was the solution adopted in the construction of the transformers C and D. It was obtained significant improvements in the performance of these with respect to its predecessors (A and B) in which it was used simply a Solid core, i.e. just one strand of wire per conductor.

### 7.7.7. Electrical equivalent circuit

The electrical equivalent circuit of Figure 7.19 is used to obtain the parameters for each transformer. This is simplified circuit, which reflects the secondary impedance to the primary side considering that the mutual inductance  $L_m$  is much greater than the leakage inductance  $L_1$ . Since the impedance seen at the primary side  $Z_1 = Z_L/n^2$  ( $Z_L$  is the load impedance of the secondary). Then this approximation is valid since the current in  $L_m$  and  $R_m$  is very small as compare to  $I_1$ . The effect of the capacitances is also neglected.

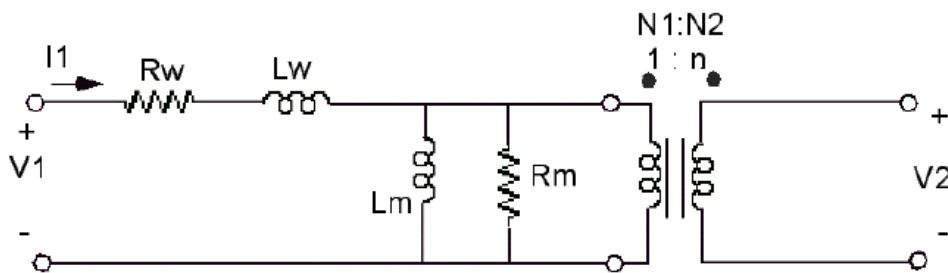


Figure 7.19 - Transformer equivalent circuit referred to the primary.

Considering that:

$R_1$  = primary winding resistance,

$R_2$  = secondary winding resistance

$R_w = R_1 + R_2/n^2 = R_1 + R'_2$

$L_1$  = primary leakage inductance,

$L_2$  = secondary leakage inductance

$L_w = L_1 + L_2/n^2 = L_1 + L'_2$

$n = N_2/N_1$  = Ratio of turns of primary and secondary windings

$R_m$  = core losses (hysteresis and eddy current losses)

$L_m$  = mutual inductance

The following relations are valid for this circuit, namely:

$$V'_2 = \left( \frac{N_1}{N_2} \right) V_2 \quad \text{Eq. 7.37}$$

$$I'_2 = \left( \frac{N_2}{N_1} \right) I_2 \quad \text{Eq. 7.38}$$

$$R'_2 = \left( \frac{N_1}{N_2} \right)^2 R_2 \quad \text{Eq. 7.39}$$

$$X'_2 = \left( \frac{N_1}{N_2} \right)^2 X_2 \quad \text{Eq. 7.40}$$

$$Z'_L = \left( \frac{N_2}{N_1} \right) Z_L \quad \text{Eq. 7.41}$$

### 7.7.8. Transformer parameters

In the short circuit test of Figure 7.20 the combined values of winding resistance ( $R_t = R_1 + R'_2$ ) and leakage inductances ( $L_t = L_1 + L'_2$ ) are evaluated. Then making a short circuit test in the secondary side, that is for  $R_{Load} = 0$  and feeding the primary side at the rated transformer current, the transformer parameters were measured and summary represented in Table 7.12 for different

frequency values. The open circuit test of Figure 7.20 enables to evaluate the magnetizing parameters, which are the magnetizing resistance (RM) and magnetizing inductance (LM). In this test, the secondary winding of the transformer is placed in open-circuit and the primary is supplied at normal voltage and frequency. Alternatively the secondary winding could be supplied and in turn the primary winding is placed in open-circuit. The parameters RM and LM were measured and are summary presented in Table 7.12 below.

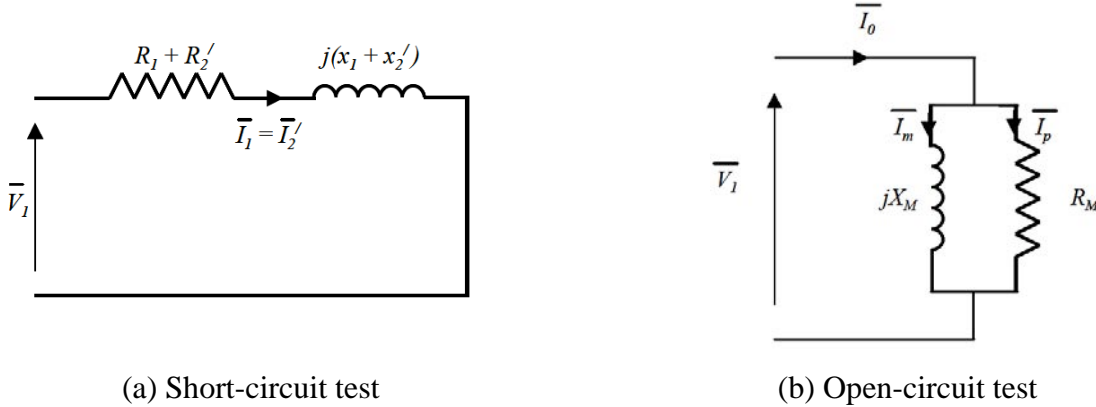


Figure 7.20- Schemes of test transformer.

### 7.7.9. Selection of the transformer

Observing the Table 7.15 below the following conclusions can be made which leads to the selection of the transformer best suited to the application.

- The winding resistance  $R_t$  and leakage inductance  $L_t$  are considerably lower for the transformers whose windings are stranded, i.e., C and D.
- The resistance value  $R_t$  varies according to the frequency operation, checking the skin effect value which is in accordance with **Figure 7.18** above, i.e. if the frequency of operation increase, the value of  $R_t$  also increases.
- The inductance value  $L_t$  practically does not vary with the frequency of operation
- The magnetizing resistance (RM) and magnetizing inductance (LM) have high values, as expected.
- Finally, the good characteristics of transformer D, including the physical ones, i.e. low values for  $R_t$  and  $L_t$  and also of dimensions and weight, this is used to make the final tests presented in the thesis.

Table 7.15–Parameters of each HF transformer implemented experimentally.

	N1	N2	n	Ferrite type Vs Size	Rt=R1+R'1		Lt=L1+L'2		RM	LM
					1KHz	33KHz	1KHz	33KHz		
A (Unifilar)	4	46	12	UI ferrites Medium	0.22	7.39	1.18E-05	1.18E-05	42	5.49E-03
B (with tape)	4	13	3.25	UU ferrites Big	0.18	5.96	9.70E-06	9.70E-06	146.2	6.84E-04
C (Stranded)	4	18	4.5	UI ferrites Medium	0.04	1.44	6.09E-06	6.09E-06	286.2	9.29E-04
D (Stranded)	2	20	10	EE ferrites Small	0.03	0.18	2.10E-06	2.10E-06	286.2	9.29E-04

## 7.8. Design and implementation of the control circuits

As explained above, the strategy of control adopted includes two loops of control. The fast loop, that keeps the output voltage ( $V_{out}$ ) at a constant value and a slow loop, which keeps the PEM to work under optimal conditions, ie, with minimum consumption of hydrogen and high efficiency for a request made by a specific load. Thus, the control to implement that meets these two objectives is presented in Figure 7.21 and

Figure 7.22. According to the same, it has been made the design, development and implementation of several board circuits including:

1. The voltage control oscillator board: this board measures the error, implements the PI controller and the voltage control oscillator signals.
2. The frequency divider board: this board divides the frequency of the oscillator into two equal parts and prepare them for later "needle" for the respective IGBTs. This board also serves to implement the controller of the PEM.
3. Drive circuits– it was necessary to implement two drive boards for sending signals to the IGBTs properly.
4. Voltage sensor – this board measures the output voltage of the converter giving this information to the controller.

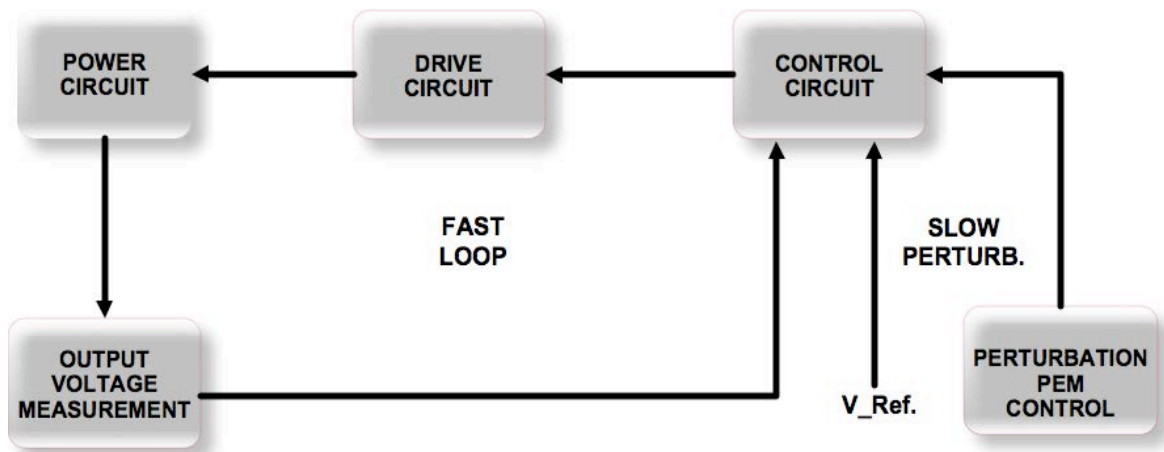


Figure 7.21 - Modular scheme of the main blocks of control.

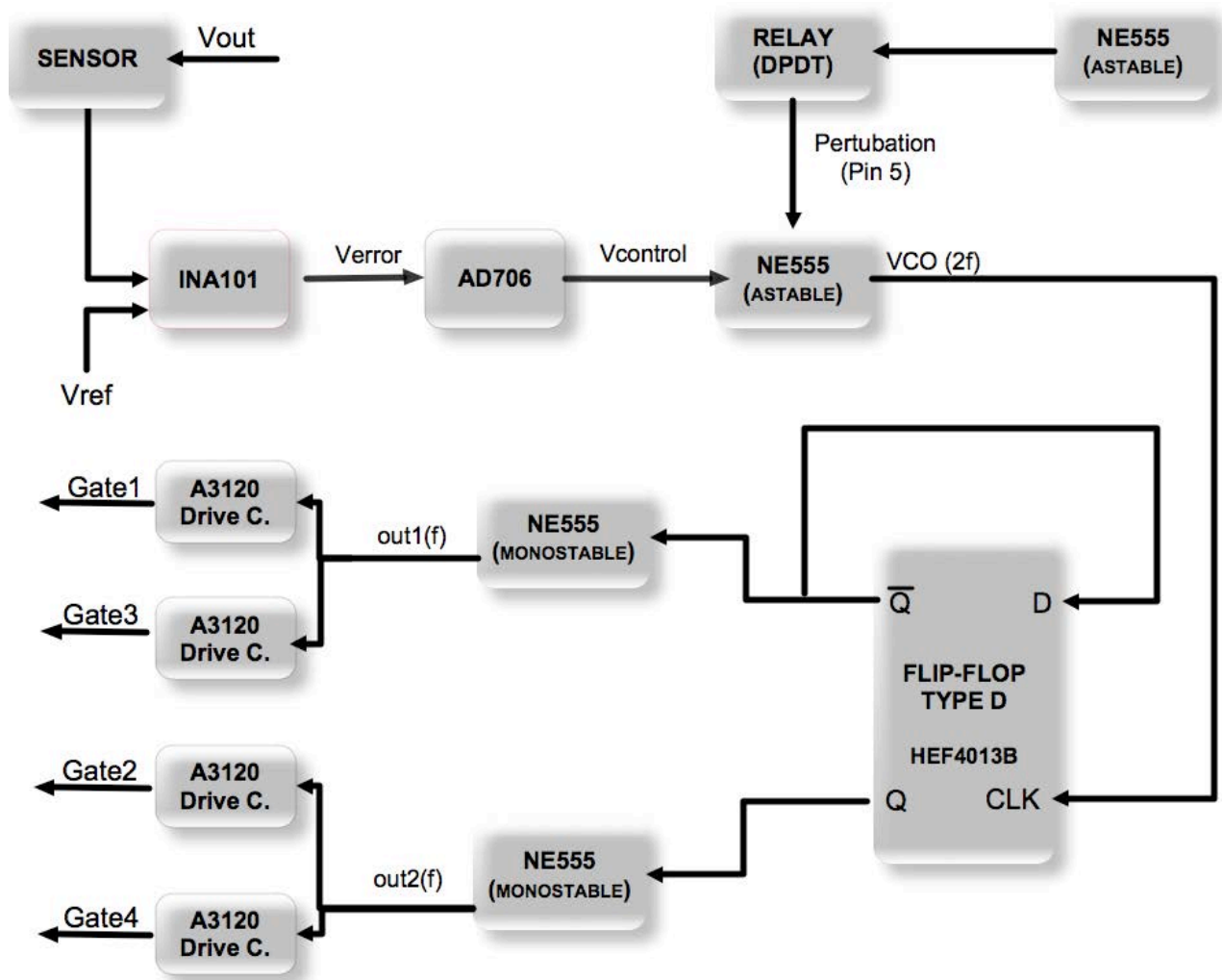


Figure 7.22 – Modular scheme with the device names.

### 7.8.1. The voltage control oscillator

The voltage control oscillator board consists to generate the VCO signal as is shown in Figure 7.23. This step includes the elements of error processing, which is made by the INA101, the PI controller, which is made with the AD706, and the NE555 that generates an oscillating signal of frequency  $2f$ .

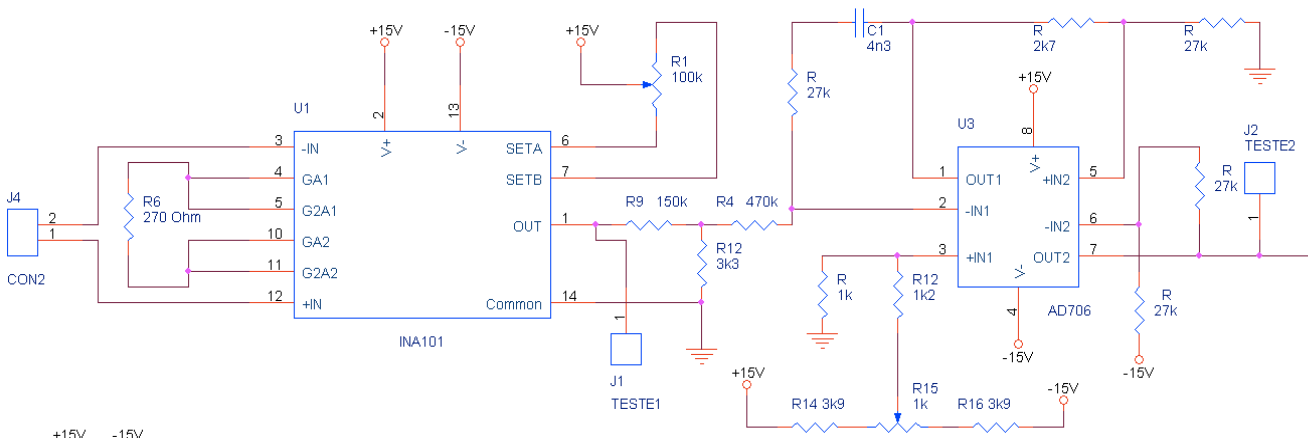


Figure 7.23 – Orcad scheme of voltage control oscillator.

### ➤ Error of output voltage

The measurement of the error of the output voltage (VError) is through the INA101 component, which is a high accuracy instrumentation amplifier. This component is also used to make the proportional gain (P) of the controller.

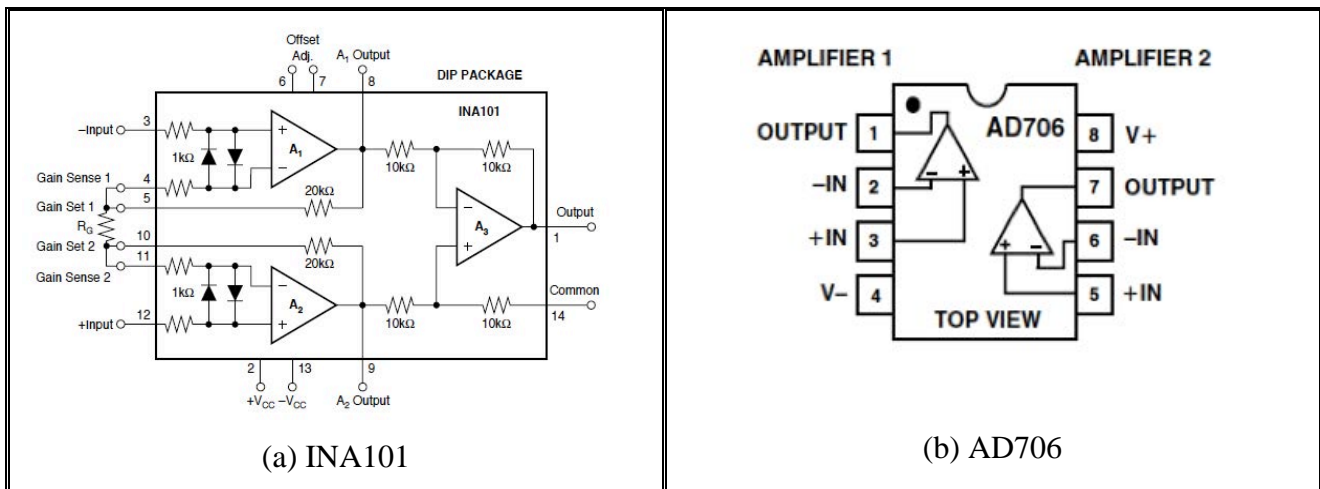


Figure 7.24 - Internal schemes of INA101 and AD706.

### ➤ INA101 circuit

The INA101 is a high accuracy instrumentation amplifier designed for low-level signal amplification and general-purpose data acquisition. Three precision op-amps and laser-trimmed metal film resistors are integrated on this monolithic integrated circuit. It is a Plastic DIP 14-Pin which works at temperature range 0°C to +70°C.



The INA101 is used to give the proportional gain of the controller. Figure 7.24(a) shows the internal connections of INA101 for the DIP package. The (-) input signal is PIN3, which corresponds to the reference signal (Vref). The (+) signal PIN12 is used as the input of the output voltage measured, that is, the error of voltage is,  $\varepsilon = V_{\text{measured}} - V_{\text{reference}}$ .

#### ➤ Reference voltage of INA101

The schematic of Figure 7.25 is used to generate the reference voltage signal (Vref) to INA101. The voltage applied to pin 3 terminal of INA101 allows getting high sensibility with this option.

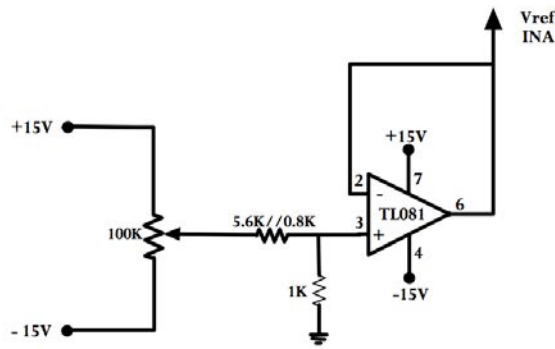


Figure 7.25 - Reference voltage signal (Vref) to INA101

#### ➤ Proportional gain of the controller

Several component parts produce the proportional gain of the controller namely: a part of the gain is given by connecting a single external resistor,  $R_G$ , which sets the gain of the INA101. For the case, the resistor  $R_G = 270\Omega$  is selected for a gain of the INA,  $G=100$ , according to the manufacturer's datasheet. The  $40k\Omega$  term in equation corresponds to the sum of the two internal feedback resistors. This is performed by resistor  $R_6$  in the scheme of Figure 7.23 above.

$$G = 1 + \frac{40k\Omega}{R_G} \Rightarrow G = \frac{R_G + 40k\Omega}{R_G} = 100 \Rightarrow R_G = 270\Omega \quad \text{Eq. 7.42}$$

Another path of the proportional gain is given by the values of  $R_9$  and  $R_4$ , which allow at adjusting precisely the required gain. Thus after some adjustments, the value of these resistors is, it was necessary to lower the value of these resistors to,  $R_4=470k\Omega//4.7k\Omega$  and  $R_9=150k\Omega//3.3k\Omega$ .

### ➤ Offset adjustment of INA101

The offset in the output-voltage is adjusted by connecting a potentiometer (R1) between PIN6 and PIN7 and is used to null the offset voltage in high gain ( $G \geq 100$ ) with both inputs connected to ground. In order to get a larger gain in the output signal of the INA, the output-offset voltage was adjusted with the optional schematic circuit connected to the Common pin as shown in Figure 7.26. The voltage applied to Common terminal is summed with the output. Low impedance must be maintained at this node to assure good common-mode rejection. The op-amp connected as a buffer provides low impedance. The signal VCOM has approximately  $\pm 15\text{mV}$  of range. In this case, the output signal of INA is given by equation Eq. 7.43

$$V_0 = G(V_{out_{med}} + V_{ref}) + V_{COM} \quad \text{Eq. 7.43}$$

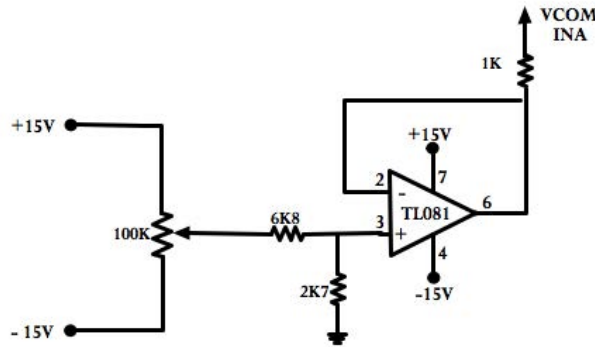


Figure 7.26 - Output-offset voltage.

### ➤ Integral gain of the controller and voltage follower using the AD706 device

The AD706 device is a dual, low power, bipolar amp-op that has the low input bias current ( $I_B$ ) of a JFET amplifier, but which offers a significantly lower  $I_B$  drift over temperature. The top view of this analogue device and its internal diagram is represented in Figure 7.24 (b).

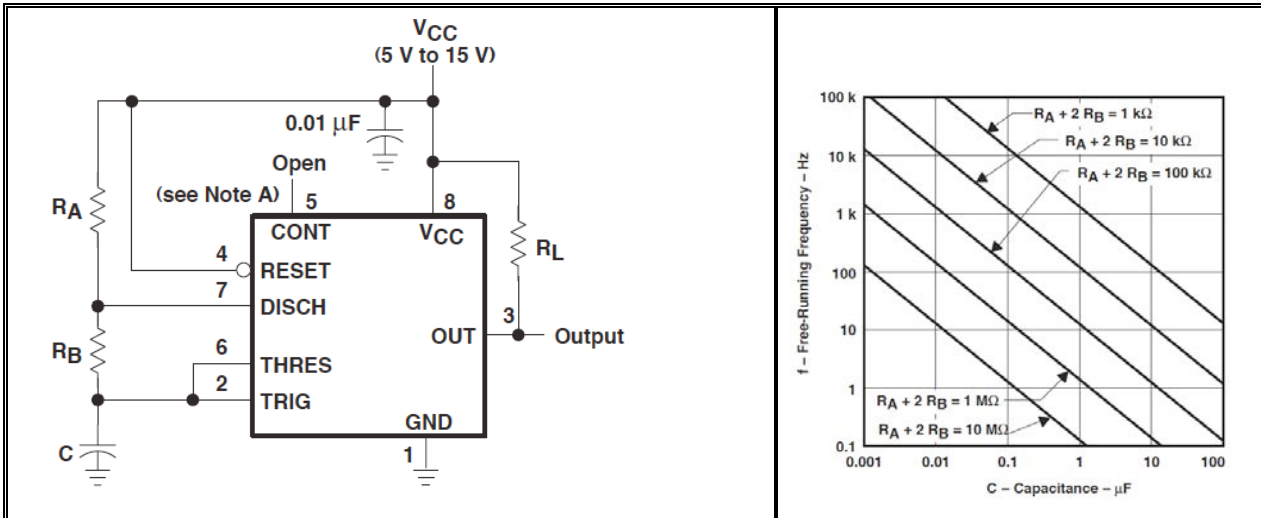
The Amplifier 1 (pins 1 to 3) is part of the integral PI controller. Once known the value of the process variable (the output signal of INA101), the error is minimized. Then with resistor R4 and capacitor C1 the integral part of the controller is made. Resistors R14, R15 and R16 introduce a necessary offset in the reference. In this stage, it is necessary to isolate the signal source by connecting it to a voltage follower to the next stage. The Amplifier 2 of AD706 (pins 5 to 7) performs the voltage follower or buffer. It provides a high-impedance in the input, low-impedance in the output and unity gain.

➤ **Oscillator made by the NE555 operating in astable mode**

The NE555 is a stable 8-pin device very popular and useful precision timing that can act as either a simple timer to generate single pulses or long time delays, or as a relaxation oscillator producing stabilized waveforms of varying duty cycles from 50 to 100%. It can be operated either as Astable, Monostable, or Bistable mode. A simplified "block diagram" representing the internal circuitry of the NE555 is given in Figure 7.27 below.

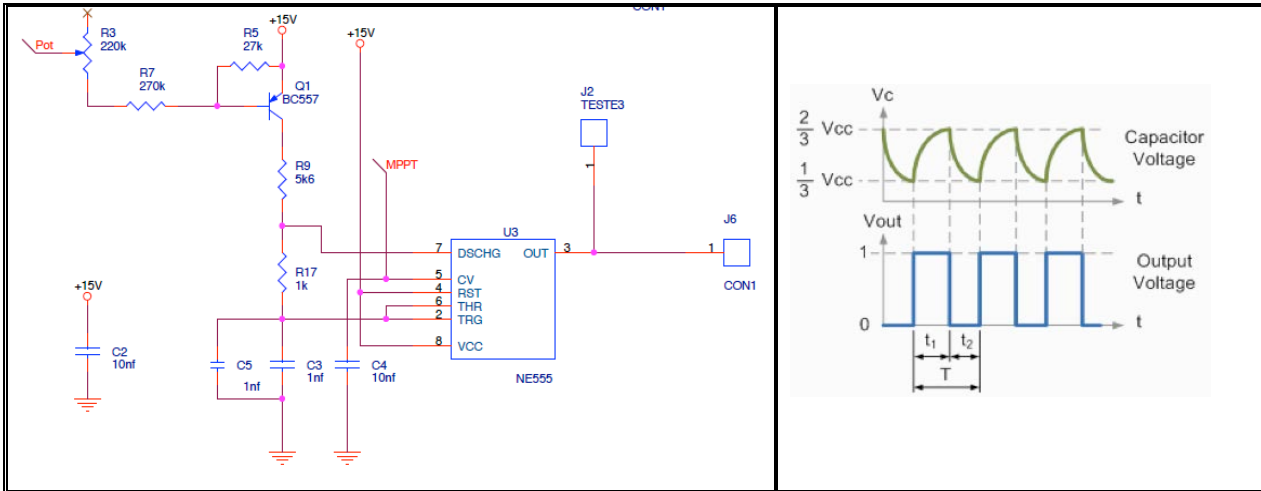


151



(a) NE555 in astable operation

(b) Resistor values selection



(c) Design implementation

(d) Operation waveforms

Figure 7.28 - Schematic of the NE555 in astable operation.

The schematic of Figure 7.28 (c) shows how this topology allows to control the value of resistor  $R_A$  that is  $R_A = V_{CE}(Q_2)/I_c + 5K6$  and  $I_c = h_{fe} \cdot I_B$ , being that  $I_B$  is controlled by resistors  $R_5$  and  $R_{10}$ , which adjust the base current of transistor  $Q_2$ .

In astable mode, the capacitor  $C_3//C_5=2nF$  (pin 6) is charging and discharging between the threshold-voltage level ( $\approx 2/3V_{CC}$ ) and the trigger-voltage level ( $\approx 1/3V_{CC}$ ), which are independent of the supply voltage. The period of operation is  $T=t_1+t_2$  as can be seen in Figure 7.28 (d). Then in these conditions frequency is;

$$f_{osc} = \frac{1.44}{(R_A + 2R_B) \times C} \quad \text{Eq. 7.44}$$

Thus, the oscillated frequency experimentally measured is for the case 66 kHz.

The capacitor C4=10nF (pin 5) is used in the case of a missing pulse or abnormally long spacing between consecutive pulses in a train of pulses. It safeguards for example the situation of low operating frequency of the converter with long intervals pulses spaced. Capacitor C2=10nF allows removing any ripple coming from the source. The output signal (pin 3) of the NE555 is adjusted between 0 and 1 whose frequency ranges from the  $f_{min}$  and  $f_{max}$  as a function of the signal input (pin 2).

### 7.8.2. The frequency divider

The 4013B device is a D-type flip-flop, which processes the frequency divider as is shown in Figure 7.29. The inverted output terminal is connected directly back to the data input terminal D giving the device "feedback" as shown in schematic of Figure 7.29 (a). By "feeding back" the output from  $\bar{Q}$  to the input terminal D, the output pulses at Q have a frequency that are exactly one half ( $f/2$ ) that of the input clock frequency, as can be seen from the frequency waveforms of Figure 7.29 (b) below. Thus, for the oscillation frequency of 66 kHz (measured), each output branch ( $Q$ -pin1 and  $\bar{Q}$ -pin2) attacks (triggers) the NE555 as timer with the frequency 33 kHz.

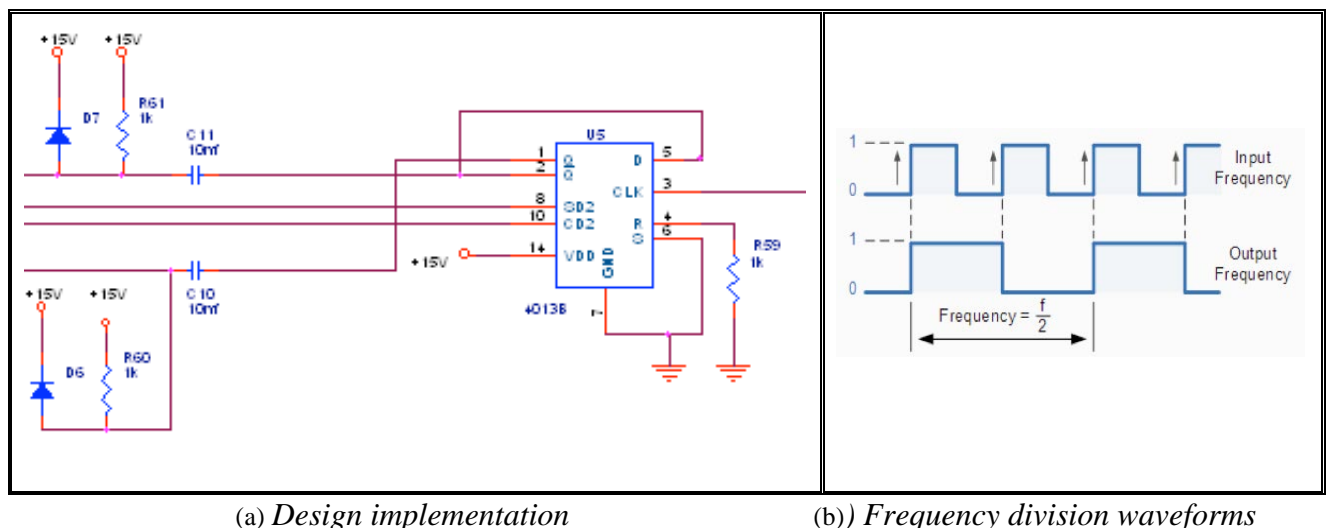


Figure 7.29 - Schematic of the HEF4013B.

The capacitors C10 and C11 are used to decoupling the signals to be sent to NE555. Diodes D6 and D7 and resistance R60 and R61 are used to protect the NE555. In turn, each output of the NE555

(pin 3) corresponds to the signal to be sending to two IGBT gates, 1 & 3 (OUT1) or 2 & 4 (OUT2), as exemplified schematically in Figure 7.29.

### ➤ NE555 in monostable operation

Monostable operation is initiated when TRIG voltage (pin2) falls below the trigger threshold ( $\approx 1/3 \times V_{CC}$ ). Once initiated, the sequence ends only if TRIG is high at the end of the timing interval ( $\approx 2/3 \times V_{CC}$ ). Because of the threshold level and saturation voltage of Q1, the output pulse duration is approximately  $t = 1.1RAC$  as can be seen in the waveforms of Figure 7.30 (d). The timer operating in the monostable repeats the process, with output pulse duration approximately  $13\mu s$  in the output of NE555 (pin 3). i.e.,  $t = 1.1 \times (5.6 \times 10^3 \times 2 \times 10^{-9}) = 12.32 \times 10^{-6}$  ;  $13\mu s$ .

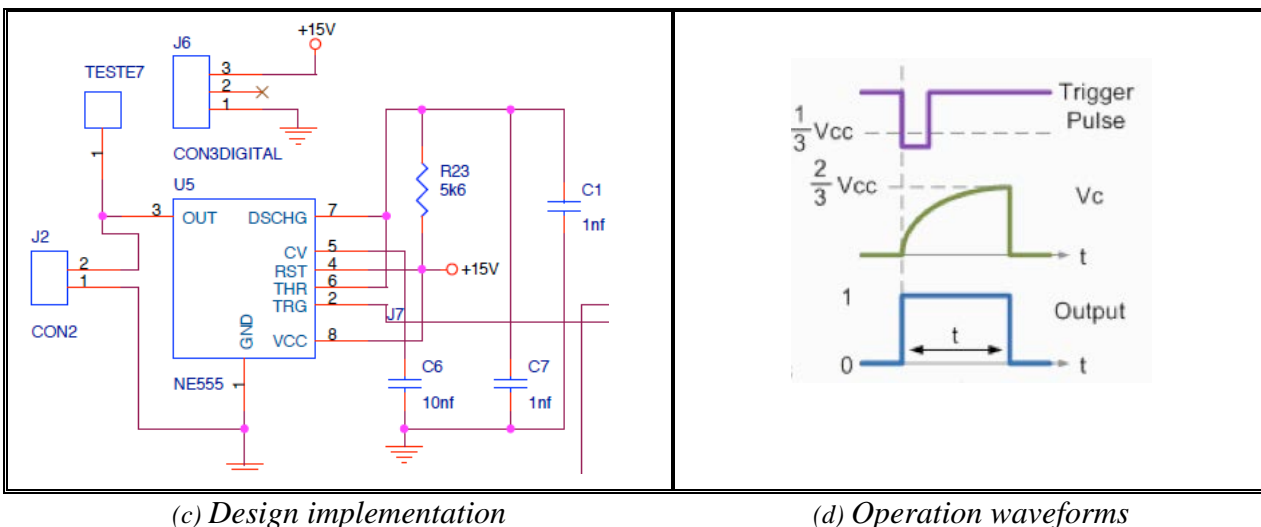
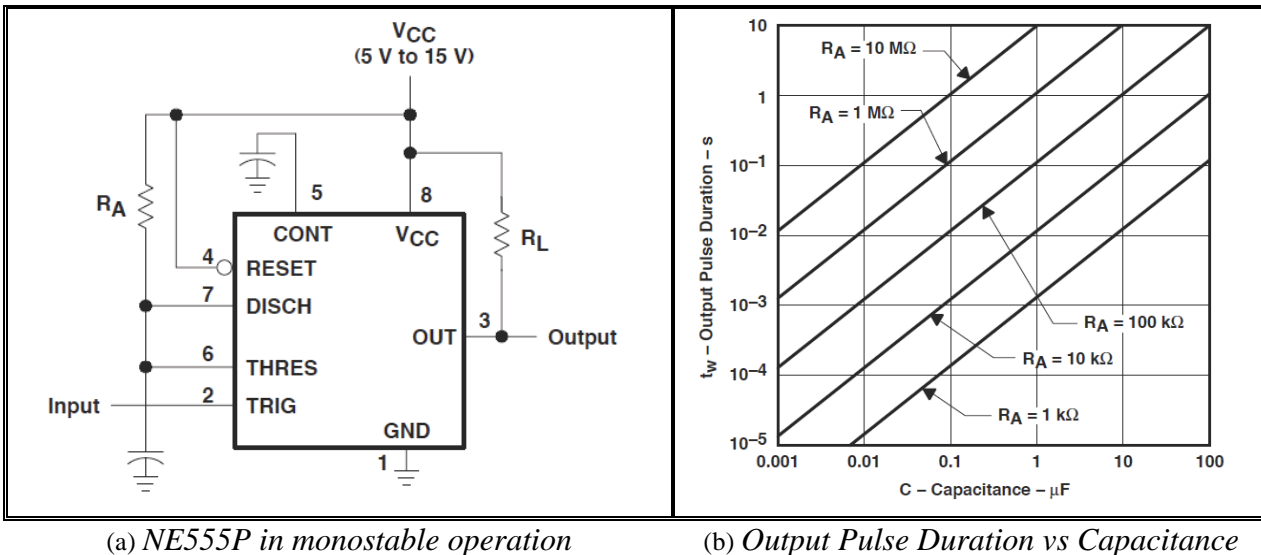


Figure 7.30 - Schematic of the NE555 in monostable operation.

### 7.8.3. Test and validation of the voltage control circuit

To ensure the correct functionality of the system, the board that performs the voltage control oscillator which is represented in Figure 7.31 is validated. The most important signals were measured and adjusted to meet the objectives.

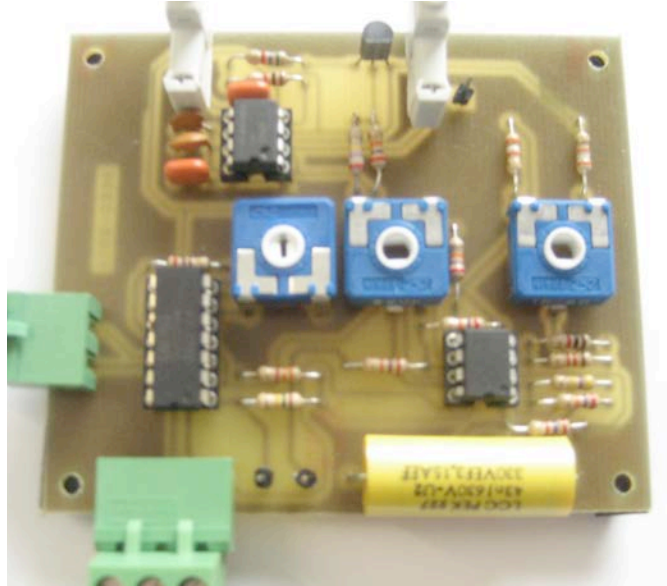
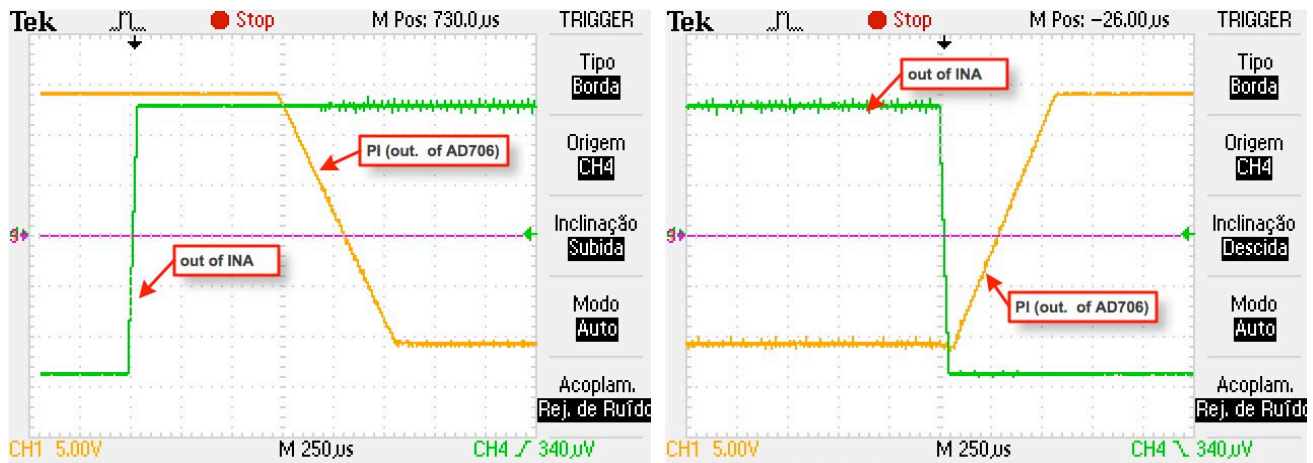


Figure 7.31 – Layout of the voltage control oscillator circuit.

The error validation is represented in Figure 7.32. This error is minimized by the action of the PI controller, represented in Figure 7.33. The frequency of the oscillator depends of the voltage control oscillator signal (VCO) and of the charge and discharge of the two parallel capacitors connected to pin6. As is shown in Figure 7.33 if  $PI > 0$  there is no oscillation while if  $PI < 0$  the oscillation appears. A very important point is to define accurately the value of the oscillating frequency as is represented in detail in Figure 7.34. During a period of oscillation the capacitor charges and discharges between the threshold-voltage level that is  $\approx 2/3 \times V_{CC}$  and the trigger-voltage level  $\approx 1/3 \times V_{CC}$  which value is applied to pin6. The frequency is divided by the flip-flop 4013B, as presented in Figure 7.35. Each output branch of the flip-flop that is  $Q$  and  $\bar{Q}$  triggers the NE555 as timer with a period of oscillation  $\approx 6 \times 5 \mu s = 30 \mu s$  and frequency of 33 kHz for each case.

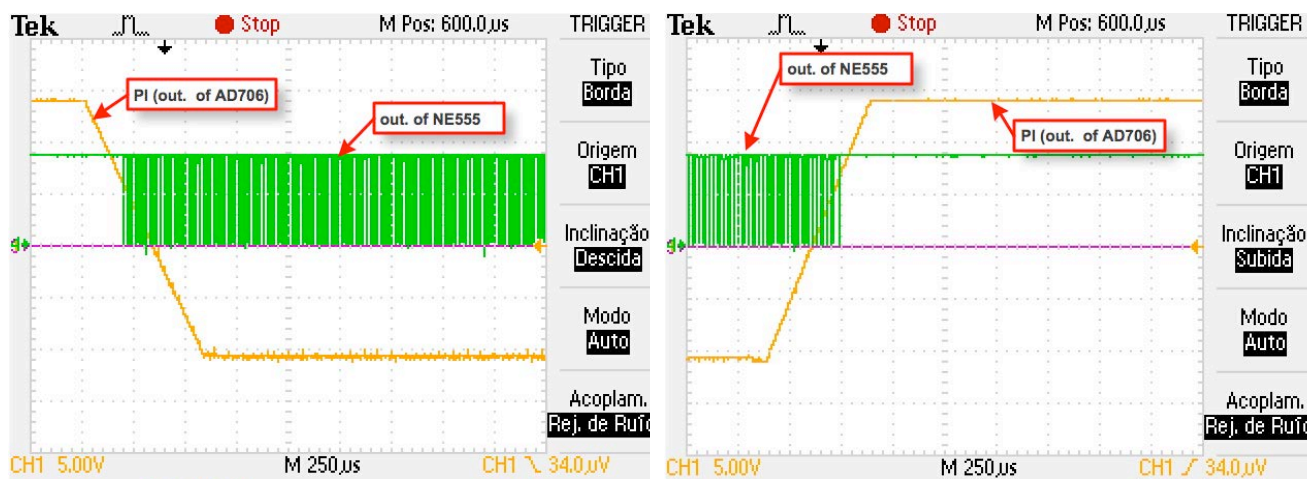




a) With the increase in the error

b) With the decrease in the error

Figure 7.32 –Response of PI to the error signal produced in INA.



a) With the reduction of PI

b) With the increase of PI

Figure 7.33 – Oscillator response to the PI controller signal produced in AD706.

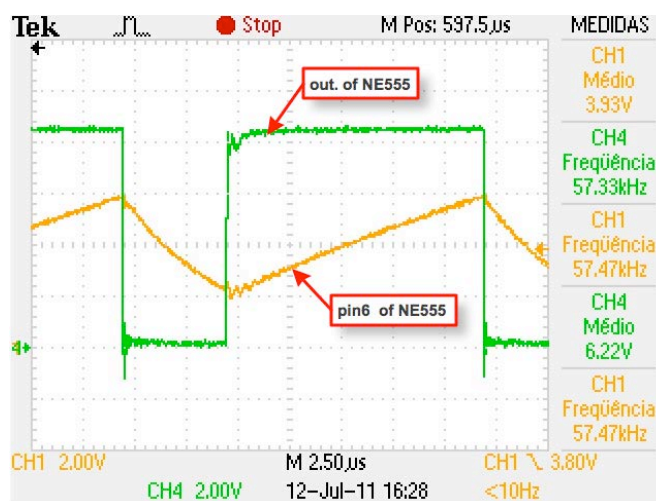


Figure 7.34 –Period of oscillation showing the charge and discharge of the capacitors at pin6.



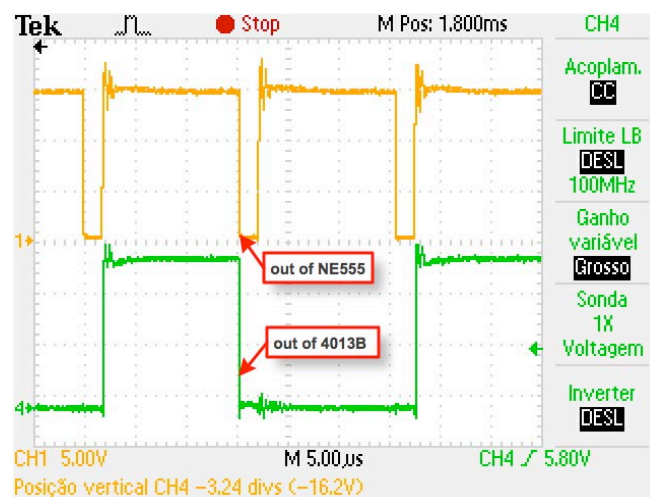


Figure 7.35 – Frequency divider performed by the 4013B device.

## 7.9. Design of the drive circuits

One of the important features of any switching device is its switching characteristic (turn-on and turn-off states), since significant power losses are incurred during these switching states. The drive circuit acts as an interface between the control circuit and the power circuit, the isolation between the high voltage and the low voltage devices is also required. The optocoupler HCPL-3120 satisfies these two criterions' then it is the solution adopted for the case. Corresponding scheme and specifications are represented in the Table 7.16 below.

Table 7.16 – Specifications of the gate drive circuitry HCPL-3120.

IGBT/MOSFET Driver	Specifications
	<ul style="list-style-type: none"> <li>• “Low” Peak Output Current <math>I_{OLPEAK}=2.5\text{ A}</math></li> <li>• “High” Peak Output Current <math>I_{OHPEAK}=2.5\text{ A}</math></li> <li>• Average Input Current <math>I_{FAVG}=25\text{ mA}</math></li> <li>• Power Supply Voltage <math>(V_{CC} - V_{EE}) = 15\text{ to }30\text{ V}</math></li> <li>• Maximum Low Level Output Voltage <math>V_{OL}=0.5\text{ V}</math></li> <li>• Output power dissipation <math>P_{Diss}=45\text{ mW}</math></li> </ul>

The conditions of operation recommended for the HCPL-3120 device should be respected. The parameters provided by the manufacturer are shown in the Table 7.17 below.

Table 7.17 – Recommended operation conditions of the IGBT/Mosfet driver HCPL-3120.

Parameter		Symbol	Min.	Max.	Units
Power Supply Voltage		(V <sub>CC</sub> - V <sub>EE</sub> )	15	30	Volts
Input Current (ON)	HCPL-3120	I <sub>F(ON)</sub>	7	16	mA
	HCPL-J312				
	HCNW3120		10		
Input Voltage (OFF)		V <sub>F(OFF)</sub>	-3.0	0.8	V
Operating Temperature		T <sub>A</sub>	-40	100	°C

Referring to Table, the voltage and current supplied by this optocoupler makes it ideally suited for directly driving IGBTs with ratings up to 1200V/100A that is, for  $I_{F_{ON}} = 16mA$ ,  $V_{F_{OFF}} = 0.8V$  and  $V_{CC} = 15V$ , a resistor must be placed in series with the diode in low voltage side (pins 2 & 3) such as:

$$\frac{15V - 1.8}{R'} = 16mA \quad \rightarrow \quad R' = \frac{15V - 1.8V}{16 \times 10^{-3}} = 825\Omega \quad R' \cong 1K\Omega(13.2mA_{max}) \quad \text{Eq. 7.45}$$

### 7.9.1. Requirements and protection of the gates

The requirement of the gate drive of the optocoupler is to supply the Minimum Output Current ( $I_{OL}$ ) needed to switch the IGBT to the low-impedance state. A common method to select the optocoupler is looking at its Maximum Peak Output Currents in the Absolute Maximum Rating in the data sheet  $I_{OH(PEAK)}/I_{OL(PEAK)}$ . To determine the suitability of a gate drive optocoupler, it is also necessary to look at the Minimum Output Currents ( $I_{OH} / I_{OL}$ ) of the gate drive optocoupler in the specifications of the data sheet. This Minimum Output Current ( $I_{OL}$ ) that is required for switching the IGBT to the low-impedance state can be easily calculated using the gate capacitance charging equations  $I_{G1}$  and  $I_{G2}$  represented in Table 7.18.

Table 7.18 – IGBT parasitic capacitances.

IGBT Parasitic Capacitances $C_{ge}$ and $C_{gc}$		
$I_{G1} = \frac{V_B \times C_{GC}}{t_{SW}}$ $I_{G2} = \frac{V_{C(GE)} \times C_{GE}}{t_{SW}}$		<p>Where,</p> <p><math>C_{GC}</math> - gate-to-collector capacitor</p> <p><math>C_{GE}</math> - gate-to-emitter capacitor</p> <p><math>V_{C(GE)}</math> - Voltage across gate-to-emitter</p> <p><math>I_G</math> - total gate current flows into gate</p> <p><math>I_{G1}</math> - gate current flows into <math>C_{gc}</math></p> <p><math>I_{G2}</math> - gate current flows into <math>C_{ge}</math></p> <p><math>V_B</math> - bus voltage</p> <p><math>t_{sw}</math> - switching time</p>

Considering the requirements of each IGBT, such as;  $V_{out}=15V$  and  $I_{out}=1.5A$  and the specifications of the HCPL-3120 driver, a resistor  $R_G$ , must be placed in the gate of the IGBTs such that the maximum peak output current rating,  $I_{OL(PEAK)}$  is not exceeded. Then using Eq. 7.46, a resistor of  $10\Omega$  is selected, that is:

$$R_G \geq \frac{(V_{CC} - V_{EE}) - V_{OL}}{I_{OLPEAK}} = \frac{15 - 0.5}{2.5} \geq 5.8\Omega \Rightarrow R_G = 10\Omega \quad \text{Eq. 7.46}$$

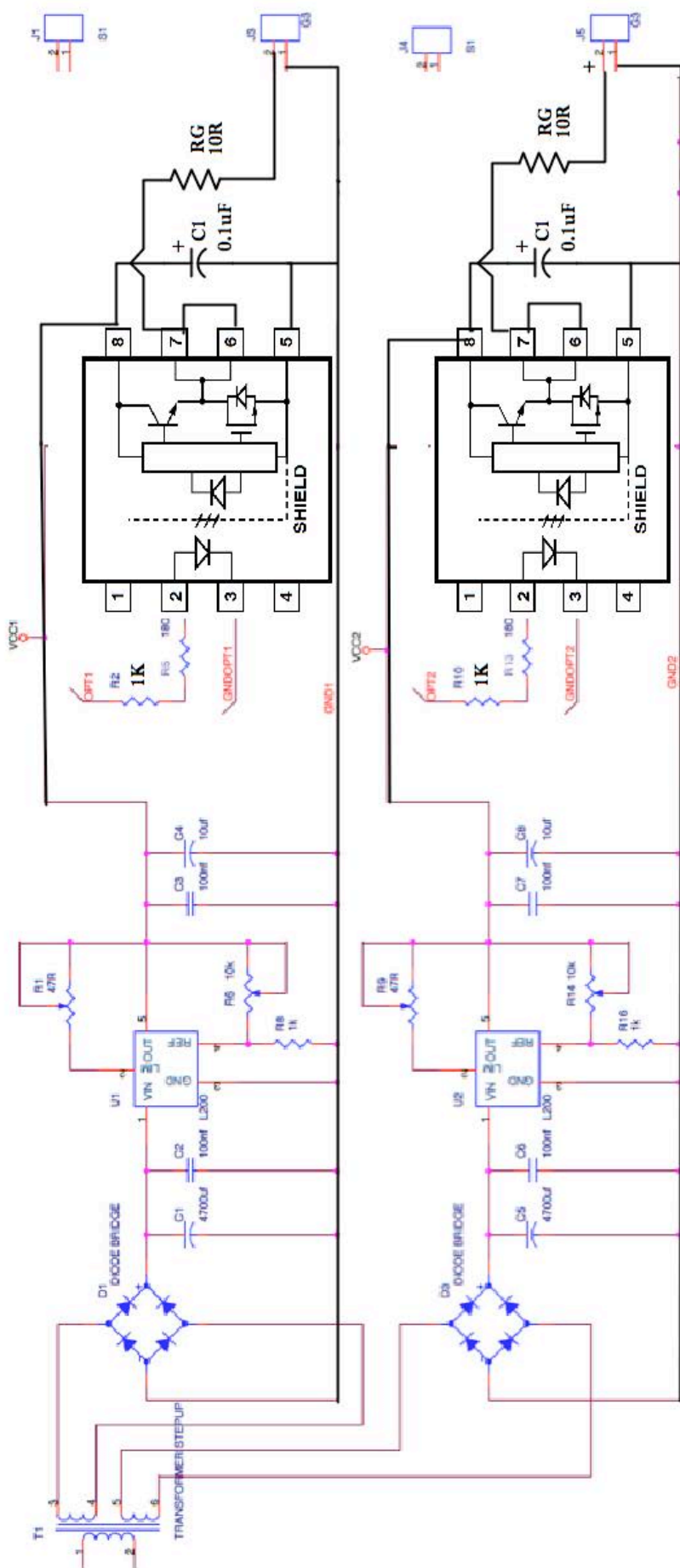


Figure 7.36 - Schematic of the driver circuits for the IGBTs 2 and 4.

### 7.9.2. Test and validation of the gate drive signals

The board used to drive the IGBTs 2 and 4 is shown in Figure 7.37. A similar one is used for the IGBTs 1 and 3. Before being sent to the gates the output signals of the boards are validated. The signals sent to the IGBTs 1 and 3 are always in opposition to the signals sent to IGBTs 2 and 4 that is they can never conduct simultaneously. A dead time between the impulses sent to the same branch of the inverter bridge must also be ensured. As shown in Figure 7.38. The dead time has been assured with the value of  $4\mu\text{s}$ .

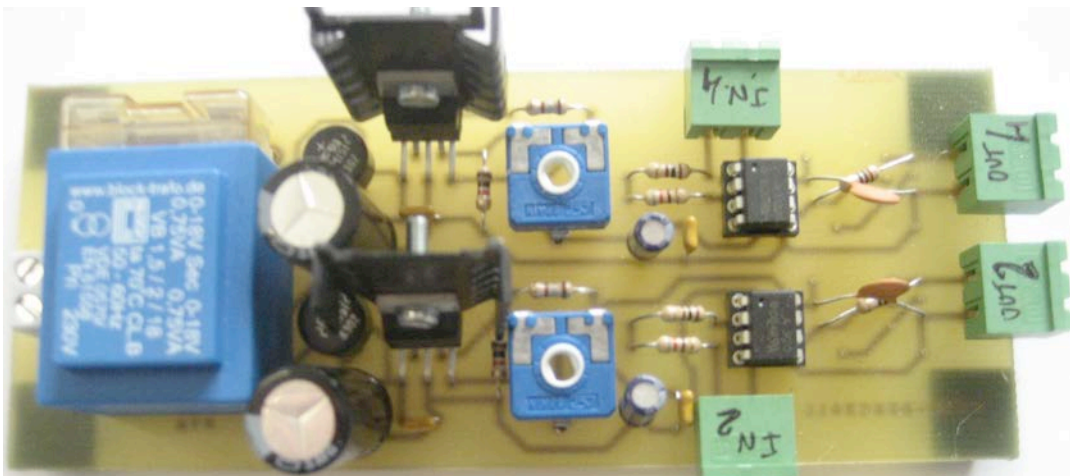


Figure 7.37 - Layout of the drive circuits for IGBT2 and IGBT4.

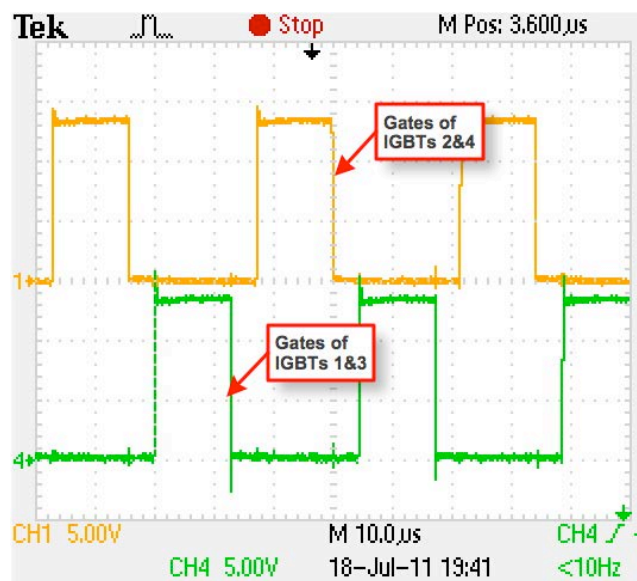


Figure 7.38 – Gate driver circuits of the IGBTs.

The analysis done for each IGBT of the full bridge is summarized in the Table 7.19. As can be observed there are minor variations between the values achieved for the four IGBTs, which ensure the correct operation of the converter, that is,  $T_{on}=12.8\mu s$ ,  $T_{off}=21.59\mu s$ ,  $T=34\mu s$  and  $f=29kHz$ , the amplitude is 12.8V for the IGBTs 1, 2 and 4 and 13.0V for the IGBT 3.

Table 7.19 - Summary of the gate signal for each igt.

IGBT 1	IGBT 2	IGBT 3	IGBT 4
CH1 Máx 12.8V	CH1 Máx 12.8V	CH1 Máx 13.0V	CH1 Máx 12.8V
CH1 Frequência 29.13kHz	CH1 Frequência 28.25kHz	CH1 Frequência 29.09kHz	CH1 Frequência 29.09kHz
CH1 Larg. Pos 12.80 $\mu s$	CH1 Larg. Pos 12.98 $\mu s$	CH1 Larg. Pos 12.74 $\mu s$	CH1 Larg. Pos 12.98 $\mu s$
CH1 Larg. Neg 21.53 $\mu s$	CH1 Larg. Neg 22.42 $\mu s$	CH1 Larg. Neg 21.64 $\mu s$	CH1 Larg. Neg 21.39 $\mu s$
CH1 Período 34.33 $\mu s$	CH1 Período 35.40 $\mu s$	CH1 Período 34.37 $\mu s$	CH1 Período 34.37 $\mu s$

## 7.10. Design of the PEM controller

The optimal operating point of the PEM whose principle has already been discussed in sections 2.3 and 6.1.5 is experimentally implemented in this section. The schematic of Figure 7.39 performs the principle and the components involved while in Figure 7.40 is represented the correspondent orcad implementation. As can be seen in Figure 7.39, the ON time of the PEM oscillator should be at least 10sec ( $\Delta t \geq 5 \times \tau_{PEM}$ ). Consequently, the selection of  $R_A$ ,  $R_B$  and C values should ensure this condition. The operation point of the PEM can be controlled actuating on the pin5 of the converter oscillator repeatedly and automatically while the optimum point of the PEM is not reached. This action is done by the two parallel resistances placed in parallel,  $R/R' = 2.5K\Omega$ . Decreasing the resistance that is applied to pin5 its voltage increases and consequently the frequency of oscillation decreases. According to the availabilities of the stock in the lab and condition required, the



components selected are  $R_A=1K\Omega$ ,  $R_B=330K\Omega$ , and  $C=47\mu F$ . For the case the values for  $T_{on}$ ,  $T_{off}$  and oscillating frequency are given by:

$$t_{ON} ; 0.7 \times (R_A + R_B) \times C ; 0.7 \times (1 + 330) \times 10^3 \times 47 \times 10^{-6} = 10.88ms \quad \text{Eq. 7.47}$$

$$t_{OFF} ; 0.7 \times (R_B) \times C ; 0.7 \times (330) \times 10^3 \times 47 \times 10^{-6} = 10.85ms \quad \text{Eq. 7.48}$$

$$f_{osc} = \frac{1.44}{(R_A + 2R_B) \times C} = \frac{1.44}{(1 + 2 \times 330) \times 10^3 \times 47 \times 10^{-6}} = \frac{1.44}{31.067} = 0.000046 (\ll 1Hz) \quad \text{Eq. 7.49}$$

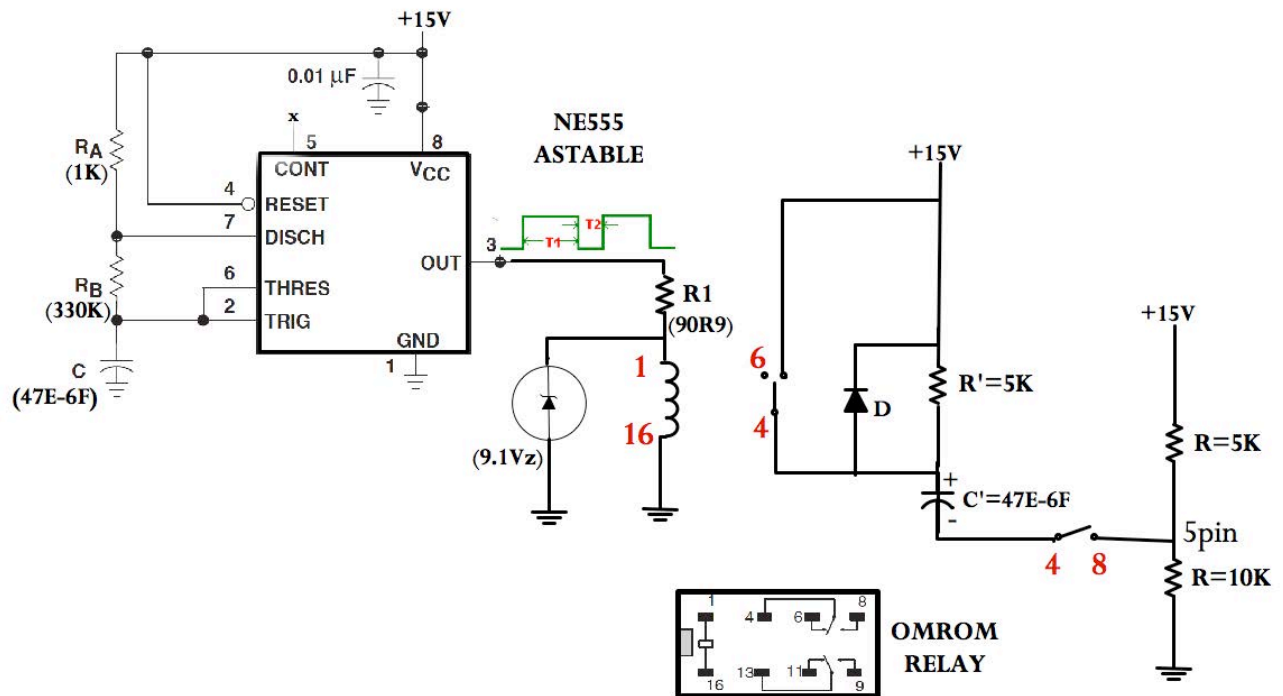


Figure 7.39 - Principle of operation and components involved controlling the PEM.

The specifications of the OMROM Relay are described in Table 7.20. The analysis of the PEM control circuit can be made in two parts namely:

### 7.10.1. Actions during $T_{ON}$

During  $T_{ON}$  as can be seen in Figure 7.39 above, the inductance of the relay (pins 1 and 16) is crossed by a current, which opens the switch 4&6, which is NC, and closes the switch 4&8, which is NO. Accordingly, the capacitor  $C'$  starts charging from the voltage source +15V through  $R'$  to a maximum value  $V_C = V_{Cf} = +15V$  which is reached when the current becomes zero, with a time


constant,  $\tau = R'C'$ . This is the time interval during which the perturbation of the pin5 of the NE555 is performed with  $V_{CO} = (2/3V_{cc} + \Delta V)$  that is  $V_{CO} > 2/3V_{cc}$ .

### 7.10.2. Actions during $T_{OFF}$

During  $T_{OFF}$  any current does not cover the inductance of the relay. The switch 4&6, which is NC, remains in this state. The same state remains also for the switch 4&8. Accordingly, the capacitor  $C'$  which has however its maximum charge,  $V_{Cf}$  puts the diode  $D$  in conduction and through its and the switch 4&6 establish a closed circuit allowing fast discharge of the capacitor  $C'$ . During this interval no signal is applied to pin 5 of the NE555 and the discharge of  $C'$  with as a time constant  $\tau = r_F C'$  (because the  $r_F$  of the diode is very small  $\Rightarrow \tau < 1\text{sec}$ ) that is the discharge of the capacitor occurs very quickly with the energy transferred from  $C'$  to the Diode.

There is still an important note to refer on this matter, if the PEM is already operating at the optimum, the application of the perturbation to the controller leads it to "take care of the process" but the ending point may be the same as starting point if this is indeed the optimum point for the conditions required by the load at the time.

Table 7.20 – Specifications of the OMROM Relay.

Omron Relay	Specifications
<b>PCB SIGNAL RELAY- G5V-2</b> 	<ul style="list-style-type: none"> <li>• Rated voltage <math>\rightarrow 9\text{ Vdc}</math> (minimum of 9Vdc)</li> <li>• Rated current <math>\rightarrow 55.6\text{mA}</math> (minimum of 16.7mA)</li> <li>• Coil resistance <math>\rightarrow R_i = 540\ \Omega</math></li> <li>• Coil inductance (Armature OFF) <math>\rightarrow L_i = 0.31\text{H}</math></li> <li>• Coil inductance (Armature ON) <math>\rightarrow L_i = 0.49\text{H}</math></li> <li>• Maximum voltage <math>\rightarrow 120\%</math> of rated voltage, <math>23^\circ\text{C}</math></li> <li>• Power consumption <math>\rightarrow \cong 500\text{mW}</math></li> </ul>



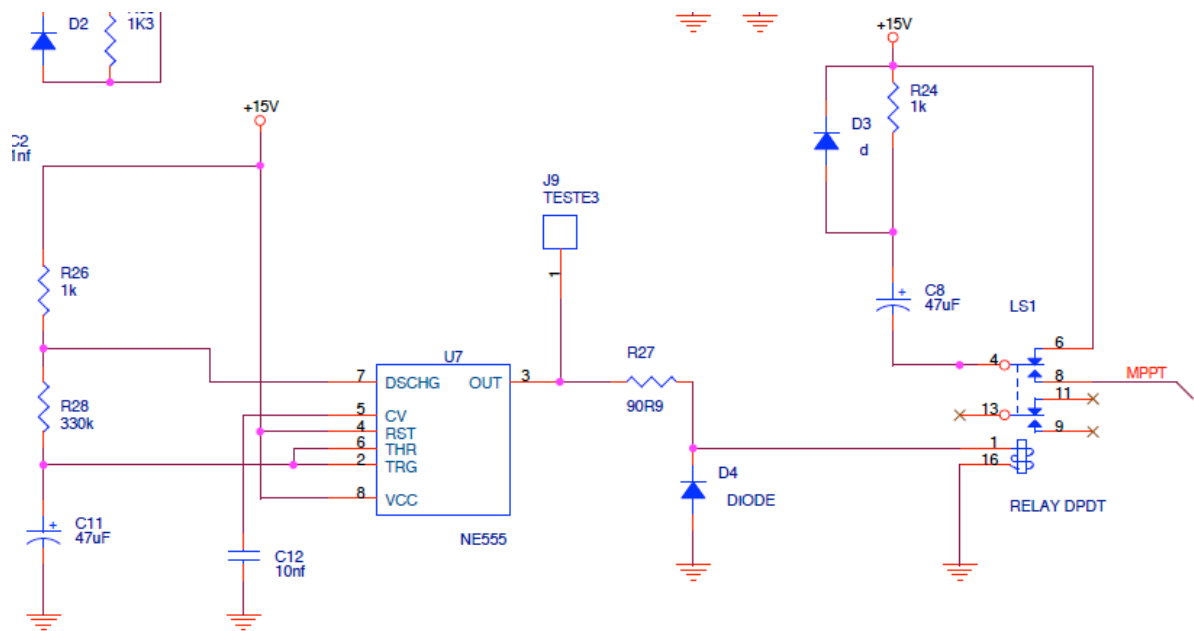


Figure 7.40 – Orcad schematic of the PEM control circuit.

### 7.10.3. Test and validation of the PEM control signals

To ensure the correct functionality of the system, the board that performs the control of the PEM which is represented in Figure 7.41 is validated. The validation was done by examining the relevant signals of the process namely; signals at pins 3 and 6 of the NE555 of the PEM, shown in Figure 7.42, signals of input of relay and perturbation made to pin 5 of NE555 of the converter, shown in Figure 7.43 and the Signals at capacitor C' with emphasis to its discharge time  $\ll 1s$  in Figure 7.44.

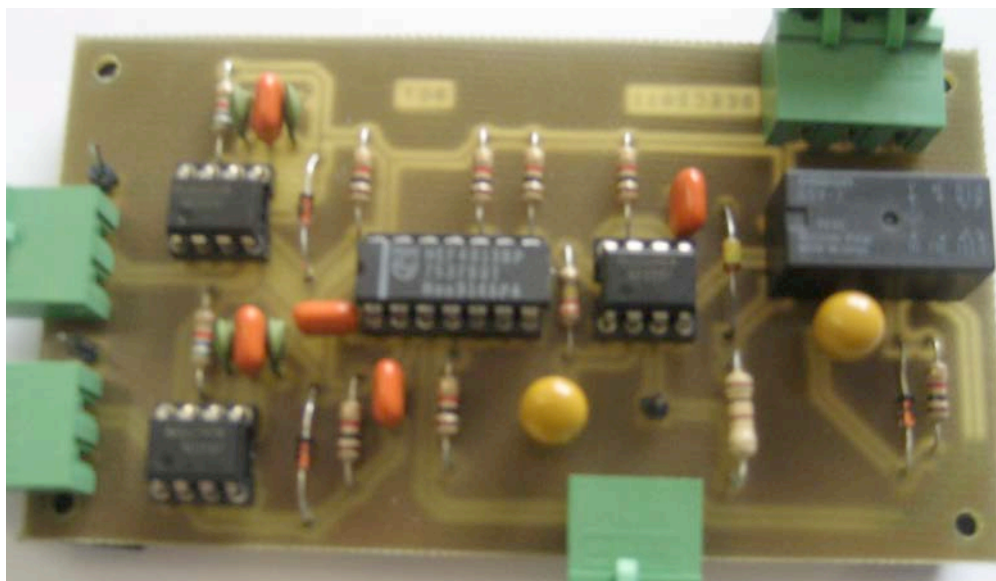


Figure 7.41 – Layout of the frequency divider and PEM control circuits.

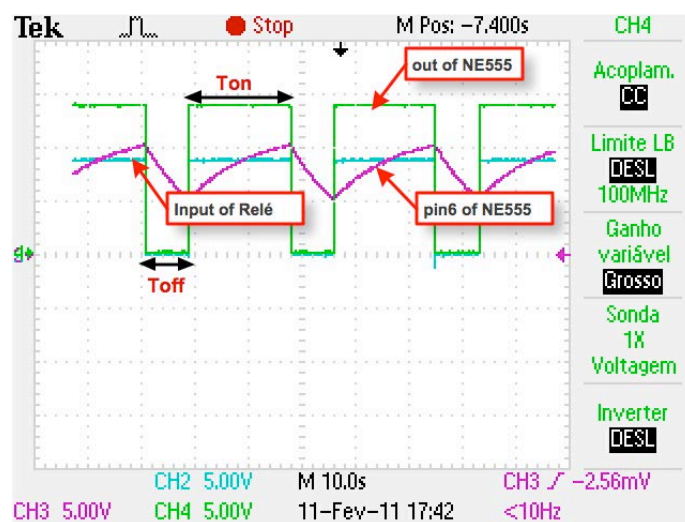


Figure 7.42 – Signals at pins 3 and 6 of the NE555 of the PEM and input of relay.

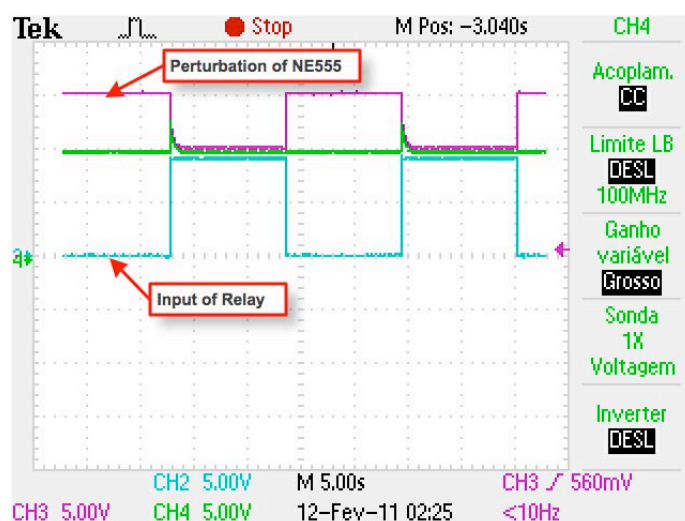


Figure 7.43 – Signals of input relay and perturbation of NE555 of the converter.

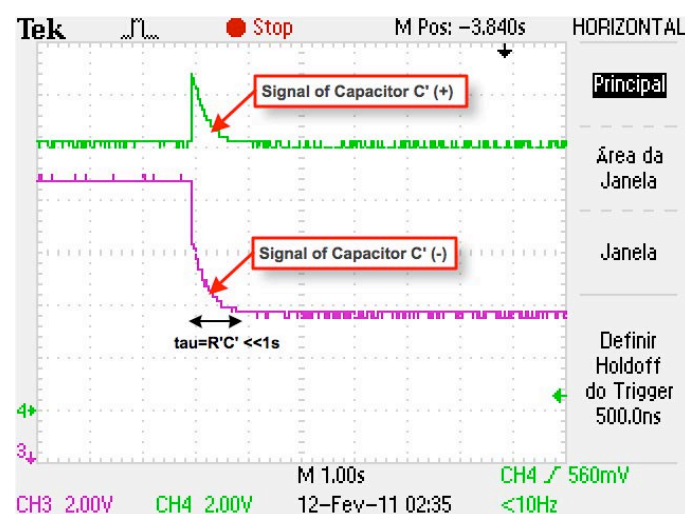


Figure 7.44 – Signals at capacitor C' with emphasis to its discharge time  $\ll 1s$ .

## 7.11. Test and validation of the signals to IGBT converter

Considering the reference of the pins of module FP40R12KE3 in Figure 7.45 below, some previous tests have been performed to analyse the conduction of the IGBTs. Thus, IGBTs 1&3 should conduct simultaneously, while IGBTs 1&2 should not. The layout of IGBT module with pins number is represented in Figure 7.45 is used for the tests. As an example, the situation of conduction of IGBTs 2&4 is presented in Figure 7.46.

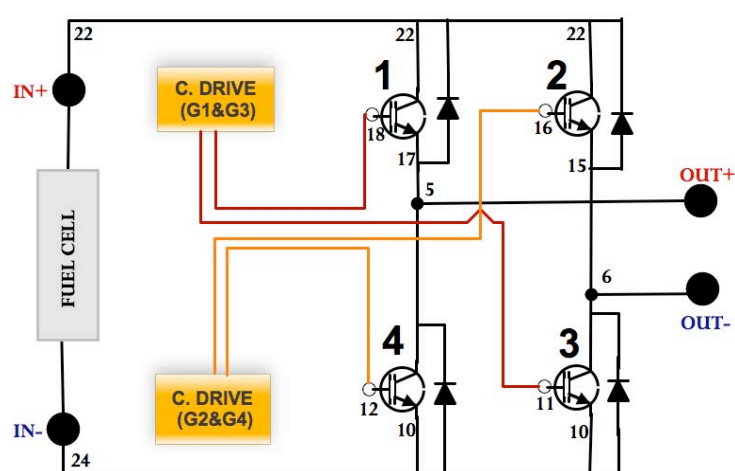


Figure 7.45 - Layout of IGBT module and pins number.



Figure 7.46 – Conduction of IGBTs 2&4.


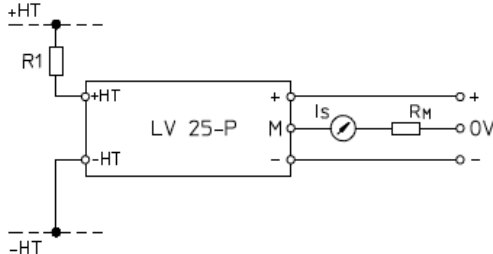
## 7.12. Output voltage measurement

The measurement of the output voltage,  $v_{out}$ , was first made with the sensor LEM and then with an optocoupler. the solution implemented with the LEM sensor was replaced by the optocouplador to solve the problem of signal delay inserted by the LEM sensor and not presented in when using the optocoupler. Both solutions implemented, are presented below.

### 7.12.1. Using a LEM sensor

The voltage transducer LV25-P which specifications are presented in Table 7.21 converts a high voltage to a low-level signal voltage with isolation between the high voltage source and the signal output. This enables a voltage signal, instantaneously proportional to the primary voltage to be transferred with fidelity and safety from high power equipment to monitoring or power measurement instrumentation. An electrically isolated current sensor is used to measure the current through the high-voltage precision resistor  $R1=39K\Omega$ , 5W connected across the high-voltage to be measured.

Table 7.21 – Specifications of the voltage transducer LV25P.

Voltage Transducer LV25-P	Specifications
	<ul style="list-style-type: none"> <li>• IPN = 10 mA, VPN = 10 to 500 V</li> <li>• KN <math>\rightarrow</math> Conversion ratio 2500:1000</li> <li>• VC Supply voltage (<math>\pm 5\%</math>) <math>\rightarrow \pm 12 - 15</math> V</li> <li>• Terminal + : supply voltage + 12 - 15 V</li> <li>• Terminal M : measurement</li> <li>• Terminal - : supply voltage - 12 - 15 V</li> </ul>
	$V_{ref} = \frac{V_{out}}{R_{1^{\circ}transf}} \times G_{transf} \times R_{2^{\circ}transf} \quad \text{Eq. 7.50}$ $V_{ref} = \frac{V_{out}}{39k} \times 2.5 \times 0.27k \quad \text{Eq. 7.51}$

The LV25-P has a primary nominal rms current of 10mA and a secondary nominal rms of current of 25 mA. The secondary current is converted to a signal voltage with a precision given by the resistor placed in the secondary side, which must be in the range of 100-350  $\Omega$ . The conversion ratio  $K_N$  of the LEM sensor is 2500:1000. The resistor selected for the measurement terminal M is  $R_2=0.27 \text{ K}\Omega$ , 1W for a supply voltage of  $\approx 15\text{V}$ .

Validation of the expression: to a desired output voltage of 100V, the value measured at the sensor output is 1.7 V, and then according the reference value must be of this order, that is:

$$V_{ref} = \frac{V_{out}}{39 \times 10^3} \times 2.5 \times 0.27 \times 10^3 \quad \text{Eq. 7.52}$$

The experimental orcad schematic and its correspondent implementation are presented in Figure 7.47 and Figure 7.48 below.

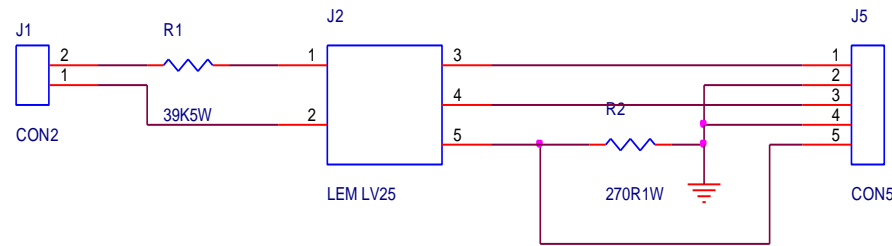


Figure 7.47 - Schematic of the LEM sensor.



Figure 7.48 - Experimental implementation of LEM sensor board

### 7.12.2. Using an optocoupler

The output voltage of the converter is measured with the Single Channel High Speed Optocoupler 6N136 accordingly to the schematic presented in Figure 7.49. This circuit allows performing the measurement of the amount of output voltage of the converter without the delay that occurs when

using the LEM LV25-P; the delay is around 2 sec. In the present application this aspect is of crucial importance because the controller response cannot contain delays. So with this new scheme this issue was safeguarded.

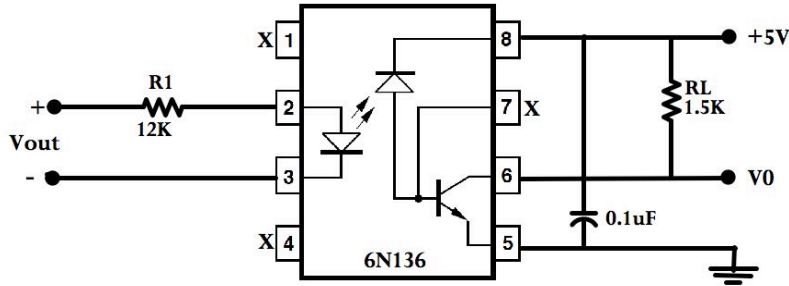


Figure 7.49 - Schematic of the Optocoupler 6N136.

This optocoupler uses an insulating layer between a LED and an integrated photo-detector to provide electrical insulation between input and output. Separate connections for the photodiode bias and output-transistor collector increase the speed up to a hundred times that of a conventional phototransistor coupler by reducing the base-collector capacitance.

#### ➤ Protection of the input of the device

The potential difference between the circuits to be coupled should not exceed the maximum permissible reference voltages. Referring to the datasheet of the device, the recommended forward current ( $I_F$ ) and related diode voltage drop  $V_{CC}$  are 16mA and 1.33V respectively. Then the resistor  $R_1$  placed in the input of the optocoupler (pin 2) is calculated considering these conditions and considering a voltage measured of 200V:

$$R_1 = \frac{(200 - 1.33)}{16 \times 10^{-3}} = 12.41 \times 10^3 \Omega \approx 12 K\Omega \quad \text{Eq. 7.53}$$

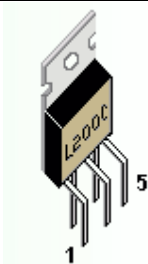
#### ➤ Protection of the output of the device

The load-resistor  $R_L$  is calculated accordingly to the typical characteristics of a transistor for a source  $V_{CC}=5V$  and the fact that it must work at the middle of the line load. Then considering the possible values of voltage to be measured, a resistor of  $1.5k\Omega$  is used as is represented in Figure 7.49. The capacitor  $0.1\mu F$  serves to eliminate the noise from the signal source.

### 7.13. Voltage regulator power supply

The voltage regulator power supply correspondent to the orcad scheme in Figure 7.50 and its experimental implementation in Figure 7.51 uses the device L200 which specifications are described in Table 7.22. The L200 is a positive variable voltage regulator that includes a current limiter and supplies up to 2 A in the range of 2.85 - 36V. The output voltage is fixed with two resistors or, if a continuously variable output voltage is required, with one fixed and one variable resistor. The transformer has a 12V, 2A rated secondary. The potentiometers 10k (R6 and R14) adjust the voltage output from 3 to 15V, and the two resistors (R1 and R9) of 47 $\Omega$  controls the current. This has a minimum current of 10mA and a maximum current of 2A. Reaching the current limit it will reduce the output voltage to zero.

Table 7.22 – Specifications of the voltage regulated L200.

Voltage Regulated- L200	Specifications
	<ul style="list-style-type: none"><li>• DC Input Voltage→40V max.</li><li>• Peak Input Voltage→ 60V max for 10mA</li><li>• Output Voltage Range→2.85 to 36V</li><li>• Output Current Range→ 0.1 to 2A</li><li>• Quiescent Current→4.2mA</li></ul>

The input capacitors  $C_1$  and  $C_2$  are used to prevent unwanted oscillations and the output capacitors  $C_4$  and  $C_8$  acts basically as line filter to improve transient response.



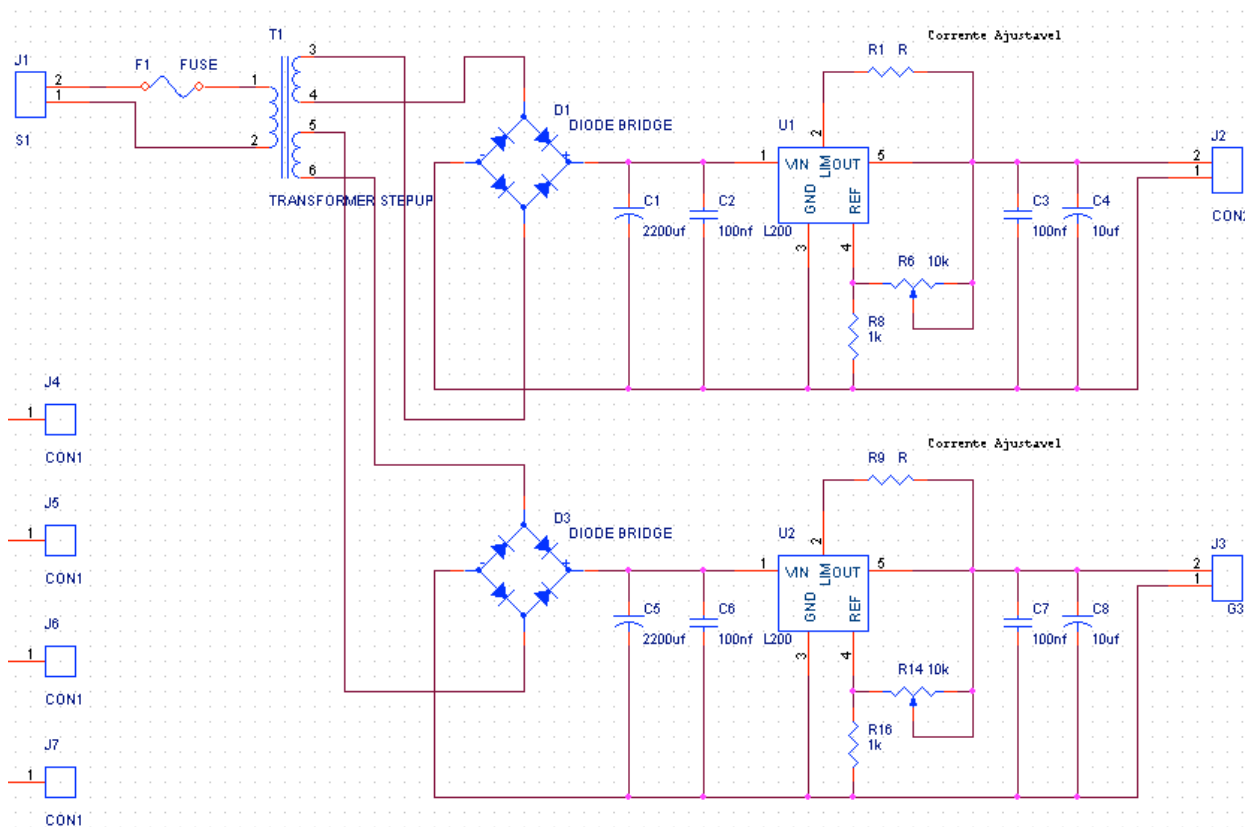


Figure 7.50 - Schematic of the power source (+/- 15V).



Figure 7.51 - Experimental implementation of the voltage regulator power supply (+/- 15V).

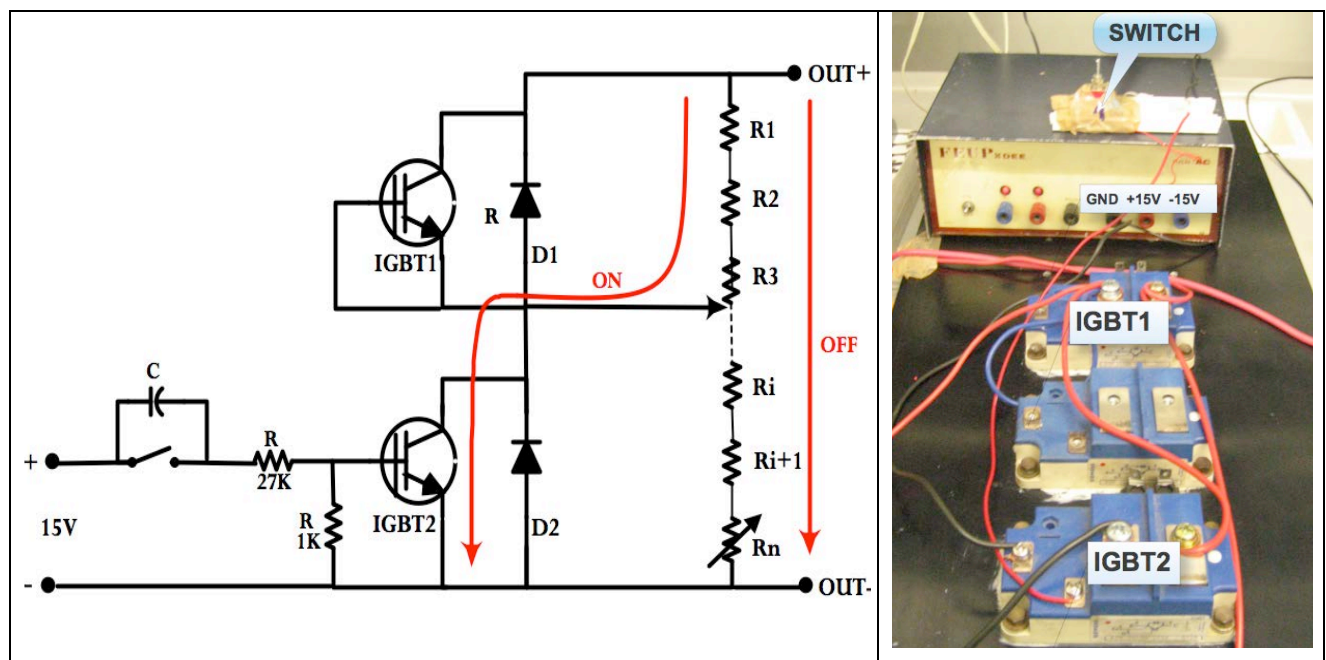


## 7.14. Variation of the load

The scheme of Figure 7.52 below was implemented to make fast load variations. Basically the auxiliary circuit changes the state of the IGBT2 and thus the value of the load presented to the converter. The diode D1 prevents circulation currents towards of the converter.

When switch control turns ON to OFF  $\Leftrightarrow 1 \rightarrow 0 \Leftrightarrow R_{\min}$  to  $R_{\max} \Leftrightarrow I_{\max}$  to  $I_{\min}$

When switch control turns OFF to ON  $\Leftrightarrow 0 \rightarrow 1 \Leftrightarrow R_{\max}$  to  $R_{\min} \Leftrightarrow I_{\min}$  to  $I_{\max}$



(a) Auxiliary circuit to control the load.

(b) Implementation.

Figure 7.52 – Control of the load.



---

# *CHAPTER 8*

## **EXPERIMENTAL RESULTS**

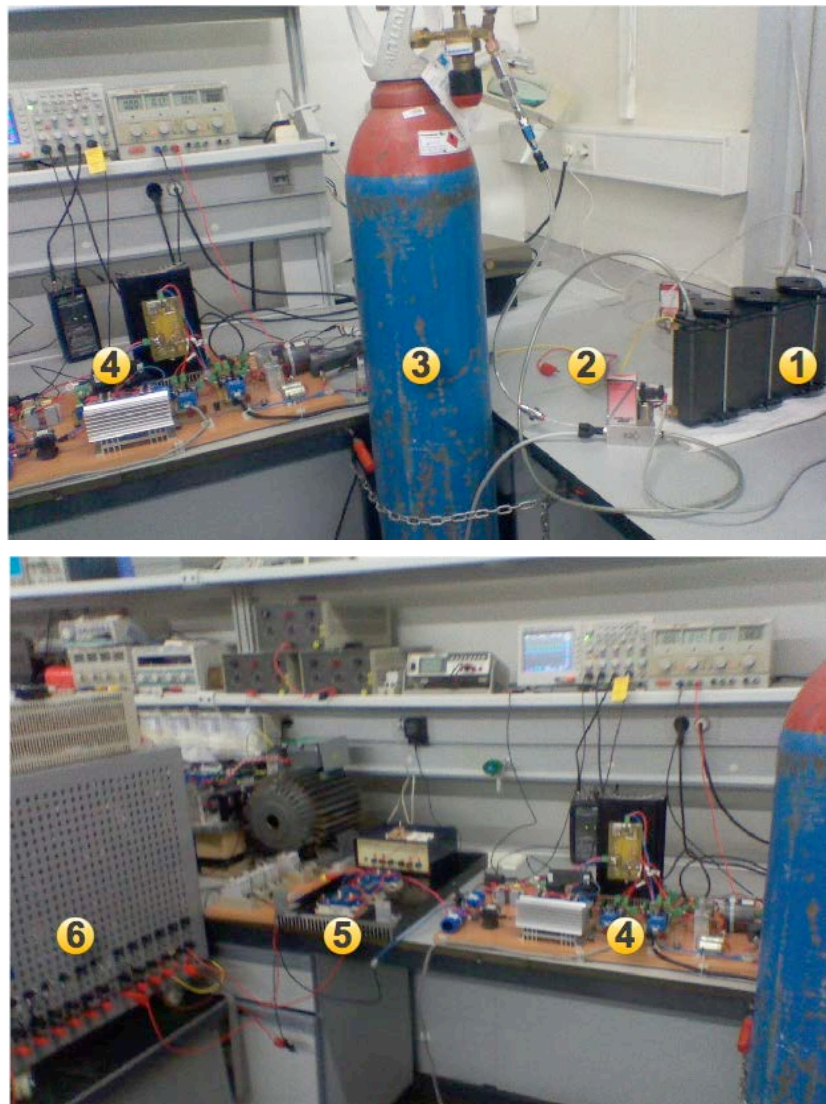
---



## 8. EXPERIMENTAL RESULTS

### 8.1. Introduction

Once analysed and implemented experimentally the SRC and the control strategy as described in previous chapters, several tests were performed to validate the goals established in this thesis, Particularly: 1) Regarding to the dynamics of the system and 2) Regarding the operation of the PEM with a minimum consumption of hydrogen and a maximum power transfer. Figure 8.1 show the global system implemented in the laboratory I-002 at FEUP to meet the objectives.



Legend: (1) PEM stack of 1kW, Mark1020 (24 cells), (2) Gas flow measurement and control, (3) Hydrogen bottle (PH<sub>2</sub>=200bar), (4) SRC, (5) Control of the load by IGBT, (6) Load.

Figure 8.1- Experimental setup in the laboratory I-002 of FEUP.

## 8.2. Dynamics of the system

Regarding the dynamics of the system, the main objectives to achieved are:

- 1) Validation of the control stability of the inner loop that is: prove that the output voltage  $V_{out}$  remains constant even for load variations. Loading variations in step-up, and step-down, are imposed on the system and the results analyzed.
- 2) Validation of the system dynamics that is: verify if the system is fast in its dynamics.

Accordingly, the following variables are analyzed: the output voltage  $V_{out}$ , the PI controller, the resonant current which allows seeing a real change in the converter frequency corresponding to the load variation, and the input voltage and current.

### 8.2.1. Output voltage and current

In the Figure 8.2 below it is validated the stability of the voltage control loop of the converter that is, it can be seen that  $v_{out}$  remains constant despite variations in load. This condition is valid to both situations, the step-up of load corresponding to Figure 8.2 a) and the step-down of load corresponding to Figure 8.2 b).

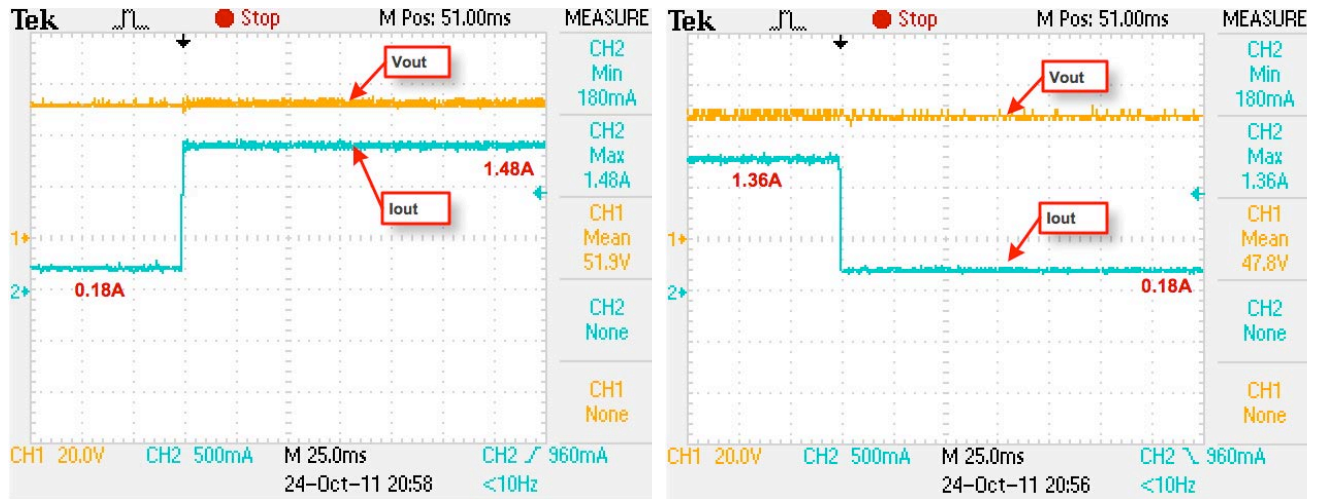
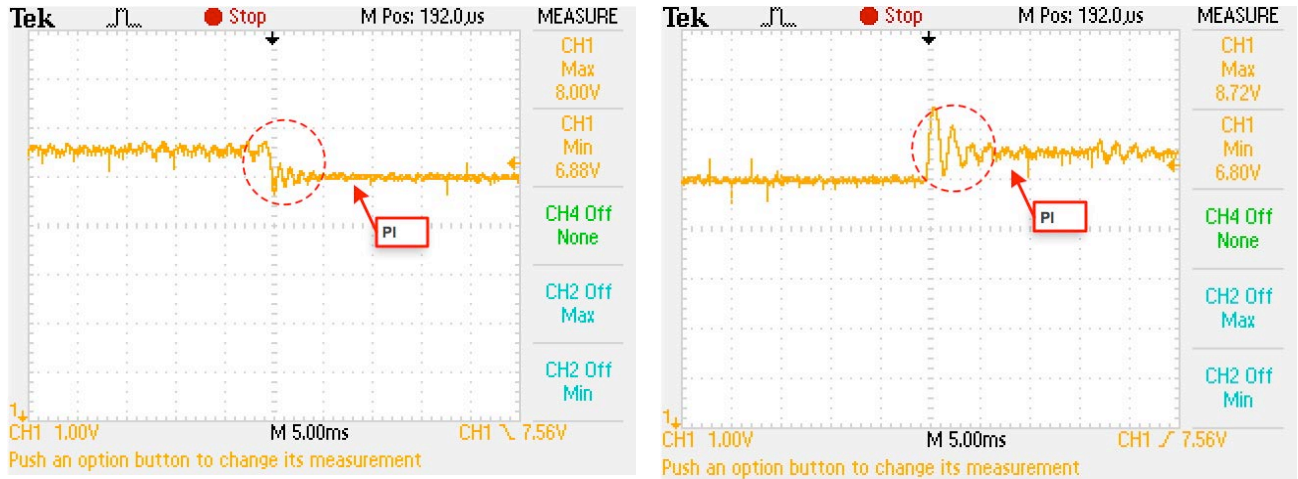


Figure 8.2 – Output voltage ( $V_{out}$ ) and Current ( $I_{out}$ ).

### 8.2.2. PI output

The dynamics of the system can be evaluated by the analysis of the PI control signal. So, once considered both situations of load variation it appears that the stabilization time of the PI controller

is approximately 7ms. In addition it presents a small oscillation which proves that the parameters of the PI control are well adapted to the system. Figure 8.3 a) corresponds to the situation of a step-up load condition while the Figure 8.3 b) corresponds to a step-down of load condition. The error of voltage is given by INA101 such as;  $\epsilon = V_{\text{measured}} - V_{\text{reference}}$  and accordingly, the objective of the PI controller is to minimize this error for any load variation, as is shown in the two figures below.



(a) Step-up of load.

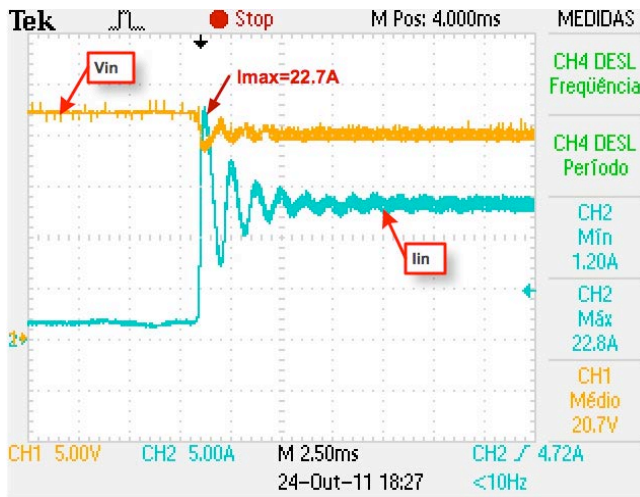
(b) Step-down of load.

Figure 8.3 - Output of PI.

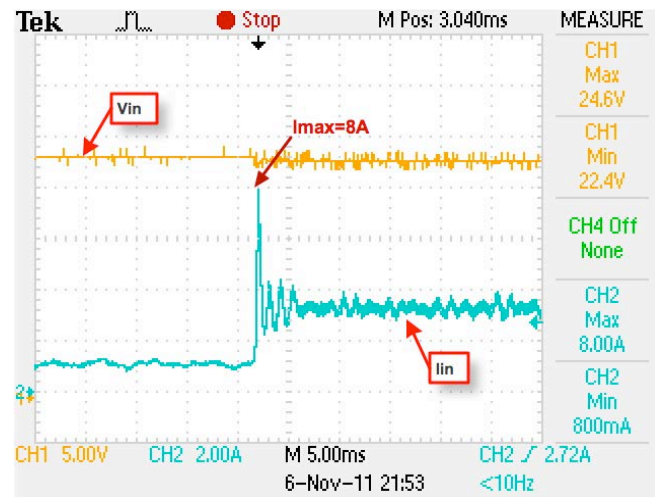
### 8.2.3. Input voltage and current

As already referred, the evolution of this study has undergone by a process of successive improvements to the system in the areas, power and control. For the case, it is presented in Figure 8.4 below the results due to the improvement of the proportional gain of the PI controller in the current. As can be observed by comparing figures a) and b) there is a significant reduction in the amplitude of the oscillation of the current, which lower from 22.8A to 8A. This corresponds to a substantial improvement of the system dynamics as intended. The effect of control is also present in the input voltage, which by observing Figure 8.4 a) and Figure 8.4 b) also shows an improvement in  $V_{\text{IN}}$  with the improved of the control system.





(a) Proportional gain is made with  $R = 4k7$

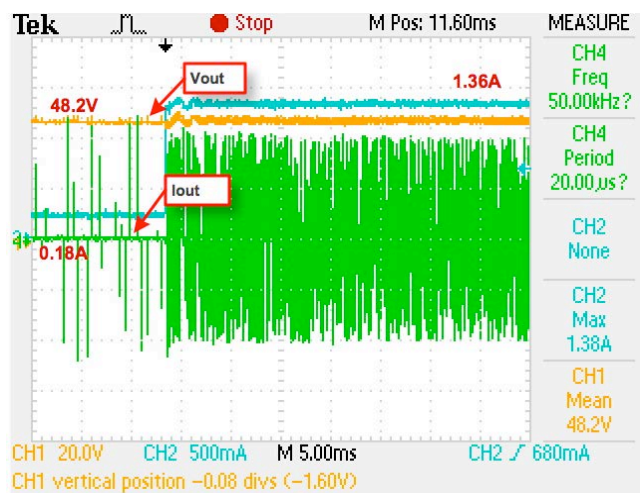


(b) Proportional gain is made with  $R = 12k$

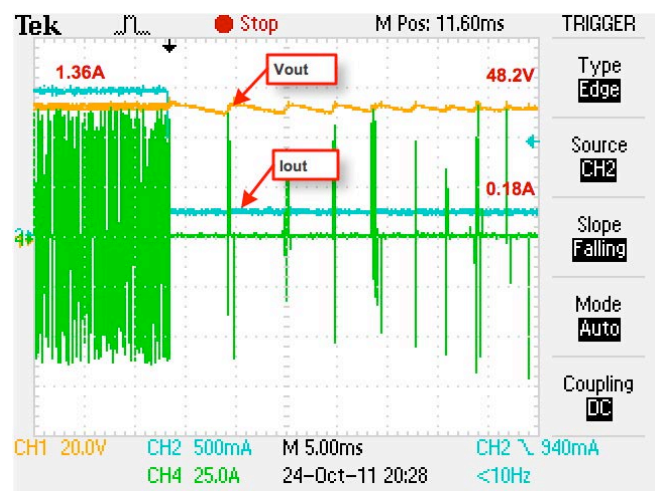
Figure 8.4 – Input voltage and current with improvement of the controller.

## 8.2.4. Resonant circuit operation

Figure 8.5 corresponds to step-up and step-down load conditions. From its analysis it follows that the converter reacts to the load variation, varying its frequency of operation. Thus, for a small load level ( $I_{min}$ ,  $R_{max}$ ) the frequency is low while for a high load ( $I_{max}$ ,  $R_{min}$ ) the frequency is high. In dynamic terms it can be seen that the transition in the frequency of operation is instantaneous, hence, we conclude that the system has good dynamic characteristics. It can be also observed that in any of the load variations the output voltage  $V_{out}$  remains constant. This analysis validates the objective defined in Section 1.2 that is the controller ensures a constant output voltage in order to satisfy the requirements imposed by the power system applications.



(a) Step-up of load.



(b) Step-down of load.

Figure 8.5 – Output voltage and current and resonant circuit operation.



### 8.3. PEM control with optimization of the hydrogen consumption

Regarding the optimum operation of the PEM, the main objectives to achieved are:

- 1) Analysis of the operation of the PEM controller.
- 2) Demonstrate that the PEM controller imposes an operating point, which guarantees a minimum consumption of hydrogen and a maximum power transferred. Once demonstrated the stability of the system that is, the conditions imposed by the inner loop control.

Demonstrate that, given the conditions of:  $V_1 \times I_1 = P^*1$  and  $V_2 \times I_2 = P^*2$ . As  $P^*1$  and  $P^*2$  belong to the same power curve in Figure 8.6, it has  $P^*1 = P^*2$  or  $\text{Area}_2 = \text{Area}_1$ , then, if  $I_1 < I_2$ ,  $V_1 > V_2$  and  $f_1 < f_2$ . The PEM controller places the converter operating at frequency  $f_1$  and the optimum point of operation is  $P^*1$ .

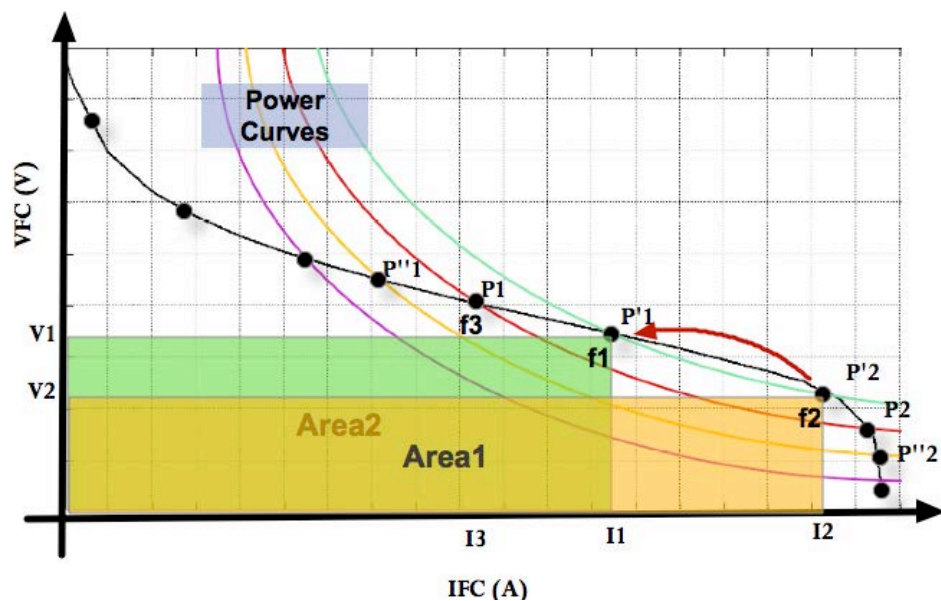


Figure 8.6 – Principle of operation of the PEM controller.

### 8.3.1. PEM controller operation

Figure 8.7 a) shows the effect of the PEM controller to an increase of the load to the system. In this case, the current required to the fuel cell system also increases. However, the action associated with an increase in the fuel cell current is opposite to the principle established by the PEM controller and this reacts to that situation in order to find a minimum value of current ( $I_{FC}$ ) and a maximum value of voltage ( $V_{FC}$ ) which conditions ensures the requirements of the load. Simultaneously, and accordingly, the output current,  $I_{out}$ , reduces its value, while the PEM stabilizes in an optimal

point, however, once the optimum point of the PEM established, the value of  $I_{out}$  returns to its steady state value. It follows that the output conditions of the converter ( $V_{out}$  and  $I_{out}$ ) do not change when the PEM controller acts on the system.

From Figure 8.7 a) it is also verified that, the time of establishment to the optimal operating point is  $\approx 3 \times 250\text{ms} = 750\text{ms}$ , which corresponds to a reduction of 2.3A in the amplitude of the output current. Considering the case of P'1 and P'2 in Figure 8.6 above, the optimal operating point, is therefore characterized by  $V_{FC} = V_1$  and  $I_{FC} = I_1$ .

The amplitude of the signal VCO (pin 6 of NE555), is responsible for the reduction of the operating frequency of the resonant converter. however once the optimum point of the PEM established, the perturbation continues, but it has no longer effect on the system operation.

Observing the Figure 8.7 b), the time of establishment PEM in the optimal point is simply defined by the variation of load imposed to the system, which is in the sense of  $I_2 \rightarrow I_1$ . In the case of Figure 8.7 b), the current required to the fuel cell system also decreases. Accordingly, the optimal operating point is naturally achieved, since this action is in accordance with the principle established by the PEM controller, with  $I_1 < I_2$  and  $V_1 > V_2$ .

Hence, in accordance with the information available in Figure 8.7 b) it can be concluded that the practical impact of the PEM controller is less visible. From Figure 8.7 b) it is also observed the time of establishment in the new operating point which is  $\approx 50\text{ms}$ .

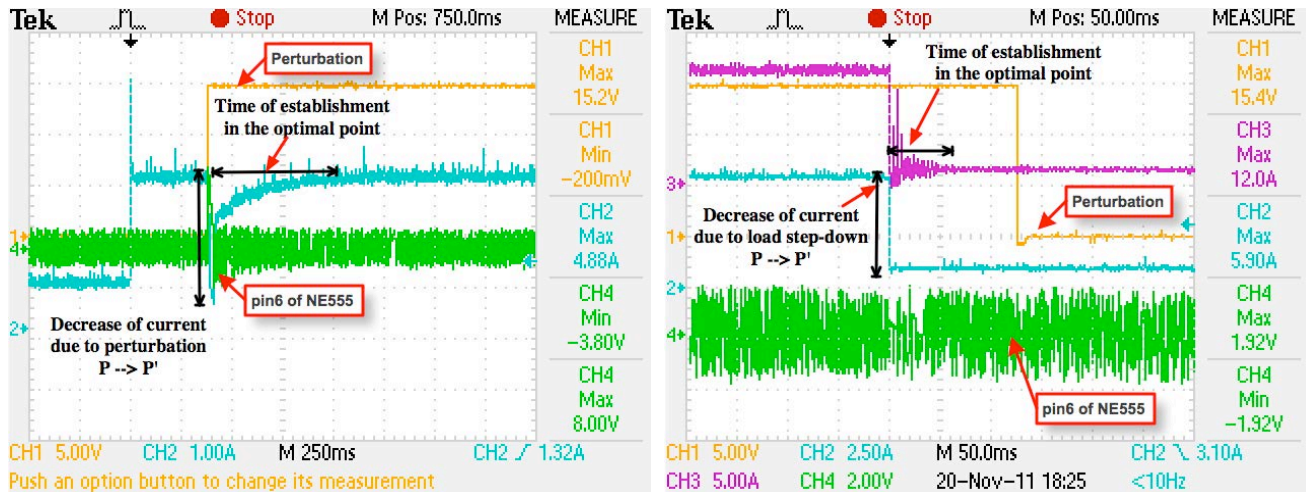


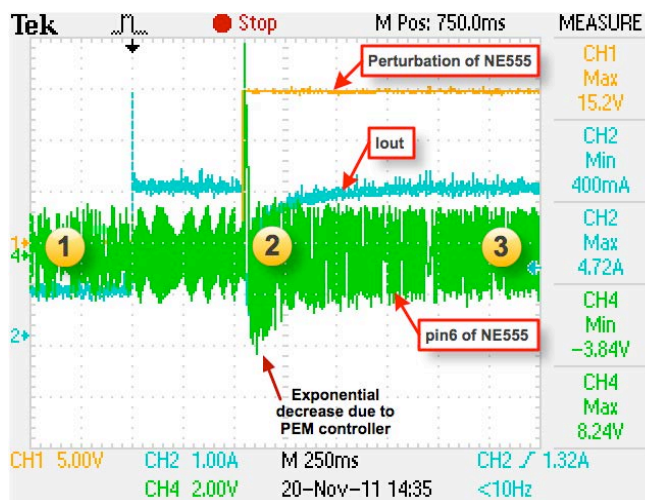
Figure 8.7 - PEM controller operation.

### 8.3.2. Effects of the PEM controller in the variables of the system

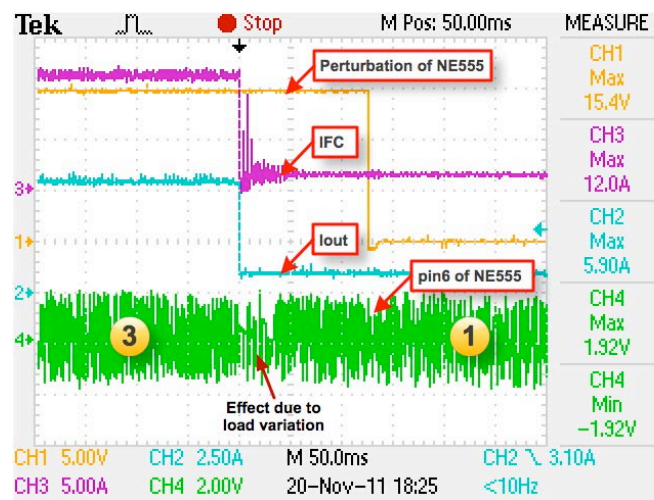
In Figure 8.8 and Figure 8.9 it is evaluated the effect of the PEM controller on VCO signal (pin 6 of NE555), on input and output currents and in the resonance frequency of the converter. Thus, analyzing the situation of step-up load condition represented in Figure 8.8 a), it appears that there are three distinct zones, namely: the zone 1, which is characterized by low frequency of operation, the zone 2, which is characterized by the exponential decrease of VCO signal and the zone 3, which is characterized by high frequency operation. For the reasons cited above, the effect characterized by the zone 2 is due to the action of the PEM controller. In Figure 8.9 a) and Figure 8.9 b) the charge and discharge of a capacitor at pin 6 of NE555 which defines the frequency operation are represented by triangular shapes instead of exponentials. This fact is only due to the number of sampling points used by the oscilloscope.

Figure 8.11 shows that the system is stable for any load condition and proves what has been said above that, the output conditions of the converter do not change with the PEM controller. With regard to the resonant current  $I_{ress}$ , it appears that for a step-up of load, the effect due to the PEM controller is reflected by an decrease of the amplitude of this current during the time that the system operates in the sense of the search from the optimum point, which amplitude increases again for the reasons already explained. In the case of a step-down change of the load represented by Figure 8.11 b), the amplitude of the current  $I_{ress}$  is not affected by the PEM controller. Observing the both figures, it appears that the power system responds to the request made by the load with a delay of order  $250\mu s$ . Thus, comparing with Figure 8.5 on which this phenomenon does not occur, it can be concluded this is due to the PEM operation.

It should be noted however that in practical terms and in the case of a power electronic system for energy production as is the case, this delay is not a problem since it is of the order of  $\mu s$ , which is insignificant in power systems.

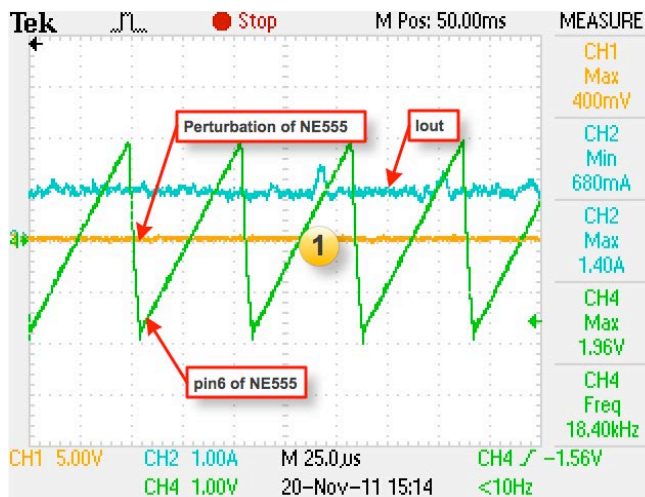


(a) Step-up load condition.

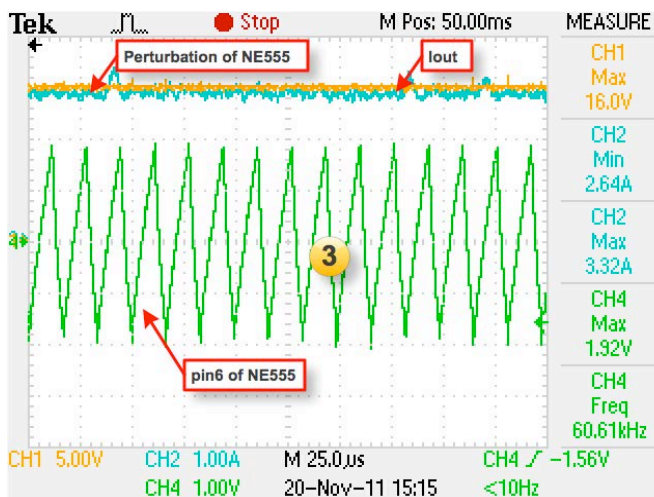


(b) Step-down load condition.

Figure 8.8 - Effects of the perturbation on VCO signal and currents.



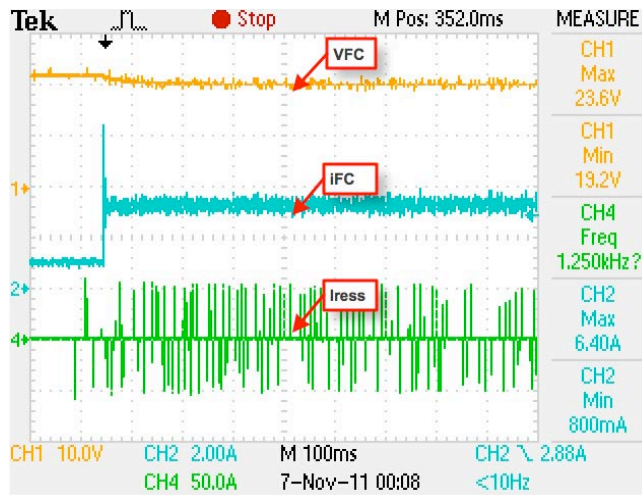
(a) For low load condition



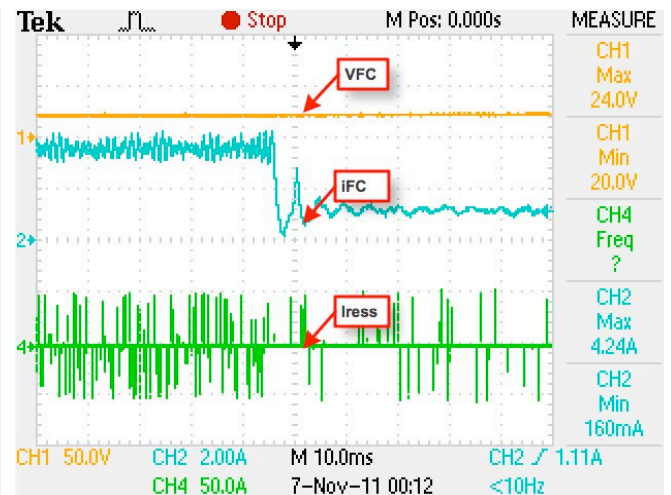
(b) For high load condition

Figure 8.9 – Effects of the perturbation on VCO signal (pin 6 of NE555).



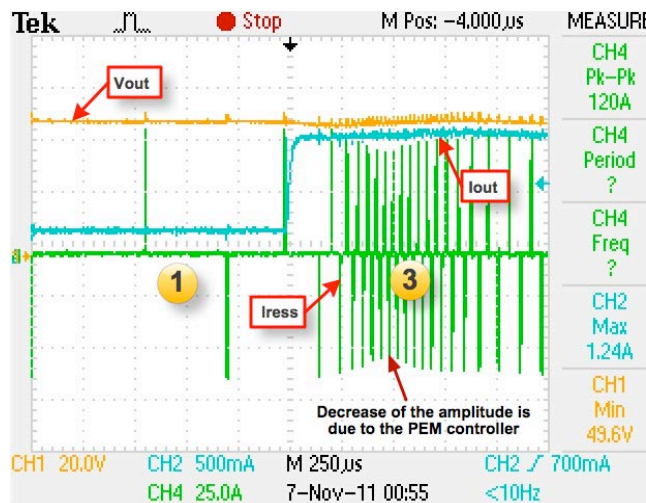


(a) Step-up load condition.

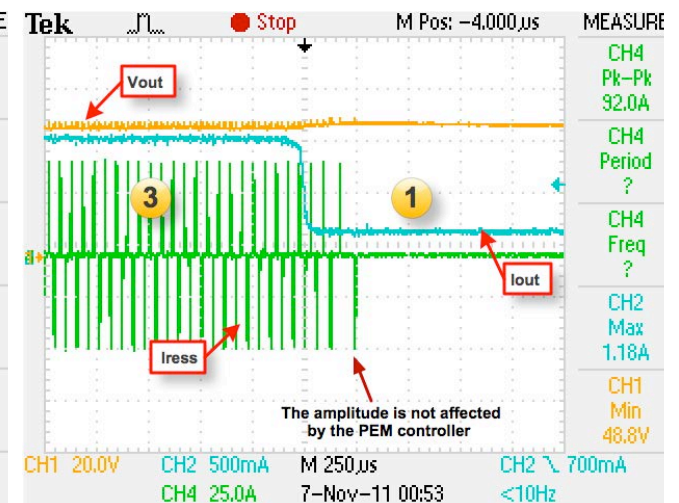


(b) Step-down load condition.

Figure 8.10 - Effects of the perturbation on ifc, vfc and Iress.



(a) Step-up load condition.



(b) Step-down load condition.

Figure 8.11 - Effects of the perturbation on the amplitude of resonant current.

## 8.4. Conclusions

This chapter evaluates the performance of the power generation system implemented experimentally. The analysis of the results is focused in two major points namely:

### 3) The stability of the system

The stability of the system was proved by the output voltage  $V_{out}$ , which remains constant even for the load variations imposed to the system. It was also proved that the resonant converter suits perfectly the changes imposed on the system by changing its operating frequency accordingly.

### 4) The PEM control with optimization of the hydrogen consumption

The characterization of the optimum point of operation as a function of the hydrogen consumption is presented. It was demonstrated that the PEM controller imposes an operating point, which guarantees the minimum consumption of hydrogen and maximum transfer of power. Considering that the operating point is for the minimum fuel cell current and maximum fuel cell voltage, and knowing that the hydrogen consumption is proportional to the current then the minimum consumption of hydrogen is assured in this way. In addition to the good conditions established by the control system, the maximum power transfer was further ensured by suitable selection of the elements of power, namely, the components of the resonant circuit and the high frequency transformer.

Finally, the analysis of the experimental results allows concluding that the system implemented provides excellent stability, robustness and good dynamic response making it a strong candidate for industrial applications in various areas of energy in accordance with the current tendencies in the sector.

---

## *CHAPTER 9*

### **CONCLUSIONS AND FUTURE WORK**

---





## 9. CONCLUSIONS AND FUTURE WORK

### 9.1. Conclusions

In this thesis a new high power efficient electronic converter for fuel cell applications was proposed and validated. The major conclusions of this thesis are summarized below.

#### *Application of The Optimization Algorithm to Extract the PEM Parameters:*

The comparison of experimental and simulation results allowed us to find an optimal set of parameters that minimizes an objective function. In each iteration, the algorithm analyses the solutions neighbouring the current solution and accepts it if it is better. Otherwise the solution can still be accepted with a given probability, thus enabling escape from local optimum.

#### *Modelling and Simulation of the PEM Fuel Cell and the Converter in Matlab/Simulink Software:*

The simulation in Matlab/Simulink software was included in the analysis of the static and dynamic performance of the PEM and the influence of parameters such as the temperature, the hydrogen pressure, and load variation. Because the time constants concerned in the system are very different (the PEM reacts very slowly in comparison to the converter) and by the fact that Matlab algorithms are all based on Runge Kutta, the simulation time sometimes becomes very long. The modelling and simulation in Matlab/Simulink, either for the PEM fuel cell or for the set including the DC-DC converter, are of extreme importance because they gave relevant information about the variables of the system, namely; variables of the converter output, variables of the resonant circuit, variables of the PEM fuel cell and even on the control of the system.

#### *Design and Implementation of the DC-DC Resonant Converter:*

An efficient DC-DC converter topology was investigated. The decision has led to the selection of the resonant converter, whose principle is based on soft-switching methodology. In this context the design and implementation of the converter consisting of a input filter followed by the full-bridge inverter and the series resonant circuit on the primary side and a diode rectifier and output filter on the secondary side was based on the exploitation of their benefits as compared to other types of converters, namely: low component stresses, high frequency operation and soft-switching commutation. A general guideline to select the resonant circuit components values when designing a resonant converter is made in Appendix C, assuming that the converter operates with a defined

input voltage range, a defined output power range and at a known maximum switching frequency. This guide provides a very useful tool for designers to select the optimum values of resonant components, which ensures the maximum transfer of power.

#### *Implementation of the Control Structure Selected:*

The control was divided into two parts namely: i) the voltage controller, which is responsible for keeping constant the output voltage of the converter even under loading variations and ii) the PEM controller, which is responsible for improving the performance by keeping the PEM fuel cell in its optimal operating point. In both simulation and experimental results a constant output voltage of the converter and a minimum of switching losses are demonstrated. The results also demonstrate that the control structure selected leads the PEM fuel cell operating in its optimal operating point i.e., with maximum efficiency.

#### *Experimental implementation of the Power System:*

The experimental implementation of the power system composed by the PEM fuel cell, the DC-DC resonant converter and load validates the methodology adopted and tested in simulation.. The experimental results confirm the simulation ones and furthermore, the setup developed can be extended to new loading conditions such as electrical vehicles and renewable energy sources like solar energy.

## **9.2. Suggestions for further work**

Among the various renewable energy sources, the fuel cell technology and particularly the proton exchange membrane (PEM) technology plays an important role in many applications when compared with other competitive types of fuel cells. The hybrid systems including the PEM should be used as the main substitution for traditional power sources in the near future especially in the automotive area, distributed generation and portable applications due to their unique advantages. However, without a doubt, the PEM systems still need research and development studies in many fields and there is still so much work to do by researchers in order to provide a better market place for this technology. The work done in this thesis was intended to provide a contribution in this direction, but it is not easy to stop this work because, some aspects should be improved and implemented in order to make it an interesting product in terms of industrial application, particularly in the automotive industry. Thus, this section presents the suggestions for future work.

#### *Efficiency and Optimization of the System:*

The nominal efficiency of a PEM fuel cell is determined by its performance characteristics and by its economics, i.e. the capital cost of fuel cell and cost of the hydrogen. Once the hydrogen pressure, the hydrogen flow and the fuel cell voltage and current density are known, the efficiency of the fuel cell system is determined. In this context, the system that provides hydrogen for the stack should be also improved since the actual system does not allow a perfect regulation of the hydrogen pressure delivered to the stack. On the other hand, it sends out the unused hydrogen. Accordingly the use of an accurately controlled system is proposed, with the possibility of recovery of the unused hydrogen. In terms of optimization, an optimal PEM fuel cell system design must be done considering the cost and efficiency together. For stationary and transportation applications, the efficiency of fuel cells is required to achieve higher or equal to 40% compared to the internal combustion engines. High efficiency means low hydrogen consumption hence, the importance of minimizing it.

#### *Topologies of DC-DC Converters and their Control:*

Different topologies of the DC-DC converter and control strategies may be implemented, tested and compared. A bidirectional full-bridge DC-DC converter with soft switching commutation is an interesting option to implement. With respect to the control issue, the requirements of system stability and maximum of power transferred should always be guaranteed.

#### *Modelling and Extraction of Parameters of the PEM Fuel Cell:*

The adoption of other models for the PEM fuel cell and other algorithms for the extraction of the PEM parameters, which have been referred to in this thesis can be made and the results compared with those corresponding obtained in the thesis such as the electrochemical model and the SA as the parameter extraction algorithm.

#### *Simulation:*

The simulation is of extreme importance because it provides relevant information on the system performance before its practical implementation. The Matlab/Simulink software was adopted in this thesis as the tool of simulation however, the simulation time was very long due to the reasons already discussed. The investigation of different software tools like PSim or SABER may constitute a very attractive solution to adopt in this matter.

### *Improvements on the Setup:*

The setup composed by the resonant converter, fuel cell and hydrogen supply system should be improved in order to make it adaptable to the applications. This process involves making the current system more compact, more robust and properly protected.

### *Investigation of Hybrid Power Sources Applied to the Electrical Vehicles:*

The fuel cells powered electrical vehicles are an interesting issue to investigate and implement in the near future because the fuel cells powered electrical vehicles are considered to be the most promising alternative to the conventional internal combustion vehicles. They combine the advantages of the battery-powered electric vehicles and the long range and rapid refuelling time of the internal combustion vehicles. In fact, actually many companies are developing and put on the market their own cars moved on fuel cell systems. Their advantages include the insertion of optional power sources such as batteries, super capacitors or flywheels in addition to the fuel cell system. In this context, an important aspect of investigation is the investigation of the fuel cell combined with other power sources, including the energy conversion (e.g., power converters) and storage devices such as batteries or super capacitors.

## **9.3. Personal retrospection**

I have learned a lot during this thesis, from both personal and professional perspectives. The implementation of the software model was sometimes tedious. However, this part of the work has become more interesting since a few particular issues of the MatLab/Simulink software have been overcome and understood. The hardware implementation of the system was my favourite due to the enormous enrichment this gave me at different levels. Although I am at the final part of this research, I feel I have not arrived to the end of my journey but at the beginning of a new phase, which I expect will be as fruitful as the one that I have lived through during the last five years.

## REFERENCES

1. Corrêa, J.M., et al., *Sensitivity analysis of the modeling parameters used in simulation of proton exchange membrane fuel cells*. IEEE Transactions on Energy Conversion 2005. **1**(20): p. 211-218.
2. Corrêa, J.M., et al., *Simulation of fuel-cell stacks using a computer-controlled power rectifier with the purposes of actual high-power injection applications*. IEEE Transactions on Industry Applications 2003. **4**(39): p. 1136-1142.
3. Corrêa, J.M., et al., *An electrochemical-based fuel cell model suitable for electrical engineering automation approach*. IEEE Transactions on Industrial Electronics, 2004. **5**(51): p. 1103-1112.
4. Forrai, H., Y. Yanagita, and Y. Kato, *Fuel-cell parameter estimation and diagnostics*. IEEE Transactions on Energy Conversion 2005. **3**(20): p. 668-675.
5. Yu, D. and S. Yuvarajan, *A novel circuit model for pem fuel cells*. in *Proceedings of IEEE Applied Power Electronics Conference and Exposition*. 2004.
6. Friede, W., S. Raël, and B. Davat, *Mathematical model and characterization of the transient behavior of a PEM fuel cell*. IEEE Transactions on Power Electronics 2004. **5**(19): p. 1234-1241.
7. Outeiro, M.T., et al., *A Parameter Optimized Model of a PEM Fuel Cell Including Temperature Effects*. Journal of Power Sources, 2008. **185**(2): p. 952-960.
8. Outeiro, M.T., et al. *Dynamic Modeling and Simulation of an Optimized Proton Exchange Membrane Fuel Cell System*. in *ASME Proceedings of International Mechanical Engineering Congress and Exposition*. 2007. Seattle, USA. .
9. Larminie, J.E. and A. Dicks, *Fuel Cell Systems Explained*. 2000, Chichester, England: John Wiley e Sons.
10. Thomas, S. and M. Zalbowitz, *Fuel cells-green power*. 1999, Los Alamos National Laboratory New Mexico.
11. Cook, B., *An introduction to fuel cells and hydrogen technology*. 2001, Heliocentris: Vancouver, Canada
12. Ramos, C.A.R., A. Giral, R. Martinez-Salamero, L. Rovira i Virgili Univ., Tarragona. *Maximum Power Point Tracking Strategy for Fuel Cell Power Systems*. in *IEEE International Symposium on Industrial Electronics*. 2007. Vigo
13. Zhong Zhi-dan, H.H.-b., Zhu Xin-jian, Cao Guang-yi, Ren Yuan, *Adaptive maximum power point tracking control of fuel cell power plants*. Journal of Power Sources, 2008. **176**: p. 259-269.
14. Jérôme Bernard, S.D., Felix N. Büchi, and Thierry Marie Guerra, *Fuel-Cell Hybrid Powertrain: Toward Minimization of Hydrogen Consumption*. IEEE Transactions on Vehicular Tecknology, 2009. **58**(7): p. 3168-3176.
15. Dongji Xuan, Z.L., Jinwan Kim and Youngbae Kim, *Optimal operating points of PEM fuel cell model with RSM*. Journal of Mechanical Science and Technology, 2009. **23**: p. 717-728.
16. *Plug Power*. Available from: <http://www.plugpower.com/>.
17. *Ballard Power Systems*. Ballard Power Systems designs and manufactures clean energy hydrogen fuel cells. J. Available from: <http://www.ballard.com/>
18. *HELION Hydrogen Power*. Available from: <http://www.helion-hydrogen.com/indexuk.php>
19. Kristina Haraldsson, K.W., *Evaluating PEM fuel cell system models*. Journal of Power Sources 2004. **126**(1-2): p. 88-97.

20. Bernardi, D.M. and M.W. Verbrugge, *A mathematical model of the solid-polymer-electrolyte fuel cell*. Journal of Electrochemical Society, 1992. **139**: p. 2477–2491.
21. Rowe, A. and X. Li, *Mathematical modelling of proton exchange membrane fuel cells*. Journal of Power Sources, 2001. **102**: p. 82-96.
22. Springer, T.E., T.A. Zawodzinski, and S. Gottesfeld, *Polymer electrolyte fuel cell model*. Journal of Electrochemical Society, 1991. **138**: p. 2334–2342.
23. Yi, J.S. and T.V. Nguyen, *Multi component transport in porous electrodes of proton exchange membrane fuel cells using the interdigitated gas distributors*. Journal of Electrochemical Society, 1999. **146**: p. 38-45.
24. Mann, R.F., et al., *Development and application of a generalised steady-state electrochemical model for a PEM fuel cell*. Journal of Power Sources, 2000. **86**: p. 173-180.
25. Amphlett, J.C., et al., *A model predicting transient responses of proton exchange membrane fuel cells*. Journal of Power Sources, 1996. **61**: p. 183-188.
26. Amphlett, J.C., et al., *A practical PEM fuel cell model for simulating vehicle powersources*, in *Proceedings of the Tenth Annual Battery Conference on Applications and Advances*. 1995: Long Beach, CA, USA. p. 221-226.
27. Corrêa, J.M., F.A. Farret, and L.N. Canha. *An analysis of the dynamic performance of proton exchange membrane fuel cells using an electrochemical model*. in *27th Annual Conference on the IEEE Industrial Electronics Society* 2001.
28. Hatti, M., M. Tioursi, and W. Nouibat, *Static Modelling by Neural Networks of a PEM Fuel Cell*. IEEE Proceedings, 2006: p. 2121-2126.
29. Shaoduan, O. and E.K. Luke, *A hybrid neural network model for PEM fuel cells*. Journal of Power Sources, 2005. **140**: p. 319-330.
30. Saengrungs, A., A. Abtahi, and A. Zilouchian, *Neural network model for a commercial PEM fuel cell system*. Journal of Power Sources, 2007. **172**: p. 749-759.
31. Jemei, S., et al., *On-board fuel cell power supply modeling on the basis of neural network methodology*. Journal of Power Sources, 2003. **124**: p. 479-486.
32. Zuyev, S., *Fuel Cell Power System Efficiency Calculation*. 2004, Central Washington University, Mechanical Engineering Technology: Washington, USA. p. 16.
33. Wang, C. and M. Nehrir, *Dynamic models and model validation for PEM fuel cells using electrical circuits*. IEEE Transactions on Energy Conversion, 2005. **2**(20): p. 442-451.
34. Al-Baghdadi, M. and H. Al-Janabi, *Optimization study of proton exchange membrane fuel cell performance*. Turkish Journal Eng. Env. Science, 2005. **29**: p. 235-240.
35. Bina, M.T. and D.C. Hamill, *Optimizing a discrete switching pattern using two simulated annealing algorithms*. The 7th Workshop on Computers in Power Electronics 2000: p. 129-133.
36. Fouskakis, D. and D. Draper, *Stochastic optimization: a review*. International Statistical Review, 2002. **Nº 3**(70): p. 315-349.
37. Pham, D.T. and D. Karaboga, *Intelligent optimisation techniques: genetic algorithms, tabu search, simulated annealing and neural networks*. 2000, New York: Springer.
38. Zolfaghari, S. and M. Liang, *Comparative study of simulated annealing, genetic algorithms and tabu search for solving binary and comprehensive machine-grouping problems*. International Journal of Production Research, 2002. **9**(40): p. 2141-2158.
39. Romero, D., J. Rincón, and N. Almao, *Optimization of the thermal behavior of tropical buildings*, in *7th International IBPSA Conference*. 2001: Rio de Janeiro, Brazil. p. 1079-1084.
40. Moins, S., *Implementation of a simulated annealing algorithm for Matlab*. 2002.

41. Anagnostopoulos, A., et al., *A simulated annealing approach to the traveling tournament problem*. Journal of Scheduling, 2006 **9**( 2): p. 177-193.
42. Soliman , S.A., Mantaway A.H. and El-Hawary M.E. , *Simulated annealing optimization algorithm for power systems quality analysis*. Electrical Power and Energy Systems, 2004. **26**(1): p. 31-36.
43. Chibante, R., *Simulated Annealing Theory with Applications*. 2010: Sciyo. 300.
44. Kirkpatrick, S., C.D. Gelatt, and M.P. Vecchi, *Optimization by simulated annealing*. Science, 1983. **220**(4598): p. 671-680.
45. Vecch, S.K.a.C.D.G.a.M.P., *Optimization by simulated annealing*. J Mathl. Comput. Modelling, 1983. **220**: p. 671--680.
46. Zhi-Jun, M., et al., *Parameter optimization for a PEMFC model with a hybrid genetic algorithm*. International Journal of Energy Research 2006. **30**: p. 585-597.
47. P.E. Gill, W.M., and M.H. Wright, *Practical Optimization*. 1981: Academic Press.
48. Alireza Askarzadeh, A.R., *Optimization of PEMFC model parameters with a modified particle swarm optimization*. International Journal of Energy Research, 2010.
49. Meiyong Yea, X.W., Yousheng Xua, *Parameter identification for proton exchange membrane fuel cell model using particle swarm optimization*. International Journal of Hydrogen Energy, 2009. **34**(2): p. 981-989
50. M. Sedighizadeh , A.R., M. Khoddam and N. Zarean, *Parameter Optimization for PEMFC model with Particle Swarm Optimization*. International Journal of Engineering & Applied Sciences (IJEAS), 2011. **3**(1): p. 102-108.
51. Haque , M.T.a.K.A.M., *Application of Neural Networks in Power Systems; A Review*. World Academy of Science, Engineering and Technology, 2005. **6**: p. 53-57.
52. Won-Yong Lee , G.-G.P., Tae-Hyun Yang , Young-Gi Yoon and Chang-Soo Kim *Empirical modeling of polymer electrolyte membrane fuel cell performance using artificial neural networks* International Journal of Hydrogen Energy, 2004. **29**(8): p. 961-966.
53. Hernán González Acuña , M.S.D., Omar Lengerke *Identification and modeling for non-linear dynamic system using neural networks type MLP*. Proceedings of the 2009 Euro American Conference on Telematics and Information Systems: New Opportunities to increase Digital Citizenship table of contents, 2009.
54. Steigerwald, R.L., *High frequency resonant transistor DC-DC converters*. IEEE Transactions on Industrial Electronics , 1984. **31**(2): p. 181-191.
55. Ned Mohan, T.U., William Robbins, *Power electronics, converters, Applications and Design*. Second Edition ed. 1995: John Wiley & sons, Inc. 802.
56. Kato, T., et al., *Modeling and simulation of a power electronic converter for EMC*. Proceedings of the IEEE Power Conversion Conference, 2002. PCC Osaka 2002. , 2002. **2**: p. 541-546.
57. Andersen, G.K., et al., *A new power converter for fuel cells with high system efficiency*. International Journal of Electronics, 2003. **90**(11-12): p. 737-750.
58. Xu, H., L. Kong, and X. Wen, *Fuel Cell Power System and High Power DC-DC converter*. IEEE Transactions on Power Electronics,, 2004. **19**(5): p. 1250-1255.
59. Shiju, W., *Design and hardware implementation of a soft-switched converter for fuel cell applications.*, in *Faculty of the Graduate School*. 2006, The University of Texas: Arlington. p. 109.
60. Krykunov, O., *Comparison of the DC/DC-Converters for Fuel Cell Applications*. International Journal of Electrical, Computer, and Systems Engineering, 2007. **1**(1): p. 71-79.

61. Rathore, A., A. Bhat, and R. Oruganti, *A Comparison of Soft-Switched DC-DC Converters for Fuel Cell to Utility Interface Application*. IEEE Proceedings, 2007: p. 588-594.
62. Rong-Jong, W. and D. Rou-Yong, *High-Efficiency Bidirectional Converter for Power Sources With Great Voltage Diversity*. IEEE Transactions on Power Electronics, 2007. **22**(5): p. 1986-1996.
63. Ying-Chun Chuang, Y.-L.K., Hung-Shiang Chuang, Hung-Kun Chen, *Implementation and Analysis of an Improved Series-Loaded Resonant DC-DC Converter Operating Above Resonance for Battery Chargers* IEEE Transactions on Industry Applications, 2009. **45**(3): p. 1052 - 1059
64. Ke Jin, X.R., *Hybrid Full-Bridge Three-Level LLC Resonant Converter—A Novel DC-DC Converter Suitable for Fuel-Cell Power System*. IEEE TRANSACTIONS ON INDUSTRIAL ELECTRONICS, 2006. **53**(5): p. 1492-1503.
65. Abu-Qahouq, J.B., I. . *Generalized analysis of soft-switching DC-DC converters*. in *IEEE Proceedings of Circuits and Systems, ISCAS 2000*. 2000. Geneva.
66. Açık, A. and I. Çadirci, *Active Clamped ZVS Forward Converter With Soft-Switched Synchronous Rectifier*. Turk Journal of Eletrical Engineering, 2002. **10**(3).
67. Cancelliere, P., et al., *Modeling and Control of a Zero-Current-Switching DC/AC Current-Source Inverter*. IEEE Transactions on Industrial Electronics 2007. **54**(4): p. 2106-2119.
68. Lee , Y.-S., Y.-Y. Chiu , and M.-W. Cheng, *Inverting ZCS Switched-Capacitor Bi-directional Converter*, in *37th IEEE Power Electronics Specialists Conference, PESC'06*. 2006: Jeju, Korea.
69. Hamill, D.C.B., K.N. , *Design oriented analysis of a resonant ZVS/ZCS DC-DC converter*. Fifth European Conference on Power Electronics and Applications, 1993. **3**: p. 23-29.
70. Ivensky, G., et al., *Reducing IGBT Losses in ZCS Series Resonant Converters*. IEEE Transactions on Industrial Electronics, 1999. **46**(1): p. 67-74.
71. Rathore Akshay K *ZVS Turn-on Soft Switched DC-DC Converters for High Voltage Applications*. ???, ??
72. Ryan, M.J., et al., *A new ZVS LCL-resonant push-pull DC-DC converter topology*. IEEE Transactions on Industry Applications, 1998. **34**(5): p. 1164 - 1174.
73. Yuang-Shung, L., et al. *Multiple Output Zero-Current Switching Bi-directional Converter*. in *33rd Annual Conference of the IEEE Industrial Electronics Society, IECON'07*. 2007.
74. N. Mohan, T.U., *Power Electronics, Converters Applications and Design*. 2003, New York: John Wiley and Sons, Inc.
75. Karlsson, P., *Quasi Resonant DC Link Converters*, in *Department of Industrial Electrical Engineering and Automation*. 1999, Lund Institute of Technology: Lund. p. 207.
76. Peng, F.Z., et al., *A New ZVS Bidirectional DC-DC Converter for Fuel Cell and Battery Application*. IEEE Transactions on Power Electronics, 2004. **19**(1): p. 54-65.
77. Hui, L., F.Z. Peng , and J.S. Lawler, *A natural ZVS high-power bi-directional DC-DC converter with minimum number of devices*. IEEE Conference on Industry Applications, 2001. **3**: p. 1874-1881.
78. Eberle, W. and L. Yan-Fei, *A Zero Voltage Switching Asymmetrical Half-Bridge DC/DC Converter With Unbalanced Secondary Windings For Improved Bandwidth*. IEEE 33rd Annual Power Electronics Specialists Conference, pesc 02, 2002. **4**: p. 1829-1834.
79. Mohammad, A., *Sliding mode control for switched mode power supplies* in *Department of Electrical Engineering of Lappeenranta*. 2004, Lappeenranta University of Technology Lappeenranta, Finland. p. 156.



80. Krykunov, O., *Comparison of the DC/DC-Converters for Fuel Cell Applications*. International Journal of Electrical, Computer, and Systems Engineering 2007. **1**(1): p. 71-79.
81. Lee, B.-T.L.K.-W.S.Y.-S., *Actively clamped zero-current-switching quasi-resonant converters using IGBTs*. Industrial Electronics, IEEE Transactions on, 1999. **46**(1): p. 75-81.
82. Nome, F.J. and I. Barbi. *A ZVS clamping mode-current-fed push-pull DC-DC converter*. in *Proceedings of IEEE International Symposium Industrial Electronics, ISIE '98*. 1998.
83. Lee, J.-Y., Y.-S. Jeong, and B.-M. Han, *An Isolated DC/DC Converter Using High-Frequency Unregulated LLC Resonant Converter for Fuel Cell Applications* IEEE Transactions on Industrial Electronics, 2011. **58**(7): p. 9.
84. Xin Kong, A.M.K., *Analysis and Implementation of a High Efficiency Interleaved Current-Fed Full Bridge Converter for Fuel Cell System*. IEEE TRANSACTIONS ON POWER ELECTRONICS, 2007. **22**(2): p. 543-550.
85. Averbeg, A.M., K.R.; Mertens, A., *Current-fed full bridge converter for fuel cell systems in IEEE Power Electronics Specialists Conference, PESC 2008*. 2008: Rhodes p. 866 - 872
86. Yang, S.-K.C.T.-J.L.J.-F.C.L.-S., *Novel High Step-Up DC-DC Converter for Fuel Cell Energy Conversion System*. IEEE Transactions on Industrial Electronics, 2010. **57**(6): p. 2007 - 2017
87. L. Schindele, M.B., H. Spath, *The Influence of Power Electronic Dynamics on PEM Fuel Cell-System*, in *European Conference on Power Electronics and Applications* 2005. p. 9.
88. Choi, W., *New approaches to improve the performance of the PEM based fuel cell power systems in Office of Graduate Studies of Texas A&M University*. 2004, Texas A&M University. p. 111.
89. Hamill, D.C. and K.N. Bateson, *An efficient active ripple filter for use in DC-DC conversion*. IEEE Transactions on Aerospace and Electronic Systems, 1996. **32**(3): p. 1077-1084.
90. Kramer, W., et al., *Advanced Power Electronic Interfaces for Distributed Energy Systems* 2008, National Renewable Energy Laboratory: **1617 Cole Boulevard, Golden, Colorado 80401-3393** p. 132.
91. Blaabjerg, F., Z. Chen, and S.B. Kjaer, *Power Electronics as Efficient Interface in Dispersed Power Generation Systems*. IEEE Transactions on Power Electronics, 2004. **19**(5): p. 1184-1194.
92. Jin, K. and X. Ruan, *Hybrid Full-Bridge Three-Level LLC Resonant Converter- A Novel DC-DC Converter Suitable for Fuel Cell Power System* IEEE Transactions on Industrial Electronics, , 2006. **53**(5): p. 12.
93. Cheron, Y., *La commutation douce dans la conversion statique de l'énergie électrique* Vol. 1. 1989: Lavoisier. 312.
94. Rivera, E.I. and L.A. Rodriguez *The Z-source converter as an introduction to power electronics and undergraduate research*. IEEE 37th annual Frontiers in education conference, FIE '07, 2007: p. T2C-5-T2C-10.
95. Peng Fang Zheng, H.Y., *Z-Source Inverter for Power Conditioning and Utility Interface of Renewable Energy Sources*. ???, ???
96. Peng, F.Z., *Z-source inverter*. IEEE Transactions on Industry Applications, 2003. **39**(2): p. 504-510.
97. Xu, L. and J. Liu, *Comparison study of DC- DC-AC combined converters for integrated starter generator applications*. 4th International Power Electronics and Motion Control Conference, IPEMC'04 2004. **3**: p. 1130- 1135.
98. Yoon-Ho, K., et al. *A fuel cell system with Z-source inverters and ultracapacitors*. in *4th International Power Electronics and Motion Control Conference, IPEMC'04*. 2004.

99. Peng, F.Z., et al., *Z-Source Inverter for Adjustable Speed Drives*. IEEE Power Electronics Letters, 2003. **1**(2): p. 33-35.
100. Erickson, R.W. and D. Maksimovic, *Fundamentals of Power Electronics*. 2001, Boulder, Colorado: Electronic Services. 871.
101. Ridley, R.B., *A new, continuous-time model for current-mode control*. IEEE Transactions on Power Electronics, 1991. **6**(2): p. 271-280.
102. Tang, W.L., F.C.; Ridley, R.B., *Small-signal modeling of average currentmode control*. IEEE Transactions on Power Electronics, 1993. **8**(2): p. 112-119.
103. P. Midya, P.T.K., M.F. Greuel, *Sensorless Current Mode Control – An Observer – Based Technique for DC-DC Converters*. IEEE Transactions on Power Electronics, 2001. **16**(4): p. 522-526.
104. Karl J. Astrom , D.B.W., *Adaptive Control*, ed. S. Edition. 2008: Dover Publications.
105. Youssef, M.Z.J., P.K. , *A review and performance evaluation of control techniques in resonant converters*. 30th Annual Conference of IEEE Industrial Electronics Society, IECON 2004, 2004. **1**: p. 215-221.
106. Fanjul, L.M.P., *Some new applications of supercapacitors in power electronic systems*, in *Electrical Engineering*. 2003, Texas A&M University. p. 113.
107. Heinz Schmidt-Walter , H.W., Thomas Zänker, Richard Morgan and Johnalan Kegan. *Design of Switch Mode Power Supplies*. Available from: [http://schmidt-walter.eit.h-da.de/smpps\\_e/smpps\\_e.html](http://schmidt-walter.eit.h-da.de/smpps_e/smpps_e.html)
108. Schmidt-Walter, H. *Design of Switch Mode Power Supplies*. Available from: [http://schmidt-walter.eit.h-da.de/snt/snt\\_eng/snte\\_pdf.html](http://schmidt-walter.eit.h-da.de/snt/snt_eng/snte_pdf.html).

---

# *APPENDICES*

---



## TABLE OF CONTENTS

<b>APPENDIX A – PEMs characterization .....</b>	<b>203</b>
<i>A.1. Introduction.....</i>	<i>203</i>
<i>A.2. PEM GenCore™.....</i>	<i>203</i>
A.2.1. Performance characteristics of the GenCore™ .....	204
A.2.2. Fuel cell stack voltage and power .....	205
A.2.3. Efficiency and hydrogen consumption .....	205
A.2.4. GenCore™ parameters .....	206
<i>A.3. PEM Nexa™.....</i>	<i>207</i>
A.3.1. Performance characteristics of the Nexa™ .....	208
A.3.2. Fuel cell stack voltage and power .....	208
A.3.3. Efficiency and hydrogen consumption .....	209
A.3.4. Nexa parameters .....	210
<i>A.4. PEM Mark1020.....</i>	<i>211</i>
A.4.1. Simulink® steady-state analysis of the 28-cells stack.....	211
A.4.2. Experimental analysis of the 28-cells stack.....	213
A.4.3. Fuel cell stack voltage and power .....	215
A.4.4. Efficiency and hydrogen consumed .....	215
A.4.5. Temperature .....	216
A.4.6. Mark1020 parameters.....	217
<i>A.5. PEM Bahia .....</i>	<i>218</i>
A.5.1. Technical characteristics and operation of Bahia.....	219
A.5.2. Bahia parameters.....	219
<i>A.6. Conclusions.....</i>	<i>220</i>
<b>APPENDIX B – Model of the PEM in neural networks .....</b>	<b>223</b>
<i>B.1. Introduction.....</i>	<i>223</i>
<i>B.2. Definition of the architecture.....</i>	<i>224</i>
B.2.1. Input and output variables .....	224
B.2.2. Data processing.....	225
<i>B.3. Training and evaluation .....</i>	<i>225</i>
<i>B.4. Modeling of the PEM Bahia.....</i>	<i>226</i>
<i>B.5. Conclusions.....</i>	<i>228</i>
<b>APPENDIX C – Numerical analysis of the series resonant converter .....</b>	<b>231</b>
<i>C.1. Introduction.....</i>	<i>231</i>
<i>C.2. Analysis based on sinusoidal approximation .....</i>	<i>231</i>

C.2.1.	Impedance .....	232
C.2.2.	Quality factor .....	234
C.2.3.	Bandwidth.....	235
C.2.4.	Operation and switching losses.....	236
C.2.5.	Full-bridge topology .....	238
C.3.	<i>Analysis based on second-order differential equation .....</i>	<i>244</i>
C.3.1.	Considerations on initial conditions .....	246
C.3.2.	Response of the circuit in underdamped case ( $Q < 0.5$ ) .....	247
C.3.3.	Response of the circuit in overdamped case ( $Q > 0.5$ ) .....	248
C.3.4.	Peak current analysis.....	250
C.3.5.	Selection of $L_r$ and $C_r$ .....	252
C.3.6.	Analysis of the results.....	255
C.4.	<i>Conclusions.....</i>	<i>255</i>
<b>APPENDIX D</b>	<b>- Operation of the series resonant converter.....</b>	<b>259</b>
D.1.	<i>Introduction.....</i>	<i>259</i>
D.2.	<i>Operation in open-loop.....</i>	<i>259</i>
D.2.1.	Open-loop response for different VCO values .....	259
D.2.2.	Open-loop response for different load values .....	260
D.2.3.	Open-loop response to step-up and step-down load conditions.....	261
D.3.	<i>Operation in closed-loop .....</i>	<i>262</i>
D.3.1.	VCO signal analysis.....	262
D.3.2.	Output voltage analysis .....	262
D.3.3.	Fuel cell current and voltage analysis.....	263
D.3.4.	Ripples of current and voltage versus PEM filter.....	264
D.3.5.	Resonant circuit analysis .....	266
D.3.6.	Ripples of current and voltage versus output filter .....	266
D.4.	<i>Conclusions .....</i>	<i>267</i>
<b>APPENDIX E</b>	<b>- Considerations on handling hydrogen safety .....</b>	<b>271</b>
E.1.	<i>Introduction.....</i>	<i>271</i>
E.2.	<i>Hydrogen production and storage.....</i>	<i>271</i>
E.3.	<i>Equipments of measurement and control .....</i>	<i>272</i>
E.3.1.	Hydrogen fuel mass flow .....	272
E.3.2.	Hydrogen leaks detector .....	273
E.3.3.	Control of the temperature .....	273
E.4.	<i>Electrical Equipment .....</i>	<i>273</i>

E.4.1.	Voltage and current measurements.....	273
E.4.2.	Digital Oscilloscope .....	275
E.4.3.	Power supply .....	275

## LIST OF FIGURES

Figure A.1– Overview of the GenCore™ 5B48 system.....	203
Figure A.2- Schematic of the GenCore™ 5B48 system. ....	204
Figure A.3– Stack voltage of GenCore™. ....	205
Figure A.4 – Stack power of GenCore™. ....	205
Figure A.5 –Efficiency of GenCore™. ....	205
Figure A.6 – Hydrogen consumed by GenCore™. ....	205
Figure A.7 - Overview of the Nexa™ system. ....	207
Figure A.8 - Schematic of the Nexa™ system. ....	208
Figure A.9 – Stack voltage of Nexa™. ....	209
Figure A.10 – Stack power of Nexa™. ....	209
Figure A.11 – Efficiency of Nexa™. ....	209
Figure A.12 - Overview of the MARK family. ....	211
Figure A.13 - Steady-state voltage conditions of the 28-cell stack of Mark1020. ....	212
Figure A.14 - Steady-state current conditions of the 28-cell stack of Mark1020.....	212
Figure A.15 - Steady-state power conditions of the 28-cell stack of Mark1020.....	213
Figure A.16 – Electrical circuit used to make the experimental tests with PEM Mark1020. ....	214
Figure A.17 – Stack voltage of Mark <sub>1020</sub> . ....	215
Figure A.18 – Stack power of Mark <sub>1020</sub> .....	215
Figure A.19 – Efficiency of Mark <sub>1020</sub> . ....	216
Figure A.20 – Hydrogen consumed by Mark <sub>1020</sub> .....	216
Figure A.21 – Temperature in Mark <sub>1020</sub> . ....	216
Figure A.22 - Overview of the Bahia system. ....	218
Figure A.23 - Schematic and graphical user interface of Bahia system. ....	219
Figure B.1 – Information processing in a neural network unit.....	223
Figure B.2 – Schematic of the NN model for the PEM fuel cell.....	224
Figure B.3 - Input data for training and validation the network.....	226
Figure B.4 - Target data of the network. ....	226
Figure B.5 – Average error of the model as a function of the epoch's number. ....	227
Figure B.6 – Performance of the method. ....	227
Figure B.7– Validation for PEM Bahia. ....	228
Figure C.1–Simple equivalent circuit of the SRC. ....	231
Figure C.2 –The series-resonant circuit waveforms. ....	232



Figure C.3 - Series resonant circuit with a resistive load.....	233
Figure C.4 – Input impedance, $Z/Z_0$ of the series resonant circuit for different values of $Q$ .....	235
Figure C.5 – Phase of the series resonant circuit for different values of $Q$ . ....	235
Figure C.6 - Bandwidth of resonant circuit.....	236
Figure C.7 - Operation of the SRC below and above the resonant frequency. ....	237
Figure C.8– Full-bridge topology of the SRC.....	238
Figure C.9 – Output voltage in a full-bridge inverter. ....	238
Figure C.10 - Amplitude of the current in the series resonant circuit.....	240
Figure C.11 - Amplitude of the power in the series resonant circuit. ....	242
Figure C.12- Bloc diagram of the voltage transfer function of the resonant inverter.....	243
Figure C.13- Representation of the SRC by a 2nd-order differential equation. ....	244
Figure C.14- Underdamped response of the RLC circuit for $Q=0.2$ .....	248
Figure C.15- Overdamped response of the RLC circuit for $Q=0.9$ .....	249
Figure C.16 - Peak of the resonant current for different values of $V_{in}$ and $C_r=4\ \mu F$ .....	251
Figure C.17- Experimental validation of the resonant current for two capacitors.....	252
Figure C.18 - Output variables for the minimum voltage of the PEM Mark1020 (19.11V). ....	253
Figure C.19 - Output variables for the maximum voltage of the PEM Mark1020 (23.71V). ....	253
Figure C.20 - Output variables for the maximum voltage of the PEM Nexa™ (44 V).....	253
Figure C.21- Operation of the SRC on its entire range for minimum input voltage. ....	254
Figure C.22- Operation of the SRC on its entire range for maximum input voltage.....	254
Figure D.1 – Output voltage of the converter for different VCO values. ....	260
Figure D.2 – Output voltage of the converter for different load values.....	260
Figure D.3 – Output voltage of converter for two initial values and two VCO values. ....	261
Figure D.4 – Open loop response to step-up and step-down load currents.....	261
Figure D.5 –VCO with a step load at time 0.04 s. ....	263
Figure D.6 – Output voltage with a step load at time 0.04 s.....	263
Figure D.7 – Fuel cell current for a change in the load at time 0.04s.....	264
Figure D.8 – Fuel cell voltage for a change in the load at time 0.04s.....	264
Figure D.9 – Ripple of current with and without filter in the PEM. ....	265
Figure D.10 – Ripple of the fuel cell voltage.....	265
Figure D.11 – Voltage and current waveforms in the resonant circuit. ....	266
Figure D.12 – Ripple of output current of the converter. ....	267
Figure E.1 –Hydrogen Production Pathway .....	271
Figure E.2- Hydrogen in a network. ....	272

Figure E.3- Hydrogen in a Tank.....	272
Figure E.4 - Mass Flow Meter and Controller.....	272
Figure E.5 - Fuel mass flow display.....	272
Figure E.6 - Gas Detector TIF8800.....	273
Figure E.7 - K-Type Waterproof Thermometer.....	273
Figure E.8 - Digital Multimeter.....	274
Figure E.9 - current probe Tektronix A622.....	274
Figure E.10 –Rogowski current transducer operating principle.....	274
Figure E.11 - Digital oscilloscope.....	275
Figure E.12 - DC Power supply.....	275

## LIST OF TABLES

Table A.1– GenCore parameters.....	206
Table A.2 - Nexa parameters .....	210
Table A.3 - Experimental results of PEM Mark1020. ....	214
Table A.4 - Mark1020 parameters .....	217
Table A.5 - Bahia parameters. ....	220
Table C.1 - Resonant peak current analysis. ....	251
Table C.2 - Comparative analysis of the performance for two sets of components Lr and Cr.....	254
Table D.1 – Fuel cell ripple analysis.....	266
Table E.1 –Digital oscilloscope characteristics .....	275
Table E.2 – DC power supply characteristics. ....	275



---

# *APPENDIX A*

## **PEM<sub>s</sub> CHARACTERIZATION**

---



## APPENDIX A – PEMs characterization

### A.1. Introduction

This appendix provides the main characteristics of the various PEM's used as already summary described in Chapter 2 of the thesis. Particularly, the GenCore of Plug Power [1], Nexa and Mark1020 of Ballard [2], and Bahia of AVERA [3] fuel cell systems are presented and characterized.

### A.2. PEM GenCore<sup>TM</sup>

The GenCore<sup>TM</sup> 5B48 is a PEM fuel cell system of Plug Power. This system is designed to provide a quality backup DC power for critical loads in DC bus applications as well as to charge an existing battery bank., which voltage varies between +42 and +60 V<sub>DC</sub>. The nominal voltage value is +48 V<sub>DC</sub>, the current varies between 0 and 109 A, and the output power from 0 to 5000 W. It has a 63 cells stack, and the operating temperature varies between +42 °C and +56 °C. The GenCore<sup>TM</sup> system must be fuelled by hydrogen with a purity of 99.95% and a pressure between 1.5 and 1.8 psig. An overview of the GenCore<sup>TM</sup> system is presented in Figure A.1.



Figure A.1– Overview of the GenCore<sup>TM</sup> 5B48 system.

The diagram of Figure A.2 shows the circulation circuits of the different subsystems involved in the process of generating energy in the GenCore™, namely; the hydrogen circulation subsystem (blue color) gets to the system through the gas inlet, then it goes pass the solenoid valves which, in case of emergency, can stop the further flow of hydrogen into the system. There is always some hydrogen getting out of the system through the cathode air exhaust, but it is an insignificant quantity. Air circulation subsystem (green color) gets to the cathode side with the help of the cathode air blower. The speed of the blower depends on the power demand from the load. The higher the current that needs to be supplied, the faster the blower works. A coolant pump produces the circulation of the coolant (light blue color) through the stack, radiator and heater. As is known the fuel cell voltage is not stable, which is why a DC/DC converter is used in the case of a drop of voltage (red color) the current flows from the fuel cell into the power converter.

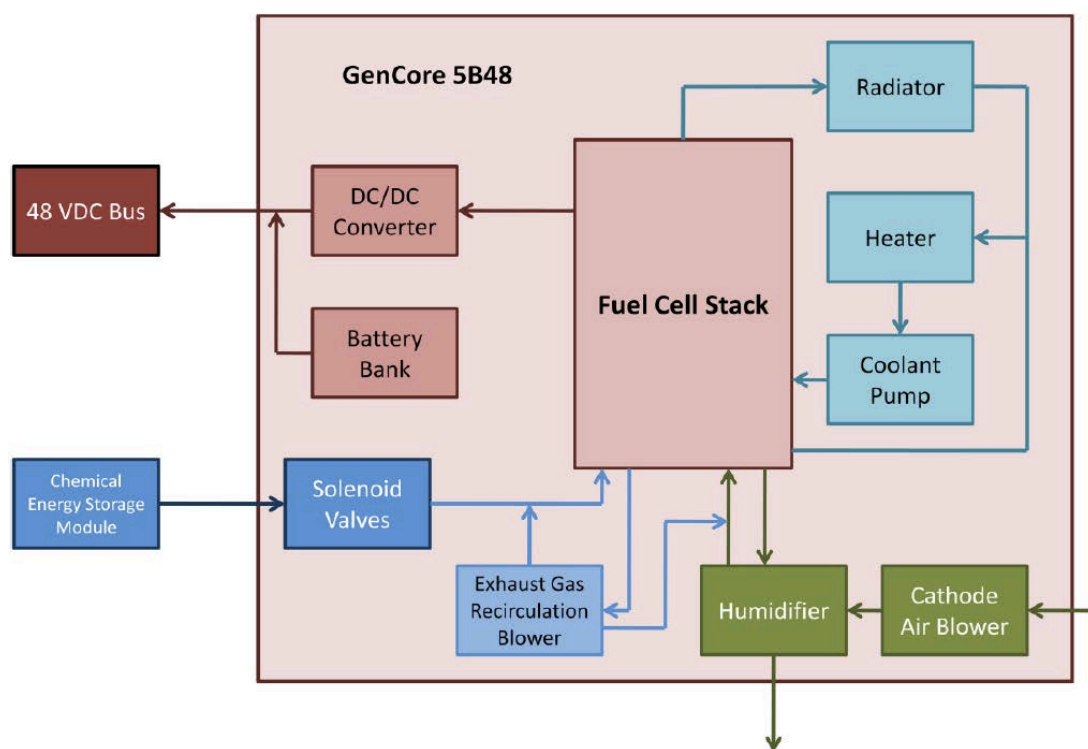


Figure A.2- Schematic of the GenCore™ 5B48 system.

### A.2.1. Performance characteristics of the GenCore™

Performance characteristics of the GenCore™ system are presented follow for the operating conditions defined above and room ambient temperature.



### A.2.2. Fuel cell stack voltage and power

Figure A.3 shows that the stack voltage in the GenCore decreases from 54.26 V to 52.5 V as the current increases to 120A. This voltage drop is due to: 1) the activation of the anode and cathode ( $V_{act}$ ), 2) the resistances to the protons conduction ( $V_{Ohm}$ ) and 3) the oxygen and hydrogen concentrations ( $V_{con}$ ). Figure A.4, shows the stack power of the GenCore, which is in accordance with the information provided by the manufacturer.

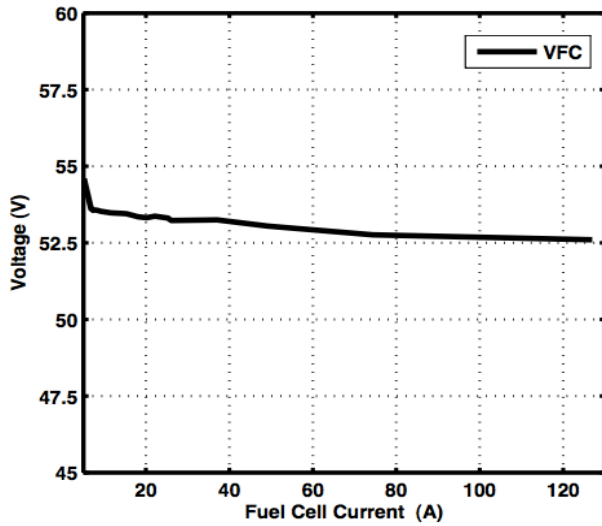


Figure A.3– Stack voltage of GenCore™.

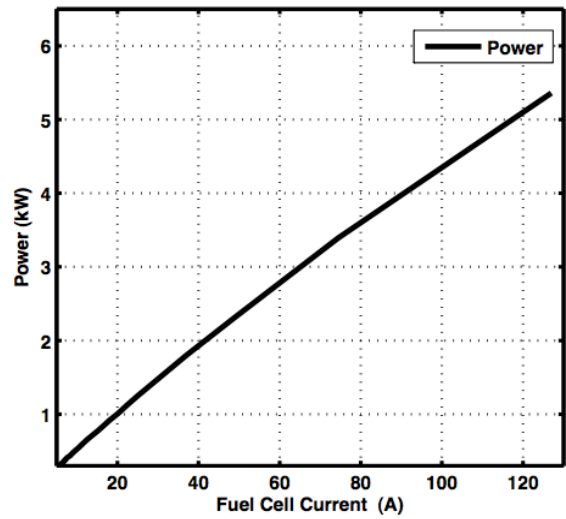


Figure A.4 – Stack power of GenCore™.

### A.2.3. Efficiency and hydrogen consumption

The efficiency is in the range of 40 to 55 %, which minimum and maximum values are respectively 45.15 % and 55.49 %. The efficiency decreases slightly with the increase of the current density as is shown in Figure A.5. The hydrogen consumption is proportional to the current density as is shown in Figure A.6.

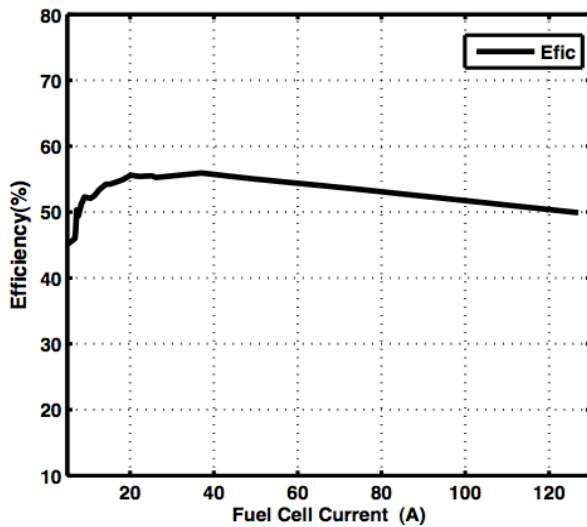


Figure A.5 –Efficiency of GenCore™.

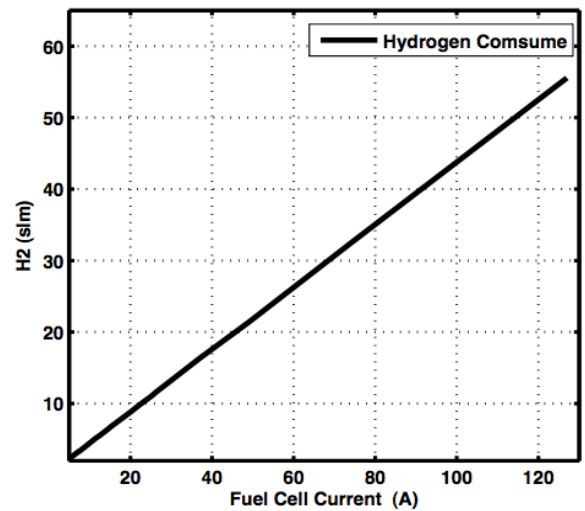


Figure A.6 – Hydrogen consumed by GenCore™.

#### A.2.4. GenCore™ parameters

The optimum set of parameters achieved by the application of Simulated Annealing SA method for the GenCore™ is presented in Table A.1. The optimization method is carried out by comparing experimental and simulated results and by analyzing objective function's evolution during the annealing process. The set of parameters presented is related to the semi-empirical model adopted by the authors.

Table A.1– GenCore parameters.

Parameter	Unit	Value
$A$	$\text{cm}^2$	69.7
$\lambda$	$\mu\text{m}$	118
$R_C$	$\Omega$	0.00019
$\xi_1$	No dimensional	-0.475
$\xi_2$	No dimensional	0.00273
$\xi_3$	No dimensional	0
$\xi_4$	No dimensional	-1.0 e-4
$\psi$	No dimensional	26.8
$B$	V	0.0171
$J_{max}$	$\text{A}/\text{cm}^2$	1600
$C$	F	2.3

### A.3. PEM Nexa™

An overview of the Nexa™ system is presented in Figure A.7. The Nexa™ system is a product of Ballard that provides a 1200 W of net output power. The output voltage varies with power, ranging from 43 V at system idle to about 26 V at full load. The Nexa™ power module operates with pure, dry hydrogen from any suitable source. About 57% of the hydrogen energy consumed by the Nexa™ system is converted into heat, while 43% is in the form of electric energy. The fuel cell stack is pressurized with hydrogen during operation. Hydrogen pressure is normally maintained at 5 psig. The fuel cell operating temperature is maintained at 65°C by varying the speed of the cooling fan. The Nexa™ system needs to provide power to support the auxiliary devices (air pump, cooling fan, as well as onboard sensors, actuators and controllers), which are approximately 35 W at system idle and 250 W at rated power.

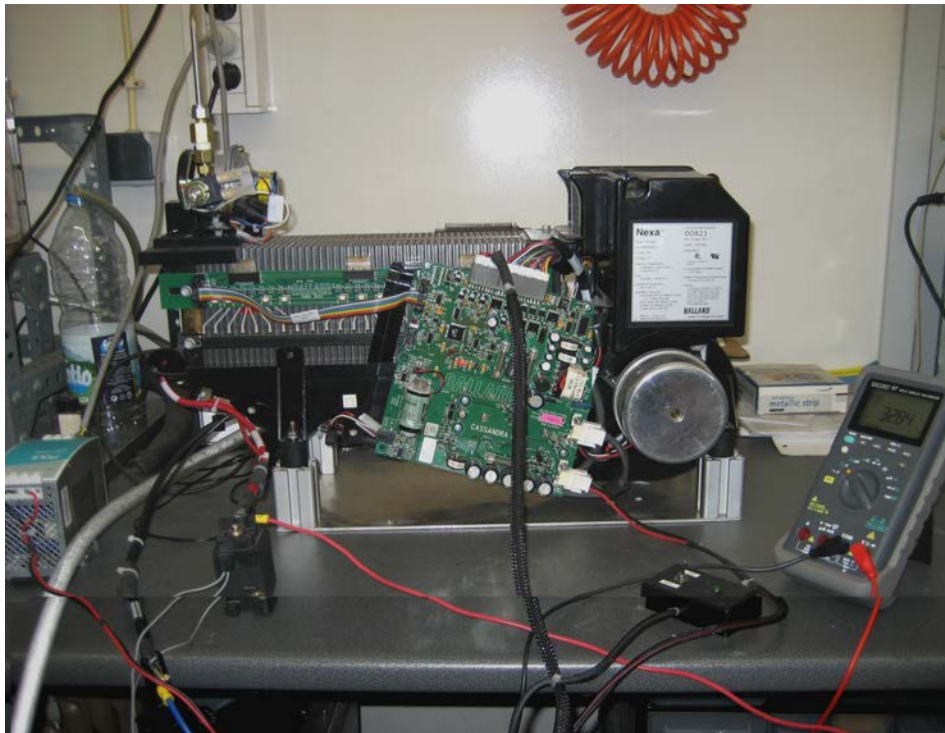


Figure A.7 - Overview of the Nexa™ system.

In Figure A.8 it is illustrated the Nexa™ system schematic [4], which is automated by an electronic control system. As can be seen, the control board receives various input signals from onboard sensors. Input signals to the control board include: fuel cell stack temperature, hydrogen pressure, hydrogen leak concentrations, fuel cell stack current, air mass flow, fuel cell stack voltage and purge

cell voltage. The status of the Cell Voltage Checker (CVC) system is also an input to the control board, presenting either a Pass or Fail result for the operational status of the stack. Finally, the ambient oxygen concentration is measured by an onboard sensor and sent to the controller, to ensure a safe operating environment for the user.

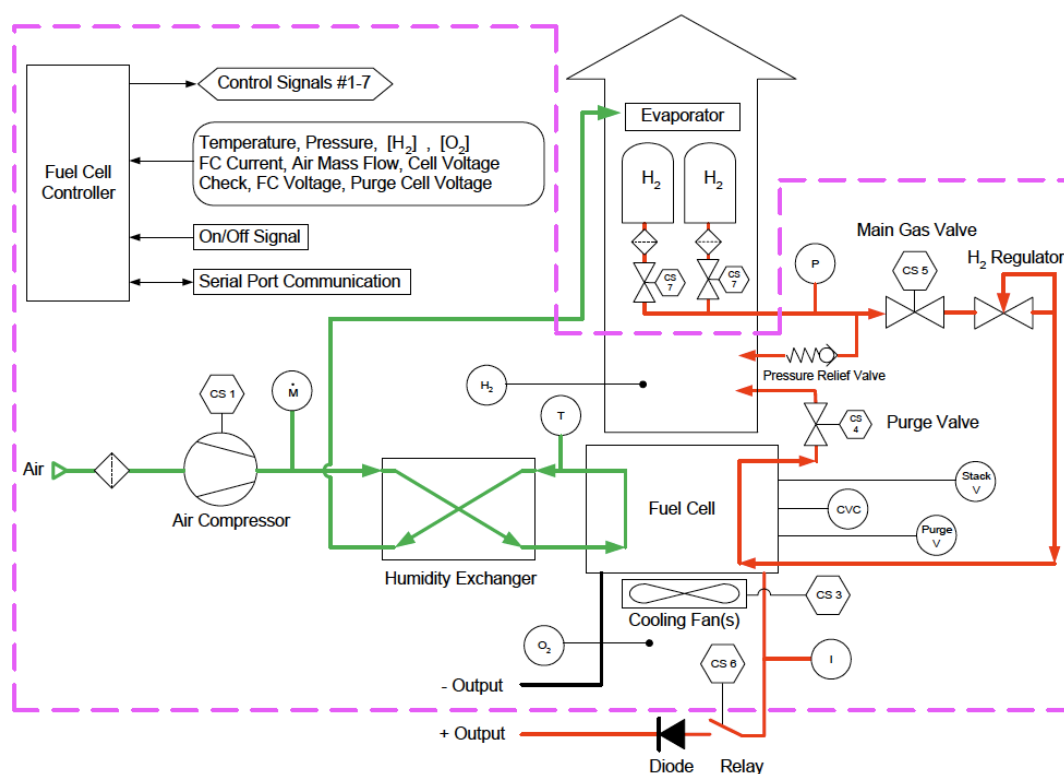


Figure A.8 - Schematic of the Nexa<sup>TM</sup> system.

### A.3.1. Performance characteristics of the Nexa™

Performance characteristics of the Nexa™ power module are presented follow for the operating conditions defined above and room ambient temperature.

### A.3.2. Fuel cell stack voltage and power

The fuel cell stack voltage of the Nexa™ system is presented in Figure A.9 As can be seen it varies from 53.46 VDC to 35 VDC with operating load according to the polarization characteristics of the fuel cell stack. The normal idle voltages of the Nexa™ system is approximately 44 V<sub>DC</sub> as the current increases from zero to 40 A. The stack power of the Nexa™ system is presented in Figure A.10, which is in accordance with the information provided by the manufacturer.

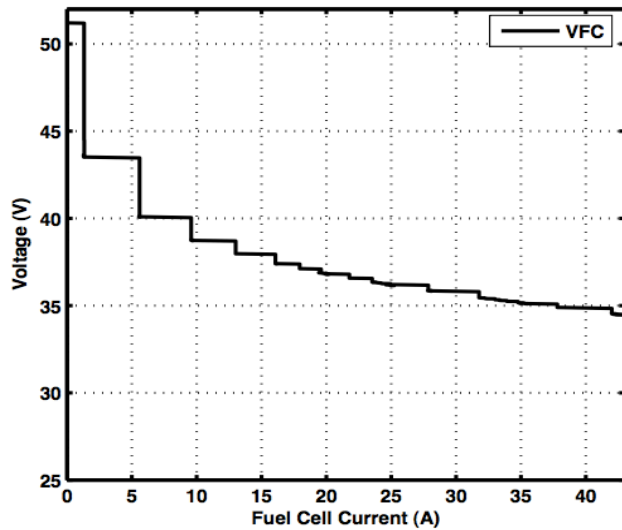


Figure A.9 – Stack voltage of Nexa™.

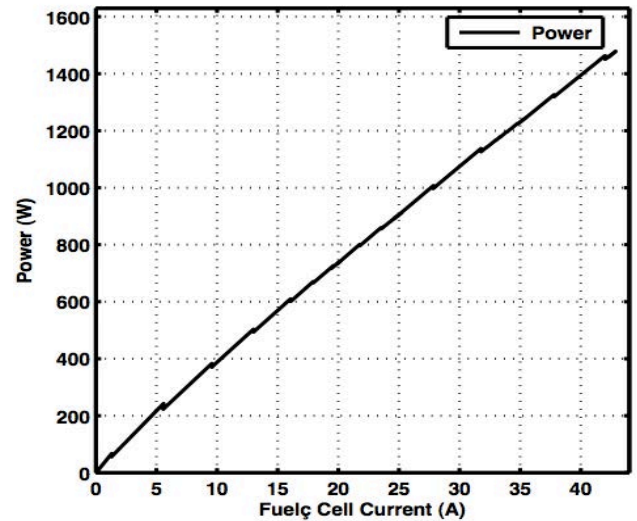


Figure A.10 – Stack power of Nexa™.

### A.3.3. Efficiency and hydrogen consumption

Figure A.11 illustrates the efficiency of the Nexa™ system as a function of output current. The efficiency of this stack is in the range of 23 % and 33 %. The system efficiency decreases quickly to loads less than 300W, as the auxiliary loads begin to dominate the requirement for hydrogen consumption. Similarly of the GenCore system previously studied, the hydrogen consumption in the Nexa™ system is proportional to the stack current.

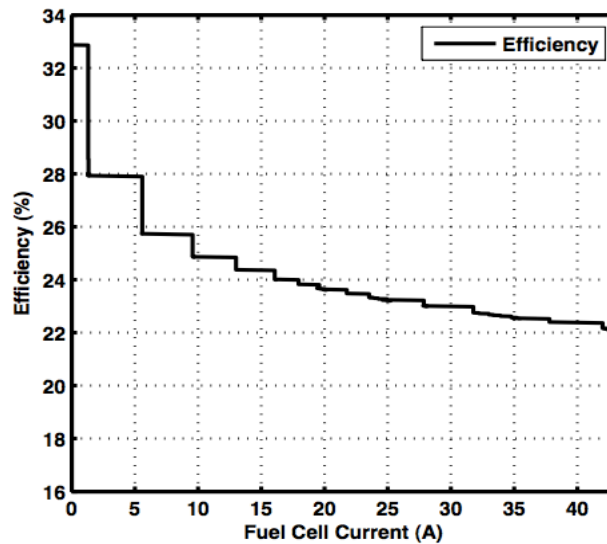


Figure A.11 – Efficiency of Nexa™.

#### A.3.4. Nexa parameters

The optimum set of parameters of the Nexa<sup>TM</sup> PEM, achieved by the application of the SA method is presented in

Table A.2. The optimization method is carried out by comparing experimental and simulated results and by analyzing objective function's evolution during the annealing process. The set of parameters presented is related to the semi-empirical model adopted by the authors.

Table A.2 - Nexa parameters

Parameter	Unit	Value
$A$	$\text{cm}^2$	53.6
$\lambda$	$\mu\text{m}$	177
$R_C$	$\Omega$	0.000275
$\xi_1$	No dimensional	-0.942
$\xi_2$	No dimensional	0.00256
$\xi_3$	No dimensional	$7.7 \times 10^{-5}$
$\xi_4$	No dimensional	$-2.04 \times 10^{-4}$
$\psi$	No dimensional	24.36
$B$	V	0.0156
$J_{max}$	$\text{A/cm}^2$	1513
$C$	F	3.049

#### **A.4. PEM Mark1020**

The Mark1020 ACS™ stack is a Ballard® fuel cell power product that produces clean DC power with can be scaled to meet power requirements from 300 W to 5000 W. The PEM Mark1020 ACS™ can be integrated into motive or stationary power applications, where durability, reliability and a simplified balance of plant are key requirements. An overview of the “Mark family” is presented in Figure A.12.

The Mark1020 ACS™ has been engineered to incorporate advanced open cathode technology and state of the art self-humidifying membrane electrode assemblies (MEAs). These features completely eliminate the need for humidification systems and simplify system integration. The result is a simple, low cost design delivering reliable operation over a wide range of challenging conditions.

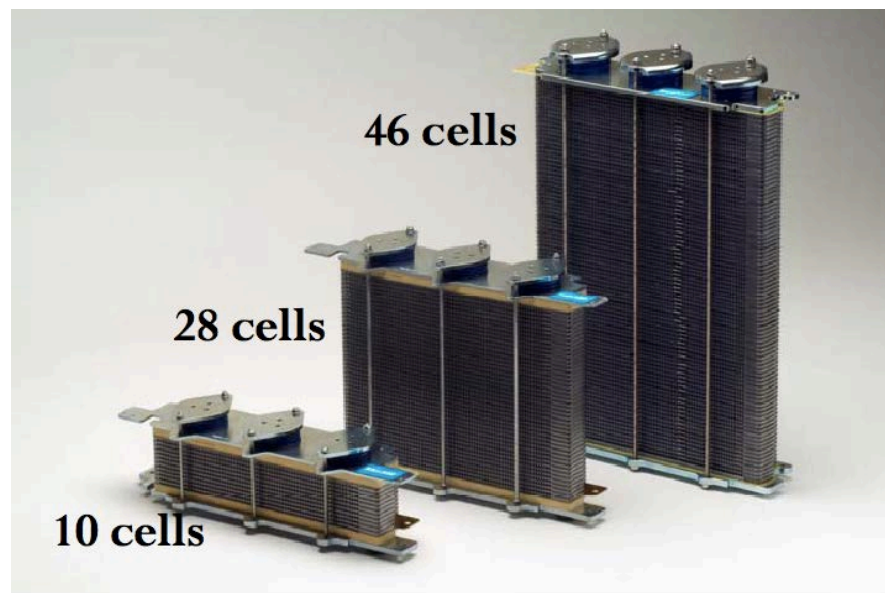
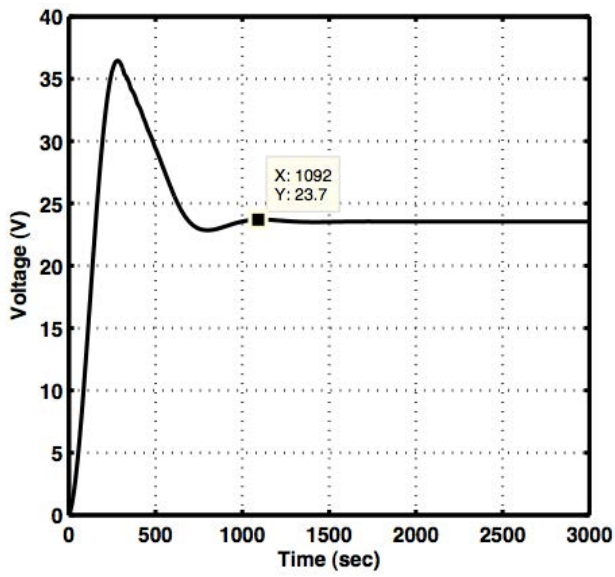


Figure A.12 - Overview of the MARK family.

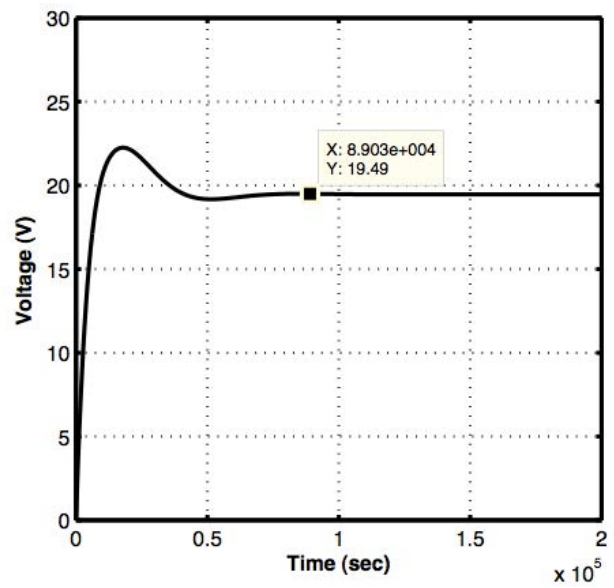
##### **A.4.1. Simulink® steady-state analysis of the 28-cells stack**

The 28-cells stack was selected to validate experimentally the investigation of this thesis. Thus, once implemented the analytical model of PEM in Simulink®, with the optimal parameters achieved by SA, the analysis of its static behavior is done. The steady-state variables analyzed are; the voltage, the current and the power, represented in the figures below. This procedure allows knowing the constraints imposed by this PEM to the power converter, that is, the minimum and maximum values imposed on the system, which defines the selection and the design of power components.



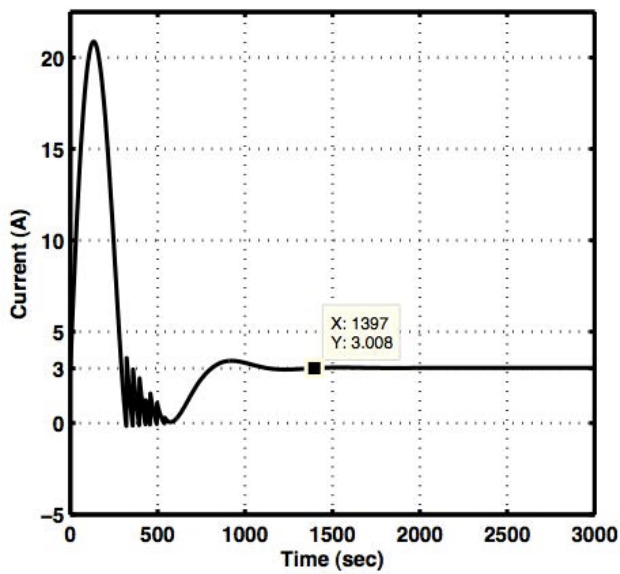


a) Maximum voltage ( $V_{max}=23.7$  V).

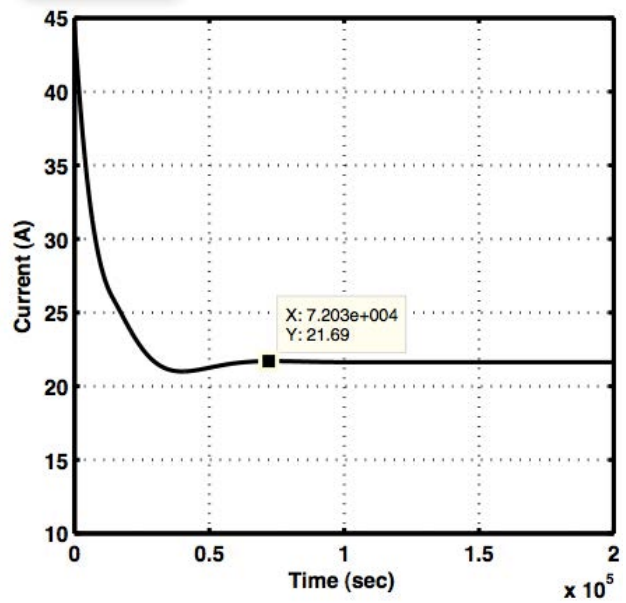


b) Minimum voltage ( $V_{min}=19.49$  V).

Figure A.13 - Steady-state voltage conditions of the 28-cell stack of Mark1020.



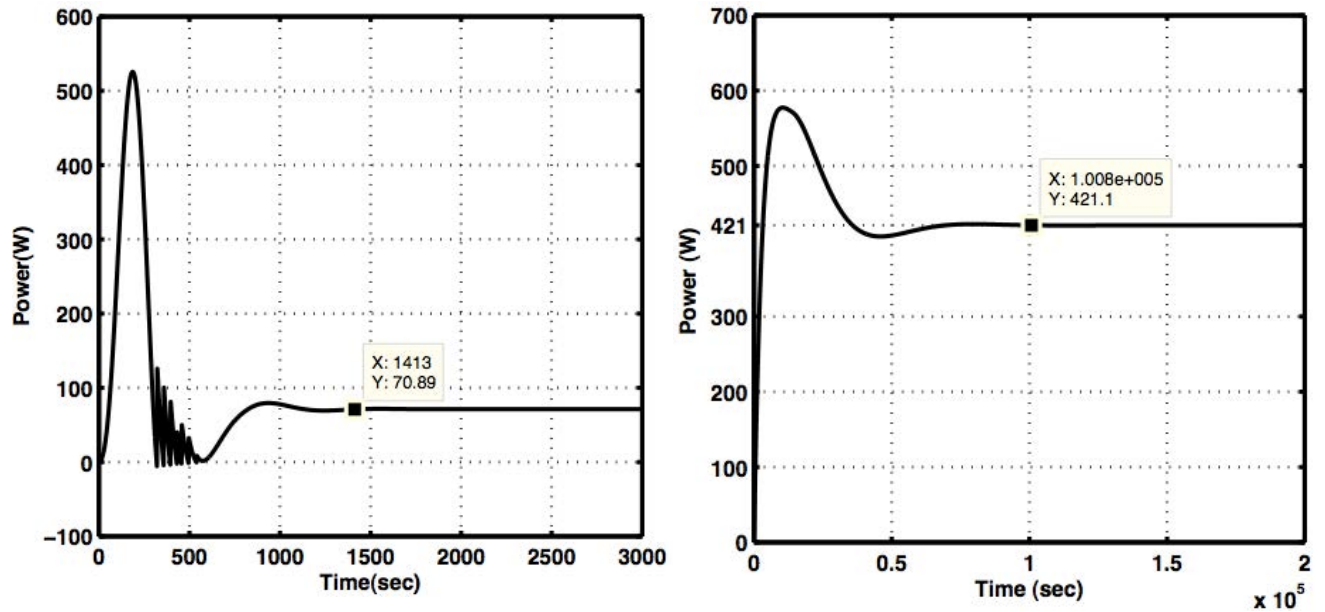
a) Minimum current ( $I_{min} = 3$  A).



b) Maximum current ( $I_{max} = 21.69$  A).

Figure A.14 - Steady-state current conditions of the 28-cell stack of Mark1020.





a) Minimum power ( $P_{min} = 70.89 \text{ W}$ ).

b) Maximum power ( $P_{max} = 421.1 \text{ W}$ ).

Figure A.15 - Steady-state power conditions of the 28-cell stack of Mark1020.

#### A.4.2. Experimental analysis of the 28-cells stack

The performance of the 28-cells stack is made experimentally using the electrical circuit of Figure A.16. The load is composed by a set of several resistors connected in parallel, whose variation is performed by manual switches. The fuel pressure that provides a PEM stack is monitored by a standard dial pressure gauge, which maintains it constant in the range of 0.3 bars to 0.5 bars. A ventilator is used to inject the oxidant flow necessary into the stack in order to produce the electrochemical reaction. The variables measured are presented in Table A.3 follow, and they are: the fuel cell voltage  $V_{FC}$  (V), fuel cell current  $I_{FC}$  (A), the power  $P$  (W), the temperature Temp ( $^{\circ}\text{C}$ ), and the hydrogen consumption  $H2_{cons}$  (L/min). However, as mentioned above, only the conditions of minimum and maximum are considered in the selection and the design of the elements of the converter. In particular, were considered the values marked with (\*).

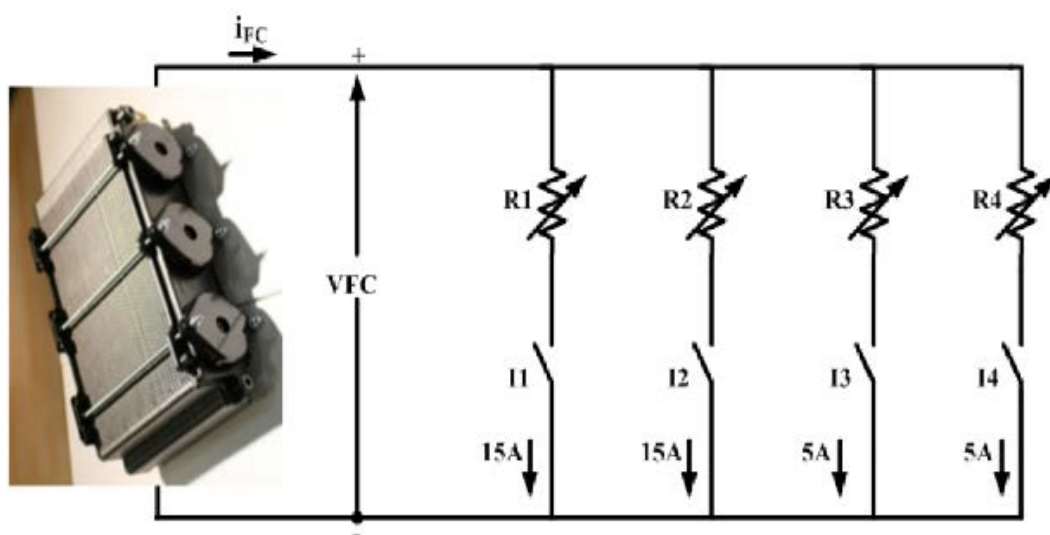


Figure A.16 – Electrical circuit used to make the experimental tests with PEM Mark1020.

Table A.3 - Experimental results of PEM Mark1020.

H <sub>2</sub> cons (L/min)	I <sub>fc</sub> (A)	V <sub>fc</sub> (V)	Power (W)	Temp (°C)
<b>5.14</b>	<b>2.8 (*)</b>	<b>23.71(*)</b>	<b>66.388(*)</b>	<b>26.8</b>
5.15	4.02	22.8	91.656	25.2
5.16	6	22	132	25.4
5.16	8	21.3	170.4	26.4
5.17	10	20.88	208.8	27.3
5.18	12	20.68	248.16	28.4
5.19	14	20.33	284.62	30.2
5.20	16	20.06	320.96	33.7
7.60	16.4	20.19	331.116	34.5
7.60	18	19.99	359.82	36
7.61	20	19.71	394.2	37.5
7.62	22	19.41	427.02	38.9
<b>7.63</b>	<b>24(*)</b>	<b>19.11(*)</b>	<b>458.64(*)</b>	<b>39.7</b>

#### A.4.3. Fuel cell stack voltage and power

The output voltage and power of PEM Mark1020 are presented in Figure A.17 and Figure A.18 respectively. As can be seen the output voltage of this PEM decreases from 23.71 V<sub>DC</sub> to 19.11 V<sub>DC</sub> as the current increases from 2.8 A to 24 A. The stack power reaches 458.64 W at 24 A of current. The output voltage of the PEM Mark1020 is 19.11 V at maximum power and current. That is, the voltage decreases and the power increases as the current increases.

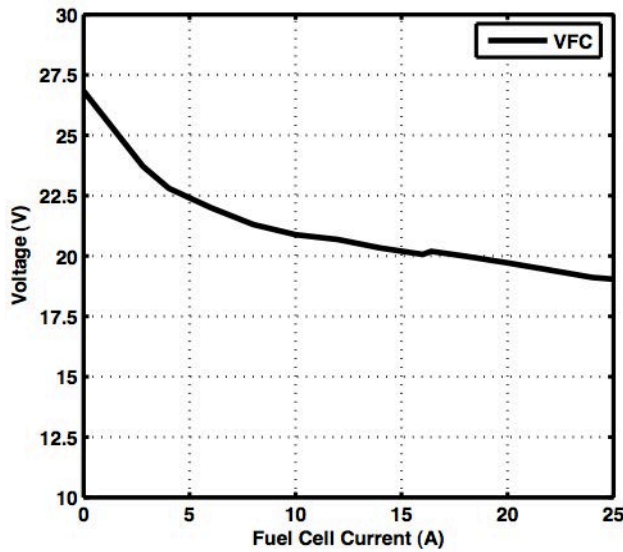


Figure A.17 – Stack voltage of Mark<sub>1020</sub>.

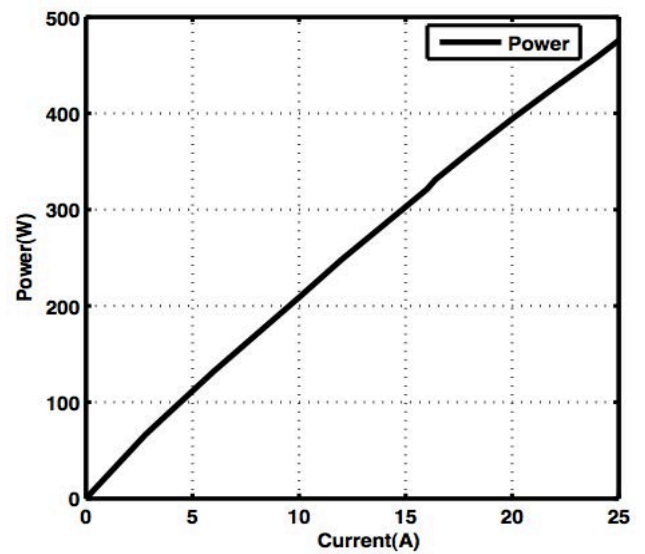


Figure A.18 – Stack power of Mark<sub>1020</sub>.

#### A.4.4. Efficiency and hydrogen consumed

As can be seen in Figure A.19 the electrical efficiency of the stack MARK1020 decreases slightly between 33% and 23% as the current increases. Similarly to the stack power, the hydrogen consumed by the stack Mark1020 with 28 cells increases with the increase of the current as represented in Figure A.20 below.

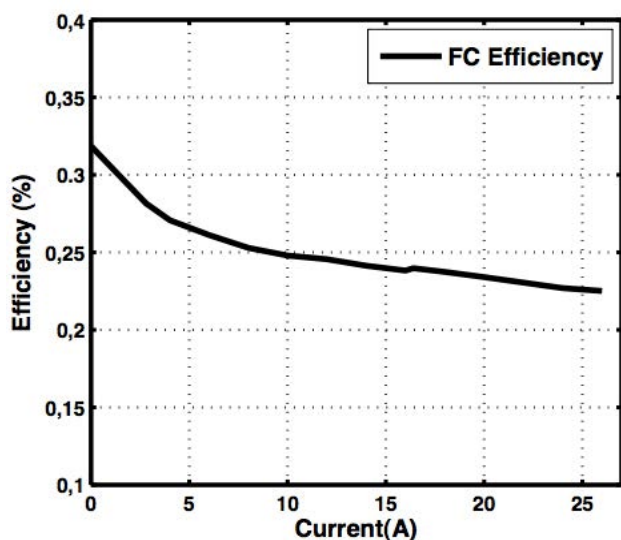


Figure A.19 – Efficiency of Mark<sub>1020</sub>.

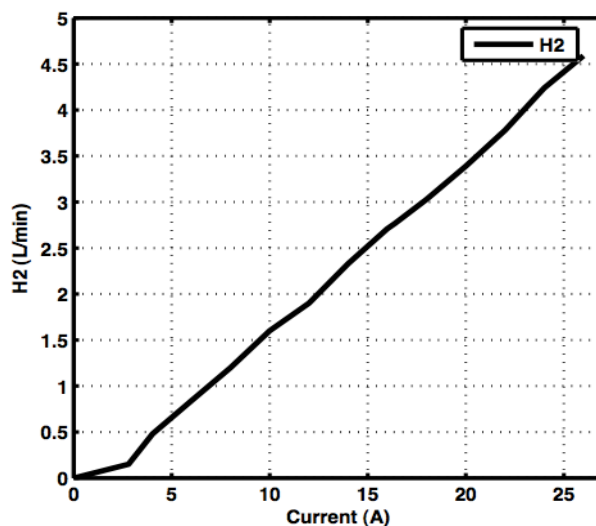


Figure A.20 – Hydrogen consumed by Mark<sub>1020</sub>.

#### A.4.5. Temperature

The temperature is measured with a HI-93530 Waterproof K-Type thermocouple, which terminal is placed inside the stack. This process has been treated as manually, consequently the results for the temperature are subject to a margin of error due to the process itself, however, it is clear by the analysis of Figure A.21 that the stack temperature increases with the increase of the load and varies between 25°C and 40 °C.

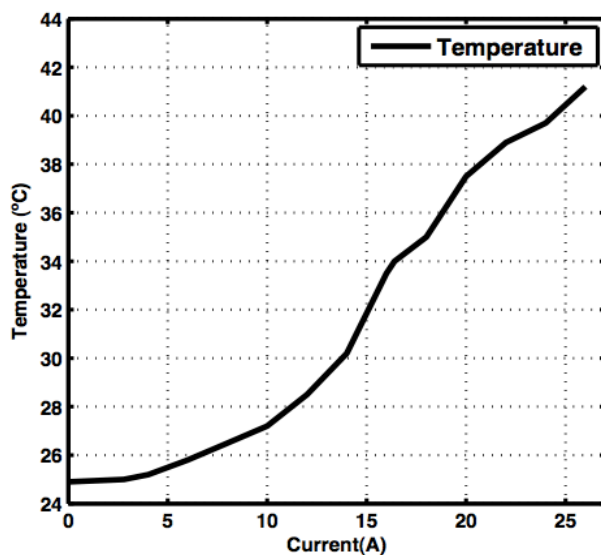


Figure A.21 – Temperature in Mark<sub>1020</sub>.

#### A.4.6. Mark1020 parameters

The optimum set of parameters related to the semi-empirical model adopted by the authors and achieved by the application of the SA method is presented in Table A.4.

Table A.4 - Mark1020 parameters

Parameter	Unit	Value
$A$	$\text{cm}^2$	29.9
$\lambda$	$\mu\text{m}$	3290
$R_C$	$\Omega$	0.000332
$\zeta_1$	No dimensional	-0.148
$\zeta_2$	No dimensional	0.00315
$\zeta_3$	No dimensional	$4.27 \times 10^{-5}$
$\zeta_4$	No dimensional	$-1.67 \times 10^{-4}$
$\psi$	No dimensional	9.79
$B$	V	0.0245
$J_{max}$	$\text{A}/\text{cm}^2$	1.47
$C$	F	2.48

## A.5. PEM Bahia

Bahia is a didactic fuel cell system of AREVA-Group developed in partnership with “Ecole Polytechnique and Ecole des Mines” in Marseille [3]. This didactic bench integrates a PEM (Proton Exchange Membrane) fuel cell stack, rated to 1kW electrical power and 1kW thermal power, enabling micro cogeneration investigation and appropriated to exploitation of operating characteristics of a fuel cell. The system provides fully integrated applications to ensure a large variety of experiments.



Figure A.22 - Overview of the Bahia system.

In Figure A.23 it is illustrated the interface of Bahia which graphical user interface allows to operate the system such as: 1) A FC simulator included in the GUI or 2) as a pedagogical support with typical practical work, theory, analysis and results with practical work requirements

Variable parameters in the graphical user interface are: Current, voltage, resistance and power profile, FC stack temperature and airflow (stoichiometry).

The values measured by the system are: Temperatures, H<sub>2</sub> pressure, Water flow, stack voltage / current and power of auxiliaries.

The values calculated by the system are: H<sub>2</sub> flow, Thermal and electrical powers, and efficiency.

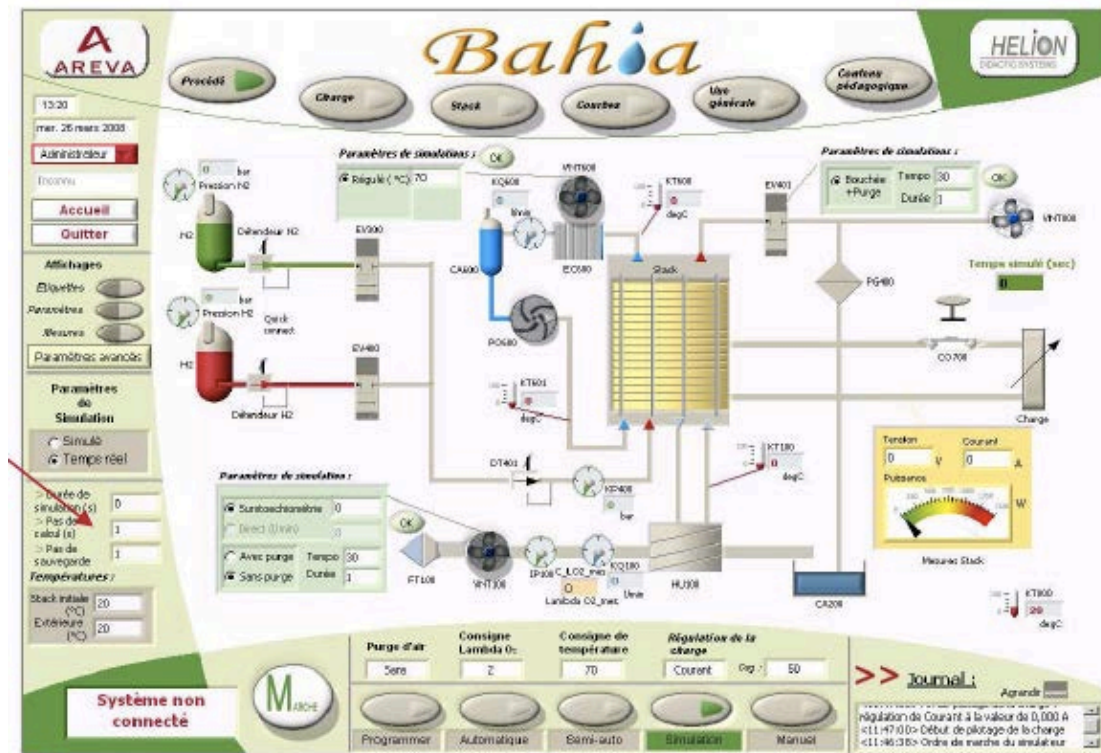


Figure A.23 - Schematic and graphical user interface of Bahia system.

### A.5.1. Technical characteristics and operation of Bahia

Nominal Electrical power: 500 W ( $U = 23 \text{ V} / I = 22 \text{ A}$ ) to 1000 W ( $U = 20 \text{ V} - I = 50 \text{ A}$ )

Electrical power: 1200 W ( $U = 19 \text{ V} - I = 62 \text{ A}$ )

Thermal power: up to 1 kW<sub>th</sub>

H<sub>2</sub> consumption: 5.5 NI/min at 500 W and 11.2 NI/min at 1000 W

Start up time lower than 1 minute.

As a demonstration system, Bahia allows operating in three distinct forms namely:

1. PC simulation: it allows simulation of the fuel cell system operation from any computer;
2. Semi automatic mode: enabling to break up the different starting phases of the system and to launch miscellaneous profiles, and
3. Automatic mode: automatic system operation (start/load profiles/stop) based on parameters defined by the user.

### A.5.2. Bahia parameters

The optimum set of parameters related to the semi-empirical model adopted by the authors and achieved by the application of the SA method is presented in Table A.5.

Table A.5 - Bahia parameters.

Parameter	Unit	Value
$A$	$\text{cm}^2$	62.05
$\lambda$	$\mu\text{m}$	131
$R_C$	$\Omega$	0.00028
$\xi_1$	No dimensional	-0.289
$\xi_2$	No dimensional	0.00266
$\xi_3$	No dimensional	$8.2 \times 10^{-5}$
$\xi_4$	No dimensional	$-1.58 \times 10^{-4}$
$\psi$	No dimensional	23.06
$B$	V	0.0179
$J_{max}$	$\text{A}/\text{cm}^2$	1537
$C$	F	2.48

## A.6. Conclusions

The PEM fuel cell system has been selected to be investigate in this thesis, based on its low operation temperature, start-up characteristics, and high energy density. In this appendix the main characteristics of the various PEM's used were presented. Particularly, the analysis of the output voltage, output power, efficiency and hydrogen consumed were analyzed. The SA was applied to each case, and it was always verified a high correlation between the experimental results and those obtained with the model, allowing the extraction of parameters safely. Despite the similarities between the various systems analyzed it was positive to investigate all of them because each one in its own way contributed to enrich the research presented in this thesis.



---

## *APPENDIX B*

### **MODEL OF THE PEM IN NEURAL NETWORKS**

---



## APPENDIX B- Model of the PEM in neural networks

### B.1. Introduction

A Neural Network (NN) is a powerful data-modeling tool that can be used to capture complex input/output relationships. NN is widely accepted as a technology offering an alternative way to tackle complex and ill-defined problems [5-7]. The NN are fault tolerant in the sense that they are able to handle noisy and incomplete data, they are able to deal with nonlinear problems and, once trained, they can perform prediction and generalization at high speed. Based on the topology, the connections in an NN can be feed forward or feed-back (recurrent) and the learning can be supervised or unsupervised [7].

The NNs have been used in various areas of science and technology, such as; control, robotics, pattern recognition, forecasting, medicine, power systems, manufacturing, optimization, signal-processing, social and psychological sciences [8;9]. They are particularly useful in system modeling such as in implementing complex mappings and system identification.

A NN model has main features, including: 1) learning from training data used for system identification; 2) generalization from inputs not previously presented during the training phase; 3) applicable to multivariable systems; 4) used as a black-box approach (no prior knowledge about a system) and implemented on compact processors for space and power constrained applications.

Many different types of NN models can be used; the most popular include multilayer-perceptron (MLP) which is generally trained with the back-propagation algorithm, learning vector quantization, radial basis function (RBF), Hopfield and Kohonen, to name a few. In Figure B.1 it is exemplified how the information is processed in a single node [9]. The node receives weighted activation of other nodes through its incoming connections, the weights are summarized and then the result is passed through an activation function; the outcome is the activation of the node.

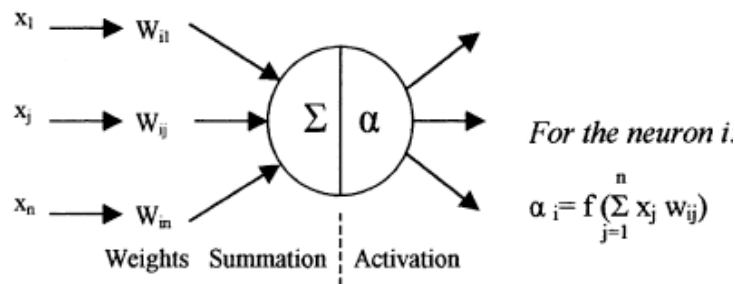


Figure B.1 – Information processing in a neural network unit.

## B.2. Definition of the architecture

The architecture of the NN includes defining the number of input and output nodes, number of hidden layers in the network and the number of hidden nodes used in each hidden layer. Typically the number of input nodes is the same as the number of state variables. The hidden layer is composed by an adequate number of neurons, specified by the user, while the output layer possesses the neurons as the outflow of the system. The schematic of Figure B.2 corresponds to the architecture of NN selected to model the PEM.

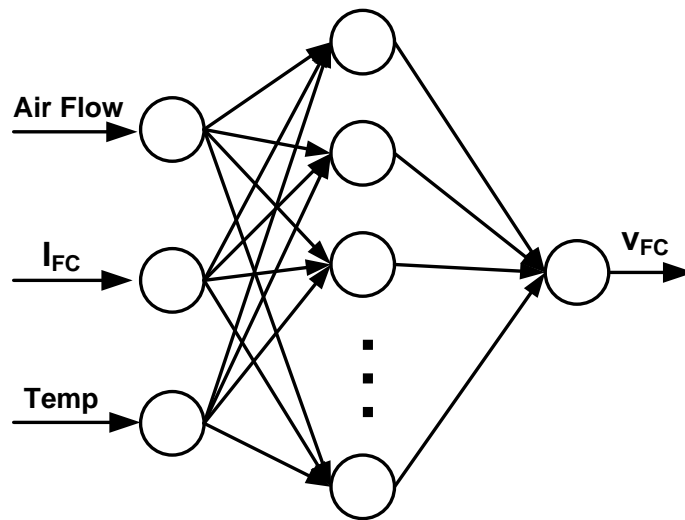


Figure B.2 – Schematic of the NN model for the PEM fuel cell.

### B.2.1. Input and output variables

To model the PEM fuel cell an important aspect is to select the reliable variables, i.e., which one are dominant and which one can be discarded to the NN model. For the case, some of the variables that has been obtained from the fuel cell system Bahia [10] are: stack voltage (V), stack current (A), air flow (slpm), air temperature (°C), stack temperature (°C), fuel pressure (barg), fuel consumption (L), Power (W), H<sub>2</sub> leak (%), O<sub>2</sub> concentration (%), purge cell voltage (V) and battery voltage (V).

Some of these variables must be selected as inputs/outputs of the NN model, however several of them can be discarded because they have been forced to be constant by the manufacturer and are not relevant in the process. Thus, the variables that has been considered as inputs are as follows: 1) stack current (I) which is function of the load applied to the system, 2) air flow (slpm), which is controlled by an air compressor, and. 3) Stack temperature (°C) which is controlled by a cooling fan. The stack voltage (V) is the only output variable considered. The hydrogen pressure is kept constant within a

regulated valve and the humidity of air is managed by a heat exchanger. Eq. B.1 below corresponds to the NN topology proposed to model the PEM Bahia.

$$V_{FC} = f(I_{FC}, Airflow, Temperature) \quad \text{Eq. B.1}$$

### **B.2.2. Data processing**

Normally NN performs better results in interpolation rather than extrapolation then, to carry out a good training the data set needs to be distributed throughout all the operation range in order to contain all the information needed. The first step is to collect the required data and prepare them. Three types of data are normally required [5]; 1) training data, 2) test data and 3) validation data. The former and the latter should contain representative samples of all the cases the network is required to handle, whereas the test file may contain about 10% of the cases contained in the training file. The normalization of the data between  $-1$  and  $+1$  or  $0$  and  $1$  is also important, in order to facilitate the training process. Figure B.3 corresponds to the input data used to train and validate the network while Figure B.4 corresponds to the target data considered to process the NN model.

### **B.3. Training and evaluation**

The training data is vital in the performance and convergence of the NN model. When training data set is presented to the NN, the weights and biases are up until the entire training data is completed. This process is called “one epoch”. The number of “epochs” indicates the speed of the training method, while the training phase is repeated until the network performs well accordingly to an error goal defined by the user. As a consequence, the validation data is presented to ensure that the network has learned the general patterns, not just simply has memorized the data set. If the network still performs well, in this phase, the training is completed and the NN can be used for whatever input data placed in the input. In the present case, the network has been trained with a back-propagation algorithm, named as Levenberg-Marquardt algorithm. The data used to train the NN is in the range of  $[1-1939]$  while the data used for the validation are in the range of  $[1400-3000]$ .

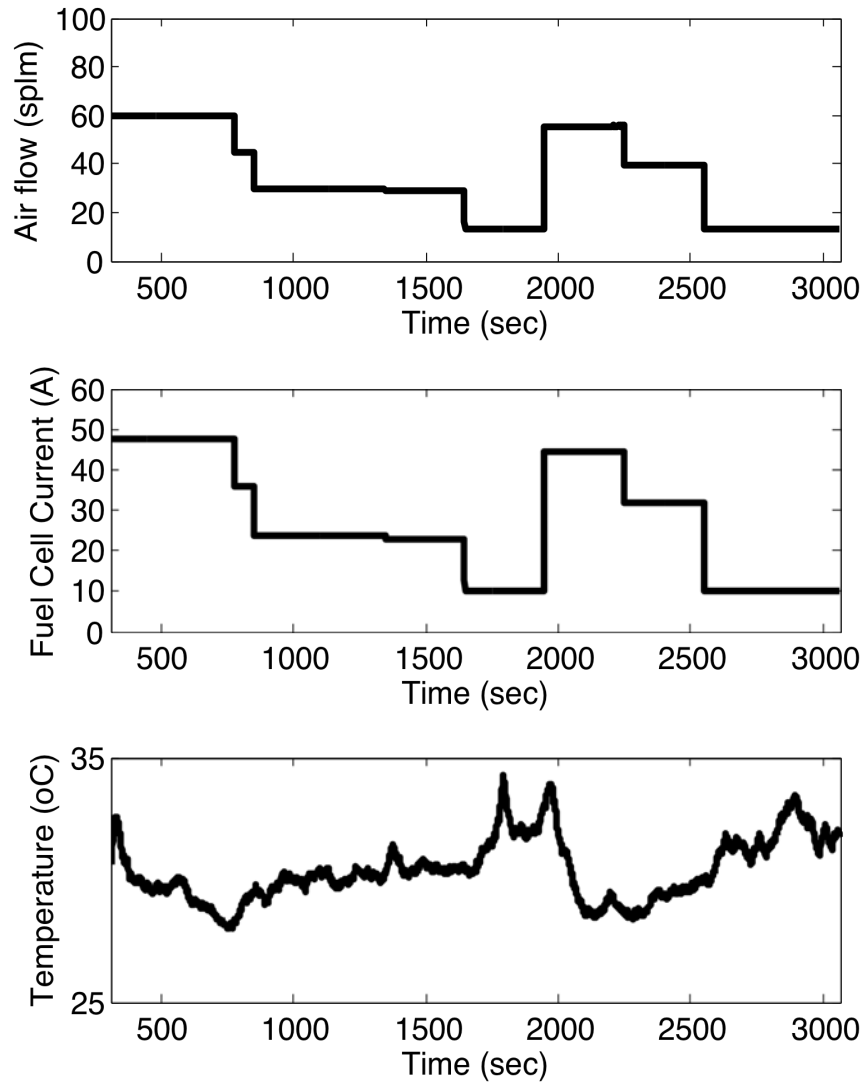


Figure B.3 - Input data for training and validation the network.

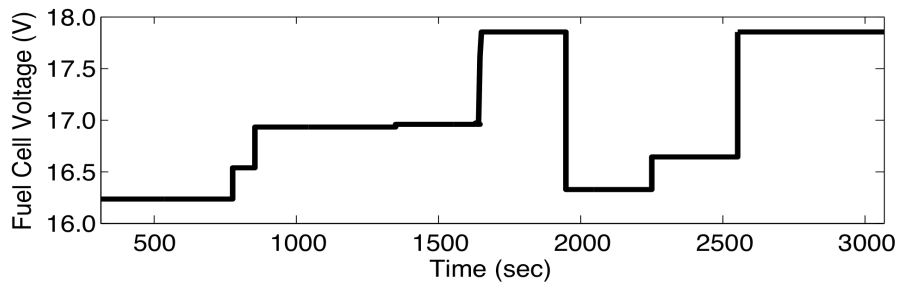


Figure B.4 - Target data of the network.

#### B.4. Modeling of the PEM Bahia

The NN method is applied to model the PEM Bahia. During the training process the error function (E) is minimized while the number of epochs increases, as can be see in Figure B.6. During this

process, the network will adjust its weights and biases until the output error reaches the designated error goal. The training process is stopped when the mean average error remains unchanged for a number of epochs.

The results achieved with the application of the NN method to model the fuel cell Bahia are presented in Figure B.7, which shows a good agreement between simulation and the experimental data results. Then, it can be stated that the NN method can be applied to predict the fuel cell voltage as a function of the stack current over the whole range current. The average value of the error shows to be below 1%, as is observed in Figure B.5 below.

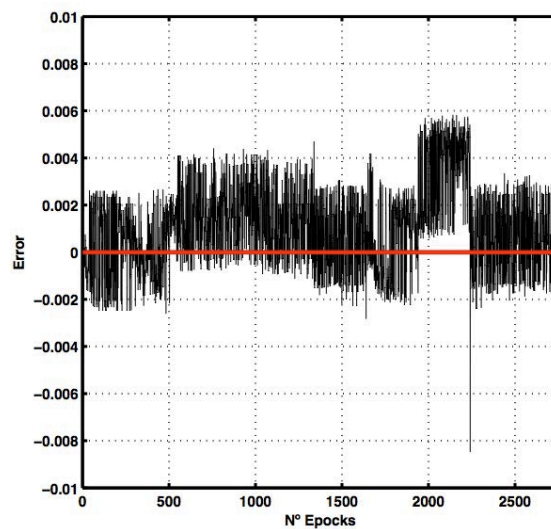


Figure B.5 – Average error of the model as a function of the epoch's number.

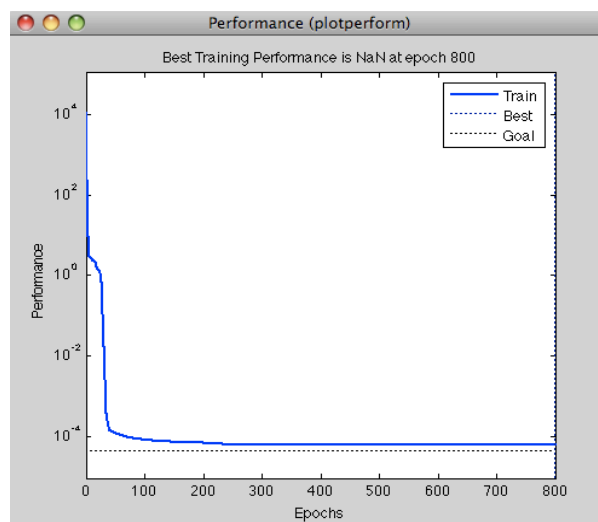


Figure B.6 – Performance of the method.

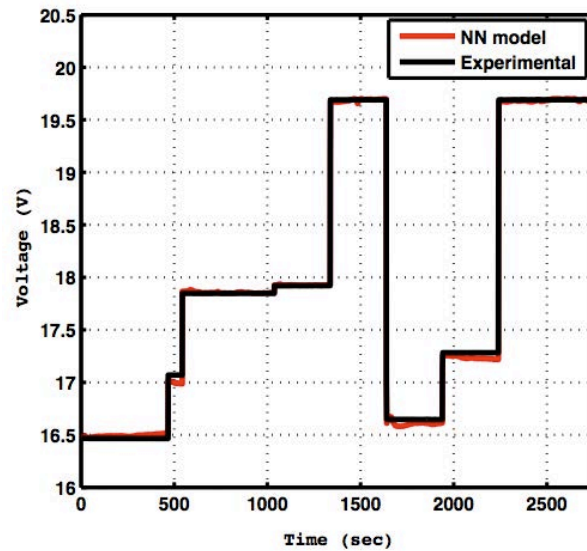


Figure B.7– Validation for PEM Bahia.

## B.5. Conclusions

In this Appendix a Neural Networks model as an alternative to the analytical and empirical modeling methods characterizes the PEM fuel cell. A multilayer perceptron trained by the Levenberg-Marquardt Back Propagation (BP) algorithm is used. The methodology was implemented in MatLab/Simulink software and the results are compared with those obtained experimentally for a commercial system. The Neural Networks proves to be well adapted to predict the behaviour of the PEM, however, the NN model operates like a “black box” and no detailed information about the PEM system is provided.



---

## *APPENDIX C*

# **NUMERICAL ANALYSIS OF THE SERIES RESONANT CONVERTER**

---



## APPENDIX C- Numerical analysis of the series resonant converter

### C.1. Introduction

In this appendix, the properties of the series resonant converters are investigated based on the sinusoidal approximation. Harmonics of the switching frequency are neglected, and the tank waveforms are assumed to be purely sinusoidal. This allows simple equivalent circuits to be derived for the bridge inverter, resonant tank, rectifier, and output filters of the converter, whose operation is solved using standard linear ac analysis. The appendix also provides a unified approach based on the differential equations of a resonant circuit in order to characterize its behaviour. The obtained results are used to calculate peak values, constraints on component values and others. The method is applied to determine the components of the resonant converter considering the power-generating source as the PEM Mark1020.

### C.2. Analysis based on sinusoidal approximation

The analysis of the SRC can be performed by a simple equivalent circuit similar to that represented in Figure C.1, whose operation can be understood and solved using standard linear ac analysis [11;12]. The analysis based on sinusoidal approximation neglects the harmonics of the switching frequency, and the tank waveforms are assumed to be purely sinusoidal. The resonant circuit is composed by the  $L_r$ - $C_r$  set of elements in series characterized by the frequency  $f_r$  and impedance  $Z_r$ .

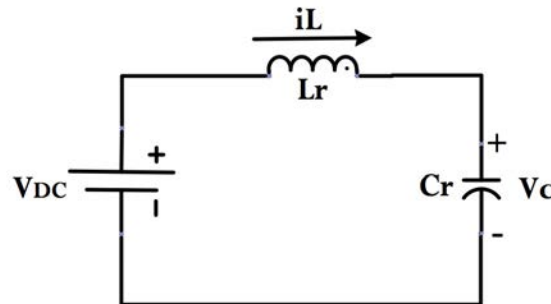


Figure C.1–Simple equivalent circuit of the SRC.

The voltage capacitor,  $V_C$  and the current inductance,  $i_L$  presented in the circuit are given by Eq. C.1 and Eq. C.2 below.

$$L \frac{di_L}{dt} + v_C = V_d \quad \text{Eq. C.1}$$

$$C \frac{dv_C}{dt} = i_L \quad \text{Eq. C.2}$$

Solving these equations for  $t > t_0$ , and considering the initial conditions of capacitor voltage  $V_{C0}$  and inductance current  $I_{L0}$ , the equations relating these variables can be defined by [13]:

$$v_C(t) = V_{in} - (V_{in} - V_{C0}) \cos(w_r(t - t_0)) + Z_r I_{L0} \sin(w_r(t - t_0)) \quad \text{Eq. C.3}$$

$$i_L(t) = I_{Lr} \cos(w_r(t - t_0)) + \frac{V_{in} - V_{Cr}}{Z_r} \sin(w_r(t - t_0)) \quad \text{Eq. C.4}$$

Figure C.2 illustrates the waveforms of the inductor current- $i_L$  and the capacitor voltage- $v_C$ , achieved from the two equations above.

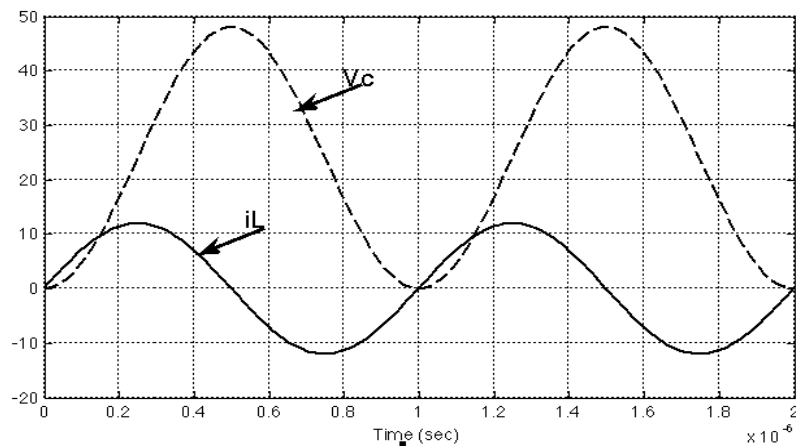


Figure C.2 –The series-resonant circuit waveforms.

As is observed in Figure C.2 the maximum and minimum capacitor voltage in the  $V_C(t)$  waveform coincide with the zero crossings of the inductor current  $i_L(t)$ , and hence the capacitor voltage changes from its minimum value to its maximum value during this interval. The capacitor voltage is therefore  $V_C = 2V_{DC}$  when the current in  $i_L(t) = 0$  after half a cycle.

### C.2.1. Impedance

Adding a resistance to the series-resonant circuit of Figure C.1 the series-resonant circuit illustrated in Figure C.3 is obtained.

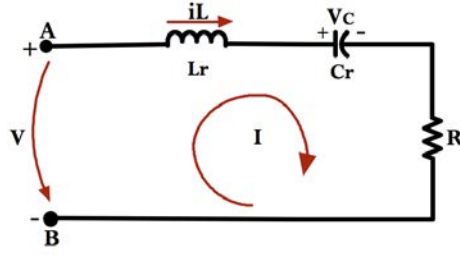


Figure C.3 - Series resonant circuit with a resistive load.

In the circuit of Figure C.3 the input impedance, Z is expressed by:

$$\bar{Z} = R + X_{Lr} + X_{Cr} \quad \text{Eq. C.5}$$

$$\bar{Z} = R + j \left( \omega L_r - \frac{1}{\omega C_r} \right) = R \left[ 1 + jQ \left( \frac{\omega}{\omega_r} - \frac{\omega_r}{\omega} \right) \right] \quad \text{Eq. C.6}$$

Which, module and phase are defined by Eq. C.7 and Eq. C.8 respectively:

$$Z_r = R \sqrt{1 + Q^2 \left( \frac{\omega}{\omega_r} - \frac{\omega_r}{\omega} \right)^2} \quad \text{Eq. C.7}$$

$$\theta = \arctan \left[ Q \left( \frac{\omega}{\omega_r} - \frac{\omega_r}{\omega} \right) \right] \quad \text{Eq. C.8}$$

And,

$$\cos \phi = \frac{1}{\sqrt{1 + Q^2 \left( \frac{\omega}{\omega_r} - \frac{\omega_r}{\omega} \right)^2}} \quad \text{Eq. C.9}$$

With,

$$\begin{aligned} R &= Z \cos(\theta) \\ X &= Z \sin(\theta) \end{aligned} \quad \text{Eq. C.10}$$

If the reactance of the resonant circuit becomes zero, that is for  $X_{Lr} = -X_{Cr}$ , then  $Z = R$  and the circuit operates at resonant conditions that is, for  $\omega = \omega_r$ . which is characterized by angular frequency  $\omega_r$  and characteristic impedance  $Z_r$  as defined by Eq. C.11 and Eq. C.12, respectively.

$$w_r = 2\pi f_r = \frac{1}{LrCr} \quad \text{Eq. C.11}$$

$$Z_r = \sqrt{\frac{Lr}{Cr}} \quad \text{Eq. C.12}$$

### C.2.2. Quality factor

The quality factor Q, of a resonant circuit measures the “goodness” or quality of the circuit. A higher value of Q corresponds to a narrower bandwidth, which is desirable in many applications. More formally, Q is the ration of the power stored in the reactance to the power dissipated in the resistance of the resonant circuit. The quality factor is defined as:

$$Q = 2\pi \frac{\text{Total energy stored at resonant frequency}}{\text{Energy dissipated per cycle at res. frequency}}$$

$$Q = \frac{w_r \times L_r}{R} = \frac{1}{w_r \times C_r \times R} = \frac{Z_r}{R} \quad \text{Eq. C.13}$$

Or, equivalently,

$$Q = \frac{1}{R} \times \sqrt{\frac{L_r}{C_r}} \quad \text{Eq. C.14}$$

Figure C.4 shows the modulus of  $Z/Z_r$  for different values of Q. As can be seen, at resonance frequency the impedance of the circuit is minimum and is purely resistive. Below resonance it is capacitive and above resonance it is inductive., The impedance of the circuit increases above or below the resonance. The slope of Q is an indication of how sensitive the circuits impedance is to frequency changes. The correspondent phase in degrees is represented in Figure C.5.

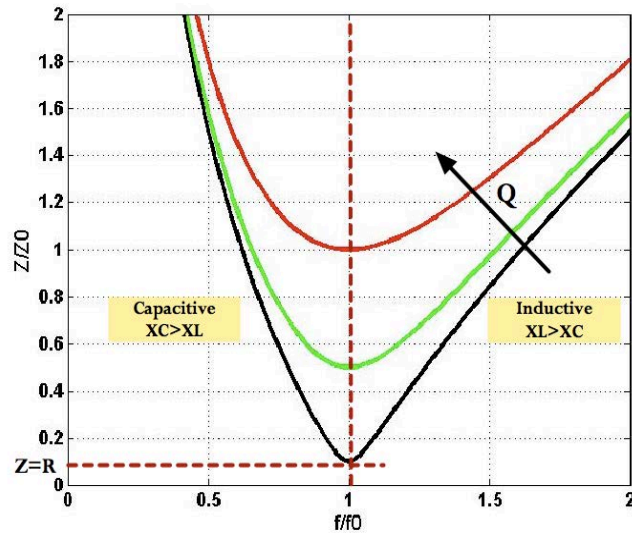


Figure C.4 – Input impedance,  $Z/Z_0$  of the series resonant circuit for different values of  $Q$ .

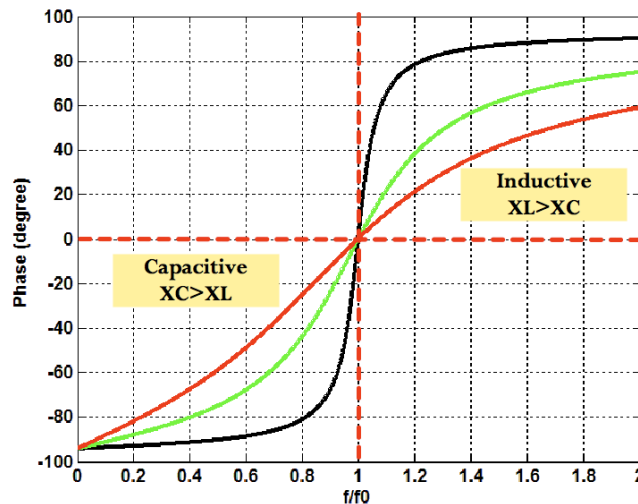


Figure C.5 – Phase of the series resonant circuit for different values of  $Q$ .

### C.2.3. Bandwidth

The bandwidth of the resonant circuit is defined as the band of two frequencies in both sides of the resonant frequency  $f_r$ , that is, where the current at both points falls to  $1/\sqrt{2}$  of its maximum value. The range of frequency  $\Delta f = (f_H - f_L)$  between the points, AB in Figure C.6 is called the Bandwidth, (BW) for which at least half of the maximum power and current is provided. Over the bandwidth range, the current is equal to or greater than  $0.707I_{max}$ . The sharpness of the peak is measured quantitatively and corresponds to the quality factor of the circuit, that is;  $Q = f_r/BW$ . The higher the  $Q$  factor is, the smaller the bandwidth is.

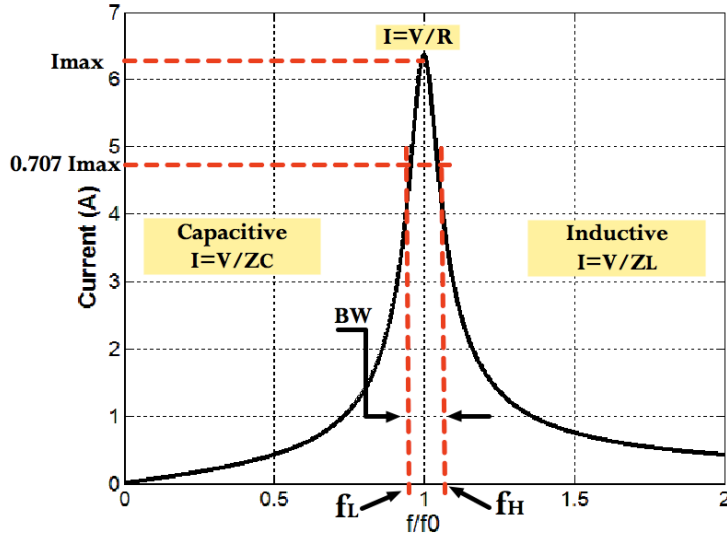


Figure C.6 - Bandwidth of resonant circuit.

The points A and B are also referred as half-power points and the power at these points is given by:

$$P_{fH} = P_{fL} = I^2 \times R = \left( \frac{I_r}{\sqrt{2}} \right)^2 \times R \quad \text{Eq. C.15}$$

The frequencies of these two points are respectively:

$$f_L = f_r - \frac{R}{4\pi L} \quad \text{Eq. C.16}$$

And,

$$f_H = f_r + \frac{R}{4\pi L} \quad \text{Eq. C.17}$$

#### C.2.4. Operation and switching losses

The SRC can operate in one of three possible modes, depending on the ratio of the operating frequency ( $f_s$ ) and resonance frequency ( $f_r$ ) [11;12;14] namely;

- i) Discontinuous-conduction mode (DCM) for  $f_s < f_r/2$ ,
- ii) Continuous-conduction mode (CCM) for  $f_r/2 < f_s < f_r$  and
- iii) Continuous-conduction mode (CCM) for  $f_s > f_r$ .

Classifying the operation of the SRC as below ( $f_s < f_r$ ) or above ( $f_s > f_r$ ) the resonance frequency  $f_r$ , as illustrated in Figure C.7 it has:



### ➤ Operation below the resonance frequency ( $f_s < f_r$ )

When the SRC is operating below resonance at turn-off, the transistor current falls to zero naturally. However, at turn-on the transistor current is not zero, as illustrated in Figure C.7(a). In this case, the turn-off switching loss is zero but the turn-on switching loss is not. The impedance of the circuit,  $Z$  is capacitive with phase angle  $\phi < 0$ .

The drawback of operating below resonance is the diode reverse-recovery stress when the diode turns-off, because it turns off at a very large  $dv/dt$  and consequently at very large  $di/dt$  generating a high reverse-recovery current spike with a magnitude over ten times of the steady-state switch current. These spikes cannot circulate through the resonant circuit because of the presence of the inductance, which does not allow the interruption of current value then they can destroy the transistors; increase the switching loss and built noise.

### ➤ Operation above the resonance frequency ( $f_s > f_r$ )

When the SRC is operating above resonance at turn-on, the current in the transistor is zero however, at turn-off instant the transistor current is not zero, as illustrated in Figure C.7(b). In this case, the turn-on switching loss is zero but the turn-off switching loss is not. The turn-off switching loss can be eliminated by adding a shunt capacitor to one of the transistors using a dead time in the drive voltages. The impedance of the circuit,  $Z$  is inductive with phase angle  $\phi > 0$ .

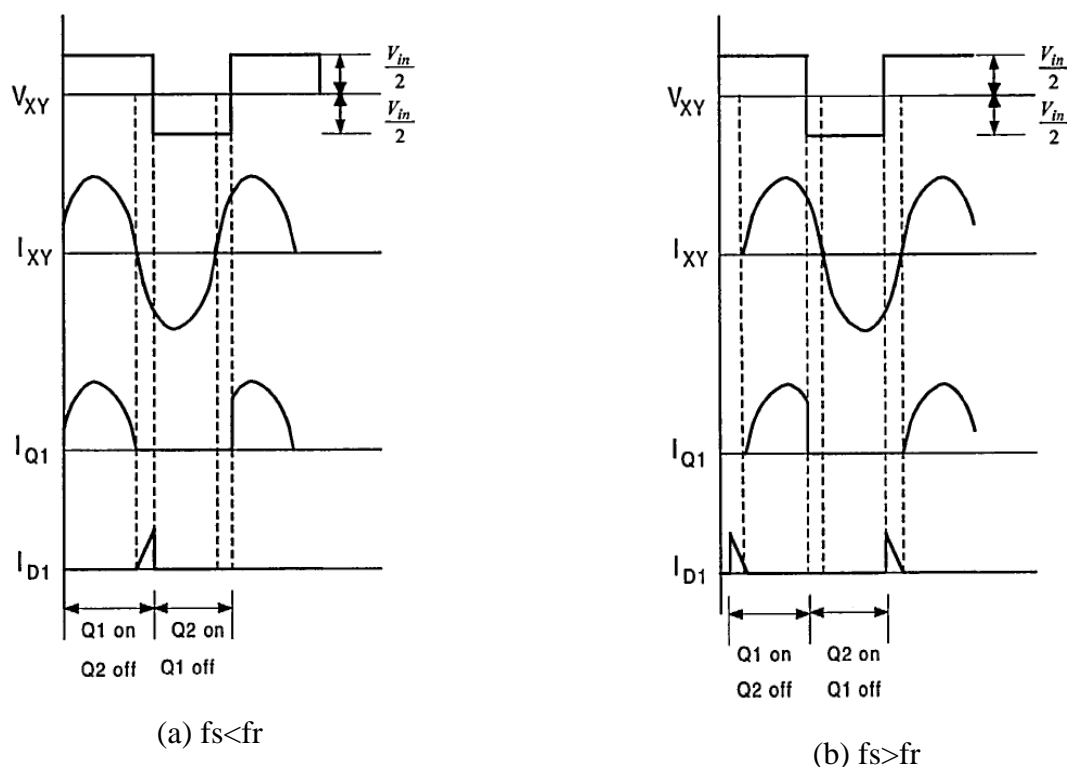


Figure C.7 - Operation of the SRC below and above the resonant frequency.

### C.2.5. Full-bridge topology

A full-bridge voltage-switching series resonant inverter topology is illustrated in Figure C.8 , it consists of four controllable switches and a series resonant circuit. The load appears in series with the resonant circuit, which leads the converter working as a current source to the load. The analysis of this circuit using sinusoidal approximation considers only the fundamental component of the voltage and current waveforms that is; the parameters previously defined and operating considerations are also valid in the analysis of this circuit.

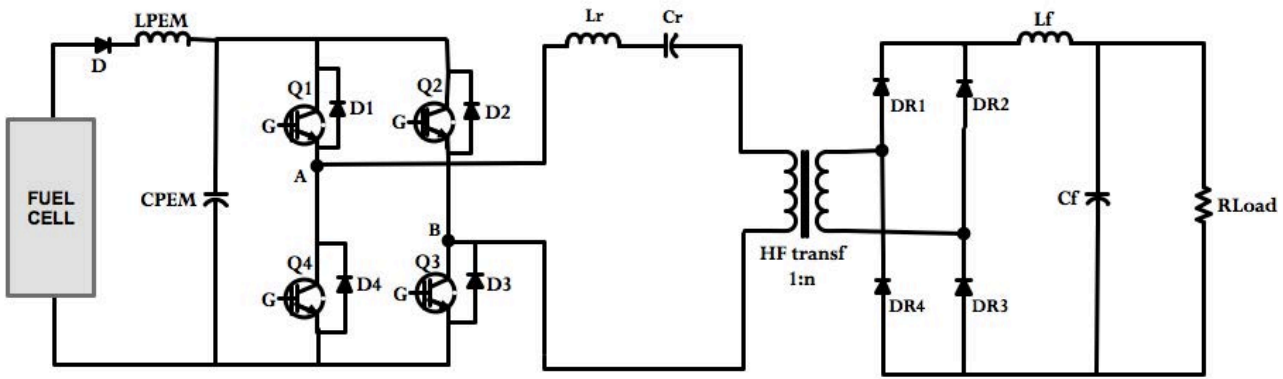


Figure C.8– Full-bridge topology of the SRC.

#### ➤ Output voltage

Referring to Figure C.8, the input voltage of the series resonant circuit, is a square-wave given by the following expression:

$$\begin{cases} +V_{FC}, & \text{for } 0 < \omega t \leq \pi \\ -V_{FC}, & \text{for } \pi < \omega t \leq 2\pi \end{cases} \quad \text{Eq. C.18}$$

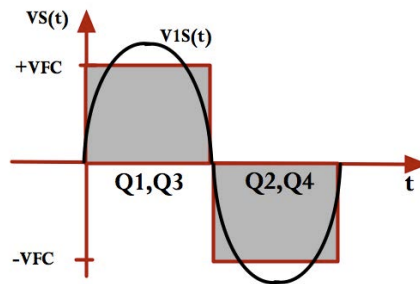


Figure C.9 – Output voltage in a full-bridge inverter.

The Fourier analysis of this voltage leads to the following expression:

$$v = \frac{4V_{FC}}{\pi} \sum_{n=1}^{\infty} \frac{1 - (-1)^n}{2n} \sin(nwt) = V_{FC} \left( \frac{4}{\pi} \sin(wt) + \frac{4}{3\pi} \sin(3wt) + \frac{4}{5\pi} \sin(5wt) + \dots \right) \quad \text{Eq. C.19}$$

The fundamental component of the voltage,  $v$  is:

$$v_1 = V_{\max} \sin(wt) \quad \text{Eq. C.20}$$

And the maximum and root mean square (rms) values considering the fundamental component  $v_1(t)$ , are respectively,

$$V_{\max} = \frac{4V_{FC}}{\pi} \approx 1.273V_{FC} \quad \text{Eq. C.21}$$

And,

$$V_{rms} = \frac{V_{\max}}{\sqrt{2}} = \frac{1}{\sqrt{2}} \times \frac{4V_{FC}}{\pi} = \frac{2\sqrt{2}V_{FC}}{\pi} \approx 0.9V_{FC} \quad \text{Eq. C.22}$$

### ➤ Current

The current  $i(t)$  is positive when the switches Q1 and Q3 conducts, and is negative when switches S2 and Q4 conducts. Under the conditions described in the previous section, the current  $i(t)$  is well approximated by a sinusoid waveform, that is:

$$i_{Q1} = i_{Q3} = \begin{cases} +I_{\max} \times \sin(wt - \Phi), & \text{for } 0 < wt < \pi \\ 0, & \text{for } \pi < wt < 2\pi \end{cases} \quad \text{Eq. C.23}$$

$$i_{Q2} = i_{Q4} = \begin{cases} 0, & \text{for } 0 < wt < \pi \\ -I_{\max} \times \sin(wt - \Phi), & \text{for } \pi < wt < 2\pi \end{cases} \quad \text{Eq. C.24}$$

The DC component of the input current of the inverter is calculated for one period, which for the case of the full bridge is  $0-\pi$ . Then, considering one period the mean value is;

$$I_{DC} = \frac{1}{\pi} \int_0^{\pi} i_{s1} d(wt) = \frac{2I_{\max} \cos \phi}{\pi} = \frac{2V_m \cos \phi}{\pi Z} = \frac{8V_{FC} \cos \phi}{\pi^2 Z} \quad \text{Eq. C.25}$$

For switching frequency equal to the resonant frequency,  $f_s=f_r$ , the circuit is purely resistive and has no phase, then the equation above can be simplified to,

$$I_{DC} = \frac{2I_{\max}}{\pi} = \frac{8V_{Fc}}{\pi^2 R} \quad \text{Eq. C.26}$$

In the resonant circuit the current is approximately sinusoidal that is,

$$I_{\max} = \frac{V_{\max}}{Z} = \frac{2V_{FC} \cos \phi}{\pi Z} \quad \text{Eq. C.27}$$

And for  $f_s=f_r$ ,

$$I_{Lr} = I_{Cr} = \frac{4V_{FC}}{\pi R} \quad \text{Eq. C.28}$$

Figure C.10 shows the amplitude of current normalized in the series resonant circuit as a function of  $f_s/f_r$  and  $R/Z_r = 1/Q$ . As can be observed, the maximum current value in the circuit occurs at the resonance frequency and with low load resistance. It is also observed that at resonance frequency  $f_r$  if the load  $R \rightarrow 0$  then the peak current  $I \rightarrow \infty$  that is, is not recommended the application of very low load conditions to this circuit.

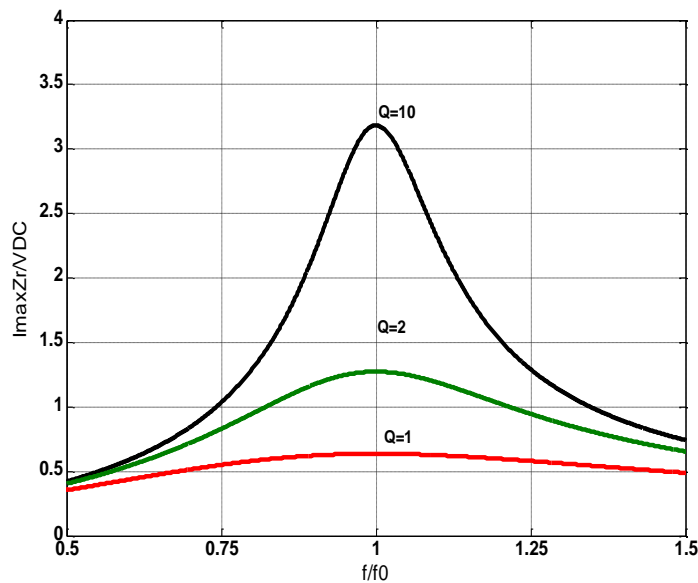


Figure C.10 - Amplitude of the current in the series resonant circuit.

➤ **Input power**

The input power,  $P_{DC}$  is the product of the voltage provided by the fuel cell, which passes through a low pass filter (PEM filter) by the DC component of the input current of the inverter. The input power is expressed by,

$$P_{DC} = I_{DC} \times V_{FC} = \frac{8V_{FC}^2 \times \cos^2 \phi}{\pi^2 R} \quad \text{Eq. C.29}$$

For  $f_s=f_r$  the input power is;

$$P_{DC} = \frac{8V_{FC}^2}{\pi^2 R} \quad \text{Eq. C.30}$$

➤ **Output power**

The output power  $P_{out}$  for  $f_s=f_r$  is:

$$P_0 = P_{Ri} = \frac{I_{\max}^2 \times R_i}{2} = \frac{8V_{FC}^2 \times R_i \times \cos^2 \phi}{\pi^2 R^2} \quad \text{Eq. C.31}$$

Figure C.11 shows the output power in the series resonant circuit as a function of  $f_s/f_r$  and  $R/Z_r = 1/Q$ , as can be observed the maximum output power occurs at the resonance frequency and with low load resistance.

At  $f_s=f_r$ ,

$$P_0 = P_{Ri} = \frac{8V_{FC}^2 \times R_i}{\pi^2 R^2} \quad \text{Eq. C.32}$$

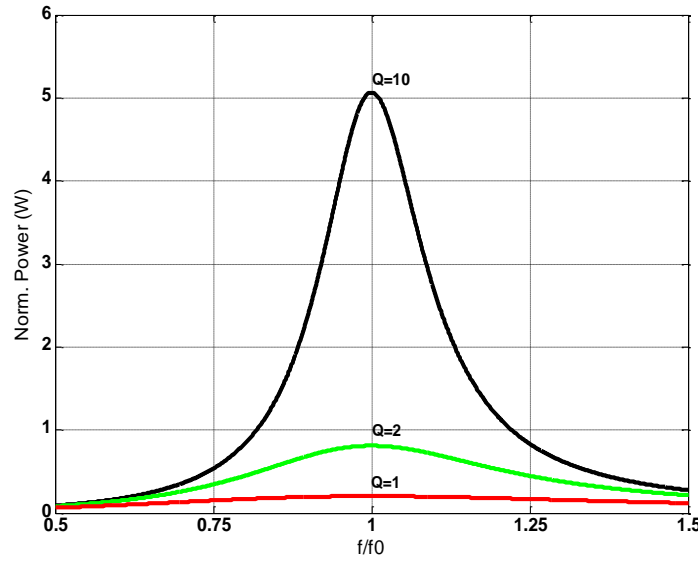


Figure C.11 - Amplitude of the power in the series resonant circuit.

### ➤ Efficiency

The efficiency is the ratio between the output and the input power,  $P_0$  and  $P_{DC}$ , respectively. The loss of power is due to several factors including the loss in every transistor; the loss in the resonant inductance and loss in the resonant capacitor, expressed by the equations follow, respectively:

$$P_{rDS} = \frac{I_{\max}^2 r_{DS}}{4} \quad \text{Eq. C.33}$$

$$P_{rL} = \frac{I_{\max}^2 r_L}{2} \quad \text{Eq. C.34}$$

$$P_{rC} = \frac{I_{\max}^2 r_C}{2} \quad \text{Eq. C.35}$$

Then the conduction power loss,  $Pr$ , is:

$$Pr \approx 2P_{rDS} + P_{rL} + P_{rC} \quad \text{Eq. C.36}$$

For operation below resonance, the overall power dissipation in the inverter is;

$$P_T = Pr + 4P_{sw} + 4P_G \quad \text{Eq. C.37}$$

Hence, the efficiency of the full-bridge inverter for operation below resonance is:

$$\eta = \frac{P_{Ri}}{P_{Ri} + P_T} = \frac{P_0}{P_{DC} + P_r + 4P_{sw} + 4P_G} \quad \text{Eq. C.38}$$

For operation above resonance, the overall power dissipation in the inverter is;

$$P_T = P_r + 4P_{toff} + 4P_G \quad \text{Eq. C.39}$$

Hence, the efficiency of the full-bridge inverter for operation below resonance is:

$$\eta = \frac{P_{Ri}}{P_{Ri} + P_T} = \frac{P_0}{P_{DC} + P_r + 4P_{toff} + 4P_G} \quad \text{Eq. C.40}$$

### ➤ Voltage transfer function

The functionality of this converter type can be divided into two parts: the switching part and the resonant part, as represented in Figure C.12. The switching part ( $M_{Vs}$ ) is comprised of a DC input voltage and a set of switches. The switches are controlled to produce a square-wave voltage. Since resonant part forces a sinusoidal current, only the fundamental component of the power is transferred from the switching part to the resonant part. Resonant part ( $M_{Vr}$ ) is considered for a resistor load  $R_i$  and for the rms of the fundamental component of the square-wave voltage. Then, these considerations leads to the definition of the voltage transfer function of the resonant inverter such as:

$$M_{VI} = M_{Vs} M_{Vr} = \frac{V_{Ri}}{V_I} \quad \text{Eq. C.41}$$

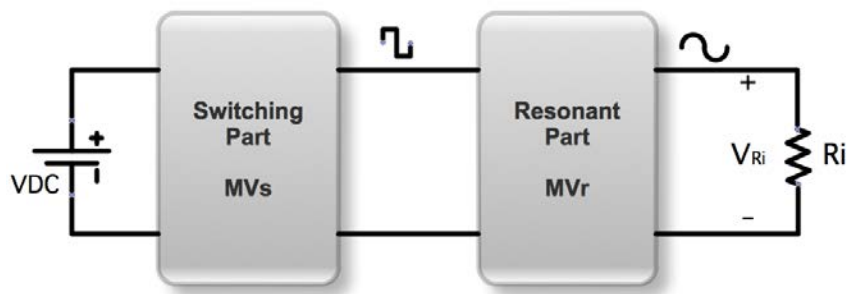


Figure C.12- Bloc diagram of the voltage transfer function of the resonant inverter.

### ➤ Short-circuit and open-circuit operating conditions

The SRC can operate safely with an open-circuit in the load ( $R_i \rightarrow \infty$ ) at the output however, if it operates closely to the resonant frequency,  $f_s = f_r$  a short-circuit in the load ( $R_i \rightarrow 0$ ) is not recommended due to very high values of current that appears in this situation as already explained.

### C.3. Analysis based on second-order differential equation

Second order differential equations have a variety of applications in science and engineering, particularly in electrical circuits. In this section the analysis of the different modes of operation of the resonant circuit is based on second-order differential equation method. Each one of the operation modes is treated separately, even though they are very similar. Thus the full-bridge topology of the SRC of Figure C.8 can be simplified to an RLC circuit such as that shown in Figure C.13, which corresponds to a 2nd-order differential equation with two independent energy-storage elements, the inductor and the capacitor. Thus, considering the conditions imposed by the PEM fuel cell (VFC), the HF transformer ( $R_t$  and  $L_t$ ) and the load referred to the primary of the transformer ( $R'_{load}$ ), the selection of the resonance components,  $L_r$  and  $C_r$  is made, which in turn determines the frequency of operation of the converter as well as the conditions for maximum power transfer of the SRC.

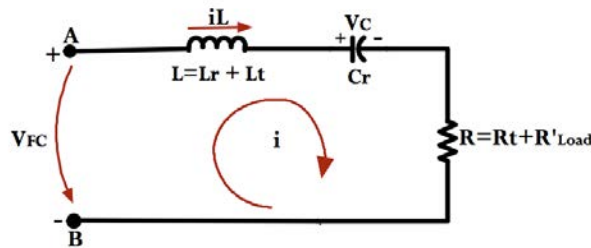


Figure C.13- Representation of the SRC by a 2nd-order differential equation.

Applying the Kirchoff loop equation,  $-V_{FC} + V_L + V_C + V_R = 0$  (sum of voltages around loop equals zero), to the RLC series circuit above to obtain the loop current, and considering that the inductor and capacitor are both in series with the voltage source that is, the loop current cannot change instantly and the voltage across the capacitor cannot change instantly, the solution leads to the general form of the second order differential equation follow, where  $\alpha$  is called the “dampening coefficient” and  $\omega_r$  is called the “resonant or natural frequency”.



$$\frac{d^2 i}{dt^2} + \frac{R}{L} \times \frac{di}{dt} + \frac{1}{LC} \times i = 0 \quad \text{Eq. C.42}$$

Assuming solutions of the form  $y(t) = k \times e^{-st}$  this leads to the "characteristic equation" as follow.

$$s^2 \times e^{st} + 2\alpha s \times e^{st} + w_r^2 \times e^{st} = 0 \Rightarrow s^2 + 2\alpha s + w_r^2 = 0 \quad \text{Eq. C.43}$$

With,

$$w_r = \frac{1}{\sqrt{LrCr}} \quad \text{Eq. C.44}$$

And,

$$\alpha = \frac{R}{2L} \quad \text{Eq. C.45}$$

Solving the "characteristic equation" above, there are two values of s that satisfies the differential equation.

$$s_{1,2} = -\alpha \pm \sqrt{\alpha^2 - w_r^2} \quad \text{Eq. C.46}$$

Since both values of s satisfy the differential equation, the solution will consists of two terms, one for each value of s. Three different cases, with somewhat different solution forms, arise, depending on the relative values of  $\alpha$  and  $w_r$ , that is:

**Case 1) Damping coefficient less than undamped resonant frequency:**  $\alpha < w_r$

This case is also called the “**underdamped**” case, with damping is smaller than oscillations. In this case, the square root term in the equations for s leads to a complex number,  $s_{1,2} = -\alpha \pm jw_d$  and the solution has the form:

$$i(t) = e^{-\alpha t} (A_1 \cos(w_d t) + A_2 \sin(w_d t)) \quad \text{Eq. C.47}$$

With,

$$\alpha < w_r \Rightarrow \alpha^2 - w_r^2 < 0 \quad \text{Eq. C.48}$$

And,

$$w_d = \sqrt{w_r^2 - \alpha^2} \quad \text{Eq. C.49}$$

In this equation,  $i(t)$  is decaying exponentially but an oscillatory behavior occurs before the final steady state value is reached.

**Case 2) Damping coefficient greater than undamped resonant frequency:**  $\alpha > \omega_r$

This is the “overdamped” case, where damping dominates. In this case the roots are real and distinct:

$s_1 = -\alpha + \sqrt{\alpha^2 - \omega_r^2}$  and  $s_2 = -\alpha - \sqrt{\alpha^2 - \omega_r^2}$  and the solution has the form:

$$i(t) = A_1 e^{s_1 t} + A_2 e^{s_2 t} \quad \text{Eq. C.50}$$

This equation shows that  $i(t)$  changes exponentially (sum of two decaying exponentials).

**Case 3) Damping coefficient equal to the undamped resonant frequency:**  $\alpha = \omega_r$

This is the “degenerate” case, or also called the “critically damped” case. The square root term is zero and the two values of  $s$  reduce to a single value. The roots are repeated  $s_1 = s_2 = s = -\alpha$  and the solution is of the form:

$$i(t) = A_1 t e^{st} + A_2 e^{st} \quad \text{Eq. C.51}$$

### C.3.1. Considerations on initial conditions

In order to determine the two unknown coefficients of the equation  $i(t)$  two initial conditions are necessary. One of those conditions, as in the case of first order equations, is the value of  $i(t)$  at  $t = 0$ . Moreover, the change in voltage cannot appear across the capacitor (whose voltage cannot change instantly). Since the current cannot change instantly (due to the series inductance), the current through and the voltage across the resistor cannot change instantly. Therefore, the entire change in source voltage must appear across the inductor. Since the voltage across an inductor depends on the current through the inductor according to  $V_L(t) = L di_L/dt$ , the initial change in voltage across the inductor gives the derivative value of the loop current at time  $t = 0$ . Then, the second condition will be the value of the derivative of  $i(t)$  at  $t = 0$ . That is

Condition 1:  $i(t) | t = 0+$

Condition 2:  $di_L(t)/dt | t = 0+ = V_L(t)/L$

### C.3.2. Response of the circuit in underdamped case ( $Q < 0.5$ )

The quality factor  $Q$  previously introduced in Eq. C.14, defines the range of load that can be applied to the circuit and consequently the amount of power that can be transferred through this. The calculation of the power transferred depends on the value of the rms current in the circuit, the higher the current value, the higher the amount of power transferred. For the case, the current in the circuit can be calculated, by Eq. C.52 and the initial conditions as follows:

Using condition 1 it gives:

$$i(t) = 0 \Rightarrow A_1 \cos(0) + A_2 \sin(0) = 0 \Rightarrow A_1 = 0 \quad \text{Eq. C.53}$$

$$i(t) = e^{-\alpha t} \times A_2 \sin(\omega_d t) \quad \text{Eq. C.54}$$

And, using the condition 2 it is:

$$L \frac{di(t)}{dt} = V_s \Rightarrow \frac{V_s}{L} = \omega_d \times A_2 \Rightarrow A_2 = \frac{V_s}{\omega_d \times L} \quad \text{Eq. C.55}$$

Applying the values for  $A_1$  and  $A_2$  the new equation of the circuit is;

$$i(t) = e^{-\alpha t} \times \left( \frac{V_s}{\omega_d \times L} \right) \sin(\omega_d t) \quad \text{Eq. C.56}$$

And the current is....

$$\int_0^{2\pi} i^2(\omega t) d\omega t = \frac{A^2}{2} \times \{ \boxed{1} - \boxed{2} + \boxed{3} \} \quad \text{Eq. C.57}$$

Where:

$$B = \frac{-\omega_d}{2\alpha} \quad \text{Eq. C.58}$$

$$\boxed{1} = B \left[ e^{\frac{2\pi}{B}} - 1 \right] \quad \text{Eq. C.59}$$

$$\boxed{2} = \frac{B \left[ e^{\frac{2\pi}{B}} - 1 \right]}{3} \quad \text{Eq. C.60}$$

$$\boxed{3} = 0 \quad \text{Eq. C.61}$$

With the rms current in the resonant circuit calculated by the equation follow:

$$I_{rms} = \sqrt{\frac{1}{2\pi} \times \left( \int_0^{2\pi} i^2(\omega t) d\omega t \right)} \quad \text{Eq. C.62}$$

The response of the circuit in underdamped case is shown in Figure C.14 for  $Q=0.2$ ,  $R=1 \Omega$ ,  $L=5 \mu\text{H}$  and  $C=6 \mu\text{F}$ .

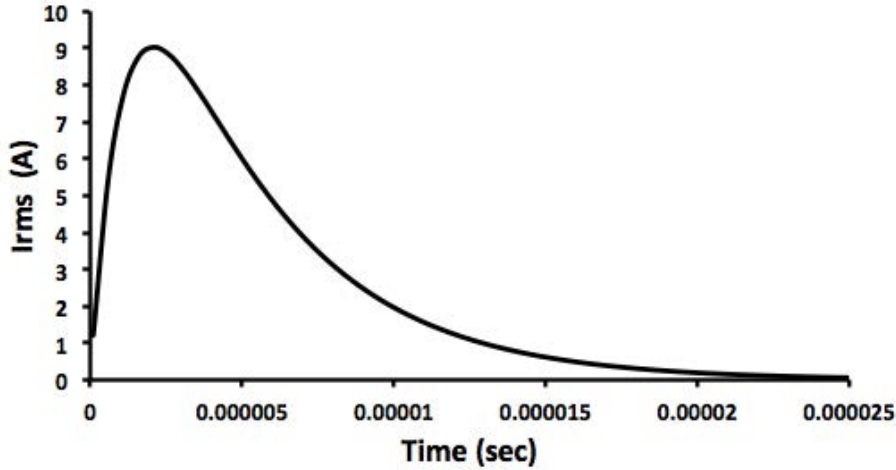


Figure C.14- Underdamped response of the RLC circuit for  $Q=0.2$ .

### C.3.3. Response of the circuit in overdamped case ( $Q>0.5$ )

In overdamped case, the quality factor of the circuit is greater than 0,5 and similarly to the underdamped case, it is necessary to calculate the value of the rms current in the circuit, which for the case can be calculated, by Eq. C.50 and using the initial conditions as follow:

Using condition 1 it gives:

$$i(t) = 0 \Rightarrow A_1 + A_2 = 0 \Rightarrow A_1 = -A_2 \quad \text{Eq. C.63}$$

$$i(t) = e^{-\alpha t} \times A_2 \sin(\omega_d t) \quad \text{Eq. C.64}$$

And, by the condition 2 it is:

$$L \frac{di(t)}{dt} = V_s \Rightarrow \frac{V_s}{L} = s_1 A_1 - s_2 A_1 \Rightarrow A_1 = -A_2 = \frac{V_s}{L} \left( \frac{1}{s_1 - s_2} \right) \quad \text{Eq. C.65}$$

Applying the values for  $A_1$  and  $A_2$  the new equation of the circuit is;

$$i(t) = \left( \frac{V_s}{L} \frac{1}{(s_1 - s_2)} \right) (e^{s_1 t} - e^{s_2 t}) \quad \text{Eq. C.66}$$

And the current is given by;

$$\int_0^{2\pi} i^2(wt) dw t = A^2 \times \{ \boxed{1} + \boxed{2} + \boxed{3} \} \quad \text{Eq. C.67}$$

Where:

$$A = \left( \frac{V_s}{L} \frac{1}{(s_1 - s_2)} \right) \text{ and } wt = \theta \quad \text{Eq. C.68}$$

$$\boxed{1} = \left[ \left( \frac{w}{2 \times s_1} \right) \times e^{\left( \frac{2 \times s_1}{w} \right) \theta} \right]_0^{2\pi} \quad \text{Eq. C.69}$$

$$\boxed{2} = \left[ \left( \frac{w}{s_1 + s_2} \right) \times e^{\left( \frac{s_1 + s_2}{w} \right) \theta} \right]_0^{2\pi} \quad \text{Eq. C.70}$$

$$\boxed{3} = \left[ \left( \frac{w}{2 \times s_1} \right) \times e^{\left( \frac{2 \times s_1}{w} \right) \theta} \right]_0^{2\pi} \quad \text{Eq. C.71}$$

The response of the circuit in overdamped case is shown in Figure C.15 for  $Q = 0.9$ ,  $R = 1 \, \Omega$ ,  $L = 5 \, \mu\text{H}$  and  $C = 6 \, \mu\text{F}$ .

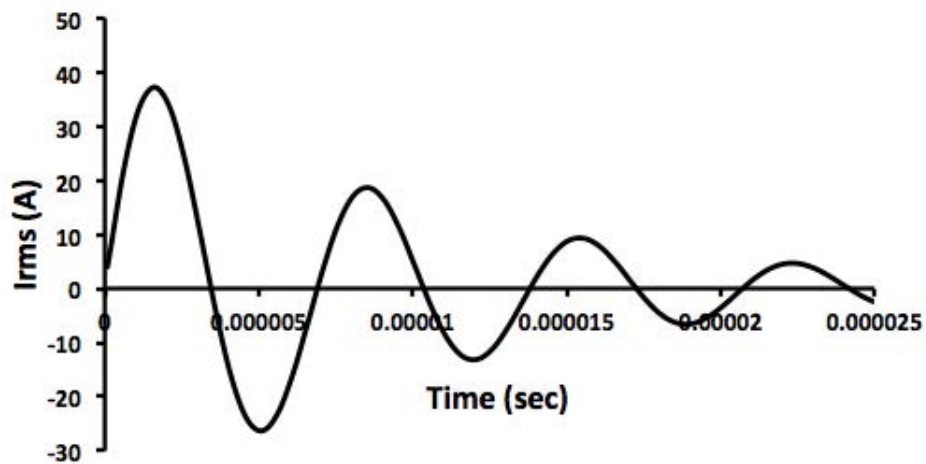


Figure C.15- Overdamped response of the RLC circuit for  $Q=0.9$ .

For this case,  $I_{rms}$  oscillates with a frequency  $f_d$  that can be calculated as follows :

$$\omega_r = \frac{1}{\sqrt{LC}} = 0.1825 \text{ rad / s}$$

$$\alpha = \frac{R}{2L} = \frac{1}{2 \times 5 \times 10^{-6}} = 10^5$$

$$\omega_d = \sqrt{\omega_r^2 - \alpha^2} = 0.91 \times 10^5 \text{ rad / s}$$

and,

$$f_d = \frac{0.91 \times 10^5}{2\pi} = 14.46 \text{ kHz}$$

with a period of  $T = 0.0000069 = 6.9 \mu s$ , the half-period is  $T/2 \approx 3.4 \mu s$  and the peak current of 37.2A occurs for the instant time 1.6  $\mu s$ .

### C.3.4. Peak current analysis

The peak current is defined by Eq. C.72, which increases as the values of the input voltage and resonant capacitor increases and the value of resonant inductor decreases.

$$I_{peak} = V_{in} \times \sqrt{\frac{Cr}{Lr}} \quad \text{Eq. C.72}$$

The plots of the resonant currents for the capacitor of 4  $\mu F$  are presented in Figure C.16 and the peak current for the both capacitors (4 and 10  $\mu F$ ), are presented in Table C.1.

As can be observed, the peak resonant current is proportional to the input voltage  $V_{in}$  and therefore, a source as high as possible would be required.

This analysis is focused on the PEM Mark1020, which voltage varies between 19.11 V and 23.71 V, and whose correspondent plots are the first and second of Figure C.16 with the peak values of 22.7 A and 27.2 A respectively. The third plot corresponds to the Nexa<sup>TM</sup> PEM, which allows working with much higher current values as can be observed. However, due to problems related to the discontinuity of this product, at the time of carrying out the experimental tests this was not available for the tests.

The analysis considers the capacitors of 4  $\mu F$  and 10  $\mu F$  and the transformer D, with the characteristics,  $L=L_t=2.1 \mu H$  and  $R'=R_t=0.18 \Omega$ .

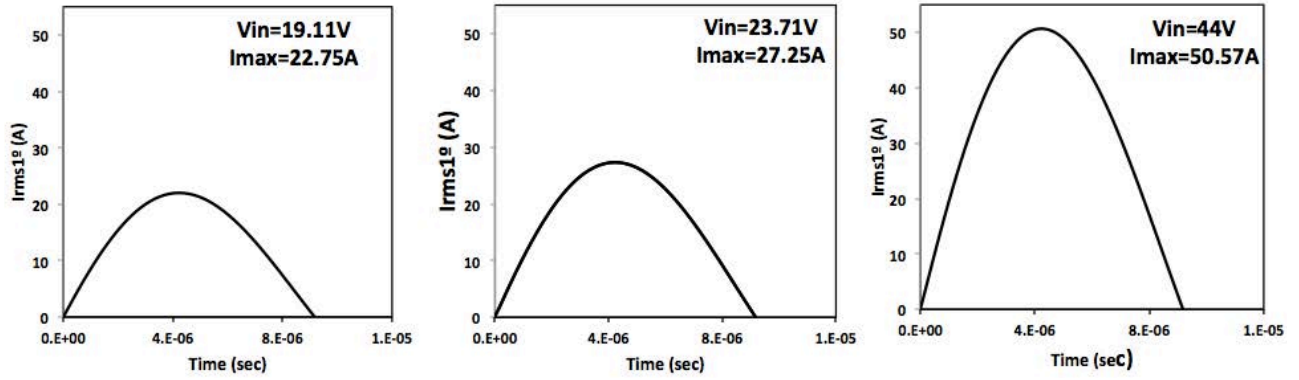
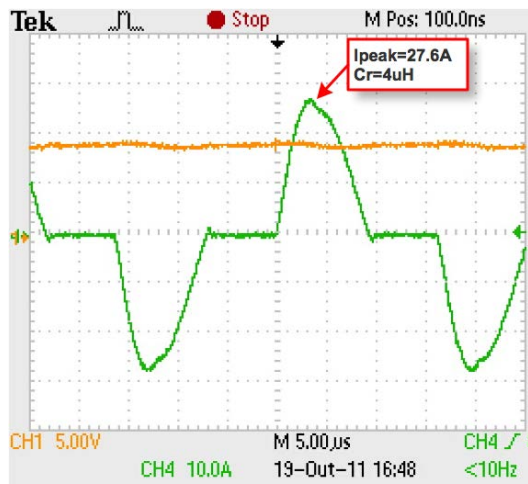


Figure C.16 - Peak of the resonant current for different values of  $V_{in}$  and  $C_r=4 \mu F$ .

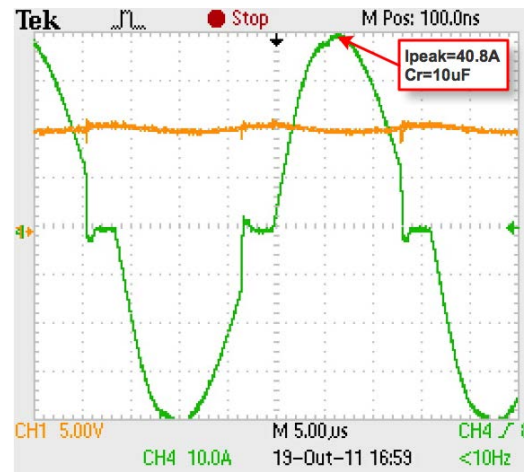
Table C.1 - Resonant peak current analysis.

	<b>I<sub>max</sub> (A)</b>		
	<b>V<sub>in</sub>=19.11 V</b>	<b>V<sub>in</sub>=23.71 V</b>	<b>V<sub>in</sub>=44 V</b>
<b>Cr=4 μF</b>	22.75 A	27.25 A	50.57 A
<b>Cr=10 μF</b>	31.67 A	39.3 A	72.93 A

Figure C.17 show the experimental results for, the capacitor of  $4 \mu F$  (a), and for capacitor of  $10 \mu F$  (b) and for  $L_r = 2.1 \mu H$  and  $R' = 0.18 \Omega$ . As can be observed, the peak current increases with the increase of the capacitor value. These results are therefore consistent with the analytical ones. In addition, it appears that the waveform current for capacitor of  $10 \mu F$  is cut off before it reaches zero, as already explained above.



(a) For  $C_r=4 \mu\text{F}$ .



(b) For  $C_r=10 \mu\text{F}$ .

Figure C.17- Experimental validation of the resonant current for two capacitors.

The Figure C.16 above shows that for the same condition of oscillation, that is for the same operation frequency, the peak current in the resonant current increases with the increase of the input voltage,  $V_{in}$ . It is also observed that it increases as the resonant capacitor value increases. Since the power transferred through the resonant circuit is  $P = R \times I_{rms}^2$ , then, the increase of the current value is required but also limited by the voltage source. On the other hand the increase of the capacitor should not increase excessively since it can produce very high peak current values endangering the system components. As a example the repetitive peak collector current of the IGBT, ( $I_{CRM}$ ) is 100 A and should never be exceeded.

### C.3.5. Selection of $L_r$ and $C_r$

Concerning the selection of the components  $L_r$  and  $C_r$ , two criteria were taken, namely: 1st)  $L_r$  must be as low as possible (within the limit is  $L_t$ ) and 2nd)  $C_r$  must be selected according to the power to transfer and operating frequency required by the control system. A third condition is imposed in this case, regarding the availability of capacitors at the lab.

Then, the conditions of voltage provided by the PEM Mark1020 and the PEM Nexa, and the leakage inductance of the HF transformer, the analysis the variables such as; the current in the resonant circuit, the power transferred and output voltage level of the SRC, made with the second order differential equation leads to the results presented in the figures below.



➤  $L_r=2.1\mu\text{H}$ ,  $C_r=4\mu\text{F}$ ,  $V_{in}=19.11\text{V}$

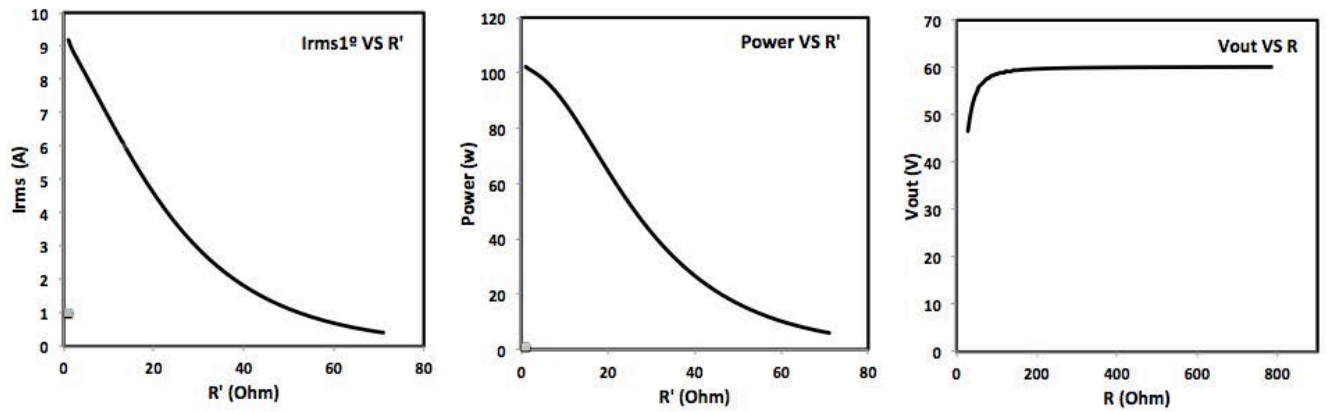


Figure C.18 - Output variables for the minimum voltage of the PEM Mark1020 (19.11V).

➤  $L_r=2.1\mu\text{H}$ ,  $C_r=4\mu\text{F}$ ,  $V_{in}=23.71\text{V}$

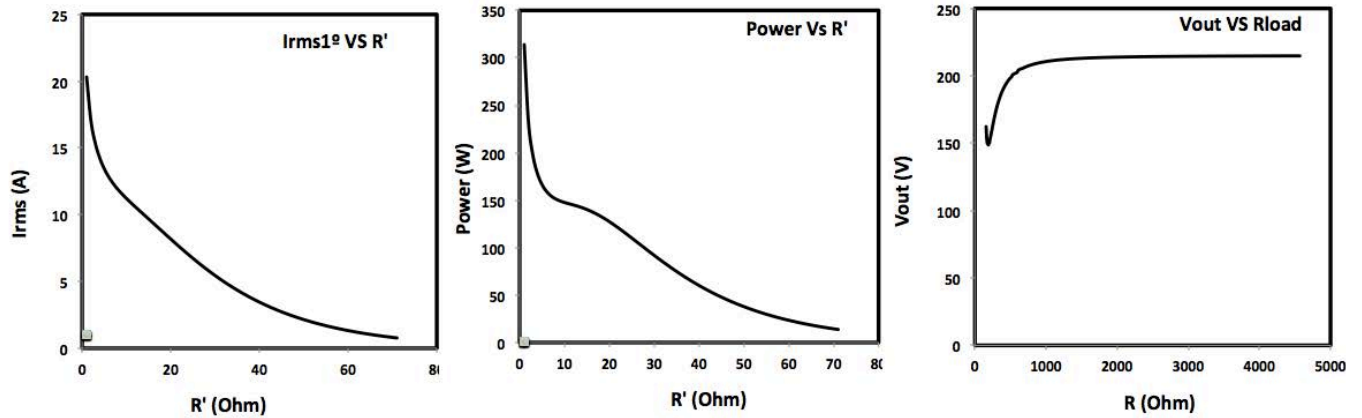


Figure C.19 - Output variables for the maximum voltage of the PEM Mark1020 (23.71V).

➤  $L_r=2.1\mu\text{H}$ ,  $C_r=4\mu\text{F}$ ,  $V_{in}=44\text{V}$

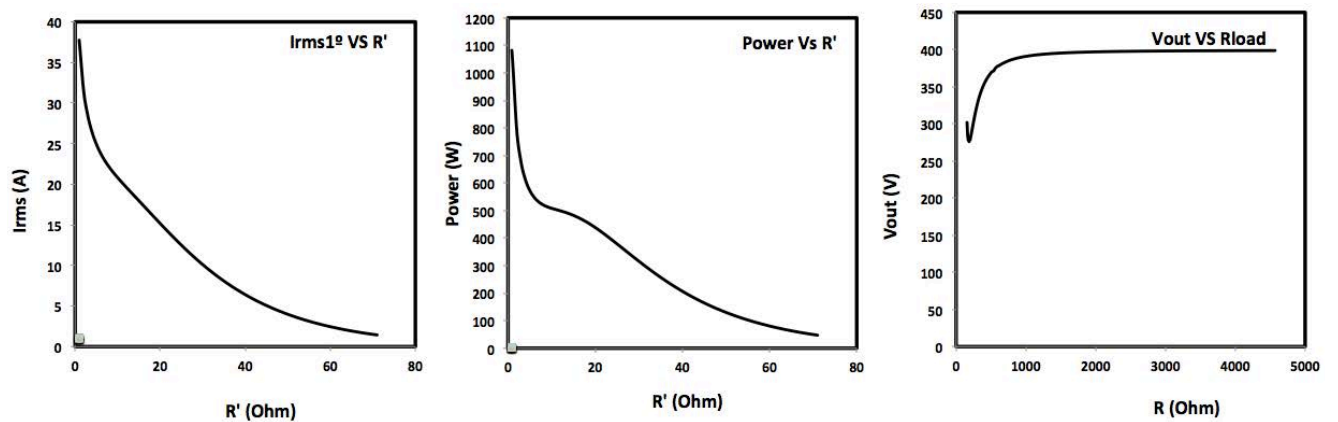


Figure C.20 - Output variables for the maximum voltage of the PEM Nexa™ (44 V).

Table C.2 - Comparative analysis of the performance for two sets of components Lr and Cr.

		Vin=19.11 V	Vin=23.71 V	Vin=44 V
<b>Lr=2.1 <math>\mu</math>H Cr=4 <math>\mu</math>F</b>	Pmax (W)	102.22	314.32	1100
	Imax_ress (A)	9.16	20.33	37.73
	Vout (V)	60.32	214.80	398.63
<b>Lr=2.1 <math>\mu</math>H Cr=10 <math>\mu</math>F</b>	Pmax (W)	340.03	487.59	1679.18
	Imax_ress (A)	26.58	31.82	59.06
	Vout (V)	60.4	234.76	398.90

The operation of the SRC in its entire range that is for  $0 < Q < 1$  is represented in the figures above.

➤ **Lr=2.1 $\mu$ H, Cr=4 $\mu$ F, Vin=19.11V**

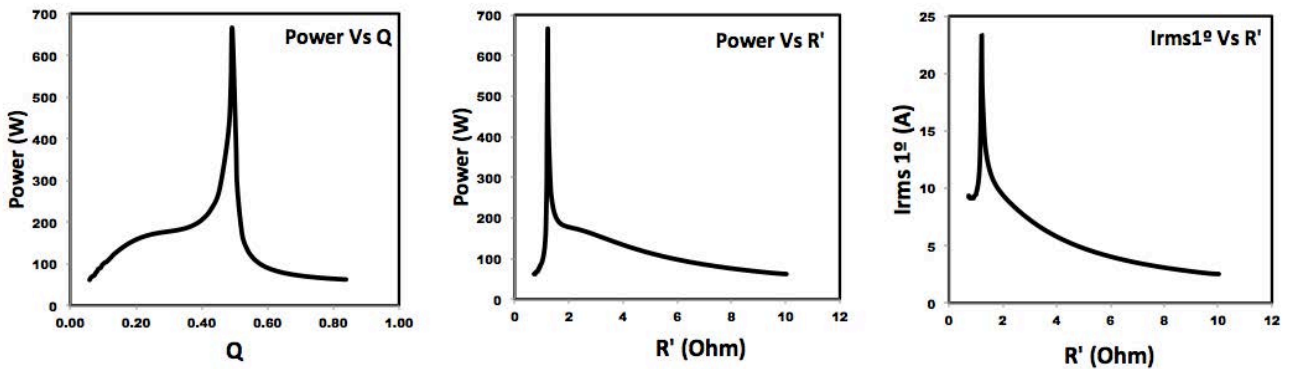


Figure C.21- Operation of the SRC on its entire range for minimum input voltage.

➤ **Lr=2.1 $\mu$ H, Cr=4 $\mu$ F, Vin=23.71V**

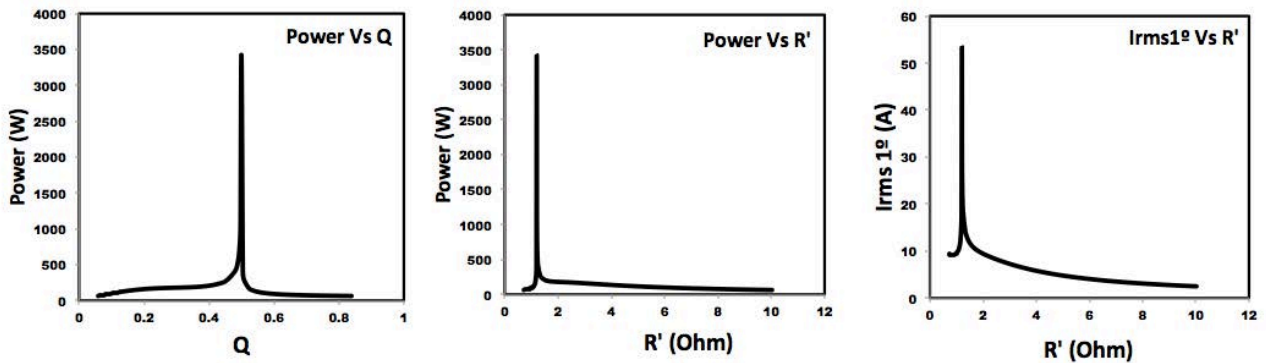


Figure C.22- Operation of the SRC on its entire range for maximum input voltage.

### C.3.6. Analysis of the results

By the analysis of the figures and tables above it is observed that the maximum power transferred and the peak resonant current, increases with the increase of the capacitor,  $C_r$ . The converter output voltage,  $V_{out}$  only depends on the value of the voltage source,  $V_{in}$ .

With regard to the output voltage  $V_{out}$ , it appears that if the PEM Mark1020 is used as the power supply system of the SRC, whose maximum output voltage is 23.71V, the output voltage can be regulated up to 234V. while if the Nexa PEM is used, the output voltage of the converter can be regulated up to 398.9V  $\cong$  400V. Another important aspect to observe is related to the peak current, which reach very high values for very low load conditions. Typically the peak current tends for infinite if a short-circuit on the load is done, which is quite obviously not recommended.

Figure C.21 and Figure C.22 show the operation of the SRC on its entire range that is for  $0 < Q < 1$ . It appears that regardless of the value of the input voltage, the threshold between the two operation modes, that is  $Q = 0.5$ , both the power as the current of the resonant circuit reach maximum values. Under these conditions the load is minimum and it can be concluded that if the series resonant converter could work in this zone it would be excellent in terms of transfer of power, however, this operating point is extremely unstable and dangerous due to the high currents that arise in the circuit.

## C.4. Conclusions

The analysis of the series resonant converter has been presented in this appendix, first based on sinusoidal approximation, and second based on second-order differential equation method.

By the analysis of the maximum power transferred and the peak resonant current, the selection of the resonant components is made accordingly to some criteria established as follows;  $L_r$  must be as low as possible and  $C_r$  must be selected accordingly of the power to be transferred and the operating frequency.

The numerical and experimental results allow concluding that the peak resonant current increases with the capacitor,  $C_r$ , while the converter output voltage only depends on the value of the input voltage. It was also found that the operation of the SRC at very low loading conditions is not recommended, because high peak current can arise. The analysis of the second order differential equation led to the selection of the resonant components, which in turn determined the frequency of operation of the system. As well as the maximum power transferred.



---

*APPENDIX D*

**OPERATION OF THE  
SERIES RESONANT CONVERTER**

---



## **APPENDIX D - Operation of the series resonant converter**

### **D.1. Introduction**

This appendix presents the simulation studies carried out in MatLab/Simulink once integrated the PEM, as the element of power generation and the SRC as the element of energy conversion. The tests were performed both in loop-open and closed-loop conditions and the PEM used is the Nexa. In order to validate the system implemented a loading variation is applied both in step-up and step-down conditions. The results achieved under these conditions are presented and analyzed.

### **D.2. Operation in open-loop**

The operation of the SRC is analyzed in open loop upon reaching steady state condition. To this analysis it is considered that the output voltage -  $V_{out}$  is a good indicator of the performance the system.in open-loop condition. Thus the situations considered for this analysis are output voltage of the converter: 1) to different VCO values, and the same load, 2) to different values for load and the same VCO, 3) to a step-up and a step-down of load. The simulation parameters introduced for this case are the following:

Method: ode23t (Stiff/ Trapezoidal),

Relative tolerance:  $1e-3$

Absolute tolerance:  $1e-6$

Max step size:  $1e-7$

#### **D.2.1. Open-loop response for different VCO values**

The tree curves represented in Figure D.1 show the variation of the output voltage  $V_{out}$  according to the reference signal VCO and the same load condition. Thus, for  $VCO = 0.9$  the voltage reaches the steady-state value at 594 V and the system remains stable at 1.204s. For  $VCO = 0.6$  the voltage reaches the steady-state value at 584 V and the system remains stable 1.207s. Finally, for  $VCO = 0.3$  the voltage reaches the steady-state value at 569 V and the system remains stable at 1.3s. Then, it can be concluded that in open-loop condition, the output voltage increases with VCO i.e., the gain of the converter increases with the operating frequency ( $f_s$ ) and the power chain is able of controlling output voltage at 400 V.

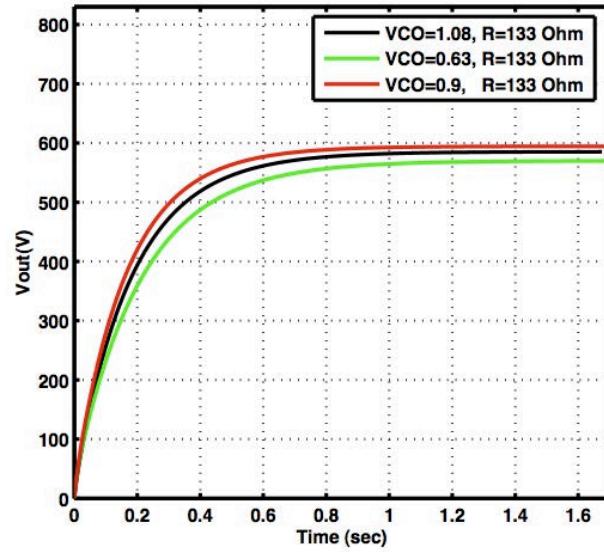


Figure D.1 – Output voltage of the converter for different VCO values.

### D.2.2. Open-loop response for different load values

For different values of load and the same VCO condition, the gain of the converter decreases with the load and the power chain keeps able of controlling output voltage at 400 V. Thus, observing the Figure D.2 below it appears that: for  $I_{load} = 0.33$  A the steady-state voltage is 700 V, for  $I_{load} = 2$  A the steady-state voltage is 622 V and for  $I_{load} = 3$  A the steady-state voltage is 591 V.

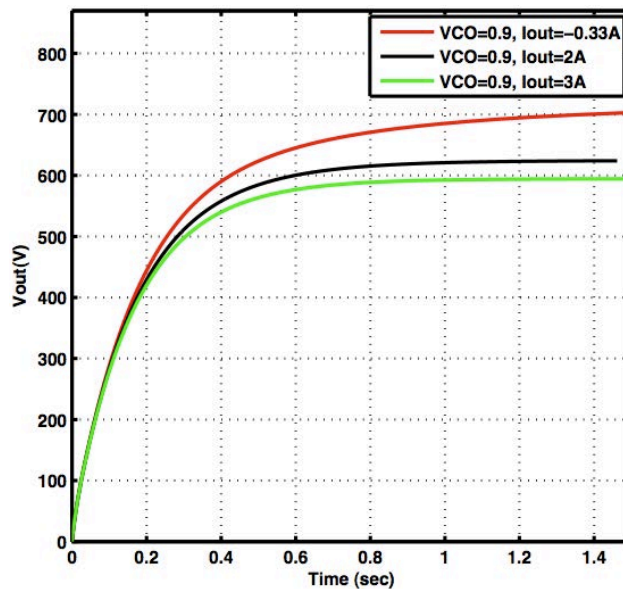


Figure D.2 – Output voltage of the converter for different load values.



### D.2.3. Open-loop response to step-up and step-down load conditions

As can be observed in Figure D.3 for the same load condition the steady-state value of  $V_{out}$  does not depend on its initial value but increases with VCO i.e., the gain of the converter increases with the operating frequency  $f_s$ , whose results are consistent with those observed in Figure D.1.

To step-up or step-down load variations, as shown in Figure D.4, the final value of  $V_{out}$  depends on the value request by the load that is; it drops if the value of the load increases and raises if the value of the load decreases.

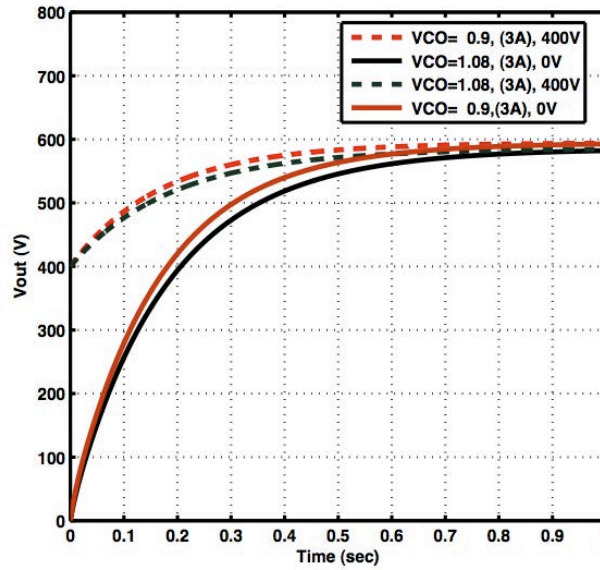


Figure D.3 – Output voltage of converter for two initial values and two VCO values.

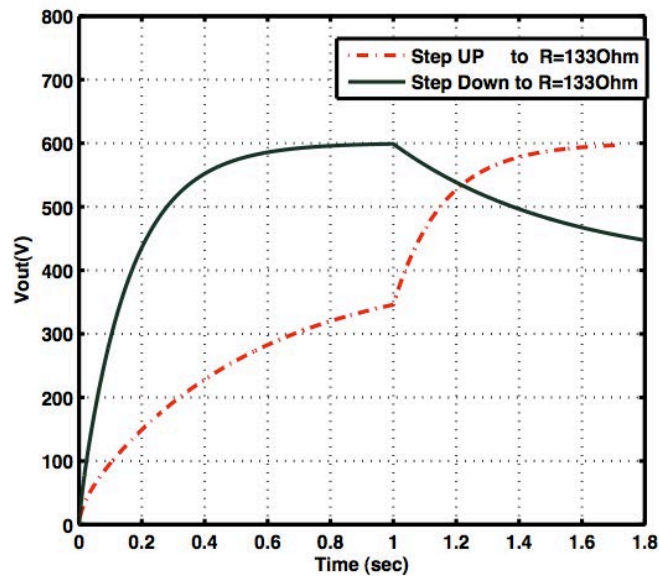


Figure D.4 – Open loop response to step-up and step-down load currents.

### D.3. Operation in closed-loop

In this section the simulation results achieved in closed-loop are analyzed and discussed. In close loop the system is controlled through the PI followed by the VCO blocks, which "forced" the output voltage  $V_{out}$  to keep in null error in steady-state operation. A second objective has to do with the robustness of the system to load variations, i.e., the system must always reach the null error independently of the load variations. In order to validate this principle it was applied a step between the minimum and maximum load current allowed by the Nexa fuel cell system. That is, a step from 0.33 A (1200  $\Omega$ ) to 1.33 A (300  $\Omega$ ) is applied for the tests. The maximum load that can be applied is for the NEXA case of 3 A (134  $\Omega$ ). The simulation results achieved under these conditions are analyzed and discussed below, in accordance with the following parameters:

Method: ode23t (Stiff/ Trapezoidal),

Relative tolerance: 1e-3

Absolute tolerance: 1e-5

Control (PI):  $k_p=1$ ,  $k_i=100$

#### D.3.1. VCO signal analysis

The signal of the voltage control oscillator (VCO) represented in Figure D.6 varies accordingly to the load requested, with a step up in 0.04 s. VCO signal is the information sent by the controller to the power converter circuit on the new load conditions. The converter in turn acts in accordance varying the frequency of operation to meet the conditions required by the load while maintaining constant output voltage. Figure D.6 also shows that for an increase on load request, the signal of VCO and hence the frequency of converter operation increases as well. VCO varies between 0 and 1, being that for  $VCO=1$  the converter works at resonant frequency, transferring the maximum power from the fuel cell to the load. In the present case for a load of 1200  $\Omega$  (0.33A) VCO is 0.1, which corresponds the frequency of 25 kHz while for the load of 300  $\Omega$  (3 A) is 0.45, which corresponds the frequency of 50 kHz.

#### D.3.2. Output voltage analysis

The output voltage of the converter is presented in **Error! Reference source not found.** as can be observed this always follows the reference value even for a load variation at the instant time 0.04 s.. The overshoot is due to the control parameters  $K_P=1$  and  $K_I=100$ . As can be seen, the output voltage remains regulated in 400V as the reference value defined by the user.

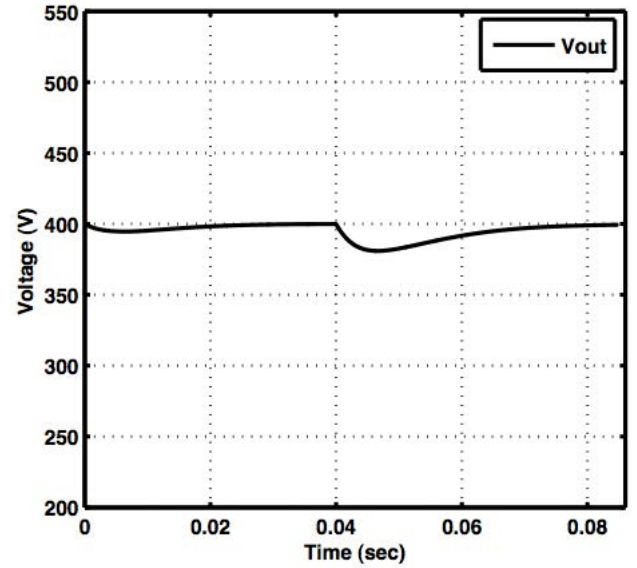
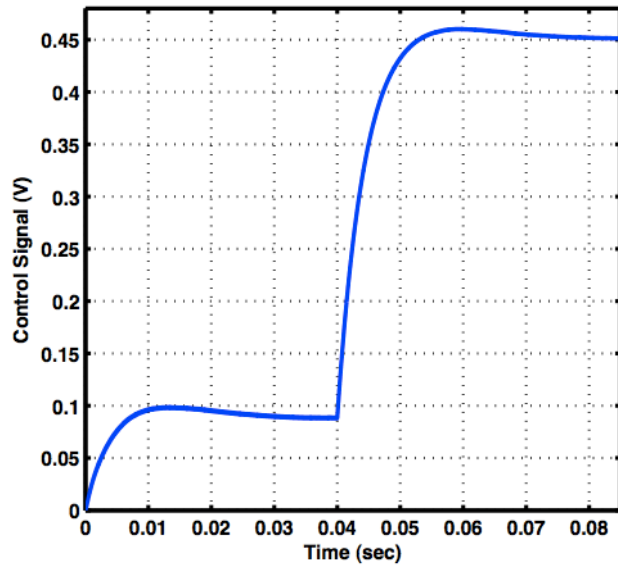


Figure D.5 –VCO with a step load at time 0.04 s. Figure D.6 – Output voltage with a step load at time 0.04 s.

### D.3.3. Fuel cell current and voltage analysis

In Figure D.7 it is observed that for the time instant of 0.04 s the fuel cell current varies according to the variation imposed by the load. A ripple is also presented in the both load levels. Figure D.8, shows the fuel cell voltage at the same conditions. As is observed, the fuel cell voltage drops when the current rises at the instant of 0.04 s. A small ripple appears also in the fuel cell voltage, which varies accordingly to the frequency operation that is if the frequency increases, the ripple decreases. That is the operating frequency increases and the ripple decreases with the load. Therefore, in closed-loop, the fuel cell current increases if the load increases while the fuel cell voltage decreases.

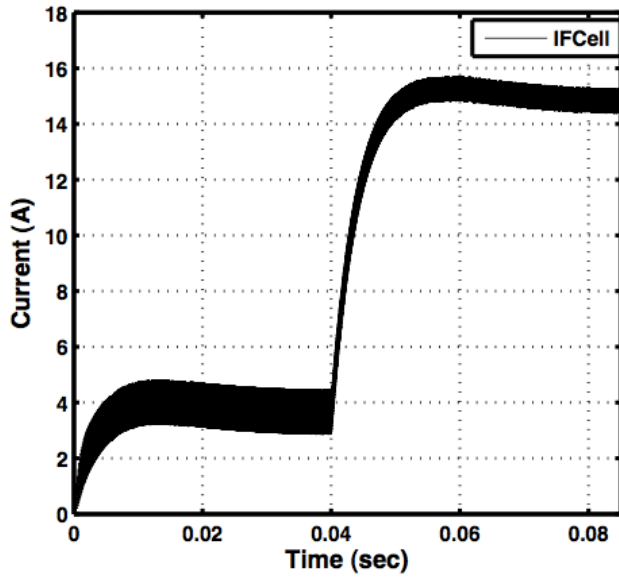


Figure D.7 – Fuel cell current for a change in the load at time 0.04s

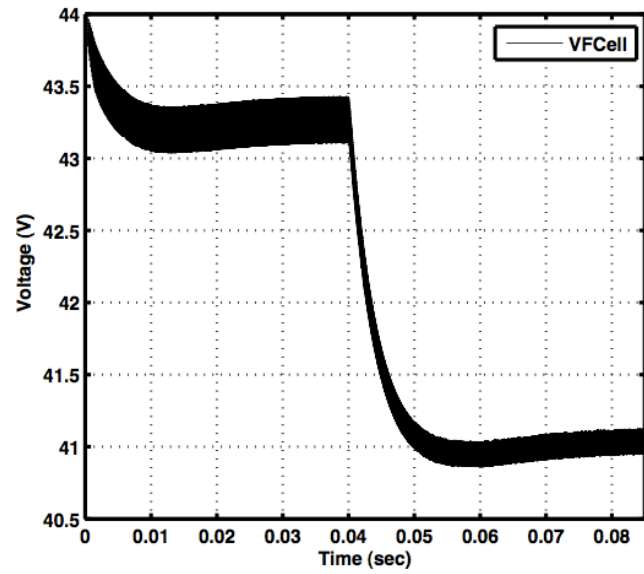
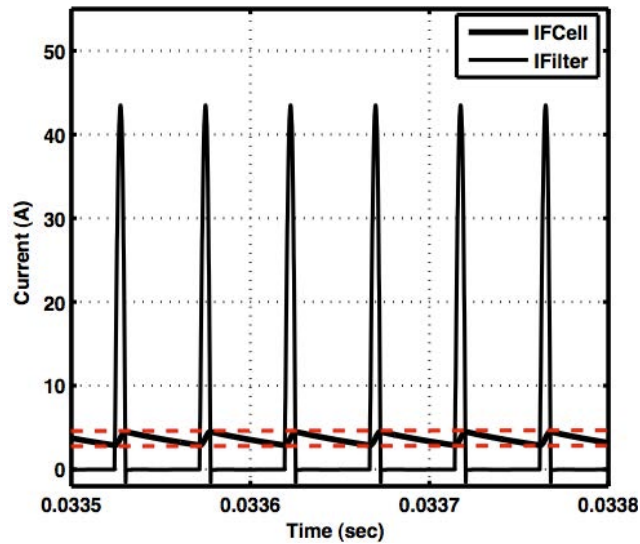


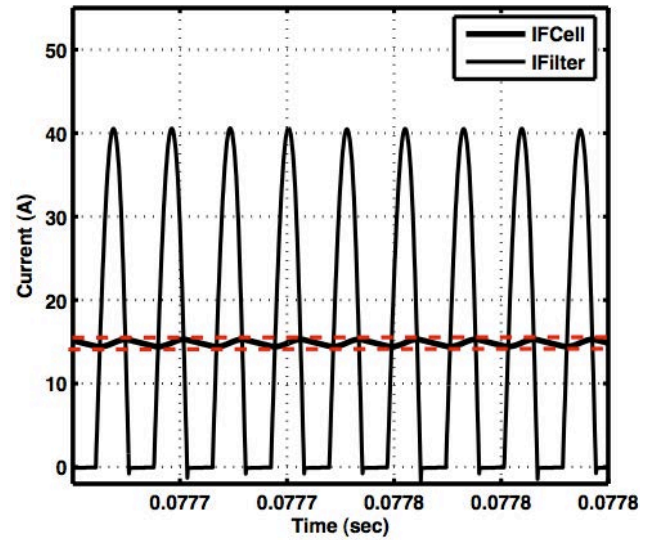
Figure D.8 – Fuel cell voltage for a change in the load at time 0.04s.

#### D.3.4. Ripples of current and voltage versus PEM filter

The ripple current affects the capacity, lifetime and also increases the hydrogen consumption of a fuel cell. While an adequate control of the converter addresses the issue of current dependence to output voltage, an adequate filter solves the ripple problems. Figure D.9 shows the difference in ripple current with and without the implementation of the filter designed to Nexa PEM for two load conditions; a) 0.33 A and b) 3 A. Through the analysis of these figures, it appears that: for the load of 0.33 A, which presents;  $I_{FCmax} = 4.495$  A and  $I_{FCmin} = 2.88$  A, the ripple of current is  $\Delta i_{FC} = I_{max} - I_{min} = 1.61$  A and the operating frequency for this load level is  $f_s = 25$  kHz. A similar analysis performed for the load of 1.33A, leads to leads to similar conclusions; in which  $I_{FCmax} = 15.28$  A,  $I_{FCmin} = 14.42$  A and ripple of current  $\Delta i_{FC} = I_{max} - I_{min} = 0.18$  A. The frequency of operation for this case is  $f_s = 50$  kHz. The ripple of voltage appears also for the two conditions, as is observed in detail in Figure D.10. Thus, it appears that for the load of 0.33A the voltage ripple is  $\Delta V_{FC} = 43.42 - 43.11 = 0.31$  V while for the load of 1.33 A, that is  $\Delta V_{FC} = 41.12 - 40.94 = 0.18$  V.

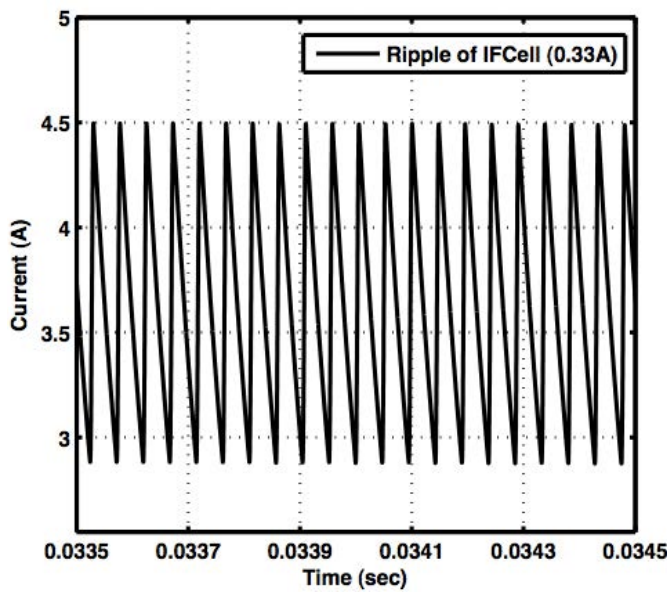


(a)  $1200\Omega$  (0.33A).

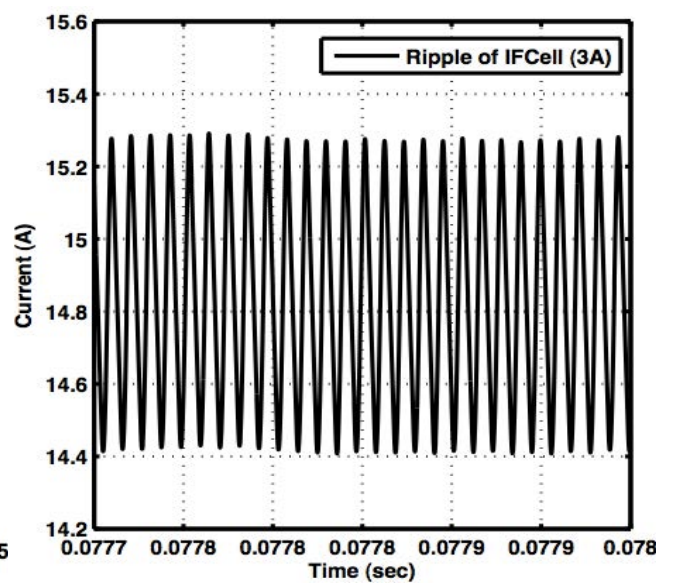


(b)  $300\Omega$  (1.33A).

Figure D.9 – Ripple of current with and without filter in the PEM.



(a)  $1200\Omega$  (0.33A).



(b)  $300\Omega$  (1.33A).

Figure D.10 – Ripple of the fuel cell voltage.

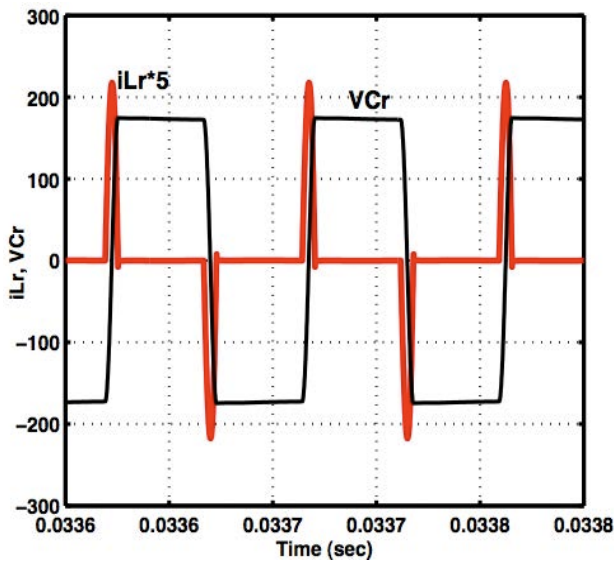
The information provided from the analysis of the figures above is summarized in Table D.1 below. From this table it appears that the ripples of current and voltage both decreases with the increase of the load level while the frequency operation increases. Another important aspect to note is relating to variation in ripples amplitude in voltage and current with the filtering, which reduction is significant. Thus, it may be concluded that it is absolutely necessary to introduce a filter on the output of the PEM, for reasons already mentioned.

Table D.1 – Fuel cell ripple analysis

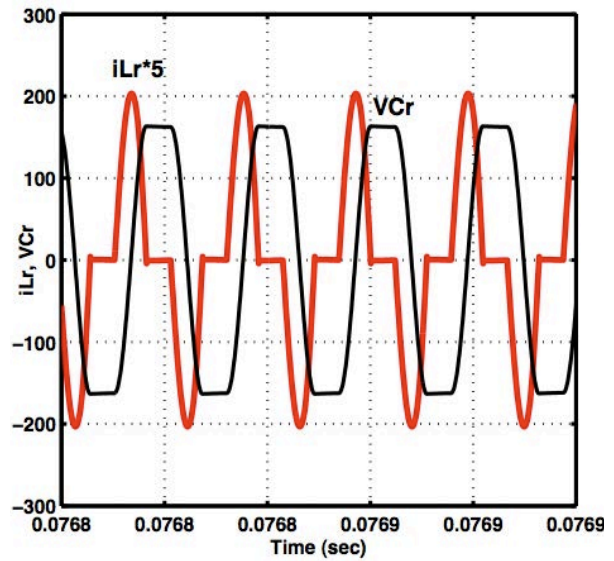
Load Condition	1200 $\Omega$ (0.33 A)	300 $\Omega$ (3 A)
VCO signal (V)	0.1	0.45
Freq (kHz)	25	50
$\Delta i_{FC}$ (A)	1.61	0.18
$\Delta V_{FC}$ (A)	0.31	0.18

### D.3.5. Resonant circuit analysis

Considering the two situations of load; a) 0.33 A and b) 1.33 A, the resonant waveforms of voltage and current are shown in Figure D.11. As can be observed, the current through the inductor -  $i_{Lr}$  is discontinuous in both situations. It crosses zero value twice during each period. At those instants (of zero current), the switches are able to switch without loss. The current in  $L_r$  is forced to flow making the antiparallel diode of the IGBT conducting and no voltage appears over the switch during the turn-off. Hence, the switches turn off naturally with zero current and zero voltage.



(a) 1200 $\Omega$  (0.33A).



(b) 300 $\Omega$  (1.33A).

Figure D.11 – Voltage and current waveforms in the resonant circuit.

### D.3.6. Ripples of current and voltage versus output filter

the voltage (and current) in secondary side transformer are both alternated. Once rectified they are filtered to reduce the ripple of voltage and current. Figure D.9 below show the effect of the



application of a low pass filter in the output of the converter. Both figures show that the output current is free of ripple due to the introduction of an inductor filter  $-L_f$ . The capacitor filter  $-C_f$  allows eliminating the voltage ripple making a constant output voltage in the converter as required. Accordingly, this capacitor value must be large enough. The values of  $L_f$  and  $C_f$  used are shown in Chapter 5.

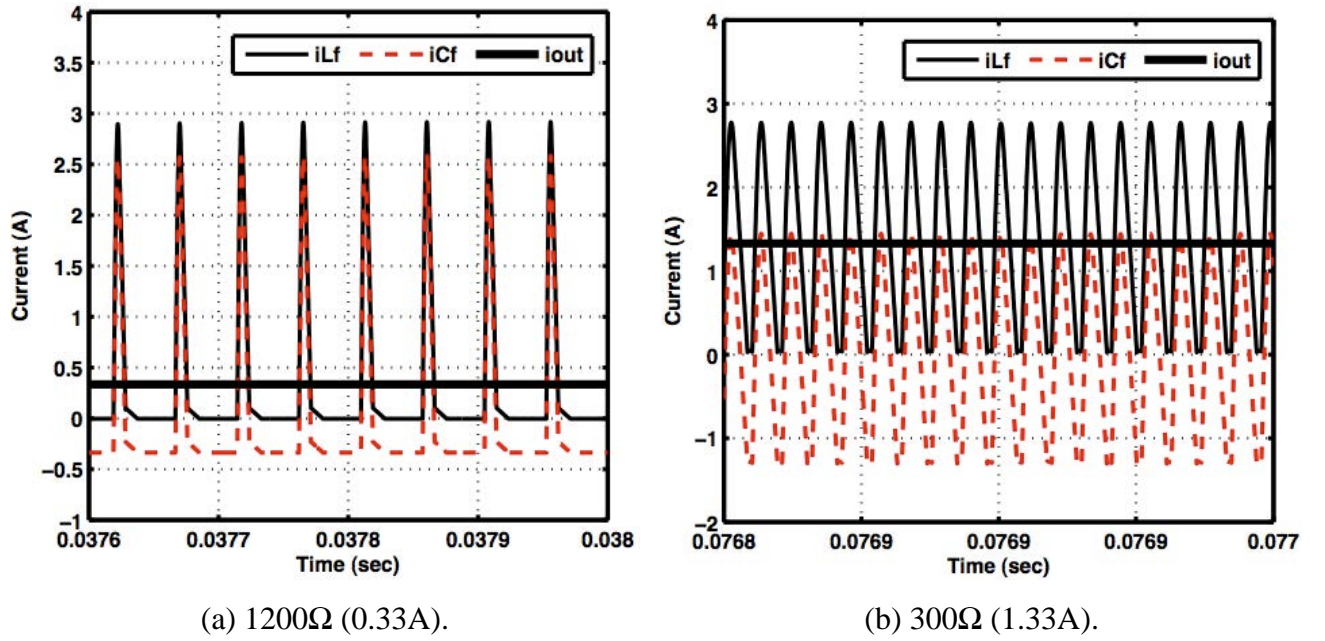


Figure D.12 – Ripple of output current of the converter.

#### D.4. Conclusions

The results presented in this appendix were used to show that the model developed and implemented in MatLab/Simulink of the series resonant converter (SRC) meets the requirements of the project, both in power and control. Through the results obtained it follows that:

- 1.The frequency of the converter varies according to the load request. That is, depending on the VCO value, which is defined in the control system.
- 2.Both filters used (PEM filter and output filter) operate properly meeting the required function,
- 3.The system works correctly in both open loop and in closed loop.
- 4.The PI controller implemented guarantees the control of output voltage.





---

*APPENDIX E*

**CONSIDERATIONS FOR  
HANDLING HYDROGEN SAFETY**

---



## APPENDIX E- Considerations on handling hydrogen safety

### E.1. Introduction

The purpose of this appendix is to provide some useful information about the procedures that have been taken during this work for a safe handling of the hydrogen. In fact the hydrogen can be safely handled like other fuels if adopted some safety rules, namely: 1) Prevent hydrogen leaks, 2) Detect accidental leaks and take proper action, 3) Prevent hydrogen accumulation and 4) Remove likely ignition sources and suspect unknown ignition sources[15].

### E.2. Hydrogen production and storage

Hydrogen can be produced through various resources including fossil fuels, such as natural gas and coal, nuclear, biomass, and other renewable energy technologies, such as wind, solar, geothermal, and hydroelectric power. The main challenge of hydrogen production is the cost. For cost competitive, the hydrogen must be comparable to conventional fuels and technologies in order to succeed in the commercial marketplace. Figure E.1 shows the pathway of production of hydrogen, which consists basically of four steps: production, handling, distribution, and dispensing [16].

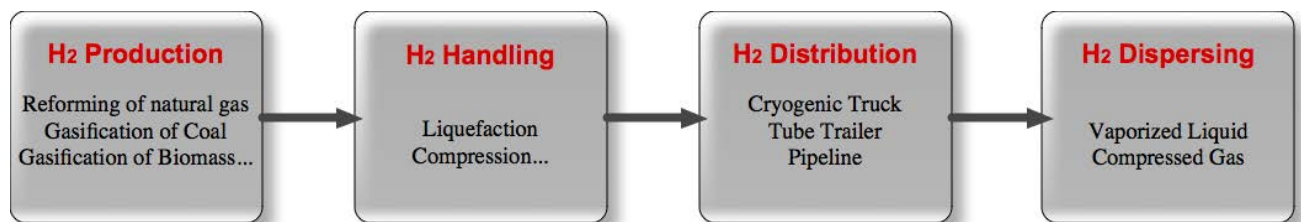


Figure E.1 –Hydrogen Production Pathway

Hydrogen storage continues to be one of the most technically challenging barriers to the widespread commercialization of hydrogen technologies such as the fuel cells. The energy density of gaseous hydrogen can be improved by storing hydrogen at higher pressures. This higher pressure requires material and design improvements in order to ensure tank integrity. The fuel supply pressure is monitored using standard dial pressure gauge as is represented in Figure E.2 and Figure E.3. The fuel pressure that provides a PEM fuel cell is maintained constant in the range of 0.3 to 0.5bar but it is not continuously monitored.

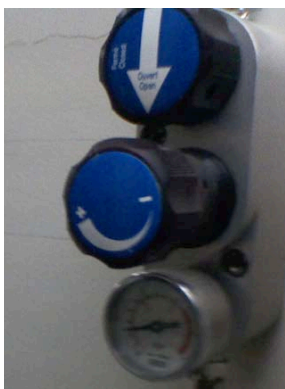


Figure E.2- Hydrogen in a network.



Figure E.3- Hydrogen in a Tank.

### E.3. Equipments of measurement and control

#### E.3.1. Hydrogen fuel mass flow

The hydrogen fuel mass flow was measured and controlled by a Mass Flow Controller (MFC) placed at the input and a Mass Flow Meter (MFM) placed at the output of the PEM. The MFC used as a controlling range of mass flow up to 50 SLM (Standard Liters per Minute); otherwise, the MFM used as a measuring range of mass flow up to 10 SLM. The digital equipment of Bronkhorst of Figure E.5 below shows the values of MFC (left) and MFM (right), which are sent to it via RS232. In the case of mass flow control; the output signal is continuously compared with a set point signal from a voltage source. Any deviations between set point signal and measured signal are translated into a solenoid control valve adjustment until the two signals are identical.



Figure E.4 - Mass Flow Meter and Controller.



Figure E.5 - Fuel mass flow display.

### **E.3.2. Hydrogen leaks detector**

Hydrogen gas is colorless and odorless and normally not detectable by human senses. Means shall be provided for detecting the presence of hydrogen in all areas in which leaks, spills, or hazardous accumulations may occur. In order to safeguard the security of persons and property of the laboratory a fuel leaks detector was used. The device used is the TIF8800 Detector of Figure E.6, which uncovers gas leaks from 50-500 ppm in gas lines and appliances.

### **E.3.3. Measurement of the temperature**

The temperature of the PEM fuel cell stack was measured by the K-Type Thermocouple HI-93530 of Figure E.7. The HI-93530N is a waterproof thermometer that can read with a resolution of 0.1 in the range of  $-149.9$  to  $999.9^{\circ}\text{C}$  ( $-24.9$  to  $999.9^{\circ}\text{F}$ ). The HOLD button freezes the display to allow the user time to record readings. The  $^{\circ}\text{C}/^{\circ}\text{F}$  button switches between the Celsius and Fahrenheit temperature scale. For high accuracy, HI 93530N features a CAL button to allow the operator a simple one point calibration in an ice bath at  $0^{\circ}\text{C}$  when probe interchange occurs.



Figure E.6 - Gas Detector TIF8800.



Figure E.7 - K-Type Waterproof Thermometer.

## **E.4. Electrical Equipment**

### **E.4.1. Voltage and current measurements**

The voltage and current measurements were made through very common equipment's such as a Digital Multimeter of Figure E.8 and a Tektronix A622 of Figure E.9, below. The A622, 100A AC/DC Current Probe enables a general-purpose oscilloscope to display AC and DC current signals up to 100 amps Peak (70 A RMS). The A622 current probe can also make AC and DC

measurements with a multimeter by using the BNC-to-banana plug adapter that is available as a recommended accessory. A Rogowski current transducer is used for measuring the electrical current. It provides an output voltage, which is proportional to current (e.g. 1mV/A). It tracks the current as it changes with time and therefore can reproduce the current waveform on the oscilloscope.



Figure E.8 - Digital Multimeter



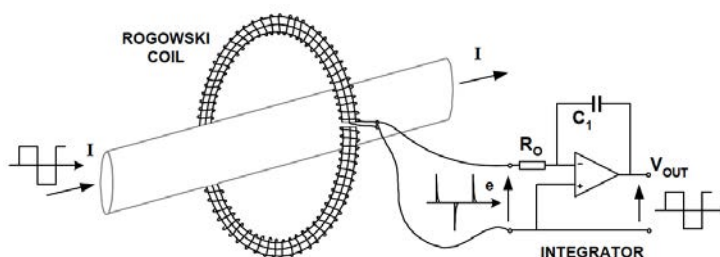
Figure E.9 - current probe Tektronix A622.

The Rogowski current transducer represented in Figure E.10 as some advantages related to the normal transducers, namely: it can measure large currents without saturating. The size of the Rogowski coil required remains the same despite the size of current. This is unlike other current transducers, which become bulkier as the current magnitude increases. For currents of several kA's or more there is really no better alternative than the Rogowski transducer. It has a very wide bandwidth extending from typically 0.1Hz up to 17MHz. It provides an isolated measurement at ground potential similar to other current transducers (except co-axial shunts) i.e. there is no direct electrical connection to the main circuit.

It can measure AC signals superimposed on large DC. The transducer does not measure direct currents - as a result it can measure small AC currents in the presence of a large DC component.



(a) Rogowski device.



(b) Operating principle.

Figure E.10 –Rogowski current transducer operating principle.

### E.4.2. Digital Oscilloscope

High-frequency transients and steady state measurements were made and recorded using a digital oscilloscope of 4 channels with color LCD Display, Tektronix TDS2024 which main features are presented in Table E.1.

### E.4.3. Power supply

A DC power supply model HY3005D-3 is used, which main features are presented in Table E.2. The HY3005S-3 units have four analogue displays allowing the output voltages and currents to be displayed simultaneously. The HY3005S-3 units also have three outputs with one output being fixed at 5V 3A. Both series and parallel connection is possible allowing twice the voltage and current and outputs can be tracked relative to the master output. The highest output is the sum of twice the voltage value in series mode.



Figure E.11 - Digital oscilloscope.



Figure E.12 - DC Power supply.

Table E.1 –Digital oscilloscope characteristics

Parameter	Value
Bandwidths	60 MHz, 100 MHz and 200 MHz
Sample Rates	Up to 2 GS/s
Record Length	2.5 k Points

Table E.2 – DC power supply characteristics.

Parameter	Value
Input voltage	220V or 110V AC $\pm$ 10%, 50Hz or 60Hz,
Output voltage	0 – 30V or 0 - 50V
Output current	2A, 3A or 5A

## REFERENCES

1. *Plug Power*. Available from: <http://www.plugpower.com/>.
2. *Ballard Power Systems*. Ballard Power Systems designs and manufactures clean energy hydrogen fuel cells. ]. Available from: <http://www.ballard.com/>
3. *HELION Hydrogen Power*. Available from: <http://www.helion-hydrogen.com/indexuk.php>
4. *Nexa Power Module User's Manual*, in *Ballard Power Systems Inc.*, B.P.S. Inc., Editor. 2003. p. 114.
5. Meireles M., A.P.M., Simões M. G., *A Comprehensive Review for Industrial Applicability of Artificial Neural Networks*. IEEE Transactions on Industrial Electronics, 2003. **50**(3): p. 585-601.
6. Won-Yong Lee , G.-G.P., Tae-Hyun Yang , Young-Gi Yoon and Chang-Soo Kim *Empirical modeling of polymer electrolyte membrane fuel cell performance using artificial neural networks* International Journal of Hydrogen Energy, 2004. **29**(8): p. 961-966.
7. Ou, S., *Modeling and optimization of PEM fuel cells*, in *Institute of Technology*. 2006, University of Connecticut: Beijing. p. 129.
8. Haque , M.T.a.K.A.M., *Application of Neural Networks in Power Systems; A Review*. World Academy of Science, Engineering and Technology, 2005. **6**: p. 53-57.
9. Kalogirou , S.A., *Artificial neural networks in renewable energy systems applications: a review*. Renewable and Sustainable Energy Reviews, 2001. **5**: p. 373-401.
10. Helion-Hydrogen. <http://www.helion-hydrogen.com/%5D>.
11. Ned Mohan, T.U., William Robbins, *Power electronics, converters, Applications and Design*. Second Edition ed. 1995: John Wiley & sons, Inc. 802.
12. Marian K. Kazimierczuk, D.C., *Power Resoant converter*. 1995.
13. N. Mohan, T.U., *Power Electronics, Converters Applications and Design*. 2003, New York: John Wiley and Sons, Inc.
14. Cheron, Y., *La commutation douce dans la conversion statique de l'énergie électrique* Vol. 1. 1989: Lavoisier. 312.
15. *Safety standard for Hydrogen and Hydrogen Systems*. 1997, National Aeronautics and Space Administration: Washington, DC 20546. p. 389.
16. *Fuel Cell Technologies Program*. Available from: <http://www1.eere.energy.gov/hydrogenandfuelcells/storage/>